Strojniški vestnik

Journal of Mechanical Engineering

VOL 71 ▪ NO 9-10 ▪ Y 2025

50 let
Univerza v Mariboru
FS30
Fakulteta za strojništvo

Strojniški vestnik – Journal of Mechanical Engineering (SV-JME)

Aim and Scope
The international journal publishes original and (mini)review articles covering the concepts of materials science, mechanics, kinematics, thermodynamics, energy and environment, mechatronics and robotics, fluid mechanics, tribology, cybernetics, industrial engineering and structural analysis.
The journal follows new trends and progress proven practice in the mechanical engineering and also in the closely related sciences as are electrical, civil and process engineering, medicine, microbiology, ecology, agriculture, transport systems, aviation, and others, thus creating a unique forum for interdisciplinary or multidisciplinary dialogue.
The international conferences selected papers are welcome for publishing as a special issue of SV-JME with invited co-editor(s).

Editorial Office:
University of Ljubljana, Faculty of Mechanical Engineering
SV-JME, Aškerčeva 6, 1000 Ljubljana, Slovenia
Phone: +386 (0)1 4771 137
info@sv-jme.eu, http://www.sv-jme.eu

Technical Editor: Pika Škraba

Guest Editors of this Special Issue:
Matej Vesenjak, Luka Lešnik, Matej Borovinšek, Simon Klančnik

Print: Grafika Gracer d.o.o. printed in 490 copies

President of Publishing Council:
Mihael Sekavčnik
University of Ljubljana, Faculty of Mechanical Engineering, Slovenia

Vice-President of Publishing Council:
Matej Vesenjak
University of Maribor, Faculty of Mechanical Engineering, Slovenia

Founders and Publishers:
University of Ljubljana, Faculty of Mechanical Engineering, Slovenia
University of Maribor, Faculty of Mechanical Engineering, Slovenia
Association of Mechanical Engineers of Slovenia
Chamber of Commerce and Industry of Slovenia,
Metal Processing Industry Association

Founding Editor:
Bojan Kraut
University of Ljubljana, Faculty of Mechanical Engineering, Slovenia

ISSN 0039-2480, ISSN 2536-2948 (online)

General information:
Strojniški vestnik – Journal of Mechanical Engineering is published in 6 double issues per year.

Institutional prices include print & online access: institutional subscription price and foreign subscription €100,00 (the price of a single issue is €20,00); general public subscription and student subscription €50,00 (the price of a single issue is €10,00). Prices are exclusive of tax. Delivery is included in the price. The recipient is responsible for paying any import duties or taxes. Legal title passes to the customer on dispatch by our distributor. Single issues from current and recent volumes are available at the current single-issue price. To order the journal, please complete the form on our website. For submissions, subscriptions and all other information please visit: *http://www.sv-jme.eu.*

You can advertise on the inner and outer side of the back cover of the journal. The authors of the published papers are invited to send photos or pictures with short explanation for cover content.

Every manuscript submitted to the SV-JME undergoes a peer-review process. We would like to thank the reviewers who have taken part in the peer-review process. SV-JME is indexed / abstracted in: SCI-Expanded, Compendex, Inspec, ProQuest-CSA, SCOPUS, TEMA. The list of the remaining bases, in which SV-JME is indexed, is available on the website.

The journal is subsidized by Slovenian Research and Inovation Agency.

Strojniški vestnik - Journal of Mechanical Engineering is available on *https://www.sv-jme.eu*.

Contents

Strojniški vestnik - Journal of Mechanical Engineering
Volume 71, (2025), Number 9-10
Ljubljana, September-Oktober 2025
ISSN 0039-2480
Published every two months

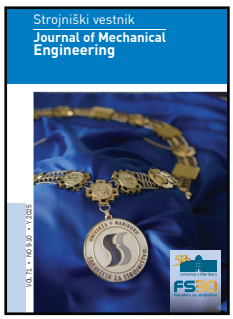

ON THE COVER
This Special Issue features a selection of articles spanning applied fluid mechanics, advanced materials and metamaterials, manufacturing science, and biomedical modelling. The collected works integrate experimental, numerical, and review-based approaches to address contemporary challenges in mechanical engineering. Beyond showcasing the scientific excellence achieved at the Faculty of Mechanical Engineering, University of Maribor, this publication also celebrates the Faculty's enduring mission — to connect knowledge, innovation, and human creativity in shaping a sustainable and technologically advanced future. The cover image depicts the Dean's chain, part of the Faculty's insignia. The photograph symbolizes the Faculty's long-standing commitment to excellence, innovation, and the integration of scientific knowledge in building a sustainable and technologically advanced society. Image courtesy: Assist. Prof. dr. Gregor Harih, Faculty of Mechanical Engineering, University of Maribor

Editorial

Special Issue of the Faculty of Mechanical Engineering, University of Maribor — 30 Years of Excellence in Engineering Research

Matej Vesenjak ✉ – Luka Lešnik – Matej Borovinšek – Simon Klančnik
Faculty of Mechanical Engineering, University of Maribor, Slovenia
✉ tajnistvo.fs@um.si

Abstract *This editorial introduces the Special Issue of the Strojniški vestnik - Journal of Mechanical Engineering dedicated to the 30th anniversary of the Faculty of Mechanical Engineering as an independent member of the University of Maribor, and the 50th anniversary of the University of Maribor. The Faculty of Mechanical Engineering is one of the most successful members at the University of Maribor and is recognised for its excellence in education, research and collaboration with industry. Its history of development, from its early beginnings in 1959 to becoming an internationally active and research-driven institution, reflects a continuous commitment to technological progress and societal impact. The Special Issue presents a selection of articles covering applied fluid mechanics, advanced materials and metamaterials, manufacturing science, and biomedical modelling. The collected works combine experimental, numerical, and review-based approaches to address contemporary challenges in mechanical engineering. This publication not only highlights the scientific excellence achieved at the Faculty of Mechanical Engineering, University of Maribor, but also celebrates its enduring mission to connect knowledge, innovation and human creativity in shaping a sustainable and technologically advanced future.*

Keywords *applied fluid mechanics, computational fluid dynamics (CFD), hydropower systems, advanced materials, metamaterials, triply periodic minimal surfaces (TPMS), biomedical modelling, inverse bioheat problem, intelligent toolpath generation, artificial intelligence in manufacturing*

Highlights

- *Special Issue marks 30 years of Faculty of Mechanical Engineering and 50 years of the University of Maribor.*
- *The contributions cover applied fluid mechanics, materials, manufacturing, and biomedical modelling.*
- *The issue showcases cutting-edge research and technological innovation in mechanical engineering.*
- *It reflects the Faculty's long-standing link between academia and industry and celebrates engineering creativity and multidisciplinary collaboration.*

1 INTRODUCTION

The Faculty of Mechanical Engineering is one of the most successful members of the University of Maribor, recognised for its achievements in education, research, professional and artistic endeavours. One of our key priorities is to strengthen the connection between academia and industry, and to co-create technological progress that drives social transformation. With our broad spectrum of knowledge and experience, we continue to preserve tradition while, simultaneously, embracing the trends of modern society. The planned renewal of infrastructure across the technical Faculties will undoubtedly contribute to the highest quality of research and educational activities in the future.

The origins of mechanical and textile engineering studies in Maribor date back to 1959, when the Technical College was established. In 1973, it evolved into the Higher Education Technical Institution, and, in 1975, it became part of the newly founded University of Maribor, which is celebrating its 50th anniversary this year. In 1985, the Higher Education Technical Institution was renamed to the Faculty of Technical Sciences, and in 1995, it was reorganised into four independent Faculties of the University of Maribor, one of which is the Faculty of Mechanical Engineering, celebrating its 30th anniversary this year.

Our Faculty places great emphasis on international cooperation, which we enrich continuously through numerous projects and collaborations with researchers from around the world. We also encourage students to participate actively in various project-based activities, providing them with valuable theoretical knowledge and practical experience, an excellent foundation for their future careers.

We place great importance on collaboration with national institutions, especially the Faculty of Mechanical Engineering, University of Ljubljana. Although both Faculties differ in their dynamics, strengths and challenges, we share a common vision, demonstrating that engineering truly knows no boundaries.

It is an honour to commemorate our anniversary with the publication of this Special Issue of the Journal of Mechanical Engineering, which, for more than 70 years, has shaped and advanced the field of mechanical engineering and related disciplines significantly, while promoting its recognition and excellence continuously.

Looking ahead, our Faculty will continue to embrace modern technologies, development, and unexplored potentials that represent limitless sources of new opportunities for engineering creativity optimistically. The word technology originates from the Greek word »techne«, meaning the art or skill of making and building. At the Faculty of Mechanical Engineering, University of Maribor, we will continue to build ideas that advance technological progress skilfully, while nurturing the art of building and maintaining a positive working environment, and valuing- human relationships — the true added value behind every achievement.

We will foster connectivity and openness, strengthen interdisciplinary academic networks, and encourage diverse

 DOI: 10.5545/sv-jme.2025.09-10.ed

perspectives that can lead to new insights and innovative solutions. In doing so, we will continue writing stories of success, innovations and progress, bringing science closer to life and creating a better future.

2 SELECTED ARTICLES OVERVIEW

This issue brings together a compact but diverse collection of contributions spanning applied fluid mechanics, advanced materials and metamaterials, manufacturing science, and biomedical modelling. The papers collected here share a common thread: rigorous modelling combined with targeted experiments or comprehensive literature synthesis, all aimed at solving pressing engineering problems with practical relevance.

In the area of hydraulic and turbomachinery flows, Vovk and Ravnik [1] compared 1D Euler-based and full 3D Navier–Stokes approaches to the water-hammer problem, showing how simplified models, if validated carefully, remain powerful engineering tools. On the other hand, the 3D viscous simulations reveal detailed cavitation dynamics and interactions with protective devices such as dynamic combination air valves. Complementing this, Kevorkijan et al. [2] presented a CFD study of particle-driven erosion in Pelton turbine runners: using Lagrangian particle tracking and the Finnie abrasion model, they quantify when sediment loading becomes critical, and where real-world wear is likely to occur, offering insights for design and maintenance in sediment-prone hydropower plants.

Fluid and process engineering are also addressed in the contribution by Založnik and Zadravec [3], who investigated gas flow distribution in fluidised beds using both the Two-Fluid Model enhanced by the Kinetic Theory of Granular Flow (TFM-KTGF) and coupled CFD-DEM simulations. Their results, validated against the experimental data, revealed that common geometric assumptions for gas distribution plates underestimate particle effects on flow distribution significantly. While CFD-DEM offers detailed particle-level resolution, the TFM-KTGF approach emerged as a computationally efficient alternative for large-scale systems

Bridging numerical analysis and healthcare, Horvat and Iljaž [4] addressed an important diagnostic challenge: they solved the inverse dynamic-thermography bioheat problem for skin tumours using a non-Fourier (dual-phase-lag) model and a boundary-element solution strategy coupled with Levenberg–Marquardt optimisation. Their results showed robust retrieval of the tumour parameters (notably the diameter and thermal relaxation time) even with noisy data, pointing to promising improvements in non-invasive early-detection methods.

Materials and structural topics are reported in the paper of Kovačec et al. [5], which presented a systematic industrial trial of rotary flux injection, to remove inclusions and alkali and alkaline-earth trace elements from Al–Mg–Si melts, demonstrating an effective salt-flux formulation that supports higher scrap fractions without compromising cleanliness.

Continuing within the field of metallic materials, Pal et al. [6] investigated the melting behaviour of magnesium during additive manufacturing using experimental testing. The study focused on understanding melt-pool dynamics, solidification characteristics, and potential defect formation mechanisms, which are critical for improving print quality and structural integrity of magnesium components. The results contribute to optimising process parameters and advancing the use of lightweight magnesium alloys in 3D printing applications.

In a materials-oriented review, Žnidarič et al. [7] synthesised the latest knowledge on fatigue behaviour of triply periodic minimal surface (TPMS) metamaterials. The review highlighted why TPMS geometries often outperform conventional lattices under fatigue loading, and clarifies fabrication and material dependent performance trade-offs.

Expanding the metamaterials perspective, the work of Novak et al. [8] provided a comprehensive review of cellular metamaterials, covering two decades of research progress. The article highlights how advanced fabrication methods, such as additive manufacturing and explosive compaction, enable the design of foams, TPMS lattices, and hybrid auxetic structures with tailored mechanical properties. The validated computational models are emphasised as indispensable tools for optimising graded and hybrid designs. Their insights underline the transformative potential of metamaterials for crash absorption, biomedical implants and defence applications.

Manufacturing and process planning received critical attention in Simonič et al [9], a systematic literature review on intelligent toolpath generation. Mapping the evolution from Industry 4.0 towards human-centric Industry 5.0, the authors spotlight AI/ML-driven feature recognition, STEPNC interoperability prospects, and the urgent need to broaden realworld validation and SME-focused adoption strategies.

Finally, the experimental–numerical study by Močilnik et al. [10] examined how pre-setting and deep-rolling sequences affect creep and long-term torque stability in torsion spring bars. Their combined FEM and long-duration tests identified a narrow process window (around moderate pre-setting levels) that balances the enhanced elastic range with acceptable creep. The results can be applicable directly to suspension component design and production.

Taken together, this issue underscores the strength of multidisciplinary engineering in terms of robust numerical tools, thoughtfully designed experiments and careful literature synthesis, which contribute to progress across domains. We thank the authors for their excellent work and the reviewers for their constructive assessments, and hope that the readers will find both inspiration and practical ideas to advance their own projects.

3 CONCLUSION

The articles presented in this Special Issue illustrate the broad scope and scientific excellence of the contemporary engineering research conducted at the Faculty of Mechanical Engineering, University of Maribor. They demonstrate collectively how fundamental understanding, advanced modelling, and innovative experimentation contribute to addressing practical challenges in engineering science, from fluid dynamics and materials development to manufacturing intelligence and biomedical applications.

This collection also symbolises the shared values of curiosity, creativity and collaboration that have defined the Faculty of Mechanical Engineering throughout its 30-year history within the University of Maribor. As we celebrate this milestone alongside the University's 50th anniversary, we reaffirm our commitment to advancing engineering knowledge and fostering connections that bridge academia, industry and society. Looking ahead, the Faculty will continue to support multidisciplinary research, collaboration, cultivate new generations of engineers, and contribute to shaping a sustainable and technologically advanced future.

References

[1] Vovk, N., Ravnik, J. Comparison of 1D Euler equation based and 3D Navier-Stokes simulation methods for water hammer phenomena. *Stroj Vestn-J Mech E* 71 337-348 (2025) **DOI:10.5545/sv-jme.2025.1340**.

[2] Kevorkijan, L., Hriberšek, M., Lešnik, L., Škerlavaj, A., Biluš, I. Numerical investigation of erosion due to particles in a cavitating flow in Pelton turbine. *Stroj Vestn-J Mech E* 71 284-293 (2025) **DOI:10.5545/sv-jme.2025.1351**.

[3] Založnik, M., Zadravec, M. Analysis of gas flow distribution in a fluidized bed using two-fluid model with kinetic theory of granular flow and coupled CFD-DEM: A numerical study. *Stroj Vestn-J Mech E* 71 349-356 (2025) **DOI:10.5545/sv-jme.2025.1365**.

[4] Horvat, I. D., Iljaž, J. Numerical solving of dynamic thermography inverse problem for skin cancer diagnosis based on non-Fourier bioheat model. *Stroj Vestn-J Mech E* 71 271-283 (2025) **DOI:10.5545/sv-jme.2025.1368**.

[5] Kovačec, U., Zupanič, F. Removal of inclusions and trace elements from Al-Mg-Si alloys using refining fluxes. *Stroj Vestn-J Mech E* 71 294-300 (2025) **DOI:10.5545/sv-jme.2025.1371**.

[6] Pal, S., Finšgar, M., Vajda, J., Maver, U., Brajlih, T., Gubeljak, N., Tiyyagura, H.R., Drstvenšek, I. Fusion behaviour of pure magnesium during selective laser melting. *Stroj Vestn-J Mech E* 71 318-327 (2025) **DOI:10.5545/sv-jme.2025.1381**.

[7] Žnidarič, Ž., Nečemer, B., Novak, N., Vesenjak, M., Glodež, S. Fatigue of triply periodic minimal surface (TPMS) metamaterials – A review. *Stroj Vestn-J Mech E* 71 357-368 (2025) **DOI:10.5545/sv-jme.2025.1369**.

[8] Novak, N., Ren, Z., Vesenjak, M. Integrated design, simulation, and experimental validation of advanced cellular metamaterials. *Stroj Vestn-J Mech E* 71 309-317 (2025) **DOI:10.5545/sv-jme.2025.1363**.

[9] Simonič, M., Palčič, I., Klančnik, S. Advancing intelligent toolpath generation: A systematic review of CAD-CAM integration in industry 4.0 and 5.0. *Stroj Vestn-J Mech E* 71 328-336 (2025) **DOI:10.5545/sv-jme.2025.1370**.

[10] Močilnik, V., Gubeljak, N., Predan, J. Effect of presetting and deep rolling on creep of torsion spring bars. *Stroj Vestn-J Mech E* 71 301-308 (2025) **DOI:10.5545/sv-jme.2025.1407**.

Acknowledgement *Gratitude is extended to all the authors for their valuable scientific contributions, and to the reviewers for their constructive and timely evaluations, which ensured the high quality of this Special Issue. Appreciation is also due to the Editorial Board and editorial team of the Journal of Mechanical Engineering for their continuous support and professional collaboration. Special recognition is given to the Faculty of Mechanical Engineering, University of Maribor, for its commitment to research excellence, innovation and education throughout its 30-year history, and to the University of Maribor for fostering an environment that encourages academic and technological advancement. Acknowledgement is also made to colleagues, research groups and students, whose enthusiasm, creativity and dedication continue to shape the Faculty's success. Recognition is likewise extended to our industrial and academic partners, particularly the Faculty of Mechanical Engineering of the University of Ljubljana, for their fruitful collaboration and shared vision. This Special Issue is dedicated to all who have contributed to the development, reputation and excellence of the Faculty of Mechanical Engineering, University of Maribor – past and present.*

Numerical Solving of Dynamic Thermography Inverse Problem for Skin Cancer Diagnosis Based on non-Fourier Bioheat Model

Ivan Dominik Horvat – Jurij Iljaž ✉
University of Maribor, Faculty of Mechanical Engineering, Slovenia
✉ jurij.iljaz@um.si

Abstract *This paper presents numerical solving of the inverse bioheat problem to estimate four skin cancer parameters; diameter, thickness, blood perfusion rate and thermal relaxation time, based on the thermal response on the skin surface obtained by dynamic thermography and numerical skin cancer model, which can greatly enhance dynamic thermography diagnostics. To describe the heat transfer inside biological tissue and thermal behavior during the dynamic thermography process as realistic as possible, the non-Fourier dual-phase-lag bioheat model was used, as well as skin cancer model has been composed of multilayered healthy skin, embedded skin tumor and subcutaneous fat and muscle. Boundary element method has been used to solve a complex non-Fourier bioheat model to simulate dynamic thermography based on the skin cancer model and guessed searched parameters to obtain the thermal response on the skin surface during the cooling and rewarming phase using a cold air jet provocation, which is needed for the solution of the inverse bioheat problem. The inverse problem has been solved by optimization approach using the hybrid Levenberg-Marquardt optimization method, while the measurement data has been generated numerically with known exact tumor parameters and added noise, to evaluate the accuracy and sensitivity of the solution. Inverse problem solution has been tested for two different thermal responses; absolute temperature and temperature difference response, as well as for two different tumor stages; early stage or Clark II and later stage or Clark IV tumor. All important tumor parameters were successfully retrieved, especially the diameter and relaxation time, even for the high level of noise, while the accuracy of obtained parameters is slightly better using absolute temperature response. The results demonstrate the robustness of the method and a promising way for early diagnosis. The findings contribute to improving bioheat modeling in biological tissues, solving inverse bioheat problems and advancing dynamic thermography as a non-invasive tool for early skin cancer diagnosis.*

Key words *numerical modeling, dynamic thermography, inverse problem, non-Fourier bioheat transfer, dual-phase-lag model, boundary element method, Levenberg-Marquardt optimization*

Highlights

- *Non-Fourier dual-phase-lag model improves the heat transfer simulation in skin cancer.*
- *Dynamic thermography with cold air jet detects tumors during cooling and rewarming.*
- *Levenberg–Marquardt algorithm estimates tumor diameter, thickness, perfusion rate, and relaxation time.*
- *Tumor parameters are estimated robustly even with high noise in thermography temperature data.*

1 INTRODUCTION

In recent years due to the development of infrared (IR) cameras, thermography has become an invaluable tool in science and engineering for many heat transfer problems and applications where measuring or monitoring of the temperature is important. IR camera detects thermal radiation emitted from the observed object, which is then converted into electrical signals to produce thermal images or thermograms. The advantage of this technique is that it measures or records the temperature in a contactless manner for the observed object compared to a thermocouple, which must be in direct contact and measures only at one point [1–3]. Of course, the disadvantage of it is that it can only measure the temperature at the surface and you have to accurately define various parameters like the emissivity of the surface, surrounding temperature, relative humidity etc. to measure surface temperature accurately in an absolute manner. However, the obtained thermal image can still be used in the relative manner, meaning that thermography is mostly used and effective to detect temperature changes based on the recorded temperature contrast of the object surface for various scientific and industrial applications [2,4–7]. For its advantage of recording thermal contrast image in non-invasive manner and the ability to screen larger areas it also found its way in various medical application from diagnostic of breast cancer, gynecology, kidney transplantation, heart treatment, fever screening, brain imaging, dentistry, cryotherapy, forensic medicine, laser treatments, burn diagnostics to dermatology [8–17].

Medical IR thermography is based on the principle of bioheat transfer govern by blood perfusion, metabolic activity, tissue conductivity and heat exchange with the environment. Therefore, a physiological or pathological change of the tissue is reflected in the change of the tissue temperature or thermal contrast on its surface that can be easily observed with the IR camera. Therefore, the deviation of the surface temperature can signal inflammation, infection, neurological, vascular or metabolic dysfunction and even malignancy due to the higher blood perfusion rate compared to the surrounding healthy tissue [2,8,18–20]. Thermography is especially effective in detecting lesions near tissue surface, like skin cancer. Skin cancer cells differ from normal cells by growing larger due to their rapid and uncontrolled division. This fast-paced growth requires more energy to maintain cellular functions, a process referred to as metabolism. To meet this increased energy demand, the body initiates angiogenesis, where new blood vessels form from existing ones. Melanoma lesions are, therefore, warmer than the surrounding healthy skin, a key indicator used in diagnostic [21–24]. Because medical IR thermography can identify small temperature differences,

DOI: 10.5545/sv-jme.2025.1368

it can also detect the growth of new blood vessels or metabolic changes associated with tumor development meaning it can also be a valuable tool for drug or treatment evaluation [25]. The most dangerous form of skin cancer is melanoma that can easily spread to other soft tissues, for which is fatal and responsible for about 75 % of all skin cancer-related deaths [18]. According to Clark et al. [26] and Breslow [27], there is a direct correlation between the survival rate and invasiveness or depth of the melanoma. Clark classified melanoma into five levels from I to V, which is still used nowadays. Clark I and II represent an early stage with more than 72.2 % survival rate, for which an early detection or diagnostic is very important factor to improve the survival in patients with malignant melanoma [26].

Currently, the detection of melanoma mainly relies on a subjective asymmetry, border, color, diameter, evolution (ABCDE) test [28] performed visually by dermatologists, general practitioners or primary care physicians. The ABCDE test provides a qualitative guideline, and it requires a trained specialist to distinguish malignant lesions from benign nevi. Moreover, the ABCDE approach has a relatively high false-alarm probability and moderate detection probability [29]. Since a false negative can lead to metastasis and death, excisional biopsies are routinely performed even on lesions that are non-cancerous [30]. For these reasons, medical IR thermography, especially dynamic thermography, is an emerging promising new technique offering a fast, painless, non-invasive and radiation-free method for early skin cancer diagnosis with high sensitivity and specificity that can achieve rates of up to 99 % [2,18,31].

Medical IR thermography can be done in two ways, first as a static or passive and secondly as dynamic or active thermography. Static thermography obtains the thermal contrast image or thermograms of the skin or tissue under the steady-state condition, while dynamic thermography uses thermal stimulus of the tissue by controlled cooling or heating and observing thermal response of the tissue during the recovery period [17–19,31–34]. Static thermography relies on the natural temperature difference between a tissue and its surroundings, with focus on detection of abnormal temperature variations, which may indicate underlying health concerns. Despite being the most used measurement strategy, it is in certain ways limited. Factors such as bone structure, distribution of blood vessels, recent food or beverage intake, patient positioning, time of day and hormonal cycles can all affect accuracy of this measurement strategy [17,31,35,36]. Feasibility in routine medical practice is further reduced by strict measurement protocols that have been proposed and the need for temperature-controlled rooms where the patient has to acclimatize [17,37]. On the other hand, dynamic thermography can provide quantitative data about investigated tissue, by transient behavior of the tissue due to the thermal stimulus and increased thermal contrast due to the changed rate of bioheat transfer during recovery phase. There are also various ways of stimulating the observed tissue, some of them using conductive heat transfer, electromagnetic radiation or convective heat transfer [17,31]. The most common used thermal stimulus is cooling the tissue with cold gel packs or cold metal disk [19,38–40], and convection cooling using cold air jets [18,33,41]. Research shows that dynamic thermography has multiple advantages over static one. First, the temperature contrast during the recovery phase is increased, making the diagnostic process more accurate, as well as more information about the tissue properties or deep lesion can be retrieved. Secondly, there is no need for the patient to acclimatize or to have a special temperature-controlled room, making the examination period much shorter [17–19,29,31].

Focusing on skin cancer or skin disease diagnosis, medical IR thermography can reach its full diagnostic value potential when paired with accurate bioheat modeling to solve direct and inverse problems [20,42–45]. Strąkowska et al. [19,20] uses simplified one-dimensional (1D) multilayered skin model to evaluate blood perfusion rate and thermal parameters of the skin tissue based on the temperature response of active thermography. Luna et al. [46] used a simple 2D numerical model composed of tumor and healthy surrounding skin to identify thickness and blood perfusion rate of the tumor based on the static thermography information. Similar model has been used by Partridge and Wrobel [47,48] to estimate blood perfusion parameters of the skin tumor, size and position using steady-state skin temperature profile, as well as, Fu et al. [49] to estimate the size and position of the circular tumor or multiple tumors using meshless generalized finite difference method combined with a hybrid optimization algorithm. Bhowmik and Repaka [42] upgraded the skin cancer model to 3D multilayered one to estimate tumor diameter, thickness, blood perfusion rate and metabolic heat generation. Bhowmink et al. [50] also included thermally significant blood vessels into their 3D multilayered skin tumor model to evaluate the effect of blood vessels on finding the position and size of the tumor. Cheng and Herman [43] used simplified 2D multilayered skin tumor model to investigate numerically what type of cooling approach would give the highest temperature contrast between the skin tumor and healthy skin during the recovery phase of dynamic thermography. Çetingül and Herman [33,44] used a more realistic 3D multilayered skin lesion model to evaluate model parameter and tumor shape sensitivity on dynamic thermography temperature contrast. Similar model has also been used by Bonmarin and Gal [51] on investigating lock-in dynamic thermography for detection of early-stage melanoma, as well as Iljaž et al. [52] to solve inverse bioheat problem to evaluate tumor size, blood perfusion rate and metabolic heat generation based on dynamic thermography thermal contrast. Later they improve the skin tumor model by including thermoregulation of the blood perfusion rate to simulate dynamic thermography [53] and solve inverse bioheat problem to evaluate several tumor parameters [45]. All the mentioned models to supplement dynamic or static thermography are based on the Pennes bioheat model that has significant limitations, including the assumption of uniform blood perfusion, the neglect of blood flow direction and countercurrent heat exchange, and the treatment of arterial blood as a constant value [54]. A major drawback of the Pennes model is the assumption of infinite heat propagation speed, which disregards thermal lag effects that become critical in conditions with large heat fluxes in a relatively short period of time especially in inhomogeneous biological structures [55–59]. In those scenarios, Fourier-based bioheat models generally tend to fail in fully capturing the process of heat propagation.

To address the limitations of traditional bioheat transfer models, non-Fourier models have been developed to account for thermal lag and microscale heat transfer effects. Maybe the most important non-Fourier bioheat model is the dual-phase-lag (DPL) model [60,61] introducing a relaxation time for heat flux and temperature gradient and has been used in many bioheat transfer applications, like laser irradiation during hyperthermia treatment, brain tissue heating during laser ablation and nano-cryosurgery [62–64]. DPL model can describe more complex bioheat transfer considering many effects that classical Pennes model cannot describe, however, it has not been used so extensively due to the hyperbolic behavior of the model and its complexity to solve it numerically, as well as unknown tissue relaxation times. The most important research has been done by Liu and Chen [65] investigated the DPL model in a bi-layer spherical tissue domain, using experimental data to estimate relaxation times and demonstrating that the DPL model better captures non-Fourier thermal behavior compared to classical bioheat transfer models, particularly in scenarios involving rapid thermal processes and finite thermal wave propagation. Similar Zhang et al. [66] used

the DPL model to study non-Fourier heat conduction in biological tissues during pulsed laser irradiation. Kishore and Kumar [67] tried to estimate thermal relaxation parameters numerically in laser-irradiated living tissue. All these papers still use very simple tissue models, usually composed out of single or double layer as 1D or 3D axisymmetric problem and constant thermal relaxation parameters.

The literature review highlights that most existing thermography-based skin cancer models rely on the classical Pennes bioheat equation, which assumes uniform perfusion, constant arterial conditions, and infinite heat propagation speed. Such assumptions neglect tissue heterogeneity, blood flow direction, and thermal lag, leading to limitations when modeling rapid transient processes in multilayered biological tissues. Although the non-Fourier dual-phase-lag bioheat model has been introduced in other biomedical contexts, it has not been extensively applied to skin cancer thermography, particularly for inverse problem formulations and the estimation of multiple tumor parameters in realistic geometries.

In this study, these gaps are addressed by applying a non-Fourier dual-phase-lag bioheat model in an axisymmetric multilayered skin tumor domain and formulating the inverse problem using a boundary element method solver combined with a Levenberg–Marquardt optimization approach. The paper is organized as follows: Section 2 introduces the model geometry, governing equations, boundary conditions, and numerical implementation, as well as describes the inverse problem formulation and optimization framework. Section 3 presents the results and discussion, and Section 4 concludes the work with key findings. Overall, this work contributes to the field of mechanical engineering by advancing thermal modeling of heterogeneous biological tissues and providing a more rigorous framework for non-invasive diagnostics using dynamic thermography.

2 METHODS AND MATERIALS

2.1 Skin Cancer Model

An axisymmetric multilayered numerical model of skin cancer is developed based on our previous work [45,53,68], work of Çetingül and Herman [44], Cheng and Herman [43] and Bhowmik and Repaka [42]. The novelty here is that the model uses non-Fourier DPL bioheat governing equation proposed by Tzou in 1990 [60] making it more general and adapted to the complex bioheat behavior, tissue non-homogeneity and other effects by adjusting the relaxation time parameter. The model presented here is used for dynamic thermography simulation by getting the tumor thermal response.

The most common thermal stimulus for dynamic thermography is cooling the tissue by applying cold gel packs, metal blocks, water immersion, alcohol sprays and even Peltier devices to control the cooling temperature [17,19,38,39,69,70]. The disadvantage of these cooling techniques is that we cannot monitor or record the thermal contrast or response during the cooling period, which can give us additional information about the investigated tissue [68]. Therefore, in this paper we are proposing to use convective cooling approach by temperature adjustable airflow like Ranque-Hilsch vortex tube [18,41]. This way, we can monitor thermal response of the tissue during the cooling and rewarming period of dynamic thermography revealing more information about the investigated tissue, which is needed for successful solving of the inverse problem.

2.1.1 Geometry

Skin cancer model is composed of six distinct layers, each with its own thermophysical properties; epidermis, papillary dermis and reticular dermis representing the skin, subcutaneous fat, muscle and tumor, making model more realistic. Çetingül and Herman [44] concluded that the shape of the tumor has little effect on the temperature response on the skin surface during the rewarming period and that most important parameters are average volume and thickness. Therefore, the tumor is represented by cylindrical shape where diameter and thickness represent its effective values. The surrounding healthy tissue has also been modeled with cylindrical shape with the lesion in the center, as can be seen from Fig. 1 showing the whole computational domain of the model. Because of the cylindrical geometry of the domain and skin tumor, as well as adiabatic boundary conditions at the side, the bioheat problem has been treated as an axisymmetric one. This reduces the computational cost due to the computational mesh dimension reduction, which is very important for inverse problem solving. Discretization of an axisymmetric computational domain needed for the numerical simulation, is therefore done with only 2D cross sectional discretization along the rotational axis, as shown in Fig. 2. This drastically reduces the number of computational elements and nodes, speeding up the computational time.

The dimension of the tumor for Clark II and Clark IV has been chosen based on our previous work [45,52,68] and for both examples are gathered in Table 1 together with the layer thicknesses that have been taken from [42–45,53]. The size of computational domain diameter D has been evaluated based on the comparison of temperature contrast from the dynamic thermography simulation, aiming to reduce the effect of adiabatic boundary conditions at the side. The appropriate and chosen domain diameter is D = 40 mm, while the height of the skin model is the sum of the heights of all layers and is H = 11.6 mm.

2.1.2 Non-Fourier DPL Model

In the wave theory of heat conduction, the heat flux and the temperature gradient, are assumed to occur at different times. In 1990, Tzou [60] introduced the DPL model with the aim of eliminating the precedence assumption in the Cattaneo–Vernotte model. It allows either the temperature gradient (cause) to precede the heat flux (effect) or the heat flux (cause) to precede the temperature gradient (effect) in the transient process. This can be mathematically represented by [60]:

$$\mathbf{q}\left(\mathbf{r},t+\tau_q\right)=-\lambda\nabla T\left(\mathbf{r},t+\tau_T\right), \tag{1}$$

where $\mathbf{q}$ is the heat flux, $\mathbf{r}$ an arbitrary space vector, t the physical time, λ the thermal conductivity, $T=T(\mathbf{r},t)$ the temperature, ∇ is the nabla operator, τ_q relaxation time of the heat flux and τ_T is the relaxation of the temperature gradient. Relaxation time of the heat flux can be also written as $\tau_q=\alpha/C_2$, where α is the thermal diffusivity and C the thermal wave speed. For the case of $\tau_T > \tau_q$, the temperature gradient established across a material domain is a result of the heat flux, implying that the heat flux vector is the cause and the temperature gradient is the effect. For $\tau_T < \tau_q$, heat flux is induced by the temperature gradient established at an earlier time, implying that the temperature gradient is the cause, while the heat flux is the effect.

In a local energy balance, the energy conservation of bioheat transfer is described as [71]:

$$-\nabla\cdot\mathbf{q}+\rho_b w_b c_b(T_b-T)+q_m=\rho c\frac{\partial T}{\partial t}, \tag{2}$$

where ρ is the tissue density, c the specific heat of the tissue, ρ_b the blood density, c_b the specific heat of the blood, w_b the blood perfusion rate, q_m the metabolic heat generation and T_b the arterial blood temperature. The first term on the left-hand side represents heat conduction or diffusion, second term the heat exchange between blood and tissue due to blood perfusion that acts like temperature dependent heat source, the third term the heat generation due to

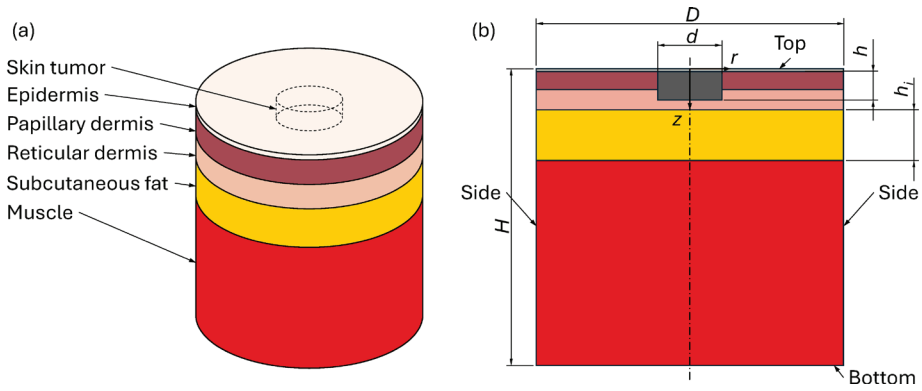

Fig. 1. Computational domain of the axisymmetric multilayered skin tumor model; a) isometric view with named tissues and b) cross sectional view with dimensions and boundary names

the metabolic activity and the term on the right-hand side the heat accumulation. The heat exchange between the arterial blood flow and the tissue proposed Pennes in 1948 [72] who assumed that it happens on the capillary level due to the large interface area. Therefore, the blood perfusion rate represents the volumetric blood flow rate through the capillary network and small arterioles per tissue volume and is non-directional.

Applying first-order Taylor series expansion of the Eq. (1), while neglecting higher-order terms, we can rewrite the definition of the heat flux as:

$$\mathbf{q}(\mathbf{r},t)+\tau_q\frac{\partial\mathbf{q}}{\partial t}(\mathbf{r},t)=-\lambda\left\{\nabla T(\mathbf{r},t)+\tau_T\frac{\partial\nabla T(\mathbf{r},t)}{\partial t}\right\}. \tag{3}$$

Implementing Eq. (3) to the Eq. (2) yields the (type I) DPL equation of bioheat transfer [61,68]:

$$\tau_q\rho c\frac{\partial^2 T}{\partial t^2}+\left(\rho c+\tau_q w_b\rho_b c_b\right)\frac{\partial T}{\partial t}=$$
$$=\lambda\nabla^2 T+\tau_T\lambda\frac{\partial\nabla^2 T}{\partial t}+w_b\rho_b c_b(T_b-T)+q_m, \tag{4}$$

where heat conductivity of the tissue and metabolic heat generation assumed to be constant; λ = const. and q_m = const. The first term on the left-hand side of the Eq. (4) represents the hyperbolic term that captures thermal inertia due to the finite speed of heat propagation, which is otherwise not present in the bioheat models using Fourier law of heat conduction. The second term on the left-hand side is the energy storage term from the classical heat conduction, that is now extended to account for the delayed effect of blood perfusion on heat transfer. The first term on the right-hand side represents classical heat conduction, while the second term, which is the mixed-derivative term dramatically alters the fundamental characteristics of heat propagation, by removing the wave behavior of the hyperbolic type of equation becoming parabolic in its nature. In the case of $\tau_q=0$ and $\tau_T=0$ or $\tau_q=\tau_T$, the DPL model reduces to the classical Pennes equation.

The non-Fourier DPL bioheat model given by Eq. (4) is written for each layer or tissue of the skin cancer model, assuming constant material properties and parameters. Equilibrium and compatibility conditions have to be prescribed at the interface between two adjoint tissues to describe the bioheat transfer in the whole computational domain. The compatibility condition at the interface is:

$$T_i(\mathbf{s},t)=T_{i+1}(\mathbf{s},t), \tag{5}$$

where indices i and $i+1$ represent adjoint layers and $\mathbf{s}$ position vector of the interface boundary. This condition represents that there is no contact resistance between the layers. While equilibrium condition represents the conservation of energy and is written as:

$$\mathbf{q}_i(\mathbf{s},t)\cdot\mathbf{n}_i=\mathbf{q}_{i+1}(\mathbf{s},t)\cdot\mathbf{n}_{i+1}, \tag{6}$$

where $\mathbf{n}$ represents the normal vector. By applying definition of the heat flux given by Eq. (3) to the equilibrium condition, it can be rewritten in the following form:

$$\left[-\lambda_i\left(\nabla T_i+\tau_{T,i}\frac{\partial\nabla T_i}{\partial t}\right)-\tau_{q,i}\frac{\partial\mathbf{q}_i}{\partial t}\right]\cdot\mathbf{n}_i=$$
$$\left[-\lambda_{i+1}\left(\nabla T_{i+1}+\tau_{T,i+1}\frac{\partial\nabla T_{i+1}}{\partial t}\right)-\tau_{q,i+1}\frac{\partial\mathbf{q}_{i+1}}{\partial t}\right]\cdot\mathbf{n}_{i+1}, \tag{7}$$

which is complex and not easy to implement. For the example when $\tau_{q,i}=\tau_{q,i+1}$ and $\tau_{T,i}=\tau_{T,i+1}$ the equilibrium condition can be rewritten in the form $-\lambda_i\nabla T_i\cdot\mathbf{n}_i=-\lambda_{i+1}\nabla T_{i+1}\cdot\mathbf{n}_{i+1}$ which is well known equilibrium condition in heat transfer.

2.1.3 Boundary Conditions

Because the bioheat problem has been treated as axisymmetrical, the tissue temperature and other field functions like heat flux has been transformed from classical cartesian coordinate system to cylindrical one which does not depend on the angle; $T(x,y,z,t) \rightarrow T(r,z,t)$, and where r represents the radial distance from the center and z the depth from the top of domain.

To simulate dynamic thermography, it is essential to define appropriate initial and boundary conditions for the computational domain. For the bottom section of the domain, Dirichlet boundary condition is applied. This choice is based on the assumption that the muscle tissue is thick enough to preserve body core temperature throughout both the cooling and warm-up phases. Therefore, at the bottom we prescribed the following condition:

$$T(r,z,t)=T_{bc},\quad z=H,\quad 0\le r\le D/2,\quad 0\le t\le t_{sim}, \tag{8}$$

where T_{bc} is the body core temperature and $t_{sim}=t_{cool}+t_{warm}$ is the total simulation time, which is composed of the cooling time t_{cool}, and the warm-up time t_{warm}. The body core temperature can vary between 36.5 °C to 37.5 °C and has chosen to be $T_{bc}=37$ °C, as this is considered to be the average core body temperature of a healthy person at rest [17,44,52].

On the sides of the domain we prescribed adiabatic boundary condition, based on the assumption that there are no side effects that will influence the thermal contrast of the lesion:

$$\mathbf{q}(r,z,t)=0\rightarrow\frac{\partial T}{\partial r}(r,z,t)=0,\ 0\le z\le H,\ r=D/2,\ 0\le t\le t_{sim}, \tag{9}$$

To simulate cooling with the cold air jet and rewarming period, we prescribed Robin boundary condition as:

$$\mathbf{q}(r,z,t)=\frac{\partial T}{\partial r}(r,z,t)=\alpha\left(T(r,z,t)-T_\infty\right),$$
$$z=0,\quad 0\le r\le D/2,\quad 0\le t\le t_{sim}, \tag{10}$$

where α represents the heat transfer coefficient of the cooling air jet during the cooling time or the heat transfer coefficient to the environment during the rewarming time, and T_∞ denotes the temperature of the cooling jet or ambient temperature. During the cooling phase, the heat transfer coefficient was set to $\alpha=50$ W/(m^{2}K) and the temperature of the cold air jet to $T_\infty=5$ °C. After cooling time t_{cool}, the cold air jet is removed, and rewarming occurs due to metabolic heat production, blood perfusion and heating from the environment. In the rewarming phase, the heat transfer coefficient is reduced to $\alpha=10$ W/(m^{2}K), and the ambient temperature is set to $T_\infty=22.4$ °C which is the same condition used for the steady-state simulation and is based on the following work [33,45,52,68].

The total simulation time has been set to $t_{sim}=80$ s, with the cooling phase lasting $t_{cool}=30$ s and the rewarming phase $t_{warm}=50$ s. The choice of a 30 s cooling phase is based on the work of Godoy et al. [73] that used a rewarming duration of $t_{warm}=120$ s. We deliberately opted for relatively short cooling and rewarming times compared to other studies [42,52], as our primary focus is to examine the thermal behavior of tissue under highly transient conditions, and to shorten the examination period of the dynamic thermography.

The initial temperature condition $T(r,z,t=0)$ was set to the steady-state solution of the bioheat problem, determined by the boundary conditions specified with Eq. (8) to Eq. (10). This approach assumes that the patient has already acclimated to the conditions in the examination room.

2.1.4 Model Parameters

Material properties for each tissue layer can vary a lot and are not determined exactly as stated by Çetingül and Herman [44]. Therefore, the material properties have been taken as an average value found in the literature and can also be found in the work of other authors [33,42-45,52]. For tumor with different stages, we assumed and prescribed the same material properties, due to the lack of more precise data; therefore, stage differs only with the size of the tumor as suggested by Clark [26]. Table 1 gathers the material properties like density, specific heat, blood perfusion rate, relaxation times etc., used in the presented skin tumor model together with the tissue dimensions.

Relaxation times τ_q and τ_T needed for the non-Fourier DPL bioheat model remains challenging to define exactly due to the lack of experimental data, significant variability and ongoing debate. For processed meat, these values are estimated to be $\tau_q=14$ s to 16 s and $\tau_T=0.043$ s to 0.056 s, while for muscle tissue from cow have shown values $\tau_g=7.36$ s to 8.43 s and $\tau_T=14.54$ s to 21.03 s [65,74]. The relaxation times τ_q and τ_T in this work were determined based on the expressions provided in the generalized DPL model by Namakshenas et al. [59] that is based on the tissue porosity as well. However, in this work the influence of porosity is taken into account through effective tissue properties instead. The relaxation times τ_q and τ_T can be estimated using the following expressions [59]:

$$\tau_q = \frac{\varepsilon(1-\varepsilon)}{\left[\frac{\varepsilon}{c_{tb}}+(1-\varepsilon)\right]}\frac{\rho_b c_b}{G}, \tag{11}$$

$$\tau_T = \frac{\varepsilon(1-\varepsilon)}{\left[\frac{\varepsilon}{\lambda_{tb}}+(1-\varepsilon)\right]}\frac{\rho_b c_b}{G}, \tag{12}$$

where $c_{tb}=\rho c/\rho_b c_b$ represents the stored energy of the tissue relative to that of the blood, while $\lambda_{tb}=\lambda/\lambda_b$ denotes the thermal conductivity of the tissue compared to the blood. G is the coupling factor between the tissue and blood, defined as [59]:

$$G = \frac{4\varepsilon\lambda_b}{d_b^2}Nu + \rho_b w_b c_b, \tag{13}$$

where Nu is the Nusselt number and d_b the representative artery diameter of the tissue.

The thermal relaxation time τ_q for all layers, except the tumor and epidermis, was determined based on Eq. (11) by prescribing Nusselt number to $Nu=4.93$ and artery diameter to $d_b=1.5$ mm, representing average value for the skin and muscle.

For tumor layer we assigned a higher τ_q value than the other tissues to reflect its increased perfusion rate and structural inhomogeneity [75], therefore, we set it to $\tau_q=3.0$ s for the tumor. In contrast, the epidermis, which lacks blood vessels and is more uniform than other tissue layers, was given a lower thermal relaxation time. We set τ_q for the epidermis to $\tau_q=0.3$ s, assuming that despite its homogeneity, it still introduces some thermal resistance due to delayed heat transfer. The values for τ_T were selected based on the stability criteria for DPL presented by Quintanilla and Racke [76]. In this study, τ_T was chosen to be half of τ_q, with $\tau_T/\tau_q=1/2$, in order to satisfy the stability limits commonly associated with higher-order Taylor series expansions. The values chosen for the τ_q and τ_T for each tissue are also gathered in Table 1.

The arterial blood temperature needed for governing equation is assumed to be as equal as defined body core temperature; $T_b=T_{bc}=37.0$ °C.

2.1.5 Solver and Discretization

Presented multilayered skin cancer model based on the non-Fourier DPL bioheat equation to simulate dynamic thermography is highly non-linear and numerically difficult to solve. For this reason, we wrote our own solver based on the subdomain BEM approach using elliptic axisymmetric fundamental solution and quadratic elements, which has been tested on bench-mark problems of other authors [77-79]. A detailed description of the solver and numerical discretization of non-Fourier DPL model with the treatment of equilibrium condition at the interface can be found in our previous work [68]. The maximum number of non-linear steps for dynamic thermography simulation and inverse bioheat problem was set to $l_{max}=20$, with a maximum error tolerance of $\varepsilon=1\cdot10^{-8}$.

To discretize computational domain, we used our own 2D structured mesh generator with the representative spatial element size of $\Delta r=\Delta z=0.5$ mm, with minimal number of 2 elements in z direction in each layer. A non-uniform mesh was used with an expansion factor of $\zeta=1.1$ in both spatial directions from the center. The reason for using own mesh generator is due to the inverse problem solving, where diameter and thickness of the tumor is changing during the optimization process where generation of a new mesh must be done. For the Clark II example, the computational mesh consists of 360 computational cells and 1517 computational nodes, while for the Clark IV example the mesh includes 442 computational cells and 1855 nodes and is presented in Fig. 2. The difference in mesh density between these two examples is because of different tumor sizes, generating different element sizes for tumor discretization, which affects the size of the structured mesh for the whole computational domain. Presented mesh density has been confirmed to be adequate following a mesh sensitivity study. Similar, by time step sensitivity analysis, we define the time step needed to describe the transient behavior of the model. For time discretization of $t_{sim}=80$ s a constant time step of $\Delta t=0.5$ s has been taken.

Table 1. Tissue dimensions and material properties of the skin cancer model

Layer	d [mm]	h [mm]	ρ [kg/m^3]	c_p [J/(kg K)]	λ [W/(mK)]	w_b [s^{-1}]	q_m [W/m^3]	τ_q [s]	τ_T [s]
Epidermis	–	0.1	1200	3589	0.235	–	–	0.30	0.15
Papillary Dermis	–	0.7	1200	3300	0.445	0.0002	368.1	2.28	1.14
Reticular Dermis	–	0.8	1200	3300	0.445	0.0013	368.1	2.46	1.23
Fat	–	2.0	1000	2674	0.185	0.0001	368.3	2.16	1.08
Muscle	–	8.0	1085	3800	0.510	0.0027	684.2	2.22	1.11
Blood	–	–	1060	3770	–	–	–	–	–
Tumor Clark II	2.0	0.44	1030	3852	0.558	0.0063	3680	3.00	1.50
Tumor Clark IV	2.5	1.1	1030	3852	0.558	0.0063	3680	3.00	1.50

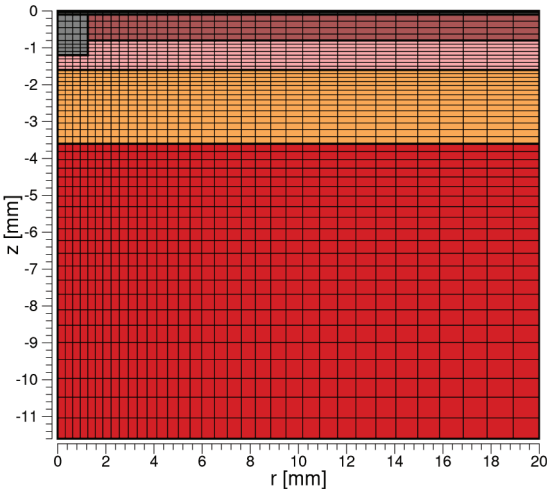

Fig. 2. 2D computational mesh representing axisymmetric cylindrical domain for Clark IV example

2.2 Inverse Bioheat Problem

When the numerical simulation of certain processes or phenomena is needed, we are talking about direct problem. For example, the simulation of dynamic thermograph is direct bioheat problem, where we must prescribe governing equation of the process, geometry, all material or model properties and boundary conditions describing the process. These problems are well-posed, meaning that they have a unique and stable solution that can be obtained using established numerical or analytical methods. However, when certain parameters, such as material properties, boundary conditions or internal sources, are unknown and must be estimated from indirect measurements, we encounter what is known as inverse problem. Inverse problems seek to determine unknown inputs based on observed outputs. Their solution depends on the mathematical model used and is often sensitive to measurement noise or model inaccuracies, which can lead to instability or non-uniqueness of the solution, characteristics that make inverse problems ill-posed by nature [42,45–47,52,80,81].

To solve inverse problem an optimization approach has been used. The inverse problem is transformed to optimization process by objective function that measures the difference between simulated temperature response and actual measurement data. The solution of the inverse problem is represented by the minimum of the objective function. A well-posed inverse problem should have only one global minimum; otherwise, the solution is not unique, making parameter estimation unreliable [42,45,52].

This paper covers two test examples; Clark II and Clark IV, to evaluate their important properties based on two different thermal responses of the tissue, first the absolute temperature; T_{abs}, and second the temperature difference regarding to the healthy skin; ΔT. Therefore, this paper covers four different inverse problems, to evaluate the feasibility of early skin cancer diagnosis and solution sensitivity regarding to type of the recorded thermal image.

2.2.1 Measurement Data

Dynamic thermography measurements have been generated numerically by solving direct bioheat problem with known searched parameters and by adding a measurement noise to simulate more realistic measurement data and not to commit inverse crime.

First test example uses early stage (Clark II) skin tumor with the following searched parameters; d=2.0 mm, h=0.44 mm, w_b=0.0063 s^{-1}, τ_q=3.0 s, and the second one the later stage (Clark IV) tumor with the following searched parameters; d=2.5 mm, h=1.1 mm, w_b = 0.0063 s^{-1}, τ_q=3.0 s, that has already been introduced in Section 1 and gathered in Table 1. These parameters are written here again due to clarity, because they represent the exact values of the considered inverse problems.

Thermal response during the dynamic thermography has been recorded in two ways, first as an absolute temperature value and second as the temperature difference. Fig. 3 shows the absolute temperature response of simulated dynamic thermography for Clark II and Clark IV tumor, while Fig. 4 and 5 show the temperature difference response. As can be seen, the temperature contrast or difference between the tumor temperature and surrounding healthy skin is increased during the cooling phase by almost two times, compared to the steady-state conditions. This is the advantage of dynamic thermography. The temperature spatial profile is the same regarding the absolute or temperature difference response, while the transient behavior is different, as can be seen from Fig. 3 and 4. For better understanding, Fig. 5 is simulating the processed IR image at the end of the cooling phase together with the tumor dimension, where enhanced contrast of dynamic thermography is obtained. It can be observed that early-stage tumors produce lower temperature contrast than later-stage ones meaning it can be harder to detect and diagnose.

Measurement data obtained at the surface of the skin z=0 for position p and time t can be written as:

$$T_{abs,s,p,t} = T(r_p, 0, t_t), \tag{14}$$

$$\Delta T_{s,p,t} = T(r_p, 0, t_t) - T(D/2, 0, t_t), \tag{15}$$

where index s represents simulation, r_p the radial position of the measurement points and t_t the time of the measurement taken. Measurement data resolution is very important for successful parameter estimation, as it needs to describe the temperature response adequately. The measurement points have been taken in the radial range of $r_p \in [0\text{ mm}, 5\text{ mm}]$ at n_p=6 equally spaced points meaning that the distance between two measurement points is δ_r=1 mm. While for the time measurement the data has been taken during cooling, as well as rewarming period of dynamic thermography; $t_t \in [0\text{ s}, 80\text{ s}]$ at intervals of δ_t=1 s generating n_t=81 time measurement

points. We notice that this measurement resolution is fine enough to capture tissue temperature response and to be able to evaluate tumor parameters. Finer resolution did not increase the accuracy of the searched parameters, while coarser resolution, especially in time domain, increased the error in the estimated parameters.

To mimic real measurement data a white noise has been added to the generated measurement data as:

$$T_{abs,m,p,t} = T_{abs,s,p,t} + \eta \Delta T_{err}, \tag{16}$$

$$\Delta T_{m,p,t} = \Delta T_{s,p,t} + \frac{\eta}{2} \Delta T_{err}, \tag{17}$$

where η represents a random number; $\eta \in [-1, 1]$, index m stands for measurement data and ΔT_{err} the temperature uncertainty level. The second term on the right-hand side represents the temperature deviation or noise. Modern IR cameras can obtain noise equivalent temperature difference (NETD) value of less than 30 mK. Therefore, we investigate test examples under three levels of uncertainty; 0 mK, 25 mK and 50 mK [45,52]. The first one represents exact measurement data, while the last two represent low and high level of noise. In the last two cases, the measurement data does not follow numerical model anymore and therefore no inverse crime is committed. Because the noisy measurement data are generated randomly, we generated three different measurement sets for each test example and noise level, except for the exact one. This way we can also analyze how the randomness of the added white noise affects the inverse solution.

For a clear presentation Fig. 6 shows the generated measurement data compared to the simulated dynamic thermography response or exact data for Clark II and Clark IV test example. As can be seen, the level of noise can affect the temperature response for the Clark II more than for Clark IV, which makes solving inverse problem more difficult and poor accuracy to be expected for early-stage tumor.

2.2.2 Objective Function

Objective function measures the difference between simulated temperature response of dynamic thermography by guessed searched parameters and generated measurement data in our case. Therefore, the objective function for the absolute temperature response can be defined as:

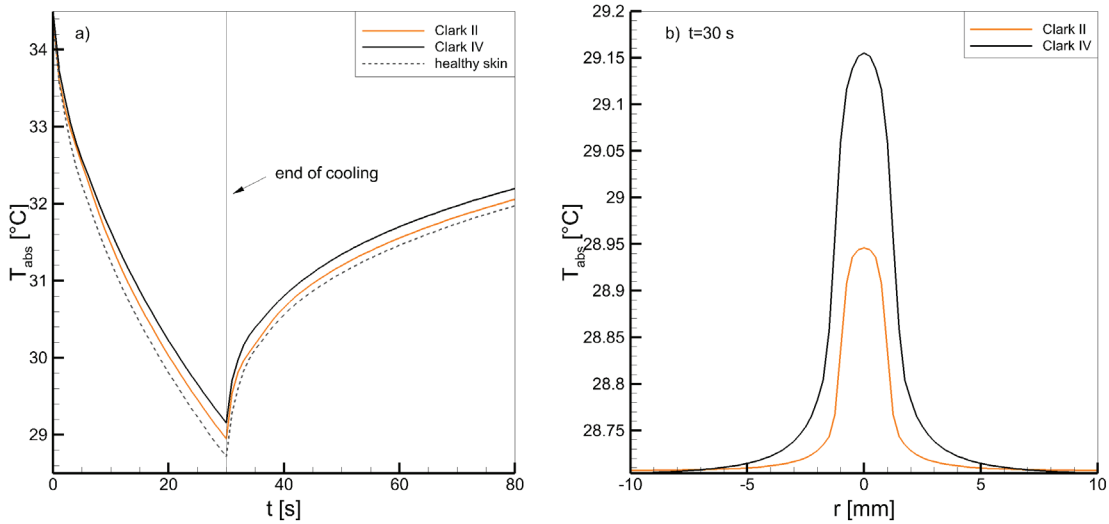

Fig. 3. Simulated absolute temperature response $T_{abs,s}$ at the skin surface for Clark II and Clark IV tumor during dynamic thermography: a) transient response for tumor position $r = 0$ and healthy skin at position $r = D/2$, and b) radial temperature distribution at the end of cooling phase $t = 30$ s

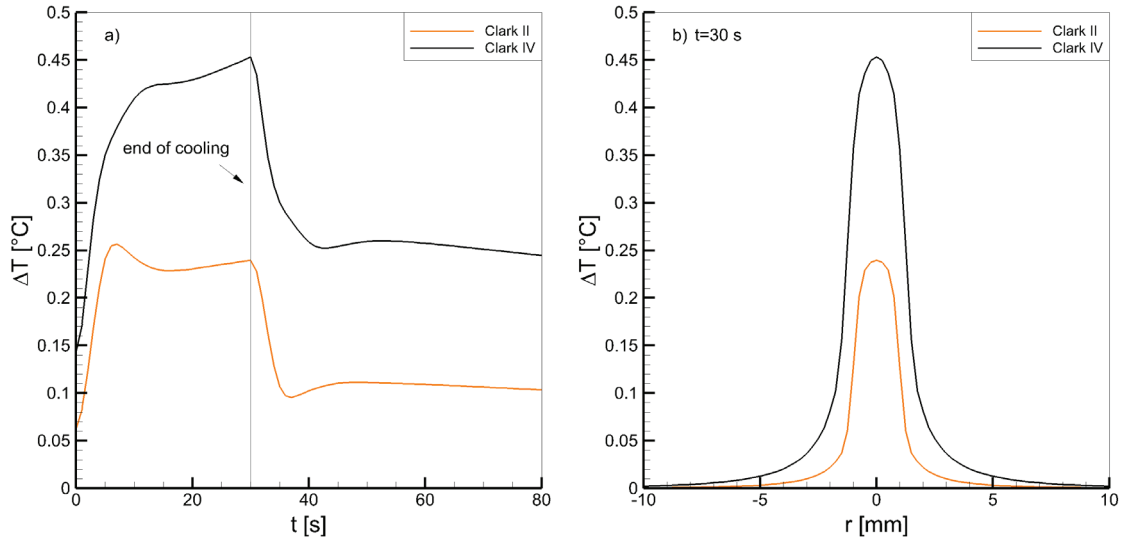

Fig. 4. Simulated temperature difference response ΔT_s at the skin surface for Clark II and Clark IV tumor during dynamic thermography: a) transient response of maximal temperature difference measured at the center of the tumor, b) radial temperature difference distribution at the end of cooling phase $t = 30$ s

$$F_1(\mathbf{y}) = \sum_{t=1}^{n_t}\sum_{p=1}^{n_p}\left(T_{abs,s,p,t}(\mathbf{y}) - T_{abs,m,p,t}\right)^2, \tag{18}$$

and for the temperature difference or temperature contrast as:

$$F_2(\mathbf{y}) = \sum_{t=1}^{n_t}\sum_{p=1}^{n_p}\left(\Delta T_{s,p,t}(\mathbf{y}) - \Delta T_{m,p,t}\right)^2, \tag{19}$$

where indices 1 and 2 stand for the absolute and temperature difference thermal response, respectively, $F(\cdot)$ is the objective function value, $\mathbf{y}$ is the vector of unknown parameters, indices t and p correspond to the time and location of temperature measurements, while n_t and n_p represent the number of observed time points and measurement locations. Vector $\mathbf{y}$ is defined as $\mathbf{y}=\{y_j; j=1,...,n\}=\{d,h,w_b,\tau_q\}$, where $n=4$ is the number of searched parameters.

2.2.3 Levenberg-Marquardt Algorithm

Deterministic optimization methods work faster and require fewer evaluations compared to stochastic methods [49] like particle swarm optimization (PSO) [82], design of experiment (DOE), differential evolution (DE) [83] or simulated annealing (SA), when objective function is smooth and computational cost for direct problem is high.

In this work, the LM optimization algorithm is chosen because it balances the advantages of the steepest descent and Gauss-Newton methods, making it well-suited for nonlinear least-squares problems [45,84].

The optimization problem is formulated as:

$$find \quad \mathbf{y}^* = \arg\min_{\mathbf{y}}\left[F(\mathbf{y})\right], \tag{20}$$

where $\mathbf{y}^*$ represents the minimum of the objective function and solution of the inverse problem. The optimization is performed iteratively, updating the unknown parameter values using:

$$\mathbf{y}_{k+1} = \mathbf{y}_k + \beta_v \mathbf{s}_k \Rightarrow F(\mathbf{y}_{k+1}) < F(\mathbf{y}_k), \tag{21}$$

where $\mathbf{s}$ represents the search direction, β is the step size, and indices k and v denote iteration and trial step indices, respectively. LM algorithm finds the search direction at each iteration step as the solution to the equation system:

$$\left(\mathbf{J}_k^{tr}\cdot\mathbf{J}_k + \mu_k\mathbf{I}\right)\mathbf{s}_k = -\mathbf{J}_k^{tr}\cdot\mathbf{f}(\mathbf{y}_k), \tag{22}$$

where $\mathbf{J}$ represents the Jacobian matrix, μ is a damping parameter, $\mathbf{I}$ the identity matrix and $\mathbf{f}(\cdot)$ represents the residual vector; $F(\mathbf{y})=\mathbf{f}^{tr}(\mathbf{y})\cdot\mathbf{f}(\mathbf{y})\rightarrow\mathbf{f}(\mathbf{y})=\{f_i; i=1,...,m\}$, where $m=n_t n_p$. In each iteration step the Jacobian matrix and damping parameter must be

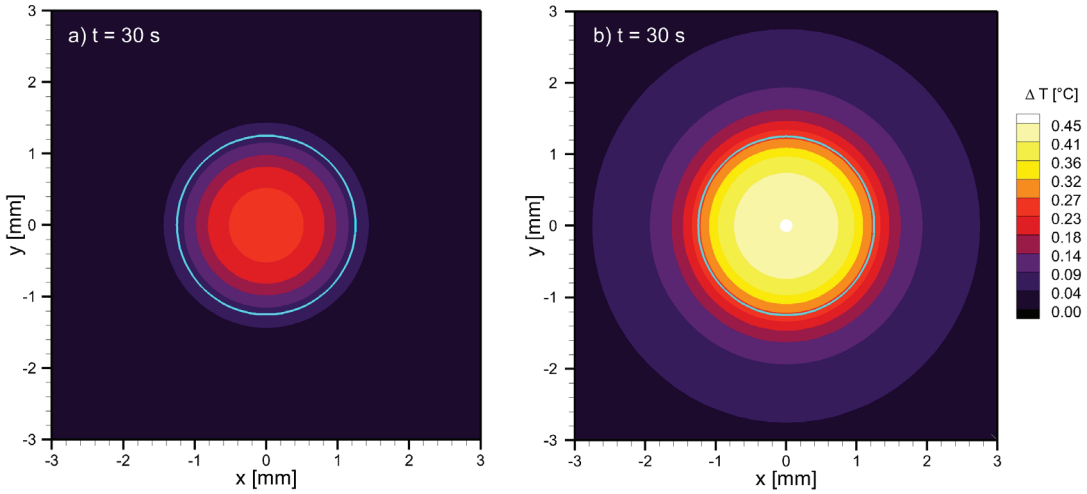

Fig. 5. Simulated temperature difference ΔT_s contour at the skin surface, simulating the IR image at the end of the cooling phase for; a) Clark II and b) Clark IV tumor, while blue line represents tumor diameter

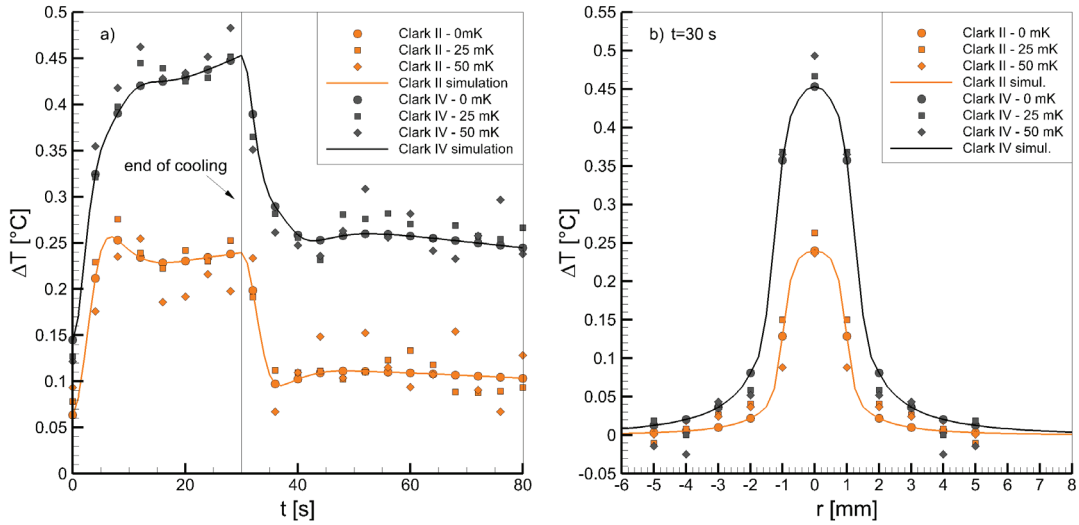

Fig. 6. Representation of numerically generated measurement data of temperature difference response ΔT_m for Clark II and Clark IV tumor using 0 mK, 25 mK and 50 mK level of noise: a) transient response at the center of the tumor, and b) radial response at the end of cooling phase t = 30 s

calculated and updated. The Jacobian matrix is evaluated numerically using first-order finite difference scheme as:

$$J_{i,j} = \frac{\partial f_i}{\partial y_j} \approx \frac{f_i(y_j + \Delta y_j) - f_i(y_j)}{\Delta y_j}, \tag{23}$$

where indices i and j represent the row and column of matrix **J**, and Δy_j represents the change of parameter j, which has been taken as 1 % of its value; $\Delta y_j = 0.01 y_j$.

Once the search direction $\mathbf{s}_k$ is known the solution can be updated using Eq. (21) where the descent criteria is checked; $F(\mathbf{y}_{k+1}) < F(\mathbf{y}_k)$. The step size is taken as $\beta_0 = 1$ for the first trial, as the search direction is also controlled by the damping parameter μ. If the descent criteria is not met, the step size is then reduced by $\beta_{v+1} = \beta_v / 2$.
The damping parameter is updated by equation:

$$\mu_{k+1} = \mu_k \max\left[\frac{1}{3}, 1 - (2\theta_k - 1)^3\right], \tag{24}$$

where θ represents the gain ratio as:

$$\theta_k = \frac{F(\mathbf{y}_k) - F(\mathbf{y}_{k+1})}{Z(0) - Z(\beta_v \mathbf{s}_k)}, \tag{25}$$

where $Z(\cdot)$ represents a linear Taylor expansion of the objective function. For the first iteration step, the damping parameter has been chosen to be $\mu_0 = 10^{-5} \max(\mathbf{J}^{tr} \cdot \mathbf{J})$.

To stop the optimization algorithm, we used three stopping criteria where only one of them has to be fulfilled:

$$k > k_{max}, \tag{26}$$

$$\left\| \mathbf{J}_k^{tr} \cdot \mathbf{f}(\mathbf{y}_k) \right\|_\infty \le \varepsilon_1, \tag{27}$$

$$\left\| \mathbf{y}_{k+1} - \mathbf{y}_k \right\| \le \varepsilon_2 \left(\left\| \mathbf{y}_k \right\| + \varepsilon_2 \right), \tag{28}$$

where k_{max} represents the maximum number of iterative steps and ε_1 and ε_2 the tolerance for the gradient and step size, respectively. The maximum number of iterative steps has been chosen to be $k_{max} = 50$, while the tolerance for the second and third criteria has been taken as $\varepsilon_1 = \varepsilon_2 = 10^{-8}$.

Table 2. Different starting points for the optimization process

Example	y_0	d [mm]	h [mm]	w_b [s^{-1}]	τ_q [s]
Clark II	1	2.3	0.60	0.0080	3.5
	2	1.9	0.50	0.0060	2.8
	3	1.7	0.30	0.0050	1.5
Clark IV	1	2.4	0.90	0.0090	3.7
	2	2.6	1.20	0.0060	2.8
	3	1.8	0.70	0.0050	1.7

2.2.4 Starting Point

To test the stability of the inverse solution depending on the initial guess, we have chosen three different starting point of optimization process. Table 2 is gathering the different initial guesses for the optimization process for Clark II and Clark IV example. One starting point is close to the exact solution, while other two are more off.

3 RESULTS AND DISCUSSION

Results of the inverse bioheat problem are presented in tables, which are the most appropriate to show the estimated value of the searched parameters. For better representation of results accuracy, the relative error for certain parameters is highlighted with the gray color in the tables where intensity reflects its level. This section covers the analysis of the starting point, measurement noise and randomness of the measurement data using the absolute temperature response, while at the end the effect of thermal response type is presented.

3.1 Starting Point

The analysis of the starting point has been carried out first to evaluate its effect on the solution of the inverse problem and stability of the optimization process. Table 3 shows the solution of the inverse problem together with the relative error regarding the starting point for Clark IV tumor using absolute temperature response. The solution for the exact measurement data; 0 mK, coincidence with the exact data and does not depend on the starting point. Solution of the inverse problem also does not depend strongly on the starting point for the noisy measurement data; however, there can be a slight difference but negligible. The average objective function value reached for the exact measurement data was $1.39 \cdot 10^{-9}$ K^2 in 12 optimization steps. While for the noisy measurement data the objective function value increased to $2.65 \cdot 10^{-2}$ K^2 for the 25 mK noise and to $1.07 \cdot 10^{-1}$ K^2 for the 50 mK with the average number of optimization steps 10, because the measurement data does not follow the numerical model exactly due to the noise. Similar observation and conclusion have been made using different set of measurement data, Clark II example and temperature difference response, and is therefore omitted here.

At this point, we can conclude that solution of the inverse bioheat problem using LM algorithm does not depend on the initial guess or starting point making optimization method stable, as well as that convergence of the optimization process is fast.

3.2 Measurement Noise and Data

Here, we would like to evaluate how the level of measurement noise and randomness of generating the measurement data set affects

Table 3. Solution of the inverse problem for Clark IV example using different starting points and absolute temperature response; $F_1(\mathbf{y})$, together with relative error

ΔT_{err}	y_0	Solution				Relative error			
		d [mm]	h [mm]	w_b [s^{-1}]	τ_q [s]	d [%]	h [%]	w_b [%]	τ_q [%]
	Exact	**2.50000**	**1.10000**	**0.006300**	**3.00000**				
0 mK	1	2.50002	1.09995	0.006300	3.00002	0.00	0.00	0.01	0.00
	2	2.50001	1.09996	0.006300	3.00001	0.00	0.00	0.00	0.00
	3	2.50002	1.09996	0.006300	3.00001	0.00	0.00	0.00	0.00
25 mK	1	2.50889	1.11174	0.006188	2.97513	0.36	1.07	1.78	0.83
	2	2.50997	1.09994	0.006230	2.97529	0.40	0.01	1.11	0.82
	3	2.50909	1.11072	0.006191	2.97496	0.36	0.97	1.73	0.83
50 mK	1	2.51047	1.00056	0.006691	3.03187	0.42	9.04	6.21	1.0
	2	2.51011	1.00098	0.006691	3.03156	0.40	9.00	6.21	1.05
	3	2.51019	1.00031	0.006694	3.03156	0.41	9.06	6.25	1.05

Table 4. Solution of the inverse problem for Clark II example using different measurement data set of absolute temperature response; $F_1(\mathbf{y})$, together with relative error

ΔT_{err}	y_0	Solution				Relative error			
		d [mm]	h [mm]	w_b [s^{-1}]	τ_q [s]	d [%]	h [%]	w_b [%]	τ_q [%]
	Exact	**2.00000**	**0.44000**	**0.006300**	**3.00000**				
25 mK	1	2.00000	0.43494	0.006380	2.99436	0.00	1.15	1.26	0.19
	2	2.00000	0.43730	0.006314	2.96224	0.00	0.61	0.22	1.26
	3	2.00000	0.44054	0.006271	3.03409	0.00	0.12	0.46	1.14
50 mK	1	2.01886	0.43046	0.006178	3.03609	0.94	2.17	1.93	1.20
	2	2.00000	0.46098	0.006174	2.91235	0.00	4.77	2.00	2.92
	3	2.00000	0.42768	0.006426	2.95631	0.00	2.80	2.00	1.46

the solution. Because, it has been shown that the solution does not depend on the starting point, we set starting point 3 for all our further calculations. Table 4 shows the obtained results for Clark II example using absolute temperature response and different data sets for 25 mK and 50 mK noise level together with relative error. As can be seen, the solution varies on the randomness of the noise or measurement data set and the relative error of the solution increases by increasing the level of noise. Diameter of the tumor d can be determined very accurately, while other parameters have the same level of error, however, still under 5 %, meaning a good estimation or retrieval of the searched parameters. Similar findings have also been found for Clark IV example and are therefore omitted here.

From this small analysis, we can conclude that the solution of the inverse problem depends on the level of the noise and randomness of the generated measurement data set. Therefore, it is important to generate or record more than one measurement data set to evaluate the deviation of the solution.

Because inverse problem solution depends on the randomness of the measurement data, it is better to use statistical indicators like mean value, deviation and coefficient of variation (COV). We are well aware that three different solutions are too small sample size to make accurate statistical analysis, however, it can still give us the insight on the accuracy of the inverse solution and its dependency. Table 5 shows the obtained inverse solution for Clark II and Clark IV examples using statistical indicators for noisy measurement data of absolute temperature response, together with the mean error.

As can be seen from Table 5 for Clark II the diameter can be determined very accurately regarding the noise level, while the accuracy of other parameters is in the same range of less than 1 % for low noise level and increases to 2 % to 3% for high noise level. The COV also shows the deviation of the estimated parameters that coinciding with the average error and increases by increasing level of noise, meaning that these parameters will be hard to evaluate in real experimental setup. Similar conclusion can be made for Clark IV example that shows good evaluation of tumor diameter and better evaluation of relaxation time than for Clark II example, while the error for tumor thickness and blood perfusion rate is slightly higher but still in the same range, less than 5 %. This shows that relaxation time can be easily obtained for later stage tumor.

Findings coincide with the findings of our previous work [45], where diameter can be determined very accurately even for the noisy measurement data, regarding the stage of the tumor. And also, that blood perfusion rate and thickness show lower accuracy and interdependence.

Table 5. Solution of the inverse bioheat problem for Clark II and Clark IV example under noisy measurement data sets of absolute temperature response; $F_1(\mathbf{y})$, showing the mean value, deviation, COV and mean relative error

	ΔT_{err}		d [mm]	h [mm]	w_b [s^{-1}]	τ_q [s]
Clark II		Exact	**2.00000**	**0.44000**	**0.006300**	**3.00000**
	25 mK	Mean value	2.00000	0.43759	0.006321	2.99690
		Deviation	0.00000	0.00281	0.00005	0.03599
		COV [%]	0.00	0.64	0.86	1.20
		Error [%]	0.00	0.63	0.65	0.86
	50 mK	Mean value	2.00629	0.43971	0.006260	2.96825
		Deviation	0.01089	0.01848	0.000144	0.06273
		COV [%]	0.54	4.20	2.30	2.11
		Error [%]	0.31	3.25	1.98	1.86
	ΔT_{err}		d [mm]	h [mm]	w_b [s^{-1}]	τ_q [s]
Clark IV		Exact	**2.50000**	**1.10000**	**0.006300**	**3.00000**
	25 mK	Mean value	2.50510	1.11683	0.006204	2.98604
		Deviation	0.01363	0.01486	0.00001	0.01856
		COV [%]	0.54	1.33	0.21	0.62
		Error [%]	0.47	1.53	1.52	0.63
	50 mK	Mean value	2.50793	1.08020	0.006355	3.00681
		Deviation	0.01973	0.06984	0.000308	0.02167
		COV [%]	0.79	6.47	4.85	0.72
		Error [%]	0.66	4.24	3.30	0.47

Table 6. Solution of the inverse bioheat problem for Clark II and Clark IV example under noisy measurement data sets of temperature difference response; $F_2(\mathbf{y})$, showing the mean value, deviation, COV and mean relative error

	ΔT_{err}		d [mm]	h [mm]	w_b [s^{-1}]	τ_q [s]
Clark II		Exact	**2.00000**	**0.44000**	**0.006300**	**3.00000**
	25 mK	Mean value	2.00045	0.45606	0.006094	2.98212
		Deviation	0.00079	0.01779	0.000302	0.08330
		COV [%]	0.04	3.90	4.95	2.79
		Error [%]	0.02	4.31	4.55	2.16
	50 mK	Mean value	2.02638	0.42853	0.006277	2.93446
		Deviation	0.03468	0.04114	0.000690	0.18607
		COV [%]	1.71	9.60	10.99	6.34
		Error [%]	1.32	6.59	8.54	5.32
	ΔT_{err}		d [mm]	h [mm]	w_b [s^{-1}]	τ_q [s]
Clark IV		Exact	**2.50000**	**1.10000**	**0.006300**	**3.00000**
	25 mK	Mean value	2.50208	1.07415	0.006387	2.99885
		Deviation	0.00561	0.01426	0.000134	0.01172
		COV [%]	0.22	1.33	2.10	0.39
		Error [%]	0.17	2.35	1.79	0.31
	50 mK	Mean value	2.52163	1.09922	0.006311	3.06237
		Deviation	0.03057	0.07763	0.000486	0.06745
		COV [%]	1.21	7.06	7.70	2.20
		Error [%]	1.15	4.98	5.44	2.42

3.3 Type of Thermal Response

Table 6 shows the obtained solution of the inverse problem using temperature difference response for both test examples. Comparing results to the one from Table 5, where absolute temperature response has been used, we can draw the same conclusion of estimating unknown parameters. Accuracy of tumor diameter and relaxation time is still better from the blood perfusion rate and tumor thickness, especially for Clark IV. The relative error of the estimated parameters based on the temperature difference response is higher than the results based on the absolute temperature response, especially for the early-stage tumor. This means it is better to use absolute temperature response to diagnose early-stage tumor. However, using temperature difference response shows that accuracy of the parameters is better for later stage tumor. These findings coincidence with our previous work [45]. Nevertheless, early-stage diagnosis is still possible using temperature difference response and good accuracy of estimated parameters can be obtain by keeping the level of measurement noise low.

From the analysis done on the solution of inverse bioheat problem, we can conclude that all searched parameters can be successfully evaluated even for high level of measurement noise, especially tumor diameter and relaxation time where relative error of the obtained parameters is less than 5 %. Based on this study, it is better to determine unknown parameters using absolute temperature response than temperature difference, especially for an early-stage tumor. However, from the practical point of view, temperature difference response is preferred because it does not depend strongly on the prescribed body core and surrounding temperature, making it more general and still accurate enough.

4 CONCLUSIONS

This paper presents a numerical framework for the non-invasive skin cancer diagnosis using dynamic IR thermography, supported by improved skin cancer model and inverse problem analysis, to estimate tumor diameter, thickness, blood perfusion rate and thermal relaxation time. A novel contribution of this work lies in the integration of the non-Fourier DPL bioheat model into a multilayered, axisymmetric skin cancer model, enabling a more realistic simulation of thermal behavior in heterogeneous biological tissues under transient thermal stimuli. The DPL model offers significant advantages over classical Fourier-based models by accounting for thermal lag, finite thermal wave propagation, and directional effects that are critical for capturing fast and localized thermal dynamics near skin tumors. To simulate dynamic thermography response, we used our own developed solver based on subdomain BEM approach that gives accurate solution and proves to be efficient, which is very important for solving inverse bioheat problems.

The inverse bioheat problem solved in this work is to find four important tumor parameters based on the non-Fourier DPL skin cancer model and transient thermal response of dynamic thermography, which also presents the novelty of this work. We analyze two different responses; absolute temperature and temperature difference response on two examples; Clark II and Clark IV stage tumor. Measurement data or thermal response has been generated numerically by prescribing known searched parameters that we would like to retrieve through inverse problem, and direct numerical simulation of dynamic thermography. A measurement noise of 25 mK and 50 mK has been added to the simulated responses for the Clark II and Clark IV tumor, to obtain more realistic measurement data. For dynamic thermography a convective cooling approach with cold air jet has been chosen, which replicates a clinically feasible dynamic thermography scenario, allowing recording of temperature response during both cooling and rewarming phases. To solve the inverse bioheat problem, a hybrid LM optimization algorithm has been implemented that was combined with direct bioheat problem of simulating dynamic thermography using BEM.

The results showed that solution of the inverse problem does not depend on the initial guess making LM algorithm robust, accurate and efficient for this type of inverse problem. All four parameters can be retrieved exactly only for the measurement data that follows numerical model exactly. However, this is not possible in real life problem. The parameters can be still retrieved very accurately even under higher level of measurement data noise, especially the diameter and thermal relaxation time for both examples using absolute temperature response. Blood perfusion rate and tumor thickness exhibit slightly higher estimation error but remain within acceptable bounds. The accuracy of the estimated parameters is lower when using temperature difference response, however, this is practically more feasible, because the temperature contrast does not depend strongly on the body core temperature or boundary condition at the bottom of the numerical model. For Clark II example, all parameters were estimated with relative errors below 5 % for lower level of measurement noise, demonstrating strong potential for early-stage skin cancer diagnosis.

Overall, this study confirms that dynamic IR thermography, combined with non-Fourier bioheat modeling and inverse analysis, is a promising tool for non-invasive skin cancer assessment. The ability to estimate not only geometric properties but also physiological such as blood perfusion and thermal relaxation time provides insight into tumor size, stage, and invasiveness.

Future work will focus on developing this approach even further in the field of numerical simulations, solving inverse problems, statistical assessment of the approach, as well as on the experimental validation of the proposed model and real-time implementation strategies.

References

[1] Wilson, A.N., Gupta, K.A., Koduru, B.H., Kumar, A., Jha, A., Cenkeramaddi, L.R. Recent advances in thermal imaging and its applications using machine learning: A review. *IEEE Sens J* 23 3395-3407 (2023) **DOI:10.1109/JSEN.2023.3234335**.

[2] Kesztyüs, D., Brucher, S., Wilson, C., Kesztyüs, T. Use of infrared thermography in medical diagnosis, screening, and disease monitoring: A scoping review. Medicina 59 2139 (2023) **DOI:10.3390/medicina59122139**.

[3] Manno, M., Yang, B., Bar-Cohen, A. Non-contact method for characterization of small size thermoelectric modules. *Rev Sci Instrum* 86 084701 (2015) **DOI:10.1063/1.4927604**.

[4] Thusyanthan, I., Blower, T., Cleverly, W. Innovative uses of thermal imaging in civil engineering. *J Inst Civ Eng* 170 1-7 (2016) **DOI:10.1680/jcien.16.00014**.

[5] Vakrilov, N.V., Kafadarova, N.M., Zlatanski, D.A. Application of infrared imaging in the field of electrical engineering. 2021 XXX International Scientific Conference Electronics (ET) 1-4 (2021) **DOI:10.1109/ET52713.2021.9579707**.

[6] Farooq, M., Shariff, W., O'Callaghan, D., Merla, A., Corcoran, P. On the role of thermal imaging in automotive applications: A critical review. *IEEE Access* 11 25152-25173 (2023) **DOI:10.1109/ACCESS.2023.3255110**.

[7] Osterman, A., Dular, M., Hocevar, M., Širok, B. Infrared thermography of cavitation thermal effects in water. *Stroj Vestn-J Mech E* 56 527-534 (2010).

[8] Lahiri, B., Bagavathiappan, S., Jayakumar, T., Philip, J. Medical applications of infrared thermography: A review. *Infrared Phys Technol* 55 221-235 (2012) **DOI:10.1016/j.infrared.2012.03.007**.

[9] Sayasneh, A., Abdelbar, A., Ramajayan, T., Lim, j., Al-karawi, D., Al Zaidi, S., et al. Thermal Camera Application in Gynecological Oncology: Feasibility Study of a Novel Technology. *J Oncol Res Ther* 9 10203 (2024) **DOI:10.29011/2574-710X.10203**.

[10] Ciappara Paniagua, M., Gutierrez Hidalgo, B., Gomez Rivas, J., Redondo Gonzalez, E., De la Parra Sanchez, I., Galindo Herrero, I., et al. Protocol description and initial experience in kidney graft perfusion using infrared thermography, *World J Urol* 42 416 (2024) **DOI:10.1007/s00345-024-05116-9**.

[11] Manullang, M.C.T., Lin, Y.-H., Lai, S.-J., Chou, N.-K. Implementation of Thermal Camera for Non-Contact Physiological Measurement: A Systematic Review. *Sensors* 21 7777 (2021) **DOI:10.3390/s21237777**.

[12] Zhou, Y., Ghassemi, P., Chen, M., McBride, D., Casamento, J.P., Pfefer, T.J., Wang, Q. Clinical evaluation of fever-screening thermography: impact of consensus guidelines and facial measurement location. *J Biomed Opt* 25 097002 (2020) **DOI:10.1117/1.JBO.25.9.097002**.

[13] Gorbach, A. M., Heiss, J. D., Kopylev, L., Oldfield, E. H. Intraoperative infrared imaging of brain tumors. *J Neurosurg* 101 960-969 (2004) **DOI:10.3171/jns.2004.101.6.0960**.

[14] PS, L., M, S., Joy, E. A review on thermography in dentistry. *J Evol Med Dent Sci* 7 1289-1293 (2018) **DOI:10.14260/jemds/2018/294**.

[15] Matos, F., Borba Neves, E., Norte, M., Rosa, C., Machado Reis, V., Vilaça-Alves, J. The use of thermal imaging to monitoring skin temperature during cryotherapy: A systematic review. *Infrared Phys Technol* 73 194-203 (2015) **DOI:10.1016/j.infrared.2015.09.013**.

[16] Ammer, K., Ring, E. Application of thermal imaging in forensic medicine. *J Imaging Sci* 53 125-131 (2005) **DOI:10.1179/136821905X50361**.

[17] Bonmarin, M., Le Gal, F. Chapter 31: Thermal imaging in dermatology. Hamblin, M.R., Avci, P., Gupta, G.K. (eds.) *Imaging in Dermatology* 437-454 (2016) Academic Press, Boston **DOI:10.1016/B978-0-12-802838-4.00031-5**.

[18] Godoy, S.E., Hayat, M.M., Ramirez, D.A., Myers, S.A., Padilla, R.S., Krishna, S. Detection theory for accurate and non-invasive skin cancer diagnosis using dynamic thermal imaging. *Biomed. Opt Express* 8 2301-2323 (2017) **DOI:10.1364/BOE.8.002301**.

[19] Strąkowska, M., Strąkowski, R., Strzelecki, M., De Mey, G., Więcek, B. Evaluation of perfusion and thermal parameters of skin tissue using cold provocation and thermographic measurements. *Metrol Meas Syst* 23 373-381 (2016) **DOI:10.1515/mms-2016-0032**.

[20] Strąkowska, M., Strąkowski, R., Strzelecki, M., De Mey, G., Więcek, B. Thermal modelling and screening method for skin pathologies using active thermography. *Biocybern Biomed Eng* 38 602-610 (2018) **DOI:10.1016/j.bbe.2018.03.009**.

[21] Elder, D. E. Tumor progression, early diagnosis and prognosis of melanoma. *Acta Oncol* 385 535-548 (1999) D**OI:10.1080/028418699431113**.

[22] Flores-Sahagun, J., Vargas, J., Brenner, F. Analysis and diagnosis of basal cell carcinoma (BCC) via infrared imaging. *Infrared Phys Technol* 54 367-378 (2011) **DOI:10.1016/j.infrared.2011.05.002**.

[23] Smith, R.L., Soeters, M.R., Wüst, R.C.I., Houtkooper, R.H. Metabolic flexibility as an adaptation to energy resources and requirements in health and disease. *Endocr Rev* 39 489-517 (2018) **DOI:10.1210/er.2017-00211**.

[24] Santulli, G., Angiogenesis. *Insights from a Systematic Overview*. (2013) Nova Publisher, Hauppauge.

[25] Jiang, L.J., Ng, E.Y.K., Yeo, A.C.B., Wu, S., Pan, F., Yau, W.Y., Yang, Y. A perspective on medical infrared imaging. *J Medical Eng Technol* 29 257-267 (2005) **DOI:10.1080/03091900512331333158**.

[26] Clark, W.H.Jr., From, L., Bernardino, E.A., Mihm, M.C. The histogenesis and biologic behavior of primary human malignant melanomas of the skin. *Cancer Res* 29 705 (1969).

[27] Breslow, A. Thickness, cross-sectional areas and depth of invasion in the prognosis of cutaneous melanoma. *Ann Surg* 172 902-908 (1970) **DOI:10.1097/00000658-197011000-00017**.

[28] Duarte, A.F., Sousa-Pinto, B., Azevedo, L.F., Barros, A.M., Puig, S., Malvehy, J., Haneje, E., Correia, O. Clinical ABCDE rule for early melanoma detection. *Eur J Dermatol* 31 771-778 (2021) **DOI:10.1684/ejd.2021.4171**.

[29] Herman, C. The role of dynamic infrared imaging in melanoma diagnosis. *Expert Rev Dermatol* 8 177-184 (2013) **DOI:10.1586/edm.13.15**.

[30] Wilson, J.B. Excisional Biopsy of Dermal and Subcutaneous Lesions. Chen, H. (ed.), Illustrative Handbook of General Surgery. (2016) 781-791 Springer International Publishing, Cham **DOI:10.1007/978-3-319-24557-7_44**.

[31] Verstockt, J., Verspeek, S., Thiessen, F., Tjalma, W.A., Brochez, L., Steenackers, G. Skin cancer detection using infrared thermography: Measurement setup, procedure and equipment. *Sensors* 22 3327 (2022) **DOI:10.3390/s22093327**.

[32] Saxena, A., Ng, E., Lim, S.T. Active dynamic thermography to detect the presence of stenosis in the carotid artery. *Comput Biol Med* 120 103718 (2020) **DOI:10.1016/j.compbiomed.2020.103718**.

[33] Çetingül, M.P., Herman, C. Quantification of the thermal signature of a melanoma lesion. *Int J Therm Sci* 50 421-431 (2011) **DOI:10.1016/j.ijthermalsci.2010.10.019**.

[34] Jiang, L., Zhan, W., Loew, M.H. Modeling static and dynamic thermography of the human breast under elastic deformation. *Phys Med Biol* 56 187-202 (2010) **DOI:10.1088/0031-9155/56/1/012**.

[35] Vardasca, R., Vaz, L., Mendes, J. Classification and decision making of medical infrared thermal images. Dey, N., Ashour, A., Borra, S. (eds.) *Classification in BioApps* 79-104 (2018) Springer, Cham **DOI:10.1007/978-3-319-65981-7_4**.

[36] Kirimtat, A., Krejcar, O., Selamat, A. A mini-review of biomedical infrared thermography (B-IRT). *Bioinformatics and Biomedical Engineering - IWBBIO* (2019) 99-110 **DOI:10.1007/978-3-030-17935-9_10**.

[37] Ammer, K., Ring, E. Standard procedures for infrared imaging in medicine, Bronzino, J.D. (ed.) *Medical Devices and Systems* (2012) 1-14 CRC Press, Taylor & Francis Group.

[38] Ring, E.F., Jones, C., Ammer, K., Plassmann, P., Bola, T.S. Cooling effects of deep freeze cold gel compared to that of an ice pack applied to the skin. *Thermol Int* 14 93-98 (2004).

[39] Carlo, A.D. Thermography and the possibilities for its applications in clinical and experimental dermatology. *Clin Dermatol* 13 329-36 (1995) **DOI:10.1016/0738-081x(95)00073-0**.

[40] Magalhaes, C., Vardasca, R., Rebelo, M., Valenca-Filipe, R., Ribeiro, M., Mendes, J. Distinguishing melanocytic nevi from melanomas using static and dynamic infrared thermal imaging. *J Eura cad Dermatol Venereol* 33 1700-1705 (2019) **DOI:10.1111/jdv.15611**.

[41] Çetingül, M., Alani, R., Herman, C., Quantitative evaluation of skin lesions using transient thermal imaging. *Proceedings of the 14th International Heat Transfer Conference* 31-39 (2010) **DOI:10.1115/IHTC14-22465**.

[42] Bhowmik, A., Repaka, R. Estimation of growth features and thermophysical properties of melanoma within 3-D human skin using genetic algorithm and simulated annealing. *Int J Heat Mass Transf* 98 81-95 (2016) **DOI:10.1016/j.ijheatmasstransfer.2016.03.020**.

[43] Cheng, T.-Y., Herman, C. Analysis of skin cooling for quantitative dynamic infrared imaging of near-surface lesions. *Int J Therm Sci* 86 175-188 (2014) **DOI:10.1016/j.ijthermalsci.2014.06.033**.

[44] Çetingül, M. P., Herman, C., A heat transfer model of skin tissue for the detection of lesions: sensitivity analysis. *Phys Med Biol* 55 5933-5951 (2010) **DOI:10.1088/0031-9155/55/19/020**.

[45] Iljaž, J., Wrobel, L.C., Gomboc, T., Hriberšek, M., Marn, J. Solving inverse bioheat problems of skin tumour identification by dynamic thermography. *Inverse Probl* 36 035002 (2020) **DOI:10.1088/1361-6420/ab2923**.

[46] Luna, J. M., Guerrero, A.H., Méndez, R.R., Ortiz, J.L.L. Solution of the inverse bio-heat transfer problem for a simplified dermatological application: Case of skin cancer. *Ing Mec Tecnol Desarro* 4 219-228 (2014).

[47] Partridge, P.W., Wrobel, L.C. A coupled dual reciprocity BEM/genetic algorithm for identification of blood perfusion parameters. *Int J Numer Methods Heat Fluid Flow* 19 25-28 (2009) **DOI:10.1108/09615530910922134**.

[48] Partridge, P.W., Wrobel, L.C. An inverse geometry problem for the localisation of skin tumours by thermal analysis. *Eng Anal Bound Elem* 31 803-811 (2007) **DOI:10.1016/j.enganabound.2007.02.002**.

[49] Fu, Z.-J., Chu, W.-H., Yang, M., Li, P.-W., Fan, C.-M. Estimation of tumor characteristics in a skin tissue by a meshless collocation solver. *Int J Comput Methods* 18 2041009 (2021) **DOI:10.1142/S0219876220410091**.

[50] Bhowmik, A., Repaka, R., Mishra, S.C. Thermographic evaluation of early melanoma within the vascularized skin using combined non-Newtonian blood flow and bioheat models. *Comput Biol Med* 53 206-219 (2014) **DOI:10.1016/j.compbiomed.2014.08.002**.

[51] Bonmarin, M., Le Gal, F.-A. Lock-in thermal imaging for the early-stage detection of cutaneous melanoma: a feasibility study. *Comput Biol Med* 47 36-43 (2014) **DOI:10.1016/j.compbiomed.2014.01.008**.

[52] Iljaž, J., Wrobel, L.C., Hriberšek, M., Marn, J. The use of design of experiments for steady-state and transient inverse melanoma detection problems. *Int J Therm Sci* 135 256-275 (2019) **DOI:10.1016/j.ijthermalsci.2018.09.003**.

[53] Iljaž, J., Wrobel, L.C., Hriberšek, M., Marn, J. Numerical modelling of skin tumour tissue with temperature-dependent properties for dynamic thermography. *Comput Biol Med* 112 103367 (2019) **DOI:10.1016/j.compbiomed.2019.103367**.

[54] Tucci, C., Trujillo, M., Berjano, E., Iasiello, M., Andreozzi, A., Vanoli, G.P. Pennes' bioheat equation vs. porous media approach in computer modeling of radiofrequency tumor ablation. *Sci Rep* 11 5272 (2021) **DOI:10.1038/s41598-021-84546-6**.

[55] Kabiri, A.,Talaee, M.R. Analysis of hyperbolic Pennes bioheat equation in perfused homogeneous biological tissue subject to the instantaneous moving heat source. *SN Appl Sci* 3 398 (2021) **DOI:10.1007/s42452-021-04379-w**.

[56] Verma, R. Kumar, S. Computational study on 2D three-phase lag bioheat model during cryosurgery using RBF meshfree method. *J Therm Biol* 114 103575 (2023) **DOI:10.1016/j.jtherbio.2023.103575**.

[57] Kang, Z., Zhu, P., Gui, D., Wang, L. A method for predicting thermal waves in dual-phase-lag heat conduction. *Int J Heat Mass Transf* 115 250-257 (2017) **DOI:10.1016/j.ijheatmasstransfer.2017.07.036**.

[58] Ma, J., Yang, X., Sun, Y., Yang, J. Thermal damage in three-dimensional vivo bio-tissues induced by moving heat sources in laser therapy. *Sci Rep* 9 10987 (2019) **DOI:10.1038/s41598-019-47435-7**.

[59] Namakshenas, P., Mojra, A. Microstructure-based non-Fourier heat transfer modeling of HIFU treatment for thyroid cancer. *Comput Methods Programs Biomed* 197 105698 (2020) **DOI:10.1016/j.cmpb.2020.105698**.

[60] Tzou, D.Y. Thermal shock waves induced by a moving crack - a heat flux formulation. *Int J Heat Mass Transf* 33 877-885 (1990) **DOI:10.1016/0017-9310(90)90071-2**.

[61] Tzou, D. Macro- To Micro-Scale Heat Transfer: The Lagging Behavior. (2014) Taylor & Francis, Chichester **DOI:10.1002/9781118818275**.

[62] Stryczyński, M., Majchrzak, E. Numerical modelling of the laser high-temperature hyperthermia using the dual-phase lag equation. *J Theor Appl Mech* 62 389-401 (2024) **DOI:10.15632/jtam-pl/186178**.

[63] Singh, S., Bianchi, L., Korganbayev, S., Namakshenas, P., Melnik, R., Saccomandi, P. Non-Fourier bioheat transfer analysis in brain tissue during interstitial laser ablation: Analysis of multiple influential factors. *Ann Biomed Eng* 52 967-981 (2024) **DOI:10.1007/s10439-023-03433-5**.

[64] Verma, R., Kalita, J.C. Numerical simulation of phase change dual-phase-lag bioheat model with nanocryosurgery using radial basis function meshfree approach. *J Heat Transf* 147 061201 (2025) **DOI:10.1115/1.4067611**.

[65] Liu, K.-C., Chen, H.-T. Investigation for the dual phase lag behavior of bio-heat transfer. *Int J Therm Sci* 49 1138-1146 (2010) **DOI:10.1016/j.ijthermalsci.2010.02.007**.

[66] Yong, Z., Chen, B., Li, D. Non-Fourier effect of laser-mediated thermal behaviors in bio-tissues: A numerical study by the dual-phase-lag model. *Int J Heat Mass Transf* 108 1428-1438 (2017) **DOI:10.1016/j.ijheatmasstransfer.2017.01.010**.

[67] Kishore, P., Kumar, S. Thermal relaxation parameters estimation of non-Fourier heat transfer in laser-irradiated living tissue using the Levenberg-Marquardt algorithm. *Numer Heat Transf A-Appl* 1-26 (2024) **DOI:10.1080/10407782.2024.2314232**.

[68] Horvat, I.D., Iljaž, J. Numerical modeling of non-Fourier bioheat transfer in multilayer biological tissue using BEM to simulate dynamic thermography in skin tumor diagnostics. *Eng Anal Bound Elem* 179 106408 (2025) **DOI:10.1016/j.enganabound.2025.106408**.

[69] Cruz, G. A.S., Bertotti, J., Dynamic infrared imaging of cutaneous melanoma and normal skin in patients treated with BNCT. *Appl Radiat Isot* 67 54-58 (2009) **DOI:10.1016/j.apradiso.2009.03.093**.

[70] Gomboc, T., Iljaž, J., Wrobel, L.C., Hriberšek, M., Marn, J. Design of constant temperature cooling device for melanoma screening by dynamic thermography. *Eng Anal Bound Elem* 125 66-79 (2021) **DOI:10.1016/j.enganabound.2021.01.009**.

[71] Liu, K.-C., Wang, Y.-N., Chen, Y.-S. Investigation on the bio-heat transfer with the dual-phase-lag effect. *Int J Therm Sci* 58 29-35 (2012) **DOI:10.1016/j.ijthermalsci.2012.02.026**.

[72] Pennes, H.H. Analysis of tissue and arterial blood temperatures in the resting human forearm. *J Appl Physiol* 85 93-122 (1948) **DOI:10.1152/jappl.1998.85.1.5**.

[73] Godoy, S.E., Ramirez, D.A., Myers, S.A., Winckel, G., Krishna, S., Berwick, M., et al. Dynamic infrared imaging for skin cancer screening. *Infrared Phys Technol* 70 147-152 (2015) **DOI:10.1016/j.infrared.2014.09.017**.

[74] Antaki, P.J. New Interpretation of Non-Fourier Heat Conduction in Processed Meat. *J Heat Transf* 127 189-193 (2005) **DOI:10.1115/1.1844540**.

[75] Mabeta, P. Paradigms of vascularization in melanoma: Clinical significance and potential for therapeutic targeting. *Biomed Pharmacother* 127 110135 (2020) **DOI:10.1016/j.biopha.2020.110135**.

[76] Quintanilla, R., Racke, R. A note on stability in dual-phase-lag heat conduction. *Int J Heat Mass Transf* 49 1209-1213 (2006) **DOI:10.1016/j.ijheatmasstransfer.2005.10.016**.

[77] Majchrzak, E., Kałuża, G., Poteralska, J. Application of the DRBEM for numerical solution of Cattaneo-Vernotte bioheat transfer equation. *Sci Res Inst Math Comput Sci* 7 111-120 (2008).

[78] Ciesielski, M., Duda, M., Mochnacki, B. Comparison of bio-heat transfer numerical models based on the Pennes and Cattaneo-Vernotte equations. *J Appl Math Comput Mech* 15 33-38 (2016) **DOI:10.17512/jamcm.2016.4.04**.

[79] Liu, K.-C., Wang, Y.-N., Chen, Y.-S. Investigation on the bio-heat transfer with the dual-phase-lag effect. *Int J Therm Sci* 58 29-35 (2012) **DOI:10.1016/j.ijthermalsci.2012.02.026**.

[80] Felde, I., Réti, T. Evaluation of hardening performance of cooling media by using inverse heat conduction methods and property prediction. *Stroj Vestn-J Mech E* 56 77-83 (2010).

[81] Roy, A.D., Dhiman, S.K. Estimation of surface temperature and heat flux over a hollow cylinder and slab using an inverse heat conduction approach. *Stroj Vestn-J Mech E* 70 342-354 (2024) **DOI:10.5545/sv-jme.2023.864**.

[82] Nguyen, T.-T., Le, M.-T. Optimization of the internal roller burnishing process for energy reduction and surface properties. *Stroj Vestn-J Mech E* 67 167-179 (2021) **DOI:10.5545/sv-jme.2021.7106**.

[83] Afsharzadeh, N., Yazdi, M.E., Lavasani, A.M. Thermal design and constrained optimization of a fin and tube heat exchanger using differential evolution algorithm. *Stroj Vestn-J Mech E* 71 10-20 (2025) **DOI:10.5545/sv-jme.2023.887**.

[84] Mei, J., Xie, S., Liu, H., Zang, J. Hysteresis modelling and compensation of pneumatic artificial muscles using the generalized Prandtl-Ishlinskii model. *Stroj Vestn-J Mech E* 63 657-665 (2017) **DOI:10.5545/sv-jme.2017.4491**.

Acknowledgements *The authors thank the Slovenian Research and Innovation Agency (ARIS) for the research core funding No. P2-0196 and No. J7-60118.*

Received 2025-04-25, revised 2025-09-01, accepted 2025-09-11
as Original scientific paper 1.01.

Data availability *The data that supports the findings of this study are available from the corresponding author upon reasonable request.*

Author contribution *Ivan Dominik Horvat: Data curation, Formal analysis, Investigation, Methodology, Software, Validation and Writing – review & editing; and Jurij Iljaž: Conceptualization, Formal analysis, Supervision, Visualization and Writing – original draft.*

Numerično reševanje inverznega problema dinamične termografije za diagnostiko kožnega raka na osnovi nefourierovega modela prenosa toplote

Povzetek *Članek obravnava numerično reševanje inverznega problema prenosa toplote za določitev štirih parametrov kožnega raka: premer, debelino, perfuzijski pretok krvi in relaksacijski čas. Določitev temelji na toplotnem odzivu kože pridobljenim z dinamično termografijo ter numeričnim modelom kožnega raka ki lahko bistveno izboljša diagnostično vrednost termografije. Za čim bolj realističen opis prenosa toplote v tkivu med procesom dinamične termografije je bil uporabljen nefourierov model z dvojnim faznim zamikom. Model kožnega raka je sestavljen iz večplastne kože, podkožne maščobe in mišice ter kožnega raka oziroma tumorja. Za rešitev kompleksnega nefourierovega modela ter simulacije dinamične termografije je bil razvit programski paket na osnovi metode robnih elementov. Simulacija dinamične termografije, ki za temperaturno vzbujanje uporablja curek hladnega zraka, je pomembna za rešitev inverznega problema, saj z njo pridemo do termičnega odziva oziroma temperaturnega kontrasta na površini kože pri predpostavljenih iskanih parametrih ter njene primerjave z meritvijo. Tako je bil inverzni problem rešen s pristopom optimizacije, pri čemer je bil uporabljen Levenberg–Marquardt algoritem. Meritve so bili pri tem generirane numerično z vnaprej znanimi parametri tumorja in dodanim šumom za ovrednotenje natančnost in občutljivost inverzne rešitve. Rešitev inverznega problema je bila pri tem testirana za dva različna temperaturna odziva, in sicer absolutno temperaturo in temperaturno razliko, kakor tudi za dve različni stadija tumorja kot je Clark II, ki predstavlja zgodnji stadij in Clark IV, ki predstavlja pozni stadij. Vsi pomembni parametri tumorja so bili uspešno določeni tudi pri visoki stopnji šuma, zlasti premer in relaksacijski čas, pri čemer je bila natančnost ovrednotenih parametrov nekoliko boljša z uporabo absolutnega temperaturnega odziva. Rezultati kažejo na robustno in obetavno metodo za zgodnjo diagnostiko kožnega raka in pomembno prispevajo na področju modeliranja prenosa toplote v bioloških tkivih, reševanju inverznih problemov ter razvoju dinamične termografije.*

Ključne besede *numerično reševanje, dinamična termografija, inverzni problem, nefourierov prenos toplote, DPL model, metoda robnih elementov, Levenberg-Marquardt optimizacija*

Numerical Investigation of Erosion Due to Particles in a Cavitating Flow in Pelton Turbine

Luka Kevorkijan[1] – Matjaž Hriberšek[1] – Luka Lešnik[1] – Aljaž Škerlavaj[2] – Ignacijo Biluš[1] ✉

1 University of Maribor, Faculty of Mechanical Engineering, Slovenia
2 Scotta Turboinštitut, Slovenia

✉ ignacijo.bilus@um.si

Abstract *Erosion of Pelton turbine components due to cavitation and particle-laden flow is a major challenge in hydropower applications, particularly in sediment-rich river environments. This study presents a numerical investigation on how solid particles contribute to the erosion of a Pelton runner. Computational fluid dynamics (CFD) simulations were conducted using ANSYS CFX 2023 R2, incorporating a Lagrangian particle tracking approach and the Finnie abrasion model to predict erosion patterns under varying sediment concentrations. The results indicate that, under normal sediment conditions, particle erosion does not significantly contribute to blade tip damage. However, under extreme sediment loading, the predicted erosion patterns closely match real-world observations, particularly at the blade tip.*

Keywords *Pelton turbine, solid particle erosion, cavitation, CFD simulation*

Highlights

- *Numerical CFD analyzis was used to evaluate erosion in Pelton turbine runners.*
- *Particle erosion is negligible under normal sediment conditions but significant under extreme loading.*
- *Erosion patterns predicted by simulations align with real-world turbine wear.*

1 INTRODUCTION

Multiphase flows occur in wide range of devices in process and energy engineering. In some cases, their occurrence is intentional due to the process taking place between the phases in the flow, such as in spray coating (spray towers), preparation of suspensions in the pharmaceutical and food industries (fluidized bed devices, mixing reactors), distillation, drying, air conditioning (air conditioning and ventilation systems), combustion in thermal machines (thermal power plants, internal combustion engines), coating removal (sandblasting), and many other processes [1].

However, multiphase flow can also arise unintentionally as a consequence of natural phenomena or engineering process, for example, solid particles in emissions during combustion (combustion in internal combustion engines, thermal power plants, fires), sediments in river flows (flow through hydraulic turbine machines) and sand particles in wind flow (wind erosion in deserts).

In general, multiphase flows are classified into stratified and dispersed types, with flows containing solid dispersed phases, such as particles in liquid flow, being a special case of the latter. Due to the frequent occurrence of such flows in process and energy devices, the interaction of particles with the walls of the devices is of significant engineering interest. These interactions can result in material loss from the wall surface, commonly referred to as abrasion. A particularly relevant issue is the damage to the flow components of turbine machines operating in rivers polluted with sediments [2].

In 2023, approximately 750 million people worldwide still lacked access to electricity [3]. In the preceding year, 4300 TWh of electricity worldwide was produced in hydropower plants, accounting for about 15 % of total global electricity production. Annual growth of production was 2 %, with projections suggesting an increase of 4 % by 2030 [4].

As further adoption of hydraulic turbines to produce electricity is pursued, several engineering challenges have emerged [5]. Hydraulic turbines are conventionally designed for operation within normal operating limits. When operating outside these limits, i.e. within temporary operating limits, the operating time is limited according to IEC 60609 standard [6]. If a turbine is operating in temporary operating limits in such a regime that pressure drops below vapor pressure, cavitation can occur. Cavitation can cause erosion of turbine components, independent of other erosion causes. Another challenge arises in rivers with suspended sediments, where the flowing water carries solid particles, which can cause additional erosion, termed abrasion.

To improve turbine design with respect to erosion phenomena, or to predict erosion in existing turbine designs, computational fluid dynamics (CFD) simulations coupled with erosion models are often utilized. In the past, various modelling approaches for cavitating flow have been adopted, and several cavitation erosion models have been developed. Research in this field remains ongoing, with recent efforts focused on phenomenological models applied to a range of engineering applications. Leclercq et al. [7] developed a cavitation erosion model based on earlier work by Fortes-Patella et al. [8] in which all cavitation collapses are considered by projecting cavitation erosion potential from interior cells to the wall using a discrete formulation. Implemented in Code_Saturne, this model was successfully applied to predict cavitation erosion on a NACA65012 hydrofoil. Schenke and van Terwisga [9] proposed a continuous formulation for the projection of cavitation potential to walls, while Melissaris et al. [10] later improved the model by considering energy focusing during cavity collapse. Using this improvement, they were able to predict more spatially focused cavitation erosion patterns in the case of a KCD-193 model propeller. Arabnejad et al. [11] further advanced modeling by considering two different mechanisms, both pressure waves and microjets, depending on the distance from the wall at which cavity collapse occurs. These complex models have been successfully used to predict erosion for various cases; however,

 DOI: 10.5545/sv-jme.2025.1351

open questions remain regarding modeling assumptions, particularly the cavitation collapse driving pressure [12].

In addition to above presented complex models, simpler models have been developed and successfully applied to predict cavitation erosion in different hydraulic systems. These simpler models are often applied to complex geometries or cases in which change in geometry needs to be considered. Such was the study by Brunhart et al. [13], where it has been determined that for the cavitation erosion prediction within a diesel fuel pump, where dynamic mesh was adopted, good agreement with experiment was obtained using an erosion indicator based on the recorded maximum of the squared total time derivative of pressure. Santos et al. [14] used three erosion indicators to predict cavitation erosion in gasoline direct injection (GDi) injector, where again dynamic mesh was adopted in the simulation. For the prediction of cavitation erosion in Pelton turbine, Jošt et al. [15] adopted criteria previously proposed by Rossetti et al. [16], which relate material damage to presence of water vapor in contact with the wall, rapid reduction in volume of this water vapor and the volume fraction of air mixed with the water (and water vapor) in the observed region. Based on this approach, Jošt et al. [15] concluded that damage of the observed Pelton rotor blades is not the result of cavitation erosion as the collapses are too slow.

Erosion of material due to particles has long been a topic of investigation of a distinct branch of engineering research – tribology. It stems from early research of contact forces due to friction by physicists such as Coulomb and later Hertz. Due to previously mentioned industry applications in which multiphase flows and subsequent abrasion occur, research into particle abrasion focused on experimental studies to obtain empirical predictive models of abrasion.

Such early study was conducted by Finnie [17], in which basic parameters that influence abrasion were determined, notably the influence of the particle impact angle on abrasion. Similarly, Bitter [18,19] identified different influencing parameters and proposed an empirical abrasion model, following by Grant and Tabakoff conducted studies [20,21] of abrasion in helicopter turbines and proposed a particle wall rebound model alongside their own abrasion model. Ahlert [22] proposed another abrasion model based on experimental investigation of particles impacting AISI 1018 steel sample. For AISI 4130 steel Forder et al. [23] conducted similar study and applied the abrasion model to predict abrasion in control valve using CFD simulations. Later multiple models have been proposed, with increasing complexity with respect to number of parameters considered, such as studies by Oka et al. [24] and Oka and Yoshida [25] and by Det Norske Veritas society (DNV) [26]. Over time adoption of empirical abrasion models in CFD has increased, Gnanavelu et al. [27] used this approach to reduce the number of experiments needed in their study of abrasion.

These empirical abrasion models have been applied to predict particle abrasion in different hydraulic systems by using CFD simulations of flows containing solid particles, where particles are considered as points and are tracked in Lagrangian frame. Peng and Cao [28] studied abrasion of pipe bends in piping found in oil industry, by comparing multiple abrasion models used in numerical simulations with experimental results, they concluded that McLaury model [29] in conjunction with the Grant and Tabakoff particle-wall rebound model [20,21] was the most accurate in predicting abrasion due to particles in liquid flow. Messa et al. [30] conducted a numerical study of abrasion in Pelton turbine injectors, where they applied the model by Oka et al. [24] and Oka and Yoshida [25] to predict abrasion of the nozzle seat and needle for different needle openings and needle vertex angles. They found enhanced abrasion for low openings and lower needle vertex angles. Many similar analyzes exist in the literature, indicating the need to better understand abrasion of Pelton injectors, particularly for full scale Pelton turbine injectors, which has recently been analyzed by Liu et al. [31].

In general, abrasion of turbine components is prevalent also on turbine runners, specifically rotor blades. Kumar and Bhingole [32] conducted a CFD study of a combined effect of cavitation and particle erosion on Kaplan turbine, with varying particle size and concentration and determined that larger particles and larger concentrations of particles produced more abrasion on the runner. Similarly, effects of particle concentration and diameter on abrasion characteristics obtained by CFD simulations on a Pelton turbine runner have been studied by Li et al. [33], where they concluded that the diameter of the particles mainly effected the distribution of predicted abrasion regions and concentration mainly influenced the intensity of abrasion. Han et al. [34] also considered cavitation to have an influence on particle abrasion of Pelton runner, which they predicted using the Finnie [17] model. They concluded that cavitation has a clear influence on particle abrasion development, especially due to its effect on motion of smaller particles at the jet interface (air-liquid interface) [34]. Table 1 summarizes the mechanisms of erosion and highlights the studies where erosion was modelled specifically in the case of Pelton runner.

Table 1. Summary of studies of erosion modelling highlighting which erosion mechanism was modelled

Reference	Mechanism of erosion
Leclercq et al. [7]	Cavitation collapse
Melissaris et al. [10]	Cavitation collapse
Arabnejad et al. [11]	Cavitation collapse
Brunhart et al. [13]	Cavitation collapse
Santos et al. [14]	Cavitation collapse
Rossetti et al. [16]	Cavitation collapse
Finnie [17]	Particle impact
Bitter [18,19]	Particle impact
Ahlert [22]	Particle impact
Oka, Okamura and Yoshida [24,25]	Particle impact
Det Norske Veritas society [26]	Particle impact
Peng and Cao [28]	Particle impact
Messa, Mandelli and Malavasi [30]	Particle impact
Liu et al. [31]	Particle impact.
Kumar and Bhingole [32]	Particle impact and cavitation collapse
Li et al. [33]	Particle impact
Han et al. [34]	Particle impact

In the present study, we investigated numerically, whether the cause of erosion of Pelton runner, found in the previous study by Jošt et al. [15], could be due to solid particles present in the water flow. For this purpose, we extended the modelling of flow through Pelton turbine by including Lagrangian particle tracking and applying Finnie abrasion model within ANSYS CFX 2023 R2 [17]. Two particle concentrations were considered, one for regular river conditions and one for the case of heightened presence of particles, for example due to the extreme weather phenomena. Unlike previous studies, such as the one by Han et al. [34], we considered fully transient behavior of the flow including particle motion and Pelton rotor rotation. For this purpose, a sliding mesh approach was adopted, specifically a rotating mesh was used for the rotor region. With this approach we managed to avoid using a simplification to steady-state.

2 METHODS AND MATERIALS

2.1 Case Description

A Pelton runner from previous study is considered [15], where a numerical simulation of the existing prototype-scale Pelton turbine was conducted for the case of cavitating flow. The purpose of that study was to determine if cavitation could be the cause of erosion on the blade tip observed after prolonged operation as shown in Fig. 1.

The authors [15] concluded that cavitation alone could not explain the erosion in the region of the blade tip. The main question then arose, whether that damage could be the result of turbine operating in a river laden with sediments (solid particles).

The presence of sediment particles was confirmed by electron microscope imaging of the river water sample and both size and chemical composition of sediment particles were determined. Sediment particles were found to be in range between 30 μm and 80 μm and are visible on an electron microscope image shown in Fig. 2.

It was then found that sand particles, which are agglomerated to form a sediment particle, are silica particles (SiO2). Chemical composition of sediment for a wider sampling region Spectrum 1 and a sampling point Spectrum 2 (elongated particle visible in Fig. 2) is shown in Table 2, where Oxygen (O) and Silicone (Si) have the highest fraction of all elements present in sediment sample for both sampling regions Spectrum 1 and Spectrum 2.

Table 2. Chemical composition of sediment

Element	Spectrum 1	Spectrum 2	Element	Spectrum 1	Spectrum 2
O	45.43	48.21	K	2.42	0.58
C	13.68	16.17	Mg	0.87	-
Si	17.12	28.55	Na	0.54	0.44
Al	6.32	0.83	Cl	-	0.11
Ca	9.29	3.42	Ti	0.33	0.18
Fe	3.67	1.51	Mn	0.32	-
			Total	100	100

2.2 Mathematical Model

An incompressible, turbulent, multiphase flow of water jet with cavitation and solid particles is considered. Multiphase flow of liquid water and due to cavitation water vapor contained within a jet, which forms an interface with respect to surrounding gas (air), is modelled using a homogeneous mixture approach. Mixture density (ρ) and mixture viscosity (μ) are determined by mixing rule as:

$$\rho = \varphi_l \rho_l + \varphi_v \rho_v + \varphi_g \rho_g, \tag{1}$$

$$\mu = \varphi_l \mu_l + \varphi_v \mu_v + \varphi_g \mu_g, \tag{2}$$

where φ_l is liquid volume fraction, φ_v is the vapor volume fraction and φ_g is gas volume fraction. Similarly, ρ_l and ρ_v are liquid and vapor density respectively and ρ_g is gas density. Finally, μ_l and μ_v are liquid and vapor dynamic viscosity respectively, while μ_g is gas dynamic viscosity. The governing equations of cavitating flow can then be written, the continuity equation as:

$$\frac{\partial \rho}{\partial t} + \nabla(\rho \mathbf{u}) = 0, \tag{3}$$

and momentum equation as:

$$\frac{\partial(\rho \mathbf{u})}{\partial t} + \nabla(\rho \mathbf{u}\mathbf{u}) = -\nabla p + \nabla \boldsymbol{\tau} + \mathbf{S}_\mathbf{M}, \tag{4}$$

where Eqs. (3) and (4) are written for the mixture of liquid and vapor phases which share the same velocity $\mathbf{u}$ and pressure p. In Eq. (4) $\boldsymbol{\tau}$ is mixture shear stress tensor and $\mathbf{S}_\mathbf{M}$ is the momentum source term accounting for the presence of particles. Since the multiphase flow is considered as a mixture of two phases, an additional equation for transport of vapor volume is needed:

$$\frac{\partial \varphi_v}{\partial t} + \nabla(\varphi_v \mathbf{u}) = \frac{\dot{m}}{\rho_l}, \tag{5}$$

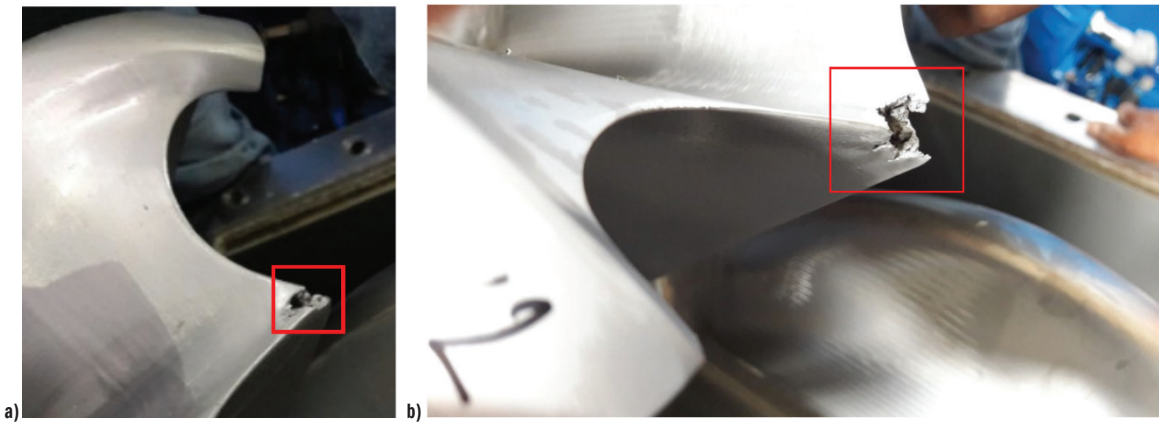

Fig. 1. Damage of a Pelton rotor blade tip (in red bracket) after prolonged operation: a) view of the back side of the blade, view of the front side of the blade

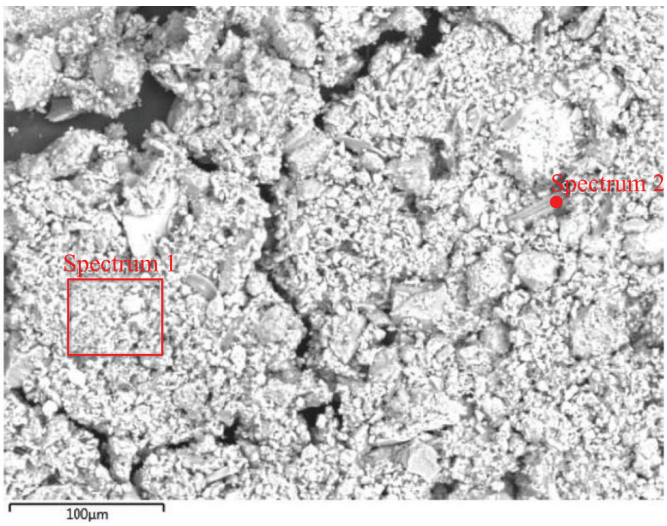

Fig. 2. Electron microscope image of the river sediment with two sampling positions to determine chemical composition indicated as Spectrum 1 and Spectrum 2

where $\dot{m}$ is the interface mass transfer rate due to cavitation, for which a cavitation model by Zwart et al. [35] was adopted in this study:

$$\dot{m}=\begin{cases}-F_e\dfrac{3r_{nuc}\left(1-\varphi_v\right)\rho_v}{R_B}\sqrt{\dfrac{2}{3}\dfrac{p_v-p}{\rho_l}}, & \text{if } p<p_v\\ F_c\dfrac{3\varphi_v\rho_v}{R_B}\sqrt{\dfrac{2}{3}\dfrac{p-p_v}{\rho_l}}, & \text{if } p>p_v\end{cases}, \tag{6}$$

where F_e is the evaporation coefficient with a recommended value of 50 [35], F_c is the condensation coefficient with a recommended value of 0.01, r_{nuc} is the nucleation site volume fraction with a default value of 5×10^{-4} and R_B is the bubble radius upon which the model is derived, with a recommended value of 10^{-6} m [35]. From Eq. (6) it is evident that the mass transfer rate was considered negative in the case of evaporation, when pressure p is bellow vapor pressure p_v, which was 1300 Pa for water. Likewise, in Eq. (6) the mass transfer rate is positive in the case of condensation, when the pressure p is above vapor pressure p_v.

Although more advanced turbulence models (hybrid Reynolds-averaged Navier-Stokes and large Eddy simulation (RANS/LES), and large Eddy simulation (LES)) have recently been used in the studies of turbulent, cavitating flows [36], even for some engineering applications [37,38], RANS two-equation models still represent a good balance between accuracy and calculation times for most engineering applications, like a Pelton turbine. Therefore, in this study turbulence was modelled using a RANS approach, specifically the $k-\omega$ SST two-equation turbulence model was used. Two additional transport equation are introduced, one for the turbulent kinetic energy k:

$$\frac{\partial\left(\rho k\right)}{\partial t}+\nabla\left(\rho k\mathbf{u}\right)=\nabla\left[\left(\mu+\frac{\mu_t}{\sigma_k}\right)\nabla k\right]+G_k-Y_k+S_k, \tag{7}$$

and one for the specific turbulence dissipation rate ω:

$$\frac{\partial\left(\rho\omega\right)}{\partial t}+\nabla\left(\rho\omega\mathbf{u}\right)=\nabla\left[\left(\mu+\frac{\mu_t}{\sigma_\omega}\right)\nabla\omega\right]+G_\omega-Y_\omega+D_\omega+S_\omega, \tag{8}$$

where G_k and G_ω are production terms for the turbulent kinetic energy and the specific turbulence dissipation rate respectively, Y_k and Y_ω are the dissipation terms for the turbulent kinetic energy and for the specific turbulence dissipation rate respectively, σ_k and σ_ω are the turbulent Prandtl numbers for k and for ω respectively, S_k and S_ω are the source terms. Since the $k-\omega$ scale-adaptive simulation model (SST) is a blended turbulence model, consisting of standard $k-\varepsilon$ and standard $k-\omega$ model, an additional term cross-diffusion term D_ω is introduced in Eq. (8) due to reformulation of $k-\varepsilon$ model for blending with $k-\omega$ model. RANS approach results in additional turbulent viscosity μ_t, which is in the case of $k-\omega$ SST model written as:

$$\mu_t=\frac{\rho k}{\omega}\frac{1}{\max\left[\dfrac{1}{\alpha^*},\dfrac{SF_2}{a_1\omega}\right]}, \tag{9}$$

where α^* is the turbulent viscosity damping coefficient, a_1 is a model constant with value of 0.31 [39], S is the strain rate magnitude and F_2 is the second blending function. A detailed description of the turbulent model used is available in [39].

Particles represent a discrete phase for which Lagrangian tracking is adopted within previously described continuous phase (mixture of two continuous phases) which was considered in Eulerian frame. In our study drag force and virtual mass force were considered, gravity effects (buoyancy) were neglected as the inertia of the flow, due to high fluid velocity, had a dominant influence on the motion of particles. Then, an additional motion equation for particles due to drag force and virtual mass force can be written in the form of particle acceleration as:

$$\frac{d\mathbf{v}}{dt}=\frac{18\mu_l}{\rho_p d_p^2}\frac{C_D Re_p}{24}\left(\mathbf{u}-\mathbf{v}\right)+\frac{1}{2}\frac{\rho_l}{\rho_p}\left(\frac{D\mathbf{u}}{Dt}-\frac{d\mathbf{v}}{dt}\right), \tag{10}$$

where $\mathbf{v}$ is the particle velocity, ρ_v is the particle density, d_p is the particle diameter and the particle Reynolds number Re_p is defined as:

$$Re_p=\frac{\rho_p d_p\left|\mathbf{u}-\mathbf{v}\right|}{\mu_l}, \tag{11}$$

The drag coefficient C_D is calculated using the Schiller Naumann correlation [40]:

$$C_D=\begin{cases}24\dfrac{\left(1+0.15Re_p^{0.687}\right)}{Re_p}, & \text{if } Re_p<1000\\ 0.44, & \text{if } Re_p\geq1000\end{cases}. \tag{12}$$

Since the volume fraction of the particles in particle-laden flow is low, interactions between particles are neglected. However, interaction of particles with the wall must be considered as it is one of the boundary conditions. For this, Hard Sphere Model is adopted, where particles are considered as nondeformable during their collision with the wall. Rebound of particles from the wall is then described with two coefficients of restitution, one in wall normal direction:

$$e_n=\frac{v_{n,2}}{v_{n,1}}, \tag{13}$$

and one in tangential direction:

$$e_t=\frac{v_{t,2}}{v_{t,1}}, \tag{14}$$

where $v_{n,1}$ and $v_{n,2}$ are particle velocities in the wall normal direction before and after rebound respectively, and $v_{t,1}$ and $v_{t,2}$ are particle velocities in the wall tangential direction before and after rebound respectively. Particle velocity in both directions after rebound ($v_{n,2}$ and $v_{t,2}$) are calculated for the known coefficients of restitution (e_n and e_t), which were determined by using Grant and Tabakoff model [19], where coefficients of restitution are given as functions of particle impact angle γ as:

$$e_n=0.993-1.76\gamma+1.56\gamma^2-0.49\gamma^3, \tag{15}$$

$$e_t=0.988-1.76\gamma+1.56\gamma^2-0.49\gamma^3. \tag{16}$$

To predict erosion of the wall due to impacting particles, we used an empirical model by Finnie [17], which gives the erosion rate as:

$$E_R=\left(\frac{\left|\mathbf{v}\right|}{v_0}\right)^n f\left(\gamma\right), \tag{17}$$

where v_0 is the empirical reference velocity with a value of 3321 m/s for steel, n is the velocity exponent with a value of 2.4 and $f(\gamma)$ is an impact angle function, given as:

$$f\left(\gamma\right)=\begin{cases}\dfrac{1}{3}\cos^2\gamma; & \text{if } \tan\gamma>\dfrac{1}{3}\\ \sin\left(2\gamma\right)-3\sin^2\gamma, & \text{if } \tan\gamma\leq\dfrac{1}{3}\end{cases}. \tag{18}$$

2.3 Boundary Conditions and Physical Properties

Based on the previously described sediment analyzis, solid silica particles with density ρ_p=2650 kg/m³ of sizes between 30 μm and 80 μm were considered in numerical simulation. To account for the varying size of particles we used the Rosin-Rammler particle size distribution, where the mass fraction of particles above a certain particle diameter d_p is defined as:

$$R = e^{\left[-\left(\frac{d_p}{d_e}\right)^{\chi}\right]}, \quad (19)$$

where d_e is the size constant and χ is the size distribution parameter. We considered a particle distribution with d_e=50 μm and χ=1.1. The resulting cumulative mass fraction distribution is shown in Fig. 3.

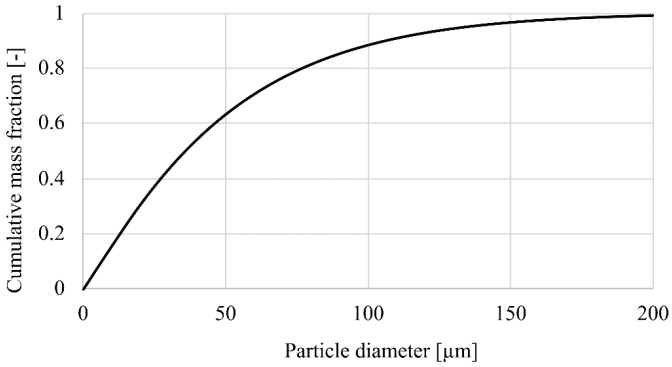

Fig. 3. Rosin-Rammler particle size distribution used in numerical simulation, represented with a cumulative mass fraction over particle diameters

Varying shape of particles was not considered in numerical simulations; therefore, particles were assumed to be spherical. Two different cases of particle loading of the flow were considered, one for the regular river flow where volume fraction of particles is 0.006 % and one for heightened particle loading scenario where volume fraction of particles is 10 times higher, resulting in volume fraction of particles of 0.06 %. Properties of liquid water, water vapor and air are presented in Table 3.

Table 3. Properties of continuous phases (liquid water, water vapor and air) used in numerical simulation

Material	Density [kg/m³]	Dynamic viscosity [Pa s]
Liquid water	999.18	0.00114029
Water vapor	0.02308	9.86e-6
Air	1.185	1.83e-5

Boundary conditions were defined as shown in Fig. 4. For the liquid jet flow, velocity components were prescribed as a function of coordinates over the nozzle area, which were determined with previous numerical simulation of flow through the injector [15] for the mean velocity magnitude of 105.233 m/s and 5 % turbulent intensity at the inlet. For the particles entering the domain with the jet, zero-slip velocity condition was used while injection of particles was realized by prescribing their number rate and mass flow rate. This is presented in Table 4 for both particle loading scenarios.

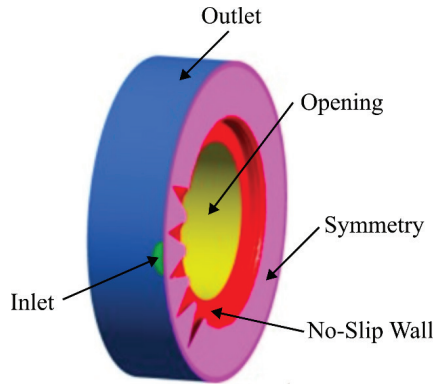

Fig. 4. Boundary conditions marked by colors: green – inlet, blue – outlet, red – no-slip wall, purple – symmetry and yellow – opening

Table 4. Particle injection definition at the inlet

Particle loading scenario	Volume fraction [%]	Number rate [s^{-1}]	Mass flow rate [kg/s]
Normal	0.006	2.81794e+7	0.048875
Heavy	0.06	2.81794e+8	0.48875

At the outlet, static pressure was prescribed with a value of 101,300 Pa for continuous phase, and particles are given the escape boundary condition by default. Same conditions were prescribed for the opening boundary condition.

To reduce computational demands, symmetry boundary condition was used at symmetry plane as shown in Fig. 4. For particles, however, this symmetry plane represented a wall, the fact that only half of the full volume (domain) was considered was accounted for when calculating particle inlet number rate and mass flow rate presented in Table 4.

Remaining surfaces (rotor blades and hub) were treated as no-slip walls for the continuous phase and solid walls with a rebound boundary condition for particles.

2.4 Mesh and Numerical Setup

To further reduce the computational demands, we considered only 5 rotor blades in the geometrical model for the meshing, since mesh around the blades require refinement resulting in higher mesh cell density. We used the mesh from the previous study [15], where a mixed hexahedral and tetrahedral mesh with 10.75 million cells was used. The mesh is presented in Fig. 5. The mesh consisted of two main regions, stationary and rotating. Rotating region of mesh

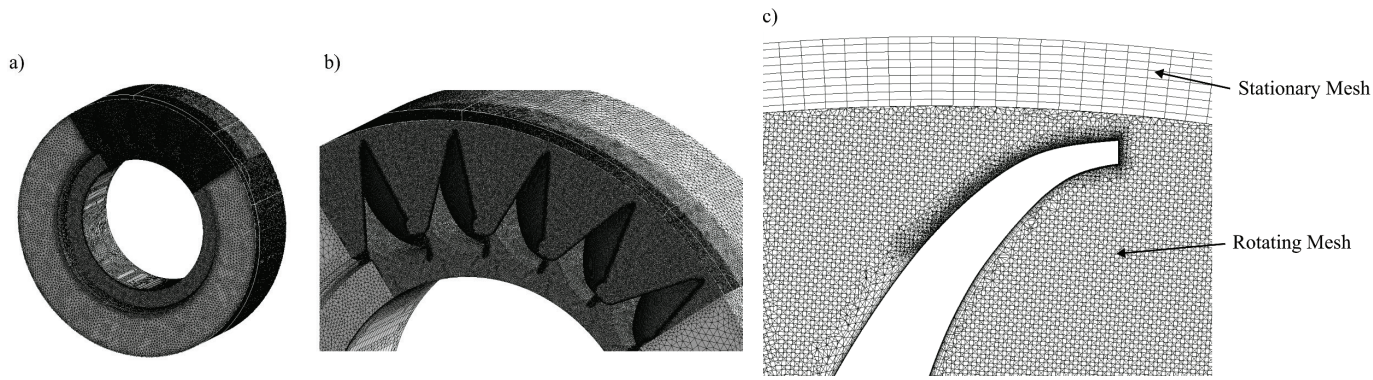

Fig. 5. Mesh showing: a) full mesh, b) detailed view of the blade region on the symmetry plane, and c) detailed view around a single blade at cross-section

was prescribed mesh rotation, such that 0.1° of rotor rotation was achieved per time step, and in total 27° of rotor rotation was achieved during the simulation.

Since the simulation was fully transient, a second order backward Euler transient scheme was adopted and for the advection terms high resolution scheme was used. Within each time step maximum 10 iterations were performed, however a residual target of 1e-4 was achieved before this limit.

3 RESULTS AND DISCUSSION

First, we present the results for the flow of sand particles in water jet impacting Pelton rotor blades, which is shown in Fig. 6 for the normal particle loading scenario and in Fig. 7 for the heavy particle loading scenario. In Figs. 6 and 7 we observe jet (green) impacting Pelton rotor blades shown at different times, with visible cavitation (magenta) shown as iso-surface with 20 % volume fraction of vapor and sand particles (black) for a normal particle loading scenario and heavy particle loading scenario, respectively. Rotor blade on which subsequent erosion is studied is highlighted with orange color. At the beginning in a) the blade is yet to come in contact with the jet, in following moments b) through e) it passes through the jet, particles in the jet impact the blade and in f) finally jet is cut-off by next passing blade

The difference in particle loading is clearly shown and discernible when comparing Figs. 6 and 7. Due to the modelling approach taken in this work, jet development and cavitation development are not influenced by particles, therefore they are identical for both particle loadings, as seen when comparing Figs. 6 and 7.

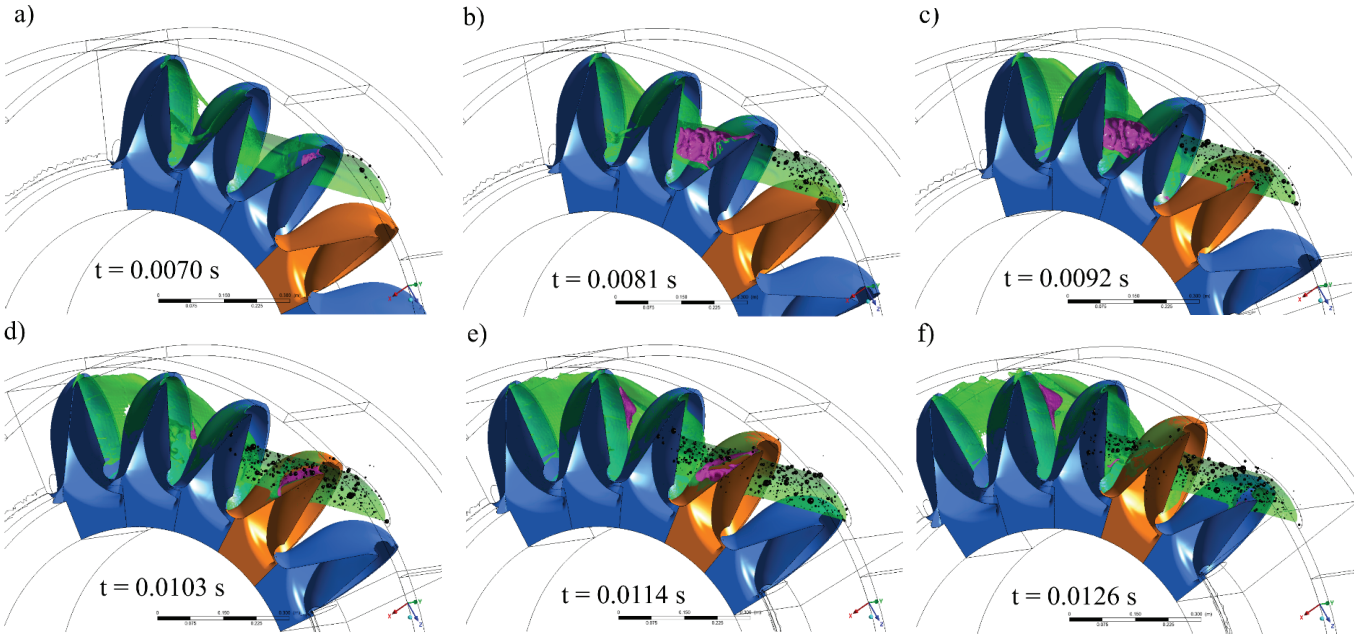

Fig. 6. Impact of jet with particles on Pelton rotor blade at different times for normal particle loading scenario

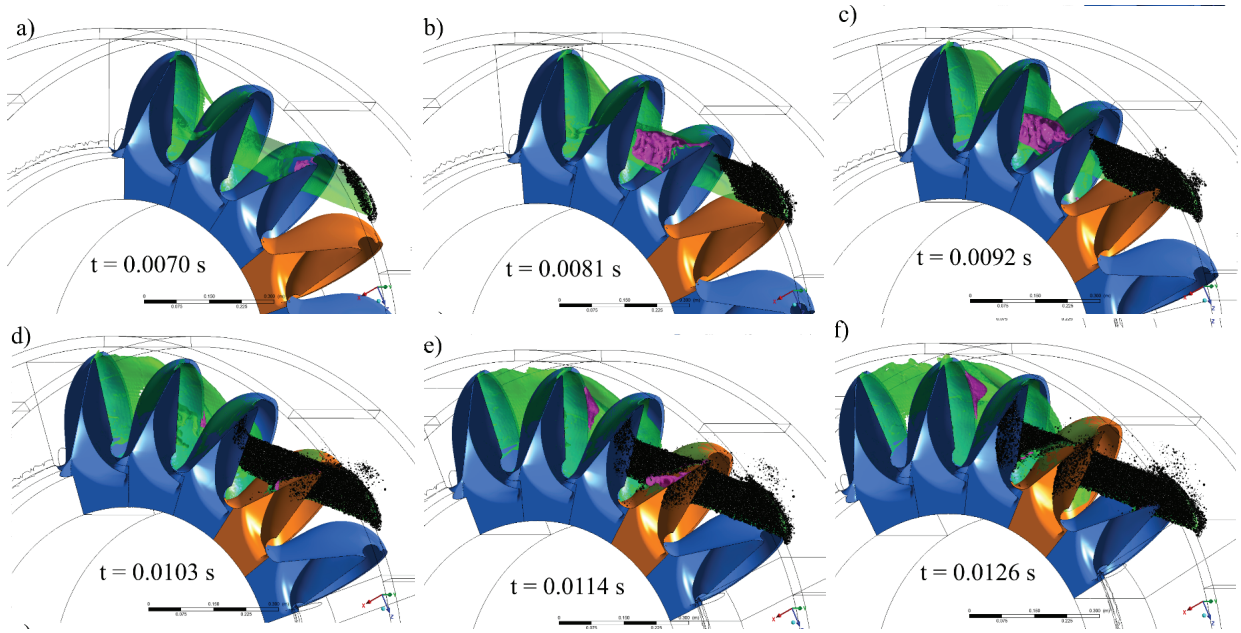

Fig. 7. Impact of jet with particles on Pelton rotor blade at different times for heavy particle loading scenario

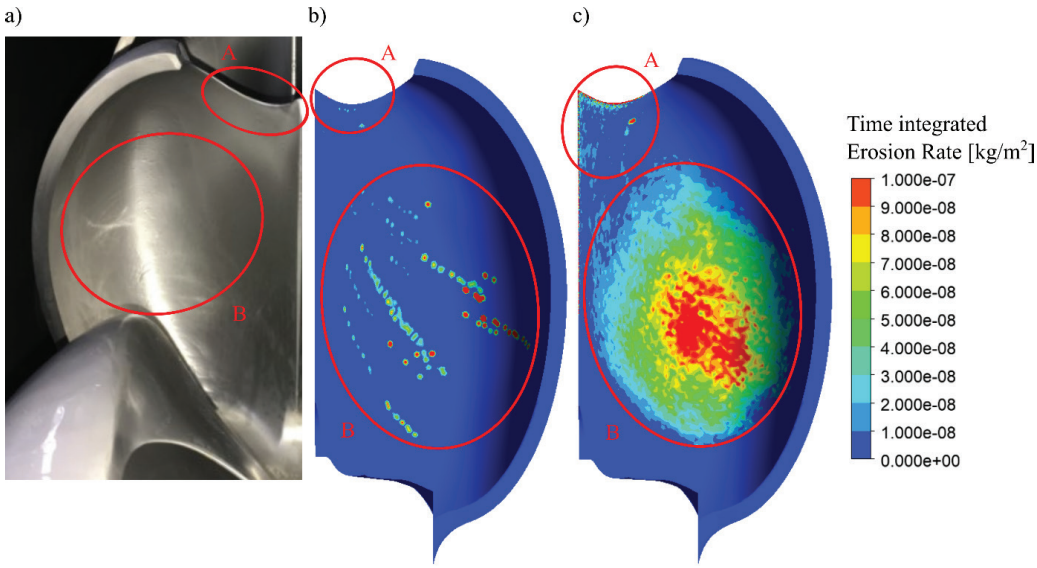

Fig. 8. Erosion on the front side of the Pelton rotor blade: a) real operating blade, b) normal particle loading scenario simulation, and c) heavy particle loading scenario simulation

Particle motion follows the motion of the water jet. Attached cavitation pocket behind the second blade, visible at time t = 0.0114 s on Figs. 6 and 7, redirects the particles around it. Within the simulated time, the second blade of five blades considered in this simulation passes through the impacting water jet carrying sand particles completely. As the second blade passes through the jet, particles entrained in the jet impact the back side of the blade as well.

This is why erosion prediction results will be presented only for the second blade, since particle erosion is expected to occur on both the front and the back side of the blade. Particle erosion on the front side of the blade is shown in Fig. 8, where contour of time integral of Eq. (17) is shown for both particle loading scenarios. Two distinct erosion zones are marked as A – blade tip region, and B – blade bucket. Difference in the pattern of zone B is observed, for heavier particle loading case (Fig. 8c) a more spread-out pattern emerges.

Presented simulation results show that the extent of abrasion is higher in the heavy particle loading case, while in both normal and heavy loading scenarios two distinct erosion zones are formed on the front side of the blade. One is at the tip of the blade and is more pronounced in the heavy particle loading scenario. Second one is in the middle of the blade bucket and is again more pronounced in the heavy particle loading scenario. The difference between the erosion zone B pattern in Fig. 8 can be explained by larger number of particles in the flow in the heavy particle loading scenario. Due to larger number of particles, which take up more configurations in space (in the water jet), they produce a more spread-out pattern. These results of erosion patterns for the front side of the blade are also in general agreement with reference lab-scale experimental investigation of Pelton bucket by Umar et al. [41], where they also observed two distinct erosion zones (one around the blade splitter and one in the middle of the bucket). Direct comparison is however limited, by different Pelton geometry, operating parameters and sediment concentration.

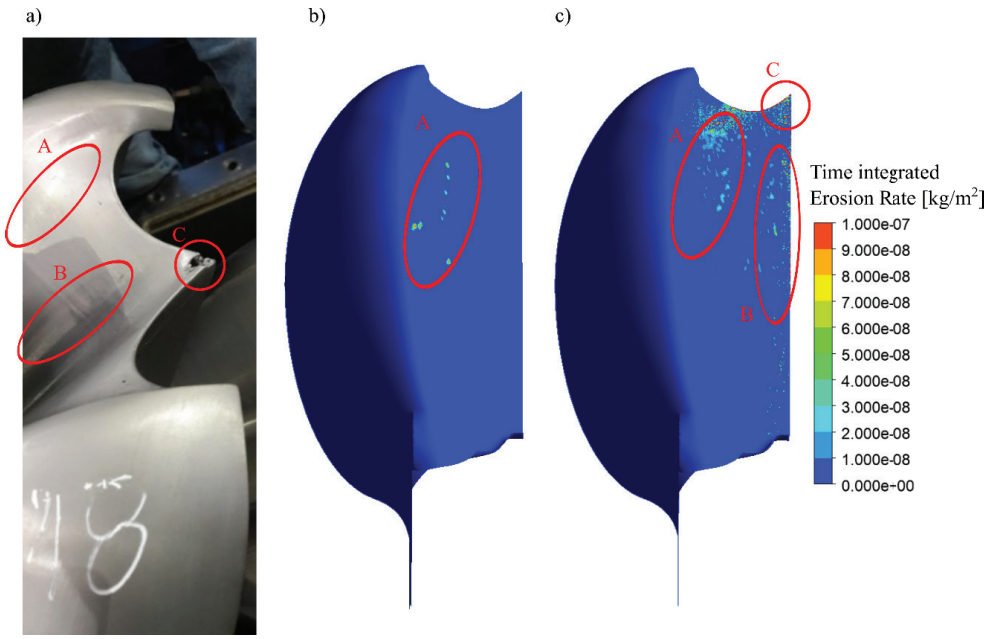

Fig. 9. Erosion on the back side of the Pelton rotor blade: a) real operating blade, b) normal particle loading scenario simulation , c) heavy particle loading scenario simulation

Similarly, we present erosion on the back side of the blade in Fig. 9. Three distinct erosion zones are marked as A – blade mid-bucket region, B – blade bucket edge, and C – blade tip region. On the blade of real operating Pelton rotor, three erosion zones can be identified, (Fig. 9a), one in the middle of the bucket, one at the edge, splitting the blade in two halves, and one around the blade tip. All three regions are observed in the case of the simulation with the heavy particle loading, however, for the normal particle loading condition only the region in the middle of the bucket (Fig. 9b) region marked with A is predicted. In general, it is observed that the extent of erosion is less on the back of the blade than on the front side.

Since from the previous study a research question was whether particles could be the cause of blade tip damage, a detailed view of the blade tip is shown in Fig. 10. Results of simulation with heavy particle loading only are shown in Fig. 10a), as in the normal particle loading no erosion of the tip was predicted (Fig. 9). Under normal particle loading of the river, tip damage observed after operation of a real Pelton rotor as seen in Fig. 10b), can't be attributed to particle erosion. However, under heavy loading conditions, particle erosion could cause damage to the tip, simulation results for these conditions show good agreement. Erosion rate is highest at the tip and the spreads out with lower intensity, and black lines in Fig. 10 indicate the extent of erosion spread.

Finally, we give brief discussion of model sensitivity to different parameters or modelling scenarios. Particles were assumed to be spherical, however real river sediment particles come in different shapes. An example of idealized non-spherical shape is a superellipsoid, for which Wedel et al. [42] found that Lagrangian tracking gives better particle motion than by using simpler shape factors, indicating the complexity of this problem. This difference in particle motion could then be reflected in the erosion pattern at the wall. The influence of particles on erosion could also be due to irregular shape of particles, for example angular particles are known to be more erosive. Yasser, Zhou and El- Emam [43] conducted detailed computational fluid dynamics - discrete element method (CFD-DEM) simulations of different angular particles and spherical particles in pipe elbow and found that particles with fewer corners (but therefore sharper edges) produced more erosion, while pattern of erosion was more localized. In addition to that, even for spherical particles different drag models exist. Likewise, there are several approaches to model cavitation and within the vapor transport equation modelling approach adopted in this study, several algebraic cavitation models exist. For an overview of different cavitation models, we refer the reader to Folden and Aschmoneit [44].

4 CONCLUSIONS

This study presents a numerical investigation into the erosion of Pelton turbine rotor due to solid particles in a cavitating flow. By extending previous research that focused on cavitation-induced erosion, we incorporated Lagrangian particle tracking and employed the Finnie abrasion model [17] to assess the effects of sediment-laden water on turbine blades. Our findings indicate that, under normal river conditions, particle-induced erosion is not a significant contributor to the observed blade tip damage but can cause erosion of the blade bucket. However, under heavy sediment loading scenario, as a result of extreme weather phenomena, erosion predictions closely align with real-world observation on an actual operating Pelton rotor, suggesting that heavy particle concentrations can lead to substantial material loss, particularly at the blade tip.

The results highlight the necessity of considering both cavitation and particle erosion when evaluating turbine durability in sediment-rich environments. Future work could focus on refining erosion models by incorporating particle shape effects, varying material properties, and exploring mitigation strategies such as optimized blade coatings or operational adjustments to minimize erosive wear.

Nomenclature

α^* turbulent viscosity damping coefficient, [-]
γ impact angle, [°]
χ size distribution parameter, [-]
φ_l liquid volume fraction, [-]
φ_v vapor volume fraction, [-]
φ_g gas volume fraction, [-]
μ mixture viscosity, [Pa s]
μ_l liquid dynamic viscosity, [Pa s]
μ_v vapor dynamic viscosity, [Pa s]
μ_g gas dynamic viscosity, [Pa s]
ω specific turbulence dissipation rate, [s^{-1}]
ρ mixture density, [kg/m^3]
ρ_l liquid density, [kg/m^3]
ρ_g gas density, [kg/m^3]

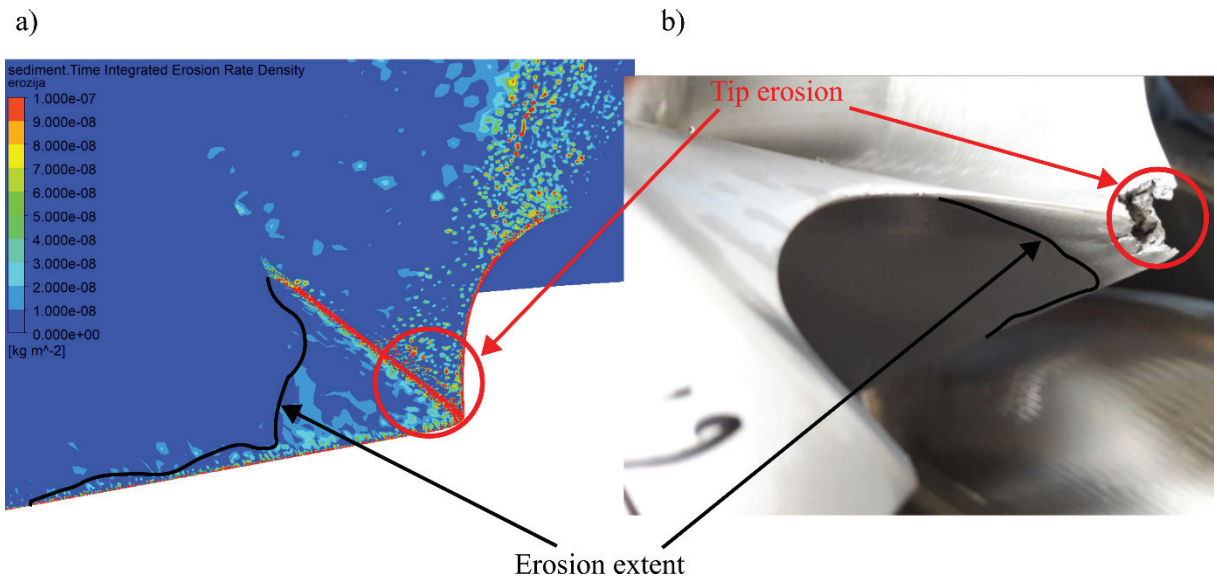

Fig. 10. Erosion of the tip of the blade: a) simulation for heavy particle loading condition, b) actual Pelton rotor blade tip

ρ_p particle density, [kg/m^3]
ρ_v vapor density, [kg/m^3]
σ_k turbulent Prandtl number for the turbulent kinetic energy, [-]
σ_ω turbulent Prandtl number for the specific turbulence dissipation rate, [-]
$\boldsymbol{\tau}$ mixture shear stress tensor, [Pa]
a_1 model constant, [-]
C_D drag coefficient, [-]
d_p particle diameter, [m]
d_e size constant, [-]
e_n coefficient of restitution in wall normal direction, [-]
e_t coefficient of restitution in wall tangential direction, [-]
F_e evaporation coefficient, [-]
F_d condensation coefficient, [-]
F_2 second blending function, [-]
$f(\gamma)$ is an impact angle function, [-]
G_k production term for the turbulent kinetic energy, [m^2/s^2]
G_ω production term for the specific turbulence dissipation rate, [m^2/s^3]
k turbulent kinetic energy, [m^2/s^2]
$\dot{m}$ interface mass transfer rate, [kg/s]
n velocity exponent, [-]
p pressure, [Pa]
p_v vapor pressure, [Pa]
R mass fraction of particles, [-]
R_B bubble radius, [m]
Re_p particle Reynolds number, [-]
S strain rate magnitude, [s^{-1}]
$\mathbf{S_M}$ momentum source term, [N
S_k source term for the turbulent kinetic energy, [m^2/s^2]
S_ω source term for the specific turbulence dissipation rate, [m^2/s^3]
t time, [s]
$\mathbf{u}$ velocity, [m/s]
$\mathbf{v}$ particle velocity, [m/s]
v_n particle velocity in the wall normal direction, [m/s]
v_t particle velocity in the wall tangential direction, [m/s]
v_0 empirical reference velocity, [m/s]
Y_k dissipation term for the turbulent kinetic energy, [m^2/s^2]
Y_ω dissipation term for the specific turbulence dissipation rate, [m^2/s^3]

References

[1] Vovk, N., Ravnik, J. Numerical modeling of two-phase flow inside a wet flue gas absorber sump. *Energies* 16 8123 (2023) **DOI:10.3390/en16248123**.

[2] Gautam S., Acharya, N., Lama, R., Chitrakar, S., Neopane, H.P. Zhu, B., Dahlhaug, O.G. Numerical and experimental investigation of erosive wear in Francis runner blade optimized for sediment laden hydropower projects in Nepal Sust. *Ener Tech Assess* 51 101954 (2022) **DOI:10.1016/j.seta.2022.101954**.

[3] IEA. SDG7: Data and Projections (2024) *https://www.iea.org/reports/sdg7-data-and-projections*, accessed 2025-09-22.

[4] Kent, R. Renewables. *Plast Eng* 74 56-57 (2018) **DOI:10.1002/peng.20026**.

[5] Giljen, Z., Nedeljković, M., Cheng, Y. The influence of pump-turbine specific speed on hydraulic transient processes. *Stroj vest-J Mech E* 70 231-246 (2024) **DOI:10.5545/sv-jme.2023.776**.

[6] CEI/IEC 60609-1:2004 *Hydraulic Turbines, Storage Pumps and Pump-Turbines -Cavitation Pitting Evaluation -Part 1: Evaluation in Reaction Turbines, Storage Pumps and Pump-Turbines*. International Organization for Standardization, Geneva

[7] Leclercq, C., Archer, A., Fortes-Patella, R., Cerru, F. Numerical cavitation intensity on a hydrofoil for 3D homogeneous unsteady viscous flows. *Int J Fluid Mach Syst* 10 254-263 (2017) **DOI:10.5293/IJFMS.2017.10.3.254**.

[8] Fortes Patella, R., Reboud, J.-L., Briancon Marjollet, L. A phenomenological and numerical model for scaling the flow agressiveness in cavitation erosion. EROCAV Workshop (2004) https://www.researchgate.net/publication/281921326, accessed 2025-09-22.

[9] Schenke, S., van Terwisga, T.J.C. An energy conservative method to predict the erosive aggressiveness of collapsing cavitating structures and cavitating flows from numerical simulations. *Int J Multiph Flow* 111 200-218 (2019) **DOI:10.1016/j.ijmultiphaseflow.2018.11.016**.

[10] Melissaris, T., Schenke, S., Bulten, N., van Terwisga, T.J.C. On the accuracy of predicting cavitation impact loads on marine propellers. *Wear* 456-457 203393 (2020) **DOI:10.1016/j.wear.2020.203393**.

[11] Arabnejad, M.H., Svennberg, U., Bensow, R.E. (2021). Numerical assessment of cavitation erosion risk using incompressible simulation of cavitating flows. *Wear* 464-465 203529 (2021) **DOI:10.1016/j.wear.2020.203529**.

[12] Kevorkijan, L., Pezdevšek, M., Biluš, I., Hren, G. Cavitation erosion modelling - comparison of different driving pressure approaches. *In. J Simul Model* 22 233-244 (2023) **DOI:10.2507/IJSIMM22-2-639**.

[13] Brunhart, M., Soteriou, C., Daveau, C., Gavaises, M., Koukouvinis, P., Winterbourn, M. Cavitation erosion risk indicators for a thin gap within a diesel fuel pump. *Wear* 442-443 203024 (2020) **DOI:10.1016/j.wear.2019.203024**.

[14] Gomez Santos, E., Shi, J., Venkatasubramanian, R., Hoffmann, G., Gavaises, M., Bauer, W. Modelling and prediction of cavitation erosion in GDi injectors operated with E100 fuel. *Fuel* 289 119923 (2021) **DOI:10.1016/j.fuel.2020.119923**.

[15] Jošt, D., Škerlavaj, A., Pirnat, V., Morgut, M. Nobile, E. Detailed analyzis of flow in two pelton turbines with efficiency and cavitation prediction. *Int J Fluid Mach Syst* 12 388-399 (2019) **DOI:10.5293/IJFMS.2019.12.4.388**.

[16] Rossetti, A., Pavesi, G., Ardizzon, G., Santolin, A. Numerical analyzes of cavitating flow in a Pelton turbine. *J Fluid Eng-T ASME* 136 081304 (2014) **DOI:10.1115/1.4027139**.

[17] Finnie, I. Erosion of surfaces. *Wear* 3 87-103 (1960) **DOI:10.1016/0043-1648(60)90055-7**.

[18] Bitter, J.G.A. A study of erosion phenomena: Part I. *Wear* 6 5-21 (1963) **DOI:10.1016/0043-1648(63)90003-6**.

[19] Bitter, J.G.A. A study of erosion phenomena: Part II. *Wear* 6 169-190 (1963) **DOI:10.1016/0043-1648(63)90073-5**.

[20] Grant, G., Tabakoff, W. Erosion prediction in turbomachinery resulting from environmental solid particles *J Aircraft* 12 471-478 (1975) **DOI:10.2514/3.59826**.

[21] Grant, G., Tabakoff, W. *An Experimental Investigation of the Erosive Characteristics of 2024 Aluminum Alloy.* NTIS, Springfield (1973).

[22] Ahlert, K.R. *Effects of Particle Impingement Angle and Surface Waiting on Solid particle Erosion of AISI 1018 Steel*. MScThesis (1994) University of Tulsa, Tulsa.

[23] Forder, A., Thew, M., Harrison, D. A numerical investigation of solid particle erosion experienced within oilfield control valves. *Wear* 216 184-193 (1998) **DOI:10.1016/S0043-1648(97)00217-2**.

[24] Oka, Y.I., Okamura, K. Yoshida, T. Practical estimation of erosion damage caused by solid particle impact: Part 1: Effects of impact parameters on a predictive equation. *Wear* 259 95-101 (2005) **DOI:10.1016/j.wear.2005.01.039**.

[25] Oka, Y.I., Yoshida, T. Practical estimation of erosion damage caused by solid particle impact: Part 2: Mechanical properties of materials directly associated with erosion damage. *Wear* 259 102-109 (2005) **DOI:10.1016/j.wear.2005.01.040**.

[26] Det Norske Veritas. Erosive Wear in Piping Systems. *https://rules.dnv.com/docs/pdf/dnvpm/codes/docs/2015-08/RP-0501.pdf*, accessed on 2025-09-22

[27] Gnanavelu, A., Kapur, N., Neville, A., Flores, J.F., Ghorbani, N. A numerical investigation of a geometry independent integrated method to predict erosion rates in slurry erosion. *Wear* 271 5-6 712-719 (2011) **DOI:10.1016/j.wear.2010.12.040**.

[28] Peng, W., Cao, X. Numerical simulation of solid particle erosion in pipe bends for liquid-solid flow. *Powder Technol* 294 266-279 (2016) **DOI:10.1016/j.powtec.2016.02.030**.

[29] McLaury, B.S., Shirazi, S.A., Shadley, J.R., Rybicki, E.F. Modeling erosion in chokes. *Proceedings of ASME Fluids Eng.* (1996) 773-782.

[30] Messa, G.V., Mandelli, S., Malavasi, S. Hydro-abrasive erosion in Pelton turbine injectors: A numerical study. *Renew Energ* 130 474-488 (2019) **DOI:10.1016/j.renene.2018.06.064**.

[31] Liu, J., Pang, J. Liu, X., Huang, Y., Deng, H. Analysis of sediment and water flow and erosion characteristics of large Pelton turbine injector. *Processes* 11 1011 (2023) **DOI:10.3390/pr11041011**.

[32] Kumar, D., Bhingole, P.P. CFD based analysis of combined effect of cavitation and silt erosion on Kaplan turbine. *Mater Today-Proc* 2 2314-2322 (2015) **DOI:10.1016/j.matpr.2015.07.276**.

[33] Li, L., Lu, J., Gong, Y., Zhao, H., Liu, X., Zhu, B. Sediment erosion characteristics of Pelton turbine runner: Effects of sediment concentration and diameter. *Renew Energ* 220 119679 (2024) **DOI:10.1016/j.renene.2023.119679**.

[34] Han, L., Guo, C., Yuan, Y., Li, D., Liu, Y., Iranzo, A., Qin, D. Investigation on sediment erosion in bucket region of Pelton turbine considering cavitation. *Phys Fluids* 36 023305 (2024) **DOI:10.1063/5.0179387**.

[35] Zwart, P.J., Gerber, A.G. Belamri, T. A two-phase flow model for predicting cavitation dynamics. *Proceedings of International Conference on Multiphase Flow* 152 (2004).

[36] Decaix, J., Goncalvès, E. Investigation of three-dimensional effects on a cavitating Venturi flow. *Int J Heat Fluid Fl* 44 576-595 (2013) **DOI:10.1016/j.ijheatfluidflow.2013.08.013**.
[37] Drešar, P. *Development of Biofluid Pump*. PhD Thesis University of Ljubljana, Ljubljana (2020). (in Slovene)
[38] Zhang, X. Transient flow characteristics of a pressure differential valve with different valve spool damping orifice structures. *Stroj vestn-J Eng E* 70 141-158 (2024) **DOI:10.5545/sv-jme.2023.691**.
[39] Menter, F.R. Two-equation eddy-viscosity turbulence models for engineering applications. *AIAA J* 32 1598-1605 (1994) **DOI:10.2514/3.12149**.
[40] Schiller, L., Naumann, A. A Drag Coefficient Correlation. *Z Ver Dtsch Ing* 77 318-320 (1935).
[41] Umar, B.M., Wang, Z., Chitrakar, S., Thapa, B., Huang, X., Poudel, R., Karna, A. Experimental erosion flow pattern study of Pelton runner buckets using a non-recirculating test rig. *Energies* 17 4006 (2024) **DOI:10.3390/en17164006**.
[42] Wedel, J., Steinmann, P., Štrakl, M., Hriberšek, M., Ravnik, J. Shape matters: Lagrangian tracking of complex nonspherical microparticles in superellipsoidal approximation. *Int J Multiphase Flow* 158 104283 (2023) **DOI:10.1016/j.ijmultiphaseflow.2022.104283**.
[43] Yasser, E., Zhou, L., El-Emam, M.A. Numerical analysis of particle shape influence on erosion and flow behavior in a 90-degree elbow pipe under Solid-Liquid flow. *Adv Powder Technol* 36 104928 (2025) **DOI:10.1016/j.apt.2025.104928**.
[44] Folden, T.S., Aschmoneit, F.J. A classification and review of cavitation models with an emphasis on physical aspects of cavitation. *Phys Fluids* 35 081301 (2023) **DOI:10.1063/5.0157926**.

Acknowledgements *The authors wish to thank dr. Dragica Jošt for her assistance in the transfer and explanation of the previous case, as well as her kind openness for discussion. Additionally, we thank the Slovenian Research Agency (ARRS) for its financial support in the framework of Research Program P2-0196 in Power, Process, and Environmental Engineering.*

Received: 2025-04-16, revised: 2025-07-13, accepted: 2025-07-24
as Original Scientific Paper 1.01.

Data Availability *The data that support the findings of this study are not available due to project confidentiality.*

Author Contribution *Luka Kevorkijan: Formal Analysis, Investigation, Writing – original draft, Software, Visualization; Matjaž Hriberšek: Conceptualization, Methodology, Project Administration, Supervision; Luka Lešnik: Investigation, Writing – review & editing, Visualization; Aljaž Škerlavaj: Conceptualization, Data curation, Methodology, Validation; Ignacijo Biluš: Investigation, Supervision, Writing- original draft, Writing – review & editing.*

Numerična raziskava erozije zaradi delcev v kavitirajočem toku skozi Peltonovo turbino

Pozetek *Erozija komponent Peltonove turbine zaradi kavitacije in toka z delci predstavlja velik izziv pri hidroenergetskih sistemih, zlasti v rekah, bogatih s sedimenti. V tej študiji je predstavljena numerična raziskava vpliva trdnih delcev na erozijo rotorja Peltonove turbine. Simulacije računalniške dinamike tekočin (CFD) so bile izvedene z uporabo programa ANSYS CFX 2023 R2, pri čemer sta bila vključena Lagrangev pristop sledenja delcev in Finniejev model abrazije za napovedovanje erozijskih vzorcev pri različnih koncentracijah sedimentov. Rezultati kažejo, da pri običajnih pogojih sedimentacije erozija zaradi delcev ne prispeva bistveno k poškodbam konic lopatic. Vendar pa pri ekstremni obremenitvi s sedimenti napovedani erozijski vzorci tesno ustrezajo dejanskim opazovanjem, zlasti na konici lopatice.*

Ključne besede *Peltonova turbina, erozija zaradi trdnih delcev, kavitacija, CFD računalniška dinamika tekočin*

Removal of Inclusions and Trace Elements from Al-Mg-Si Alloys Using Refining Fluxes

Uroš Kovačec[1,2], Franc Zupanič[1] ✉

1 University of Maribor, Faculty of Mechanical Engineering, Slovenia
2 Impol 2000 d.d., Slovenia

✉ franc.zupanic@um.si

Abstract *The cleanliness of aluminium alloys has a decisive effect on their properties and performance. In this work, the melts of several Al-Mg-Si alloys (6xxx series) were refined using rotary flux injection (RFI) of the salt fluxes in the industrial environment. A typical charge consisted of 25 % to 30 % external scrap, 45 % to 50 % internal scrap, and 20 % to 30 % primary aluminium. During injection, the entire melt volume was mixed uniformly. The melt was filtered using a porous ring filtration apparatus. The fraction and type of non-metallic inclusions were determined using light and scanning electron microscopy. The contents of alkali and alkaline-earth metals were determined using optical emission spectroscopy. The reduction of alkali and alkaline earth metals and the fraction of non-metallic inclusions were used to evaluate the process efficiency and the flux selection for the regular production. An analysis of more than 100 industry charges confirmed that the flux selected after the experimental trials, consisting of a mixture of $MgCl_2$, KCl, NaCl and CaF_2, was effective in regular production.*

Keywords *aluminium, refinement, flux, cleanliness, non-metallic inclusion, rotary injection, alkali element*

Highlights

- *Alloys were produced with an increased fraction of scrap.*
- *Melt cleaning was carried out using several salt fluxes.*
- *Systematic testing in an industrial environment using a rotary flux injection (RFI) system.*
- *Determination of non-metallic inclusions using porous disc filtration apparatus.*
- *Optimal removal of non-metallic inclusions and alkali elements by complex fluxes.*

1 INTRODUCTION

Al-Mg-Si alloys, which belong to the 6xxx series, are used widely in the automotive, aerospace, and construction industries, due to their excellent combination of properties. They have medium to high strength, good corrosion resistance, and excellent weldability [1]. They also have low density, and can be produced at moderate cost. They are suitable for extrusion processes, making them appropriate for manufacturing structural profiles and components, but they can be deformed using other forming technologies. An essential advantage of Al-Mg-Si alloys is their ability to undergo precipitation hardening, enhancing their mechanical properties considerably, such as strength and hardness, while preserving ductility and toughness [2]. Compared to other aluminium alloys, they offer a balanced combination of strength, ductility, fatigue and corrosion resistance, making them versatile for various applications.

The production of primary aluminium is highly energy-intensive; thus, the use of aluminium scrap instead of primary aluminium can save up to 95 % of energy [3]. Therefore, it is imperative for the new alloys to be produced with an ever-higher addition of aluminium scrap. The scrap fraction represents about 25 % of aluminium production in 2025, and is expected to rise to 50 % by 2050 [4]. For environmental conservation and cost reduction, it is desirable that recycled alloys retain their properties, even after multiple recycling cycles. However, in real life, different adverse effects arise when the scrap fraction is increased [5]. Oxides, paintings and other coatings can cover the surface of scrap, being a source of non-metallic inclusions and residual elements for newly manufactured alloys, worsening their properties gradually [6].

While preparing an aluminium alloy for casting, non-metallic inclusions can come into the melt from several sources. Metallic oxides on the scrap, debris from the furnace lining and agglomerates of borides in Al-Ti-B grain refiners represent the exogenic inclusions. The interaction of the melt with the surroundings, e.g., oxidation with air or reduction of water vapor, can lead to the formation of endogenic inclusions. The reaction with moisture forms aluminium oxide, introducing hydrogen into the melt simultaneously, resulting in several harmful effects [7]. Besides non-metallic inclusions, the amounts of undesired alkali or alkaline earth elements, such as Na and Ca, increase with repeated recycling.

One of the most important approaches to improving the cleanliness of aluminium melts is the application of solid salt fluxes [8]. Solid salt fluxes are mixtures of inorganic compounds, mainly chlorides and fluorides. They are used when processing molten metal, including aluminium recycling, dross treatment and molten metal treatment. Salt fluxes are also added to ensure high metal recovery and decrease oxidation and metal losses [9]. Additionally, salt fluxes are used to treat both primary and secondary molten aluminium, to remove impurities such as alkali and alkaline earth metals and oxides [10]. Chloride and fluoride fluxes in aluminium refining can lead to harmful gaseous emissions, including organochlorine compounds and toxic solid slags, which can have a negative impact on the environment and workers' safety [11]. The effect can be reduced considerably by appropriate measures in the melting plant and the use of the minimum necessary quantity of fluxes, reducing the emissions to the surroundings.

Fluxes can be introduced to aluminium melts using several methods. They can be added by manual application. The powder fluxes are sprinkled onto the surface of the molten aluminium and

 DOI: 10.5545/sv-jme.2025.1371

stirred into the melt using a tool. Some fluxes, like degassing or grain refining, are plunged to the bottom of the melt; they are typically in the form of tablets or briquettes. The powdered or granulated fluxes can be injected with an inert gas, such as argon or nitrogen. They can also be added by a rotary degasser, which is one of the most effective methods. A rotary degasser injects the flux into the melt while stirring, ensuring thorough mixing [4]. Generally, each method can be used for the introduction of different types of fluxes (cover, dross or melt cleaning fluxes). It depends on the technology which is used in a specific aluminium cast shop. However, each technology has a preferred type of flux. Rotary flux injection (RFI) typically uses granulated fluxes.

Most experiments on applying salt fluxes using RFI are conducted in a laboratory environment [12,13]. There has been no systematic research in an industrial environment yet. Some articles report general principles about mechanisms and applications [14]. This work investigates the application of several compositions of solid salt fluxes systematically on the type and amounts of non-metallic inclusions and residual alkali and alkaline earth elements in Al-Mg-Si alloys using RFI. The analyzes were done using up-to-date industrial equipment and advanced laboratory techniques, such as porous disc filtration apparatus (PoDFA), spectral chemical analysis, light and electron microscopy and microchemical analysis. The main goal of the research was to test different types of fluxes, and then, according to the experimental results, select the optimal flux for regular production.

2 METHODS AND MATERIALS

Several Al-Mn-Si alloys were tested, mainly EN AW 6082, EN AW 6182, and EN AW 6063. They varied slightly in chemical composition. However, all compositions fit inside the tolerances given in Table 1. No specific differences were observed in the behavior of these alloys in the molten state.

Table 1. Range of chemical compositions of the investigated Al-Mn-Si alloys (in wt.%)

Si	Fe	Cu	Mn	Mg	Cr	Zn	Ti	Pb	Zr
1.20	0.25	0.05	0.55	0.80	0.12	0.2	0.05	0.05	0.00
1.30		0.1	0.70	0.90	0.15				0.15

Several charges were melted in a 50 t multi-chamber gas furnace (SMS-Hertwich Engineering GmbH, Germany). A typical charge consisted of 25 % to 30 % external scrap, 45 % to 50 % internal scrap and 20 % to 30 % primary aluminium. The final temperature achieved in the melting furnace was 750 °C. The melt (26.5 t) was transferred to a one-chamber casting furnace (Sistem Teknik, Turkey), where the required chemical composition was achieved by adding clean master alloys.

The next step was cleaning and refining the melt by using several solid salt fluxes (Table 2). The temperature in the casting furnace during flux treatment was 750 ±10 °C.

Table 2. Chemical composition of the fluxes (mole and weight fraction in %)

Designation	Chemical composition
Salt#1	60 % $MgCl_2$, 40 % KCl (weight 54 % $MgCl_2$, 46 % KCl)
Salt#2	51 % $MgCl_2$, 49 % KCl (weight 45 % $MgCl_2$, 55 % KCl)
Salt#3	36 % to 40 % $MgCl_2$, 21 % to 26 % KCl, 26 % to 31 % NaCl, 1 % to 3 % CaF_2 (weight 33 % $MgCl_2$, 26 % KCl, 39 % NaCl, 2 % CaF_2)
Salt#4	30 % to 35 % $MgCl_2$, 60 % to 65 % KCl, 1 % to 3 % NaCl, 1 % to 3 % CaF_2 (weight 27 % $MgCl_2$, 68 % KCl, 3 % NaCl, 2 % CaF_2)

The compositions of the salt fluxes were selected based on their melting points, reactivity for removing alkali and alkaline earth elements, density, and their ability to reduce surface tension between the aluminium melt and the molten fluxes. The starting point was the ternary diagram KCl–NaCl–$MgCl_2$ [15]. The primary agent for removing alkali elements is $MgCl_2$. Its melting point is too high (714 °C) to be added alone in the Al-melt, because its viscosity is too high at 750 °C. Thus, Salt#1, 40 % KCl, was added to achieve the eutectic composition, with the eutectic temperature of 467 °C, much lower than the temperature of the alloy melt. The second composition, Salt#2, corresponded to the compound KCl $MgCl_2$, having a slightly higher melting point of 487 °C. Salt#3 lies close to the center of the KCl-NaCl-$MgCl_2$ phase diagram, having as low a melting temperature as 390 °C. Adding NaCl additionally decreases the melting temperature, viscosity and the cost of fluxes because of its much lower price. The Salt#4 had a ternary composition, located close to the binary diagram KCl–$MgCl_2$ (KCl + $MgCl_2$ ≈ 95 %) with up to 3 % NaCl and up to 3 % CaF_2, keeping the melting temperature at around 430 °C. The primary role of CaF_2 is to reduce the surface tension between the Al-melt and the fluxes, allowing easier separation of both phases.

In each charge, one of the fluxes given in Table 2 was added to the melt. The experimental tests were carried out using fluxes produced by the Hoesch Group and Pyrotek Incorporation, Germany, in the form of granulates up to 3 mm mesh size. The solid salt fluxes (15 kg to 25 kg; 1 kg t^{-1} melt) were added into a melt using an RFI system (STAS, France) with a feeding rate of 120 kg/h. It is of the utmost importance that the flux is dispersed uniformly in the melt, with as small droplets as possible. The optimal position of the rotor and rotation speed were determined using a mesh-less flow model [16] and experimental testing of the RFI system in the casting furnace. Uniform mixing of the melt can be achieved with the rotor angle of 45° and the rotation speed of 410 min^{-1}, using a graphite impeller with a 400 mm diameter. During mixing, argon was used for the degassing, with a flow rate of 200 L/min.

After fluxing, the melt was grain refined with AlTi3B1 feeding wire, to achieve 0.025 wt.% to 0.030 wt.% Ti in the melt. The melt was then transferred to the degassing unit (Siphon Inert Reactor (SIR), Hycast, Norway) and filtered using a 50 pores per inch ceramic foam filter (CFF). Finally, the alloy was cast into billets with hot-top, air-slip technology [17]. The diameter of the billets was 279 mm.

The alloy cleanliness was tested using different methods. The primary method was PoDFA by ABB, Switzerland [18]. A sample of the molten metal was taken from the melt 30 min after finishing the flux injection and filtered through a porous refractory disc to capture the inclusions. The sample was then prepared by grinding and polishing. The captured inclusions were analyzed using a light microscope (Axio Observer, Zeiss, Germany) and a scanning electron microscope (SEM Jeol JSM 6610LV, Jeol, Japan) equipped with an energy dispersive spectrometer (EDS) to determine their type and content. This method provided both qualitative and quantitative data on the inclusions. The quantitative value is obtained by measuring the area of the inclusions, which is then divided by the mass of the filtered melt. Thus, the unit was mm^2/kg.

The chemical analysis of the alloy, including the contents of alkali elements (Na, Ca), was carried out using Spectro S101, SPECTRO Analytical Instruments GmbH, Germany. The light microscopy (LM) and scanning electron microscopy (SEM) samples were ground mechanically using SiC papers with granulations 320 to 4000 and polished using 9 mm, 6 mm and 3 mm diamond paste. The EDS analyzes were carried out using polished samples, while LM required chemical etching with Weck's reagent, consisting of 2 g $KMnO_4$, 1 g

NaOH, and 50 mL of distilled water. The grain size of the cast billets was determined according to Standard ASTM E112-24 [19].

3 RESULTS AND DISCUSSION

3.1 Microstructure

The alloys solidified in the metallic mold. Without a grain refiner addition, columnar grains of the aluminium solid solution α-Al would grow from the mold walls towards the billet center. The solidification front pushes non-metallic inclusions and alloying elements to the billet center, strongly reducing the alloy's ductility, toughness and malleability. The addition of an effective grain refiner induces heterogeneous nucleation of the α-Al grains throughout the melt, causing the formation and growth of equiaxed crystal grains, which have a typical dendritic morphology. Fig. 1 shows a typical microstructure in the as-cast condition, at lower magnification. It consists of dendritic equiaxed grains of the aluminium solid solution, with a linear intercept length of 200 ±30 µm. Such a small and uniform grain size was obtained by adding the $AlTi_3B1$ grain refiner. Small equiaxed grains prevent stronger macrosegregations of the alloying elements, allow more uniform distribution of the non-metallic inclusions and provide improved mechanical properties. Only extremely large non-metallic inclusions can be observed in such micrographs. The grain refiner contains particles of Al_3Ti and TiB_2. Only a small part of the particles causes the heterogeneous nucleation of α-Al crystal grains. Undissolved and inactive TiB_2 particles often form agglomerates, which constitute part of the non-metallic inclusions.

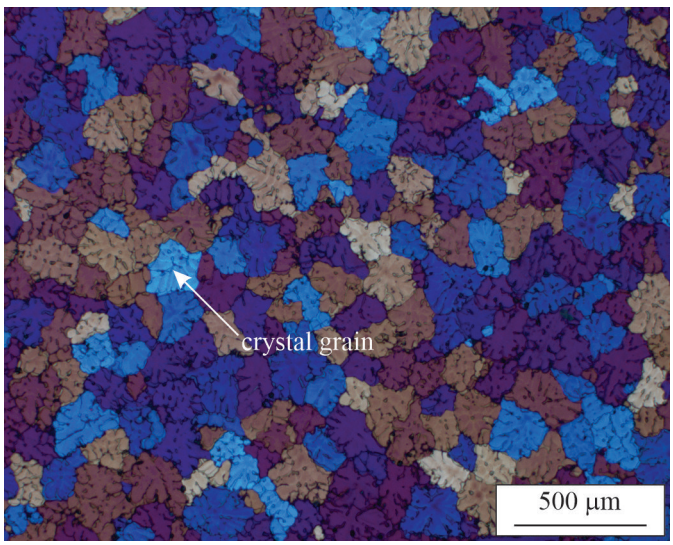

Fig. 1. The grain structure of an Al-Mg-Si cast billet (light micrograph,, depicting each grain in a different color)

Several processes occur during the solidification of Al-Mg-Si alloys. These processes lead to the formation of several other phases. The fractions of these phases are typically no more than a few per cent [20]. Figure 2a shows a SEM micrograph, revealing the dendritic shapes of the aluminium solution grain α-Al. Other phases are located in the interdendritic regions. We identified Al_2Cu, Mg_2Si and α-Al(Mn,Fe)Si phases, which are typical constituents of Al-Mg-Si alloys [2]. Oxide non-metallic inclusion $Al2O_3$ was identified with EDS analysis (Fig. 2b). It is challenging to find oxide particles, because they appear dark in the backscattered electron images, such as shrinkage porosity, gas porosity and Mg_2Si. Therefore, much meticulous work is required to obtain adequate results.

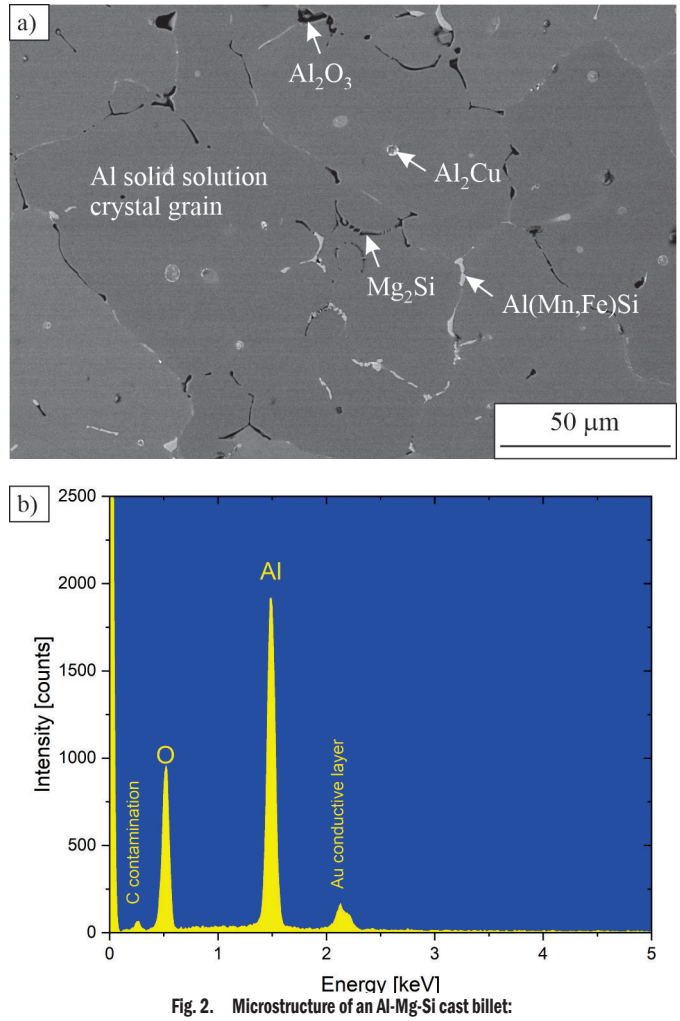

Fig. 2. Microstructure of an Al-Mg-Si cast billet: a) backscattered electron image, and b) EDS-spectrum of the oxide inclusion

3.2 Non-Metallic Inclusions

Using the PoDFA method, non-metallic inclusions in the melt become concentrated in the filter. Thus, it is possible to identify their types and quantities more easily, even with LM. SEM is used when identification with a light microscope is insufficient. Figure 3 shows a typical light micrograph of non-metallic inclusions before and after melt treatment with fluxes. There are several types of inclusions. The Spinel comes from the furnace lining, while the TiB_2 was part of the Al-Ti-B grain refiner present in the scrap. On the other hand, Al_4C_3 is formed by the reaction of Al melt with organic substances [21], and MgO with the dissolved magnesium and oxygen from the atmosphere.

Table 3 gives the results of the quantitative PoDFA analysis. The agglomerated TiB_2 particles, arising from the grain refiner debris (GF) in the scrap, present the largest fraction of the non-metallic inclusions. Thus, the results for all inclusions and the inclusions without grain refiner debris are given separately. The inclusion fraction was always higher before the melt treatment, indicating the efficiency of the fluxes.

Figure 4 shows the fractions of the non-metallic inclusions after melt treatment in dependence on their fraction before melt treatment. Fig. 4a indicates the effect of individual fluxes. Still, Fig. 4b shows

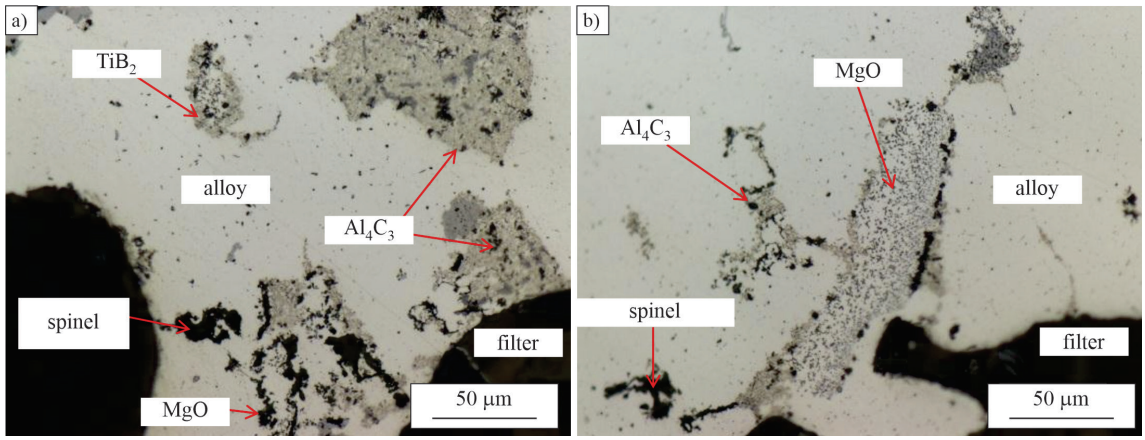

Fig. 3. Light micrographs of non-metallic inclusion in PoDFa filter; a) before, and b) after melt treatment with fluxes

Table 3. Contents of non-metallic inclusions, determined using PoDFA

	Total before [mm²/kg]	Total after [mm²/kg]	Reduction [%]	Without GF before [mm²/kg]	Without GF after [mm²/kg]	Reduction [%]
Salt#1	1.05	0.37	64.76	0.69	0.32	53.62
Salt#1	0.58	0.29	50.00	0.32	0.14	56.25
Salt#1	0.34	0.05	86.01	0.26	0.04	86.59
Salt#2	2.76	0.75	72.94	2.18	0.50	76.91
Salt#2	1.39	0.34	75.18	1.04	0.20	80.48
Salt#3	0.78	0.10	87.50	0.64	0.01	98.60
Salt#3	1.80	0.14	92.16	1.20	0.20	83.18
Salt#3	1.88	0.69	63.40	1.35	0.50	62.84
Salt#4	3.13	1.11	64.56	2.00	0.62	69.00

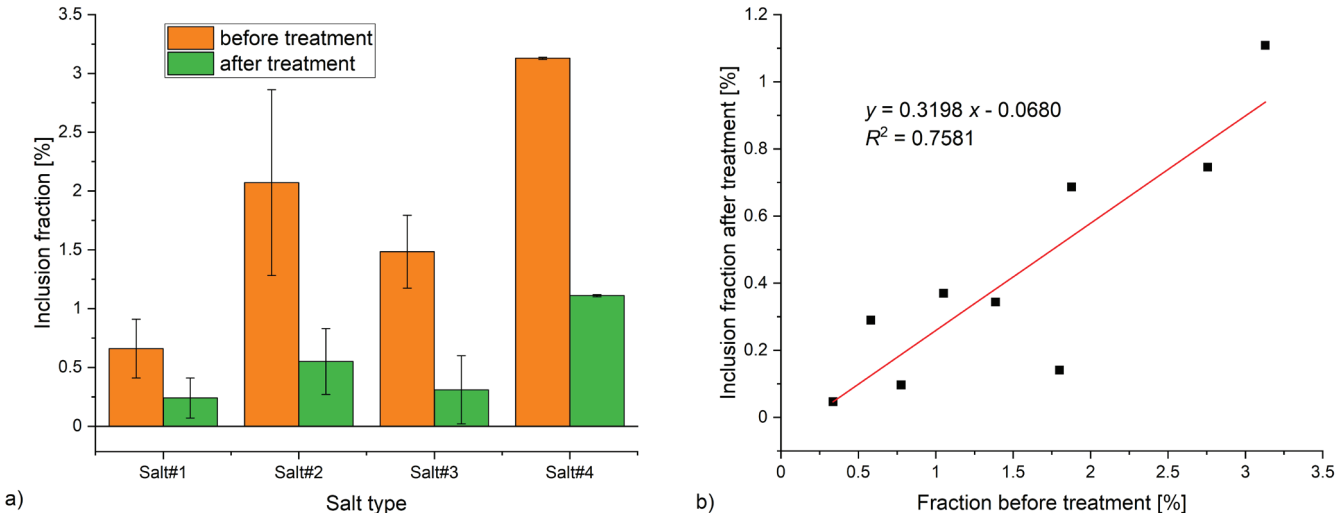

Fig. 4. Inclusions determined using PoDFa; a) the effect of different fluxes (average values from Table 3), b) effectiveness irrespective of the flux type

that the amount of non-metallic inclusion after melt treatment depends strongly on the initial fraction, and that, in each case, the reduction of non-metallic inclusions was about 70 %. Due to the small number of experiments and additional variables occurring in the industrial environment, the scattering was relatively high ($R^2 \approx 0.75$). Nevertheless, the complex salt mixture Salt#3 was the most efficient (Fig. 4a). One of the reasons can be the presence of CaF_2, which reduces the surface tension and makes the removal of redundant fluxes easier [4]. However, removing inclusions does not depend primarily on the melt treatment with fluxes. The holding time can contribute to better removal of inclusions, because they can have sufficient time either to sink to the furnace bottom or float to the melt surface, depending on their density (Stoke's law). However, the added fluxes could also stay in the aluminium melt, increasing the fraction of non-metallic inclusions [22]. The PoDFA analysis did not confirm their presence. In industrial practice, the melt is filtered just before casting to reduce the fraction of non-metallic inclusions [23]. However, the melt should contain as few inclusions as possible before filtering, because they can block the filter.

3.3 Removal of Trace Elements

One of the main functions of fluxes is to remove undesirable trace elements. Trace elements are typically present in tiny quantities, e.g.,

in ppm (parts per million), which is equivalent to 10^{-4} %, but can deteriorate the mechanical and other properties of aluminium alloys substantially [24]. Among them, alkali (Li, Na, K, Rb, Cs and Fr) and alkaline earth (Be, Mg, Ca, Sr, Ba and Ra) are very often present in Al-alloys. Mg is one of the most important alloying elements in Al-Mg-Si alloys. The chemical analyzes of all the investigated charges showed that the contents of all the aforementioned elements, except for Na and Ca, were negligible, often below their detection limits. Thus, they could not be used to evaluate the efficiency of the fluxes. Even the maximum contents of Na and Ca were very low, namely, seven ppm (7×10^{-4} %) and 14 ppm (14×10^{-4} %), respectively.

Table 4. Contents of Na and Ca using spectroscopic analysis

	Na before [ppm]	Na after [ppm]	Na reduction [%]	Ca before [ppm]	Ca after [ppm]	Ca reduction [%]
Salt#1	3.1	2.2	29.0	9.8	4.6	53.1
Salt#1	4.1	2.5	39.0	9.4	5.4	42.6
Salt#1	2.1	1.1	47.6	8.5	4.1	51.8
Salt#1	2.9	1.6	44.8	10.6	3.7	65.1
Salt#1	2.7	1.7	37.0	14.0	5.2	62.9
Salt#1	3.9	1.8	53.9	13.7	4.3	68.6
Salt#2	2.0	2.0	0.0	7.5	2.0	73.3
Salt#2	7.0	2.0	71.4	11.0	3.7	66.4
Salt#3	3.0	2.7	10.0	12.0	1.9	84.2
Salt#3	2.0	1.0	50.0	5.0	1.0	80.0
Salt#3	2.7	0.3	89.1	14.0	0.29	97.9
Salt#4	3.0	1.3	56.7	11.0	3.0	72.7

The results are depicted in Table 4 and Fig. 5. The Salt#3 and Salt#4 removed Na the most effectively. Since the overall content of Na was very low, the effect was not very pronounced (Fig. 5a). On the other hand, it can be seen easily that the Salt#3 was the most potent in removing Ca from the melt (Fig. 5b).

Chloride salt $MgCl_2$ plays the most crucial role in removing Na and Ca. In the melt, the following chemical reactions take place [25]:

$$MgCl_2\ (l) + 2[Na] \rightarrow 2NaCl\ (l) + [Mg], \quad (1)$$

$$MgCl_2\ (l) + [Ca] \rightarrow CaCl_2\ (l) + [Mg], \quad (2)$$

where (l) means the liquid state, and the parentheses [] the dissolved element in the Al-melt.

The free energies of reactions in Eqs. (1) and (2) are hugely negative (ΔG_0), having a very high equilibrium reaction constant K_p, that can be calculated using Eq. (3).

$$\Delta G_0 = -RT\ln(K_p), \quad (3)$$

where R is the gas constant and T is the absolute temperature.

The actual reaction constant for the reaction in Eq. (1) is calculated as:

$$K = \frac{a_{NaCl}^2 \cdot a_{Mg}}{a_{MgCl_2} \cdot a_{Na}^2}, \quad (4)$$

where a stands for activity. Due to the low values of Na and Mg, activities can be replaced by their concentrations.

The reaction takes place all the time as $K < K_p$. With the addition of the flux in the range of 1 kg per 1 t melt, and the amounts of Na and Ca typical in the industry practice, the reactions do not stop, and can cause a considerable decrease of Na and Ca in the melt.

Figure 5 shows clearly that the amounts of Ca and Na are practically independent of the initial content in the investigated range. It is obvious that the flux Salt#3 can decrease the quantity of Ca below two ppm, very often below one ppm. Since the typical allowed content of Ca is 20 ppm, the effectiveness of all fluxes was satisfactory. Nevertheless, Salt#3 was selected to be used in industrial applications for the Al-Mg-Si alloys.

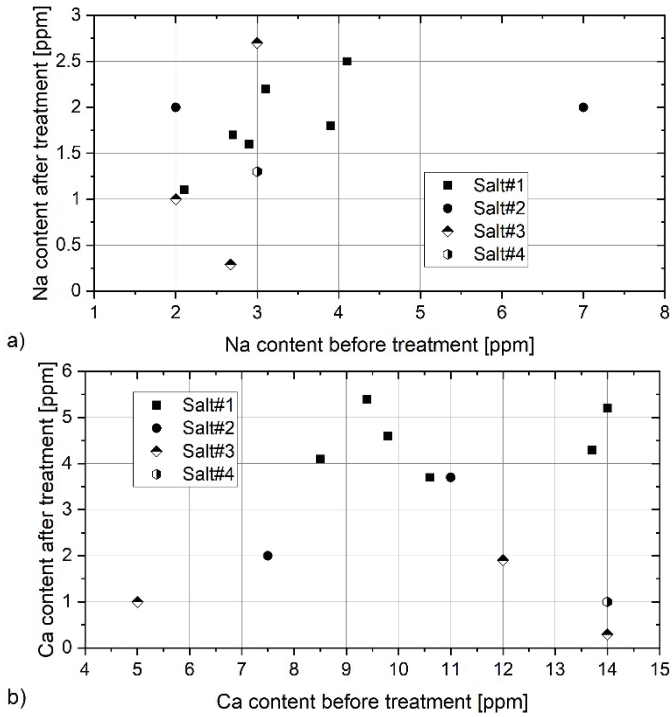

Fig. 5. The effect of different fluxes on the removal of; a) an alkali element, Na, and b) an alkaline earth element, Ca

3.4 Analysis of the Actual Charges

The industrial trials presented above can be considered experimental, because different fluxes were added to Al-Mg-Si alloys in order to select a composition which removes non-metallic inclusions and trace elements effectively from the aluminium melt, and is also cost friendly. After selecting Salt#3, it has been used in regular production.

This part shows the analysis of more than 100 charges of just one alloy EN AW 6182, which is produced in large quantities, so the number of charges is statistically relevant. The chemical analysis was taken after the melting of the alloy and after casting. The only possibility of removing Na and Ca was by melt treatment using the selected flux. All the other treatments can contribute to an increase in these two elements. In many of the investigated charges, the initial contents of Na and Ca were much higher than during the experiments. The highest contents of Na and Ca were 27 ppm and 73 ppm, respectively, thus representing tougher conditions for their removal.

In Fig. 6a, only two charges with less than five ppm Na are shown, indicating the final content of Na below its detection limit. All the other charges (50 charges) contained more than five ppm. The maximum content of Na in the cast billets was three ppm. It was higher only in three charges, suggesting inappropriate handling of the melt in these cases. Only charges with nine or more ppm Ca were selected (70 charges) for the analysis (Fig. 6b). The Ca-content was higher than six ppm only in five charges, showing the efficiency of the Ca removal. It is to be stated that the data for Fig. 6 were shown only for charges having a higher content of Na and Ca. The thermodynamic considerations using Eq. (4) indicate that the final content of harmful trace elements should be independent from their initial content. However, the results of the chemical analyzes in Fig. 6 show a slight dependence on the initial content for both Na and Ca.

Thus, one can expect that also the kinetics of reaction and handling of the aluminium melt can affect the final content of trace elements.

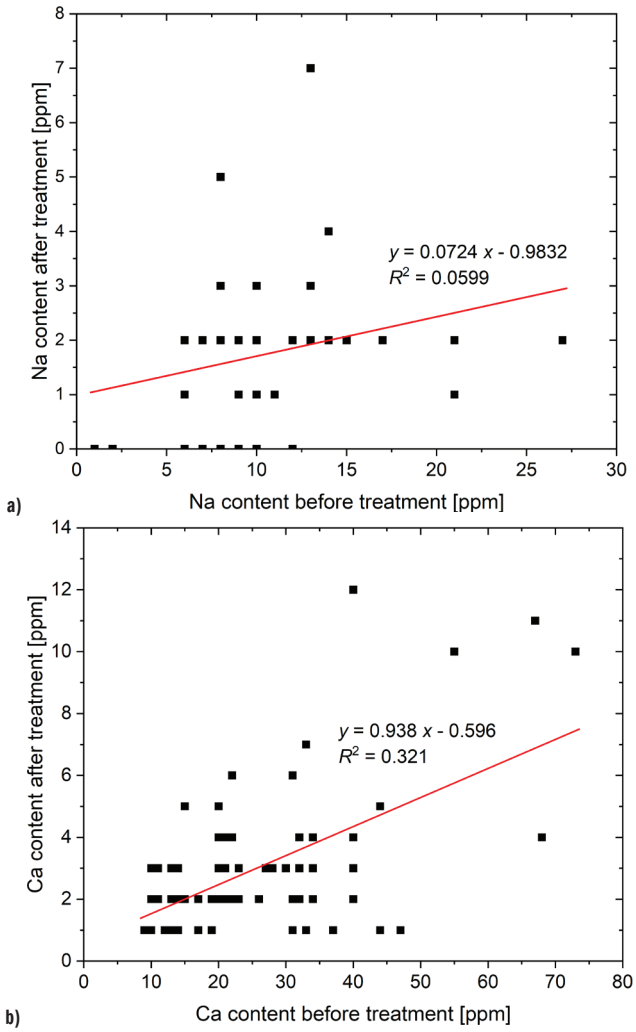

Fig. 6. Removal of Na and Ca from the melt in the actual industrial production; a) the removal of Na, b) the removal of Ca

The industrial production of aluminium alloys is a highly complex technology. Already in the near future more and more additional parameters will be monitored during production, delivering a lot of data. It is expected that it will be necessary to apply different methods of deep learning and artificial intelligence to obtain strong correlations between the processing parameters and final characteristics of the alloys, similar to the application of deep learning in the production of primary aluminium [26] and other applications [27,28]. One of the important areas will be predictions for the removal of non-metallic inclusions and harmful trace elements in aluminium alloys.

4 CONCLUSIONS

The investigation of the effectiveness of different fluxes leads us to the following conclusions:

- The fraction of non-metallic inclusions and the contents of trace elements can be kept at a sufficiently low level after flux treatment of Al-Mg-Si alloy, containing 25 % to 30 % external scrap.
- Using an RFI system allowed adding fluxes into the melt reliably.
- The fractions and types of non-metallic inclusions were determined by analyzing the sample after filtering through a porous ceramic filter.
- Among the possible trace elements, the Na and Ca contents were determined in detail because of their sufficient amount.
- The alkali and alkaline-earth elements were removed most efficiently using a complex salt mixture containing 36 % to 41 % $MgCl_2$, 21 % to 26 % KCl, 26 % to 31 % NaCl and 1 % to 3 % CaF_2.
- The efficiency of the selected flux in removing Na and Ca was demonstrated by analyzing more than 100 actual charges of the alloy EN AW 6182.

References

[1] Polmear, I., StJohn, D., Nie, J.F., Qian, M. *Light Alloys: Metallurgy of the Light Metals*. Elsevier Ltd. Butterworth-Heinemann Oxford (2017) **DOI:10.1016/B978-0-08-099431-4.00001-4**.

[2] Zupanič, F., Steinacher, M., Žist, S., Bončina, T. Microstructure and properties of a novel Al-Mg-Si alloy AA 6086. *Metals* 11 368 (2021) **DOI:10.3390/met11020368**.

[3] Wu, Y., Oudshoorn, T., Rem, P. Modelling and optimization of an innovative facility for automated sorting of aluminium scraps. *Waste Manag* 189 103-113 (2024) **DOI:10.1016/j.wasman.2024.08.018**.

[4] Milani, V., Timelli, G. Solid salt fluxes for molten aluminum processing - a review. *Metals* 13 832 (2023) **DOI:10.3390/met13050832.**

[5] Capuzzi, S., Timelli, G. Preparation and melting of scrap in aluminum recycling: A review. *Metals* 8 249 (2018) **DOI:10.3390/met8040249**.

[6] Škůrková, K.L., Ingaldi, M. Recycling process of the aluminium cans as an example of the renewable material sources. *Adv Mater Res* 1001 103-108 (2014) **DOI:10.4028/www.scientific.net/AMR.1001.103**.

[7] Puga, H., Barbosa, J., Soares, D., Silva, F., Ribeiro, S. Recycling of aluminium swarf by direct incorporation in aluminium melts. *J Mater Process Technol* 209 5195-5203 (2009) **DOI:10.1016/j.jmatprotec.2009.03.007**.

[8] Máté, M., Tokár, M., Fegyverneki, G., Gyarmati, G. The comparative analysis of the inclusion removal efficiency of different fluxes. *Arch Foundry Eng* 20 53-58 (2020) **DOI:10.24425/afe.2020.131302**.

[9] Damoah, L.N.W., Zhang, L. Alf3 reactive Al2O3 foam filter for the removal of dissolved impurities from molten aluminum: Preliminary results. *Acta Mater* 59 896-913 (2011) **DOI:10.1016/j.actamat.2010.09.064**.

[10] Gaustad, G., Olivetti, E., Kirchain, R. Improving aluminum recycling: A survey of sorting and impurity removal technologies. *Resour Conserv Recyc* 58 79-87 (2012) **DOI:10.1016/j.resconrec.2011.10.010**.

[11] Brough, D., Jouhara, H. The aluminium industry: A review on state-of-the-art technologies, environmental impacts and possibilities for waste heat recovery. *Int J Thermofluids* 1-2 100007 (2020) **DOI:10.1016/j.ijft.2019.100007**.

[12] Piękoś, M., Smorawiński, Z. Introduction of powder fluxes in rotary degassing system towards intensifying refining process of aluminium alloys. *Arch Foundry Eng* 24 89-94 (2024) **DOI:10.24425/afe.2024.151315**.

[13] Wan, B., Chen, W., Mao, M., Fu, Z., Zhu, D. Numerical simulation of a stirring purifying technology for aluminum melt. *J Mater Process Technol* 251 330-342 (2018) **DOI:10.1016/j.jmatprotec.2017.09.001**.

[14] Breton, F., Larouche, A., Waite, P., Côté, P. Rotary flux injector (RFI): Recent development towards an autonomous technology. Hyland, M. (ed.) *Light Metals* Springer International Publishing Cham 901-904 (2016) **DOI:10.1007/978-3-319-48248-4_151**.

[15] Villada, C., Ding, W., Bonk, A., Bauer, T. Engineering molten $MgCl_2$-KCl-NaCl salt for high-temperature thermal energy storage: Review on salt properties and corrosion control strategies. *Sol Energy Mater Sol Cells* 232 111344 (2021) **DOI:10.1016/j.solmat.2021.111344**.

[16] Mramor, K., Vertnik, R., Sarler, B. Meshless approach to the large-eddy simulation of the continuous casting process. *Eng Anal Bound Elem* 138 319-338 (2022) **DOI:10.1016/j.enganabound.2022.03.001**.

[17] Faunce, J.P., Valdo, A. The air-slip casting mold - an established technology (reprinted from light-metals, 1985). *Light Met Age* 43 10-15 (1985).

[18] Gauthier, P., Bilodeau, V., Sosa, J. A PoDFA benchmarking study between manual and ai-supervised machine learning methods to evaluate inclusions in wrought and foundry aluminum alloys. *Light Metals* (2024) 970-976 **DOI:10.1007/978-3-031-50308-5_121**.

[19] E112-24. *Standard Test Methods for Determining Average Grain Size*. ASTM International West Conshohocken.

[20] Engler, O., Schröter, T., Krause, C. Formation of intermetallic particles during solidification and homogenisation of two Al-Mg-Si alloys. *Mater Sci Technol* 39 70-84 (2023) **DOI:10.1080/02670836.2022.2102279**.

[21] Mendoza-Duarte, J.M., Estrada-Guel, I., Garcia-Herrera, J.E., Perez-Bustamante, R., Arcos-Gutiérrez, H., Martinez-García, A. et al. Aluminum carbide formation in Al-graphite composites: In situ study and effects of processing variables and sintering method. *Mater Today Commun* 38 108396 (2024) **DOI:10.1016/j.mtcomm.2024.108396**.

[22] Majidi, O., Shabestari, S.G., Aboutalebi, M.R. Study of fluxing temperature in molten aluminum refining process. *J Mater Process Technol* 182 450-455 (2007) **DOI:10.1016/j.jmatprotec.2006.09.003**.

[23] Kvithyld, A., Syvertsen, M., Bao, S., Eriksen, U.A., Johansen, I., Gundersen, E., Akhtar, S., Haugen, T., Gihleengen, B.E. Aluminium filtration by bonded particle filters. *Light Metals* (2019) 1081-1088 **DOI:10.1007/978-3-030-05864-7_132**.

[24] Casari, D., Ludwig, T.H., Merlin, M., Arnberg, L., Garagnani, G.L. The effect of Ni and V trace elements on the mechanical properties of A356 aluminium foundry alloy in as-cast and t6 heat treated conditions. *Mater Sci Eng A* 610 414-426 (2014) **DOI:10.1016/j.msea.2014.05.059**.

[25] Utigard, T. Thermodynamic considerations of aluminum refining and fluxing. Sahoo, M., Pinfold, P. (eds.), *Extraction, Refining, and Fabrication of Light Metals*. Pergamon (1991) Amsterdam 353-365 **DOI:10.1016/B978-0-08-041444-7.50034-2**.

[26] Wang, J., Xie, Y., Xie, S., Chen, X. Optimization of aluminum fluoride addition in aluminum electrolysis process based on pruned sparse fuzzy neural network. *ISA Transactions* 133 285-301 (2023) **DOI:10.1016/j.isatra.2022.06.039**.

[27] Babič, M., Kovačič, M., Fragassa, C., Šturm, R. Selective laser melting: A novel method for surface roughness analysis. 70 12 (2024) **DOI:10.5545/sv-jme.2024.1009**.

[28] Van, A.-L., Nguyen, T.-C., Bui, H.-T., Dang, X.-B., Nguyen, T.-T. Multi-response optimization of gtaw process parameters in terms of energy efficiency and quality. 70 11 (2024) **DOI:10.5545/sv-jme.2023.890**.

Received: 2025-04-24, revised: 2025-07-04, accepted: 2025-07-17
as Original Scientific Paper 1.01.

Data Availability *The data supporting this study's findings are available from the corresponding author upon reasonable request.*

Author Contribution *Uroš Kovačec: Conceptualization, Data curation, Investigation, Writing – original draft; and Franc Zupanič: Conceptualization, Methodology, Writing – review & editing, Supervision.*

AI-Assisted Writing *The AI tool Grammarly was used to prepare this manuscript for grammar and language editing. All the content and conclusions remain the responsibility of the authors.*

Odstranjevanje vključkov in elementov v sledovih iz zlitin Al-Mg-Si z rafinacijskimi talili

Povzetek *Čistoča aluminijevih zlitin ima odločilen vpliv na njihove lastnosti in uporabnost. V industrijskem okolju smo rafinirali taline več Al-Mg-Si zlitin (serija 6xxx) s solnimi talili, ki smo jih vnašali v talino z rotacijskim vpihovanjem. Običajni vložek je bil sestavljen iz 25 % do 30 % zunanjega odpada, 45 % do 50 % notranjega odpada in 20 % do 30 % primarnega aluminija. Talina je bila med vpihovanjem talil enakomerno premešana in nato je bila filtrirana skozi porozni obročasti filter. Za opredelitev deleža in vrste nekovinskih vključkov smo uporabili svetlobno mikroskopijo in vrstično elektronsko mikroskopijo. Z optično emisijsko spektroskopijo je bil izmerjen delež alkalijskih in zemljoalkalijskih kovin. Zmanjšanje deleža alkalijskih in zemljoalkalijskih kovin ter deleža nekovinskih vključkov je bilo merilo za ovrednotenje učinkovitosti rafinacije in za izbiro rafinacijskega sredstva za redno proizvodnjo. Analiza več kot sto industrijskih vložkov je potrdila, da je bilo izbrano talilo, sestavljeno iz zmesi $MgCl_2$, KCl, NaCl in CaF_2, učinkovito tudi pri redni proizvodnji.*

Ključne besede *aluminij, rafinacija taline, talilo, čistoča, nekovinski vključek, rotacijsko vbrizgavanje, alkalijski element*

Effect of Presetting and Deep Rolling on Creep of Torsion Spring Bars

Vinko Močilnik – Nenad Gubeljak ✉ – Jožef Predan
University in Maribor, Faculty of Mechanical Engineering, Slovenia
✉ nenad.gubeljak@um.si

Abstract *This study investigates the creep behavior of torsion spring bars by combining experimental testing and numerical modeling. Experimental investigations were performed on torsional specimens subjected to different presetting levels and deep rolling surface treatments, showing different effects on stress relaxation at a constant torsion angle. Finite element method (FEM) simulations incorporating elasto-visco-plastic material behavior successfully reproduced the time-dependent deformation observed experimentally. Material parameters for the FEM model were derived from experimental data. The findings show that a two-stage presetting process combined with intermediate deep rolling results in higher residual compressive stresses in the surface layers compared to a single-stage presetting process. Although this method aims to mitigate creep under constant loading conditions, its effectiveness is limited. A reduction in creep strains is only observed up to a presetting level of approximately 4.3 %; above this threshold, creep strains increase significantly and loading capacity decreases.*

Keywords *creep; torsion bar; FEM analyzis; presetting, deep rolling; torque, twist angle*

Highlights
- *The material parameters for the FEM model were derived from experimental creep data.*
- *The experimental measured tensile creep data can be used to numerical simulation of creep torque.*
- *The optimal life is within a narrow range of prestressing and rolling-induced residual stresses.*

1 INTRODUCTION

Torsion bars are commonly used in suspension systems to absorb road surface irregularities and shocks in both wheeled and tracked vehicles. To increase the elastic (linear) operating range, torsion bars are strain-hardened—preset in the direction of subsequent torsional loading—to introduce compressive stresses into the surface layers. An additional component of compressive stress is introduced into the surface layers through the deep rolling process.

Previous investigation shows that the stress state of a torsion bar under torsional loading by analyzing the effects of various distributions of residual and applied stresses, using the Drucker-Prager criterion to assess the actual stress condition [1]. The findings indicate that the fatigue limit is maintained as long as the combined principal stresses remain within the safe zone. However, increasing compressive residual stresses near the surface can alter their distribution in depth and potentially shift the principal stress amplitude outside the safe zone as defined by the Drucker-Prager criterion.

In [2], a dynamic explicit simulation was used to analyze the residual stresses induced by the deep rolling process on a high-strength steel torsion bar. A three-dimensional simulation of a representative section effectively replicated the residual stress profile generated during deep rolling. The final stress magnitude is significantly influenced by the process input parameters. Additionally, the depth distribution of these residual stresses is strongly dependent on the dimensions of the extracted model. Therefore, it is crucial to carefully choose modeling assumptions and simplifications, as they directly affect the accuracy of the simulation results. The finite element model developed for the deep rolling process provides a solid foundation for future numerical studies.

It was an established model for fatigue lifetime prediction where the torsion-bar springs show different fatigue behavior depending on the applied elastic-plastic preset torque [3]. The study analyzed how presetting the twist angle affects fatigue life under various strain conditions. Presetting causes plastic deformation at the outer surface, while the core remains elastic, leading to compressive residual stresses. Increasing the preset torque allows for a larger twist angle but reduces fatigue life. Experiments showed that fatigue life strongly depends on the ratio between preset load and fatigue loading range.

Perenda et al. [4] highlighted the significant influence of residual stresses on the fatigue life and load capacity of torsion bars. Deep rolling induces compressive stresses in the subsurface, which suppress crack formation. Presetting overstrains and hardens the bar, increasing residual shear stresses and material yield strength, thereby enhancing load capacity. The study simulated various sequences of deep rolling and presetting using mapping and FE analyzis on a cut-out model, with results validated by measured residual stresses.

Residual stresses were measured on the surface of a round specimen during torsional presetting, specifically in the principal directions of +45° (compressive) and −45° (tensile) [5]. These stresses follow a linear distribution in the elastic range and become nonlinear once the material exceeds its elastic limit. Initial residual stresses were introduced by surface cold rolling, which plastically deforms a shallow surface layer. This process induces anisotropic strain due to material flow in both axial and circumferential directions, resulting in a helical lattice structure and differing stress values in each direction. Torsional characteristics derived from converted tensile data (σ–ε to τ–γ) showed slight deviations from direct torsion test results. Residual stresses were analytically calculated based on both datasets and compared. Additionally, FEM simulations using ABAQUS Release 2025, based on tensile properties, confirmed the analytical results.

Blum et al. [6] were compared experimental results on creep kinetics and microstructural evolution with the predictions of a simple, spatially homogeneous plastic deformation model. The model

DOI: 10.5545/sv-jme.2025.1407

describes the development of the dislocation structure as well as the creep kinetics.

Kolev et al. [7] were introduced a new expression for the creep law aiming to study in detail the behavior of simple structures using a generalized creep law with separable variables. The new expression, based on experimental data, combines the primary, secondary, and tertiary regions of the creep curve. The relaxation functions for bending and torsion depend solely on the maximum stress in the cross-section that occurs on the outer surface.

In [8], the main objective is to derive exact closed-form expressions for torsional and flexural creep in isotropic materials, based on generally accepted constitutive laws. The Norton–Bailey, Prandtl–Garofalo, and Naumenko–Altenbach–Gorash laws permit a closed-form solution. A partial generalization of the Norton–Bailey law is also solved in closed form. Stress relaxation was studied for structural elements subjected to torsional and flexural loads. The structures examined—such as a beam in bending, a bar in torsion, and a coil spring—demonstrate the fundamental characteristics of nonlinear creep. Closed-form solutions, using common creep models, provide a deeper understanding of the inherent effects in structural elements and support the design process.

Several authors have investigated biaxial loading with torsion and axial force on cylindrical specimens.

Šeruga at al. [9] developed a software tool for predicting creep damage in thermo-mechanically loaded components. It enables master curve determination using time-temperature parameters and calculate creep damage based on Robinson's rule and simple time integration. The software also allows separate evaluation of fatigue and creep damage. The article presents commonly used time-temperature parameters, a fast and user-friendly method for master curve generation, and an example of creep damage calculation using real data with a simple temperature-stress history [9].

Makabe and Socie [10] analyzed the fatigue crack growth in precracked torsion specimens and find that friction of the crack surfaces prevented shear mode crack growth. Yang and Kuang [11] examined the crack paths and growth rates of S45 steel specimens under various combinations of torsional and constant axial loads. They reported that the crack propagation angle was approximately 45° for different load amplitudes. Static tension combined with axial force and cyclic torsion accelerated crack growth and reduced service life, while compressive axial force combined with torsion significantly increased service life without affecting the crack propagation angle. They also found that the crack propagation direction depended on the alternating stress amplitude and was independent of the mean stress.

Tanaka et al. [12] tested hollow lead-free solder samples under torsional and combined torsional and compressive axial loads. They found that the crack initially propagated in the direction of maximum shear stress and later in the direction perpendicular to the maximum principal stress. Numerous microcracks formed between individual phases within the material's lattice, which later coalesced into a single crack.

Grigoriev at al. [13] investigated that grinding kinematics play a key role in the efficiency of creep-feed grinding. Paper examines non-traditional parameters—such as removal area, force ratios, and depth-to-diameter ratio—through three case studies on turbine blades, gears, and broaches using low-speed vitrified alumina wheels. Though experimental details are omitted, practical guidelines for improving productivity and quality are provided.

Nagode and Fajdiga [14] investigate that the isothermal strain-life method, commonly used for low-cycle fatigue, is fast and typically based on elastic finite element analyzis. Adapted for variable temperatures using a Prandtl-type operator, it assumes stabilized hysteresis loops and neglects creep. Reversal point filtering is examined, and the method is compared with thermo-mechanical fatigue tests and the Skelton model. In [15], the authors use the same approach when considering creep in the case of a press fit load capacity study.

This article investigates the creep behavior of torsion bars for two levels of presetting, specifically 4.3 % and 5.1 % surface shear strain. For each case, creep was comparatively evaluated for both manufacturing technologies, Technology A and Technology B. The creep of the torsion bars was assessed through experimental testing and FEM numerical simulation.

2 METHODS AND MATERIALS

The final geometry of the torsion bar is produced using a suitable material and appropriate mechanical properties. The manufacturing process involves rolling, hardening, tempering, and mechanical cutting. This is followed by deep rolling, which smooths the surface and introduces significant compressive residual stresses into the surface layers of the torsion bar. In addition to inducing compressive residual stresses, deep rolling also improves corrosion resistance and surface wear characteristics.

After deep rolling, the process of increasing the elastic operating range—known as presetting—is carried out. During presetting, the torsion bar is strain-hardened by controlled multiple transitions into the plastic region of the material under torsional loading [4]. This establishes a new, higher elastic limit. Upon unloading, residual torsional deformation remains, along with significant residual stresses. In the surface layers, these residual stresses are compressive, while in the core of the torsion bar, they are tensile. The compressive surface stresses enhance the cyclic fatigue strength, which is critical since torsion bars are designed for a defined service life with a limited number of load cycles. The torsion bar manufactured in this way is intended to be loaded with a unidirectional torsional moment, in the same direction as the presetting.

The introduction of residual stresses through deep rolling enhances the cyclic endurance of the torsion bar, while the presetting process tends to reduce its service life. It has been shown that performing presetting after deep rolling reduces the compressive residual stresses at the surface [4,5]. The number of loading cycles until failure depends on the degree of presetting as well as the load magnitude during testing or in actual use of the torsion bar [3]. In addition to reducing service life, increased presetting also leads to larger creep or yielding strains of the torsion bar under constant load.

To stabilize creep, a slightly modified manufacturing process has been adopted in practice. It has been shown that maintaining sufficiently high compressive stresses on the surface during the production of the torsion bar is crucial. This modified process involves partial presetting before deep rolling, followed by final presetting after deep rolling. This approach helps preserve a relatively high level of compressive residual stresses on the surface of the torsion bar [4] and reduces creep.

The first process, referred to as Technology A, consists of deep rolling followed by presetting the torsion bar into the plastic region. The second process, referred to as Technology B, involves partial presetting into the plastic region, then deep rolling, and finally final presetting [2].

2.1 Material Properties and Manufacturing Technology

Torsion bars were manufactured from high-strength, fine-grain spring steel grade 150VCN (according to EN 10027-1:2016 [16] 50CrV4, W. Nr. 1.8159). Figure 1 shows tensile tests results.The chemical composition (in weight %) and mechanical properties are listed in Tables 1 and 2, respectively [3]. Material has high yield strength Re

and ultimate tensile strength (UTS) Rm more than 2000 MPa. The material used was hot-rolled, forged, and soft annealed during the manufacturing process. The final shape and properties were achieved through the following mechanical processes: programmed turning, milling, and polishing.

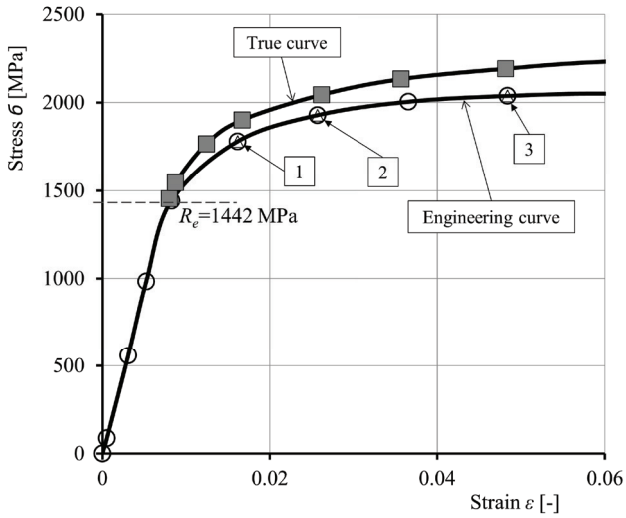

Fig. 1. True and engineering curves

The torsion specimen shown in Fig. 2b had a diameter of d = 10 mm, with a root-split section and a calculated effective length of l = 250 mm. The surface of the bar was polished to a roughness of Ra = 0.2 µm. The torsion bars were hardened using a dedicated process to achieve a target hardness of 54 ±1 HRC. Surface rolling and pre-setting were carried out as described in [4].

Table 1. Chemical composition in weight % of the used material, as specified in [4]

	C	Si	Mn	Ni	Cr	Mo	V	Cu	S	P
Actual val.	0.44	0.28	0.56	1.41	0.87	0.26	0.11	0.12	0.002	0.009
Min.	0.42	0.17	0.5	1.3	0.8	0.2	0.1	0	0	0
Max.	0.5	0.37	0.8	1.8	1.1	0.3	0.18	0.25	0.002	0.009

Figure 1 presents the engineering and true stress-strain curves for the material in its tempered condition. The engineering curve was obtained through tensile testing at ambient temperature, while the true curve was derived by calculation. The yield strength was determined using the following expression:

$$\sigma_f = \sigma(1+\varepsilon), \tag{1}$$

and logarithmic strain:

$$\varepsilon' = \ln(1+\varepsilon), \tag{2}$$

where σ_f is the true stress [MPa], σ engineering stress [MPa], ε engineering strain [-], and ε' true strain [-].

Table 2. Average mechanical properties of the torsion bar for different loading ratio $R = \sigma_{min} / \sigma_{max}$

Yield strength, Re [MPa]	UTS, Rm [MPa]	Poisson, ν [-]	Torsion elastic limit, τ_e [MPa]	Shear modulus, G [GPa]	Modulus, E [GPa]	Tensile fatigue limit $R = 0$, [MPa]	Tensile fatigue limit $R = -1$, [MPa]	Torsion fatigue limit $R = -1$, [MPa]
1442	2010	0.3	800	80	193	1200	800	520

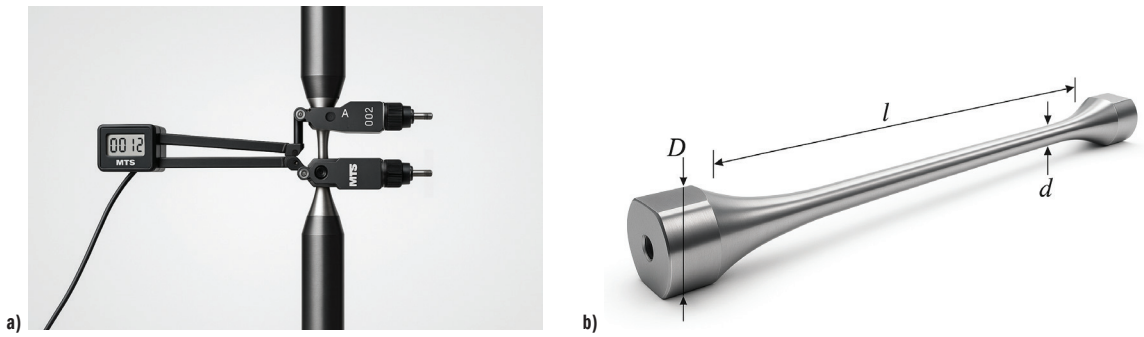

Fig. 2. Setup for creep tension testing with; a) elongation measurement, and b) torsion bar specimen

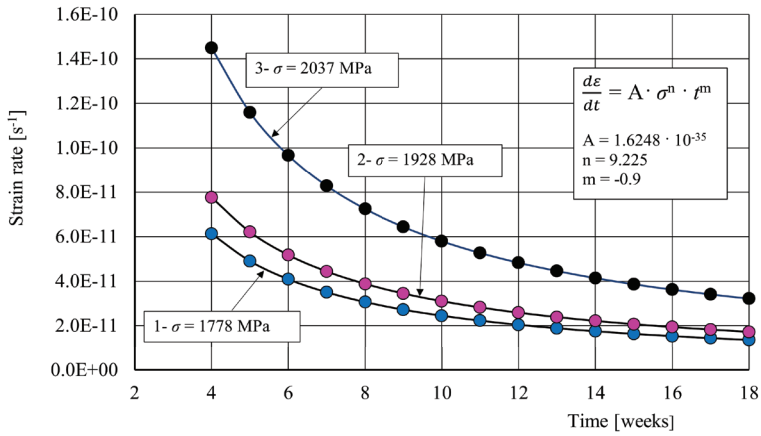

Fig. 3. Time dependent properties of the used material

A creep test under constant stress was performed on the material. Figure 2a shows the setup for creep tension testing with elongation measurement on the INSTRON 1255 servo-hydraulic testing machine. In Figure 1, points 1, 2, and 3 indicate the locations where stress relaxation was measured. Three tensile specimens were loaded to specific stress levels and then held under constant plastic strain. Plastic strain was measured using an extensometer, and the moment when the target stress was reached was defined as time zero. Figure 3 illustrates the dependence of creep strain rate on time under constant stress. The three stress levels considered were 1778 MPa, 1928 MPa, and 2037 MPa. The parameters A, n, and m were experimentally determined for use in ABAQUS finite element simulations.

$$\dot{\varepsilon} = A\sigma^n t^m, \tag{3}$$

where $\dot{\varepsilon}$ is uniaxial equivalent creep strain rate; σ uniaxial equivalent deviatoric stress, and A, n, m are constants determined experimentally at room temperature.

2.2 Torsion Specimen Preparation

The specimens were manufactured using the same technological process as that used for standard torsion bar production. The final shape and properties were achieved through programmed turning, milling, and polishing of the torsion bar body to a surface roughness of 0.2 µm. The geometry of the specimen is shown in Fig. 2b.

In Figure 4 provides a recommended presetting level for achieving optimal service life during torsion bar production, depending on the magnitude of the load applied during testing or actual use [3]. In the diagram, the presetting shear strain (γ_{ps}) and the applied shear strain (γ_{app}) represent the surface strain on the torsion bar. The upper curve denotes the elastic limit, while the lower curve corresponds to the high-cycle fatigue limit. The area between these two curves represents the optimal service life range for torsion bars. Red lines within this area are isolines indicating constant service life.

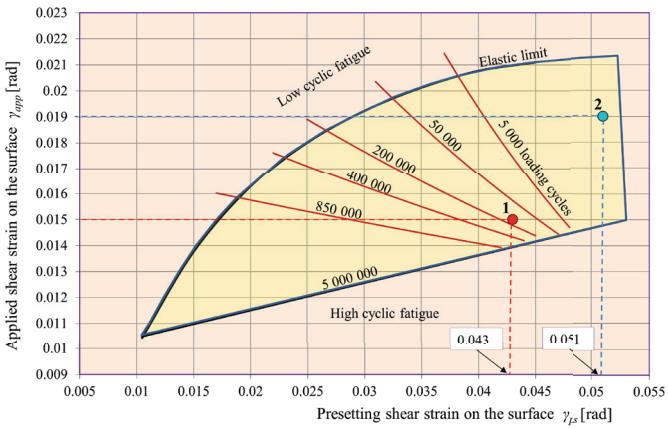

Fig. 4. Lifetime optimum zone of the torsion bar [3]

The service life of a torsion bar is influenced by the degree of presetting and the intensity of the cyclic torsional loading during operation. Additionally, presetting introduces creep, which results in vehicle settling under a constant load. In practice, a presetting surface shear strain of γ_{ps} = 4.3 % is generally considered an acceptable upper limit, beyond which both service life and creep behavior remain within acceptable bounds. However, in some cases, presetting beyond 4.3 % may be required, though this leads to a significant increase in creep.

Experimental results have shown that, in terms of minimizing creep, it is more favorable to perform presetting in two stages with intermediate deep rolling. As outlined in the introduction, two torsion bar preparation methods are considered in this study: Technology A, involving a single presetting after deep rolling, and Technology B, which uses a two-step presetting process with intermediate deep rolling.

In the diagram shown in Fig. 4, points 1 and 2 indicate the preparation and testing parameters of the torsional specimens. For both points, the two technologies, Technology A and Technology B were applied. The diagram reflects the results of long-term torsional testing, thereby indirectly accounting for creep behavior as well.

Table 3 presents the preparation parameters of the specimens used in the torsional creep tests. The symbols in the table represent: g_{ps} [%] shear strain on the surface of the torsion specimen at presetting, f_{ps} [°] twist angle of the torsion specimen at presetting, g_{app} [%] shear strain on the surface of the torsion specimen at application or at testing, f_{app} [°] twist angle of the torsion specimen at application or testing, and T_0 [Nm] initial torque.

Table 3. Preparation of torsion specimens (DR – Deep rolling; P – Presetting)

Point	g_{ps} [%]	f_{ps} [°]	g_{app} [%]	f_{app} [°]	Initial torque T_0 [Nm]	Technology
1	4.3	123	1.5	43	206	A (DR–P)
1	4.3	123	1.5	43	206	B (P–DR–P)
2	5.1	146	1.9	54.4	237	A (DR–P)
2	5.1	146	1.9	54.4	237	B (P–DR–P)

Figure 5 illustrates the preparation parameters for torsional specimens used in creep testing. The points labeled 1-A, 1-B, 2-A, and 2-B correspond to the positions in the diagram in Fig. 4, representing the respective technological preparation methods A and B. Each of these marked points indicates the starting point for measuring the time-dependent torque during creep at a constant twist angle.

After the torsional specimens were prepared through deep rolling and presetting, they were loaded to a twist angle of either 43° (initial torque T_0 = 206 Nm) or 54° (T_0 = 237 Nm), respectively. The change in torque over time due to creep was then measured and recorded.

2.3 Torsion Test Method

During the presetting phase, the torsion bar must be deliberately overloaded in a controlled manner into the plastic region, while measuring both torque and twist angle. A dedicated torsional loading device was designed for this purpose, as shown in Fig. 6.

On one end of the tested torsion specimen, a clamping sleeve is connected to a WATT DRIVE gear unit, type FUA 65A 101LA4 BR20 FL, 3 kW, 10 min^{-1}. The gear is driven by an electric motor, with speed regulated by a V2500 frequency control unit from the same manufacturer. On the opposite side of the gear's hollow shaft, a SIMODRIVE incremental encoder (Siemens, Germany) is installed, offering an angular measurement resolution of 5000 pulses per revolution.

Torque is measured using a DF-30 (500 Nm) torque sensor from Lorenz Messtechnik. For data acquisition and visualization, the torque sensor and incremental encoder are integrated into a measurement chain consisting of Spider-8 universal PC measuring electronics and the Catman EASY software, both from HBM.

2.4 FEM Simulation

The finite element analyzis of the stress–strain state was conducted using the SIMULIA Abaqus 2025 software suite [17]. A comprehensive three-dimensional simulation of a torsion spring was performed, employing a single-layer discretization of finite elements

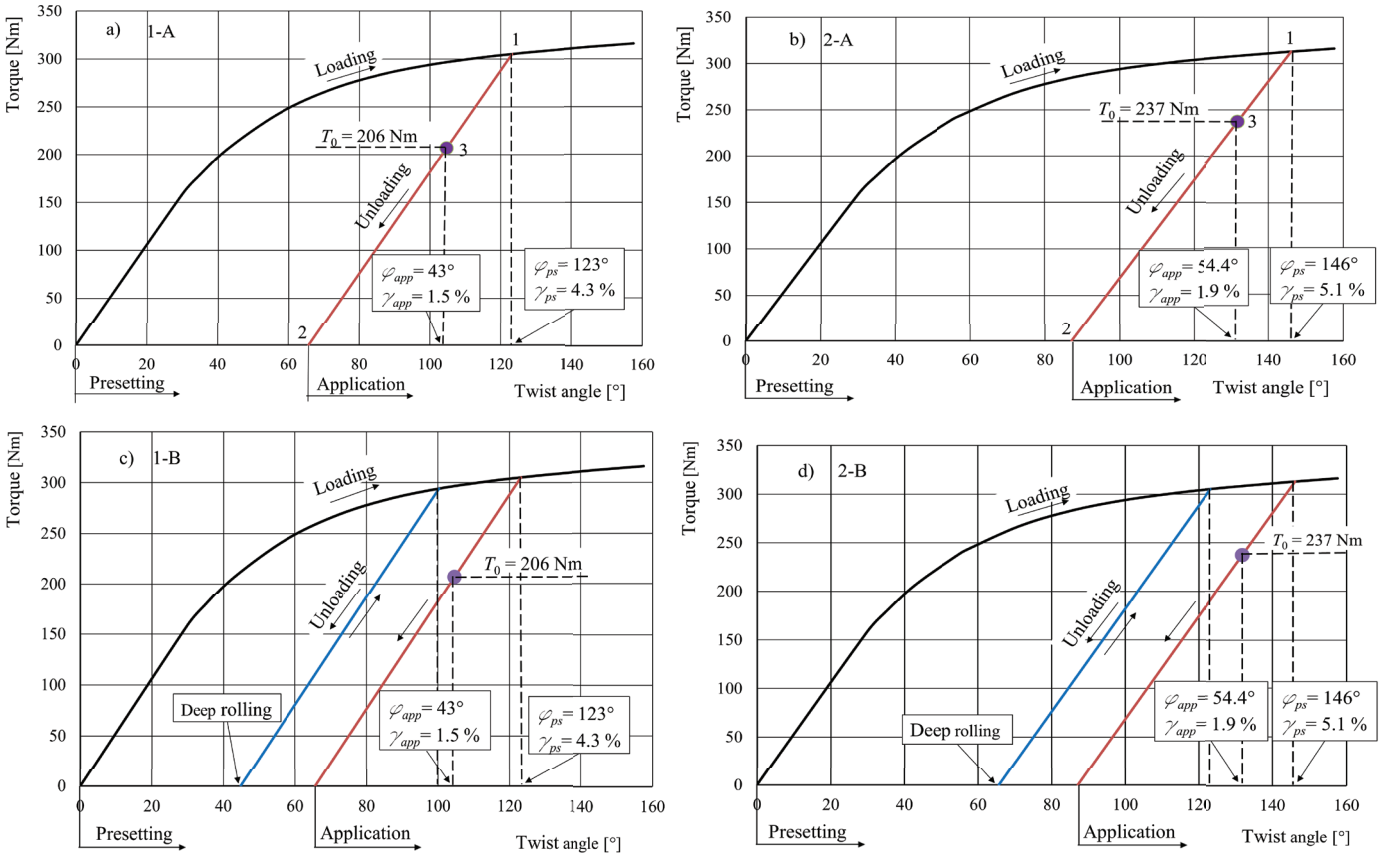

Fig. 5. Preparation of torsion specimens with presetting

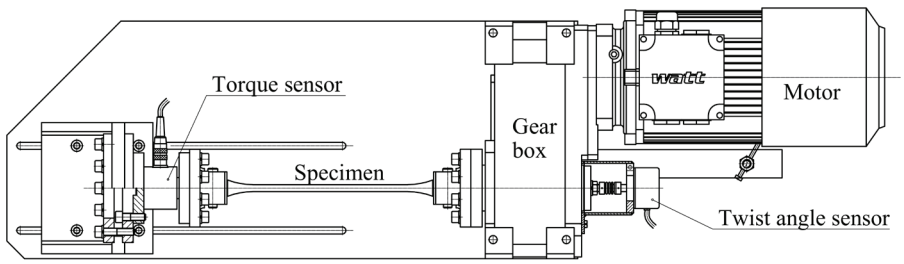

Fig. 6. Presetting device [3]

along the spring's axial direction. Eight-node brick elements (C3D8) were utilized throughout the model. Appropriate boundary conditions were imposed on the free end surfaces of the thin, single-layer configuration to ensure well-posedness of the problem and to enable the accurate determination of stress–strain responses under torsional loading. This modeling strategy significantly reduced the computational complexity and numerical size of the model, thereby enabling rapid and efficient numerical simulations, while still capturing the complete stress–strain field that would be observed in a full-length spring model. The material analyzed in this study is isotropic and homogeneous spring steel. Therefore, it was essential to determine the key material parameters through experimental testing in order to accurately describe its elastic–plastic and additional viscoelastic behavior. Similar approach was applied in the research study [18] where analyzes the evolution patterns of damage parameters concerning sheet metal and corresponding temperatures. Possible applications are described in testing of in special off-road vehicles and their parts [19].

The material behavior was characterized using an elastic–plastic–visco-plastic constitutive model. This allowed for the accurate simulation of key physical phenomena, including material yielding, the development of residual stresses due to preloading, and long-term stress relaxation effects attributable to creep. In the linear elastic regime, the material was defined by a Young's modulus of 193 GPa and a Poisson's ratio of 0.3. The yield strength was specified as 1442 MPa, with strain hardening extending to 2010 MPa. Time-dependent material behavior was modelled using a creep formulation that incorporated experimentally determined hardening parameters: $A = 1.6248\times10^{-35}$, $n = 9.47$, and $m = -0.9$. The final simulation employed a total of 47.630 C3D8 elements within the single-layer model, achieving a high-fidelity representation of the stress–strain field in the torsion spring.

3 RESULTS AND DISCUSSIONS

Figure 7 displays the measured torque values at a constant twist angle as a function of time for all four torsion bar cases. The measured data in the graphs are approximated using an analytical logarithmic function, given by Eq. (4). Table 4 summarizes the constants a and b

for each of the four torsional moment measurements. The analytical function in Eq. (4) describes the experimental results with a mean coefficient of determination of $R^2 = 0.98$.

Sudden drops observed in the torque measurements due to creep are attributed to the fact that the measured decrease in torque is smaller than the resolution of the measurement system.

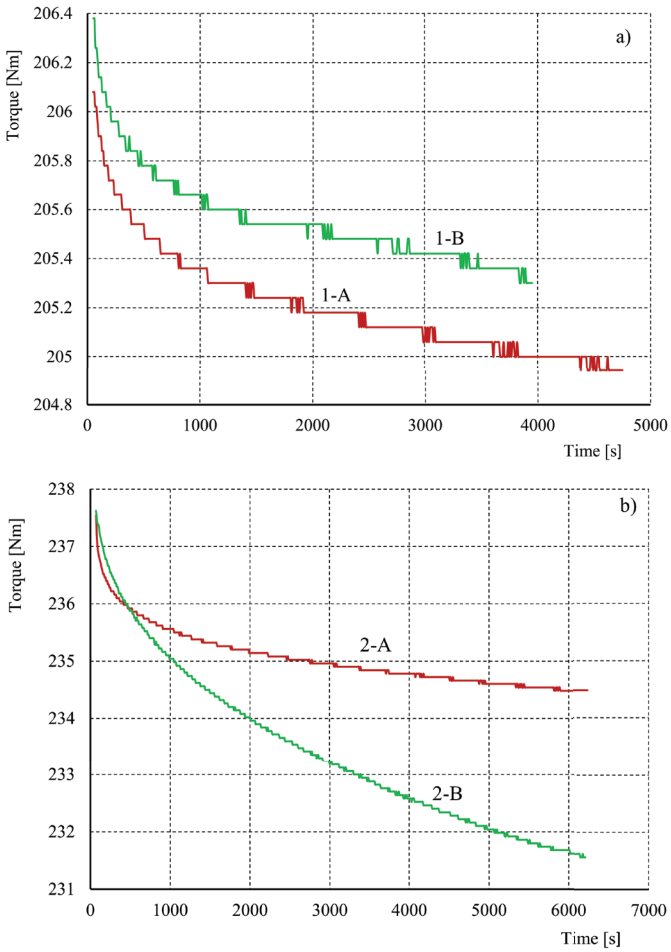

Fig. 7. Time dependent torque measured at a constant twist angle; a) 1-A and 1-B, and b) 2-A and 2-B

Table 4. Constants a and b for Eq. (4)

Point	a	b
1-A	–0.24313	216.53131
1-B	–0.21623	207.14633
2-A	–0.56792	239.46698
2-B	–0.56792	245.73548

$$T(t) = a \cdot \ln(t) + b, \tag{4}$$

where $T(t)$ is dependent torque, t time and a, b are constants.

Figure 8 illustrates the relative torque drop over time. The curves represent the predicted torque reduction as a function of the specimen preparation technology, based on Eq. (4). For comparison, the torque drop predicted by FEM simulation is also shown for case 1-A. The most significant creep is observed at point 2 using Technology B, with a torque drop exceeding 7 %. In contrast, much smaller creep is observed at point 1, where Technology B results in less creep than Technology A.

The results of the creep analyzis for the torsion bars are summarized comparatively in Table 5. After 18 weeks of creep testing, the largest relaxation was observed at point 2 for Technology B, despite the fact that Technology B was designed to reduce torsion bar relaxation. Using the diagram in Fig. 4, the service life of a cyclically loaded torsion bar can be estimated as a function of the applied surface shear strain and the surface presetting shear strain. The upper region of the diagram corresponds to low-cycle fatigue, while the lower region corresponds to high-cycle fatigue. Within the hatched area, lines indicate constant service life. By locating the operating point on the diagram—point 1 or 2 in our case—it is possible to estimate the expected service life of the torsion bar.

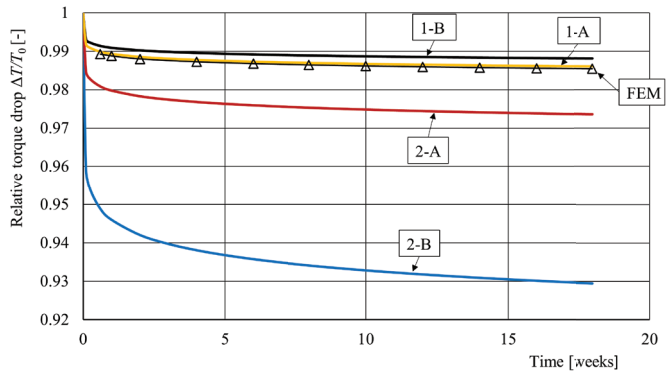

Fig. 8. Prediction of relative time dependent torque drop; ΔT is torque drop

Table 5. Relative torque drop in 18 weeks at a constant twist angle and estimated lifetime

Point	Initial torque T_0 [Nm]	Relative torque drop in 18 weeks [%]	Estimated lifetime, Fig. 4 [cycles]
1-A	206	1.39	200,000
1-B	206	1.19	200,000
2-A	237	2.64	< 40,000
2-B	237	7.05	< 40,000

A comprehensive three-dimensional simulation of a torsion spring was performed, employing a single-layer discretisation of finite elements along the spring's axial direction, as shown in Fig. 9. Figure 10 presents the results of the FEM analyzis performed to simulate the specimen preparation process, which includes both presetting and creep. Fig. 10a illustrates the residual stresses at point 2 after the presetting step, while Figs. 10b and c depict the applied stresses at point 3, captured before and after the creep process, respectively. The locations of points 2 and 3 are marked in Fig. 5 for reference.

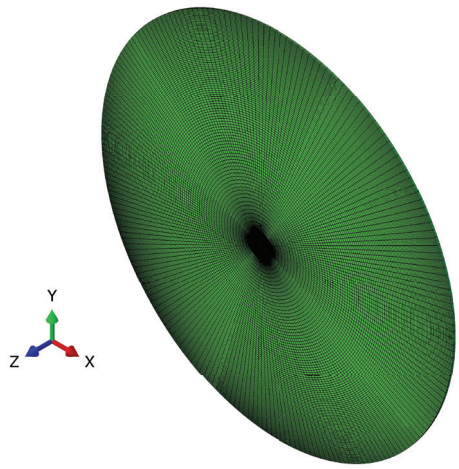

Fig. 9. Finite element model, mesh and interaction constraints

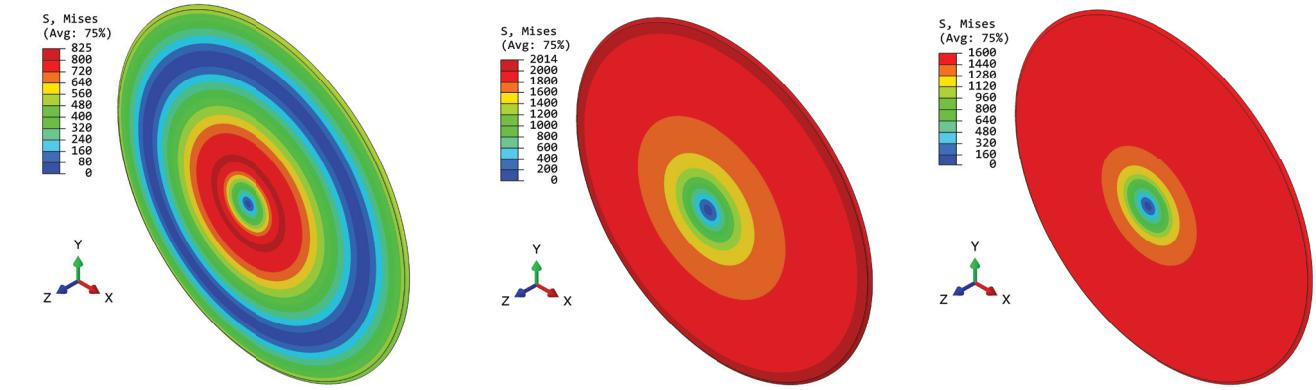

a) b) c)

Fig. 10. The Von Mises stresses obtained from the FEM analyzis at points 2 and 3, as marked in Fig. 5, a) residual stresses after presetting at Point 2, b) applied stresses at point 3, and c) aplied stresses at Point 3

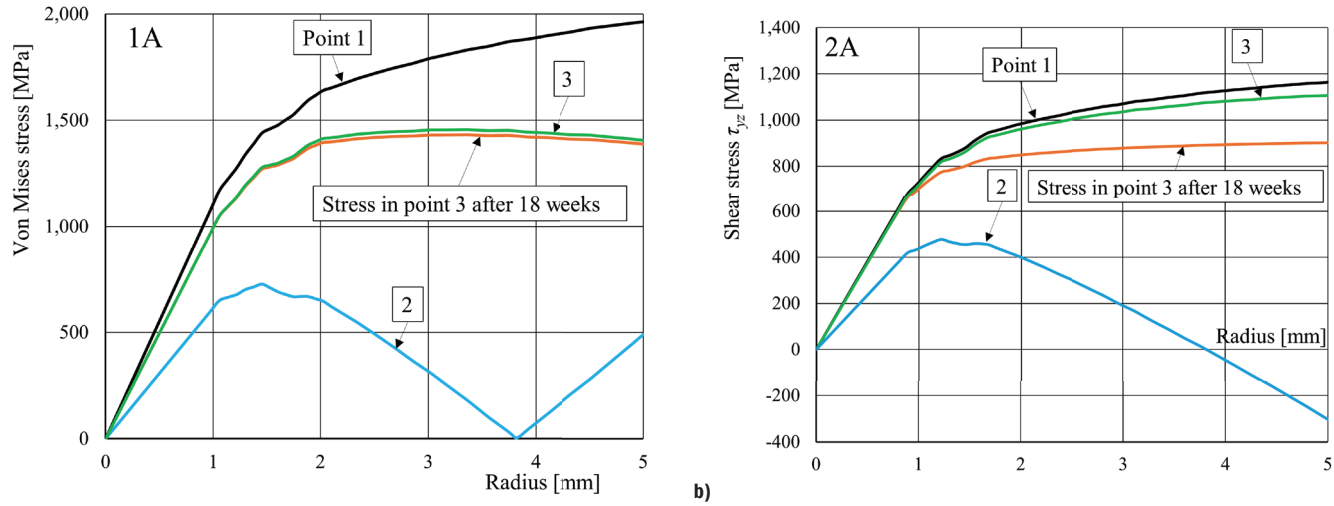

a) b)

Fig. 11. a) Von Mises, and b) Shear stress distribution across section of torsion bar calculated using FEM analyzis at point 1, point 2 and point 3 from Fig. 5

Figure 11 illustrates the distribution of Von Mises and shear stresses across the cross-section of the torsion bar, as determined by FEM analyzis. Curve 1 represents the stresses introduced during presetting, while Curve 2 shows the residual stresses remaining after unloading. Curve 3 depicts the stresses under the applied load, including the additional creep stresses accumulated over a period of 18 weeks. Measurement points 1, 2, and 3 correspond to the locations identified in Fig. 5.

4 CONCLUSIONS

This study investigated the creep of torsion bars subjected to different manufacturing processes involving presetting and deep rolling. Two technological approaches were compared: Technology A (deep rolling followed by presetting) and Technology B (partial presetting, deep rolling and final presetting).

Experimental results showed, that at moderate levels of presetting (4.3 % shear strain), Technology B resulted in lower torque release over time compared to Technology A, confirming the advantage of maintaining high surface compressive stresses via intermediate deep rolling. At higher presetting levels (5.1 % shear strain), creep increased significantly regardless of the process used. However, Technology B resulted in an even higher creep rate than Technology A, likely due to the redistribution of internal stresses caused by excessive plastic deformation.

The FEM numerical simulations accurately captured the time-dependent stress relaxation behavior observed in the experiments, demonstrating the capability of the model to reflect real material responses over time. Furthermore, the results validated the application of visco-plastic material models for simulating long-term deformation processes. The simulations also provided strong support for the experimental findings, confirming the reliability and consistency of the observed phenomena.

In conclusion, a balanced presetting rate combined with an optimized deep-rolling sequence can significantly affect the long-term performance and dimensional stability of torsion bars. Excessive presetting should be avoided as it leads to undesirable creep effects that compromise component reliability. Future work should include a more detailed parametric study of the visco-plastic behavior under different temperature and loading conditions, and an analyzis of the interaction between fatigue and creep.

References

[1] Močilnik, V., Gubeljak, N., Predan, J. Effect of residual stresses on the fatigue behaviour of torsion bars. *Metals* 10 1-16 (2020) **DOI:10.3390/met10081056**.

[2] Perenda, J., Trajkovski, J., Žerovnik, A., Prebil, I. Residual stresses after deep rolling of a torsion bar made from high strength steel. *J Mater Process Technol* 218 89-98 (2015) **DOI:10.1016/j.jmatprotec.2014.11.042**.

[3] Močilnik, V., Gubeljak, N., Predan, J. Model for fatigue lifetime prediction of torsion bars subjected to plastic Pre-setting. *Tech Gazette* 18 537-546 (2011).

[4] Perenda, J., Trajkovski, J., Žerovnik, A., Prebil, I. Modeling and experimental validation of the surface residual stresses induced by deep rolling and Pre-setting of a torsion bar. *Int J Mater Form* 9 435-448 (2016) **DOI:10.1007/s12289-015-1230-2**.

[5] Močilnik, V., Gubeljak, N., Predan, J. Surface residual stresses induced by torsional plastic pre-setting of solid spring bar. *Int J Mech Sci* 92 269-278 (2015) **DOI:10.1016/j.ijmecsci.2015.01.004**.

[6] Blum, W., Eisenlohr, P., Breutinger, F. Understanding Creep-a Review. *Metall Mater Trans* 33 291-303 (2002) **DOI:10.1007/s11661-002-0090-9**.

[7] Kobelev, V. Relaxation and creep in twist and flexure. *Multidiscip Model Mater Struct* 10 304-327 (2014) **DOI:10.1108/MMMS-11-2013-0067**.

[8] Kobelev, V. Some basic solution for nonlinear creep. *Int J Solids Struct* 51 3372-3381 (2014) **DOI:10.1016/j.ijsolstr.2014.05.029**.

[9] Šeruga, D., Fajdiga M., Nagode M. Creep damage calculation for thermo mechanical fatigue. *Stroj Vestn-J Mech E* 57 371-378 (2011) **DOI:10.5545/sv-jme.2010.108**.

[10] Makabe, C., Socie, D.F. Crack growth mechanisms in precracked torsion fatigue specimens. *Fatigue Fract Eng Mater Struct* 24 607-615 (2001) **DOI:10.1046/j.1460-2695.2001.00430.x**.

[11] Yang, F.P., Kuang, Z.B. Fatigue crack growth for a surface crack in a round bar under multi-axial loading condition. *Fatigue Fract Eng Mater Struct* 28 963-970 (2005) **DOI:10.1111/j.1460-2695.2005.00929.x**.

[12] Tanaka, K., Kato, T., Akinawa, Y. Fatigue crack propagation from a precrack under combined torsional and axial loading. *Fatigue Fract Eng Mater Struct* 28 73-82 (2005) **DOI:10.1111/j.1460-2695.2005.00861.x**.

[13] Grigoriev, N.S., Starkov, K.V., Gorin, A.N., Krajnik, P., Kopač, J. Creep-Feed Grinding: An overview of kinematics, parameters and effects on process efficiency. *Stroj Vestn-J Mech E* 60 213-220 (2014) **DOI:10.5545/sv-jme.2013.1547**.

[14] Nagode, M., Fajdiga, M. Thermo-mechanical modelling of stochastic stress-strain states. *Stroj Vestn-J Mech E* 52 74-84 (2006).

[15] Močilnik, V., Gubeljak, N., Predan, J. Time dependent load capacity of the press fit. *Tech gasette* 19 434-441 (2025) **DOI:10.31803/tg-20250115224222**.

[16] EN 10027-1:2016. *Designation systems for steels - Part 1: Steel names*, European Committee For Standardization, Brussels.

[17] *Simulia Abaqus 13.0*. Dassault Systems, Vélizy-Villacoublay.

[18] Wu, D., Li, D., Liu, X., Li, Y., Wang, Y. i Liu, S. Temperature dependence of meso constitutive parameters for advanced high-strength steel. *Trans FAMENA* 48 87-102 (2024) **DOI:10.21278/TOF.484063324**.

[19] Stodola, J., Stodola, P. Accelerated Reliability Tests Of Characteristics Of Off-Road Vehicles And Their Parts. *Trans FAMENA* 48 31-44 (2024) **DOI:10.21278/TOF.482049422**.

Acknowledgement *Authors gratefully acknowledges the support of the Slovenian Research and Innovation Agency (ARIS) conducted through the research programme P2-0137 "Numerical and Experimental Analyzis of Mechanical Systems". In addition, this paper has been written to mark the 30th anniversary of the Faculty of Mechanical Engineering and 50th anniversary of the University of Maribor.*

Received: 2025-05-26, revised: 2025-07-21, 2025-08-17, Accepted: 2025-08-27 *as Original Scientific Paper 1.01.*

Data availability *Data supporting the findings of this study are available from the corresponding author upon reasonable request.*

Author contribution *Vinko Močilnik: Conceptualization, Metodology, Computational Analyzis, Measurements, Validation, Writing – Original Draft; Nenad Gubeljak: Conceptualization, Metodology, Computational Analyzis, Validation, Writing – Review and Editing; Jožef Predan: Conceptualization, Metodology, Computational Analyzis, Validation, Writing – Original Draft.*

Vpliv prednapetja in globokega valjanja na lezenje paličaste torzijske vzmeti

Povzetek *Prispevek obravnava obnašanje lezenja torzijskih vzmetnih palic s kombinacijo eksperimentalnega testiranja in numeričnega modeliranja. Eksperimentalne raziskave so bile izvedene na torzijskih vzorcih, ki so bili podvrženi različnim stopnjam prednapenjanja in različnim površinskim obdelavam z globokim valjanjem, pri čemer so se pokazali različni učinki na sproščanje napetosti pri konstantnem kotu zasuka. Simulacije z metodo končnih elementov (MKE), ki vključujejo elasto-visko-plastično obnašanje materiala, so uspešno reproducirale časovno odvisno deformacijo, ki smo izmerili tudi med eksperimentom. Materialni parametri za model MKE so bili izpeljani iz eksperimentalnih podatkov. Ugotovitve kažejo, da dvostopenjski postopek prednastavitve v kombinaciji z vmesnim globokim valjanjem povzroči višje preostale tlačne napetosti v površinskih plasteh v primerjavi z enostopenjskim postopkom prednastavitve. Čeprav je cilj te metode ublažiti lezenje pri konstantnih pogojih obremenitve, ugotavljamo, da je njena učinkovitost omejena. Zmanjšanje deformacij lezenja je opaziti le do stopnje prednastavitve približno 4,3 %; nad tem pragom se deformacije lezenja znatno povečajo in vzmet zgublja na nosilnosti.*

Ključne besede *lezenje, torzijska palica, metoda končnih elementov (MKE), prednapenjanje, globoko valjanje, torzijski moment, kot vzvoja*

Integrated Design, Simulation, and Experimental Validation of Advanced Cellular Metamaterials

Nejc Novak ✉ – Zoran Ren – Matej Vesenjak
University of Maribor, Faculty of Mechanical Engineering, Slovenia
✉ n.novak@um.si

Abstract *Cellular metamaterials offer supreme properties for engineering, medicine, and defence, but their transition to industrial use faces design, fabrication, and characterisation challenges. This review provides an overview of 20 years of advancements in cellular structures, from open-cell foams to triply periodic minimal surfaces (TPMS), presenting novel fabrication techniques (e.g., explosive compaction for UniPore structures) and demonstrating validated computational models for optimising graded auxetic and hybrid TPMS lattices. The study indicates that porosity and base material primarily govern energy absorption, with closed-cell foams and TPMS outperforming other geometries. Additive manufacturing enables spatially graded designs with tailored mechanical properties. This work accelerates the development of next-generation metamaterials for crash absorption, blast protection, and biomedical devices.*

Keywords *cellular structures, metamaterials, experimental testing, computational simulations, mechanical properties*

Highlights

- *Modern metamaterials are set to revolutionise engineering, transportation, medicine, and sports.*
- *Design, fabrication, modelling, and characterisation of cellular structures are covered.*
- *The article offers a comparative analyzis of mechanical responses of various cellular structures.*
- *Validated computational models are crucial for optimising metamaterial design.*

1 INTRODUCTION

Modern engineering faces dual challenges: escalating material costs and stringent sustainability requirements. Cellular metamaterials—engineered porous structures with tunable mechanical, thermal, and acoustic properties—have emerged as a transformative solution. These materials leverage hierarchical architectures spanning nano- to macro-scales to achieve unprecedented performance-to-weight ratios, making them indispensable for aerospace (impact-absorbing components), biomedical (tissue scaffolds), and defence (blast-resistant panels) applications [1,2]. Cellular materials excel in mechanical and thermal properties and enable multifunctionality. They serve as structural components (cores for sandwich panels, enhancing stiffness and damping [3]), functional systems (heat exchangers, acoustic isolators, and fluid filters [4]) and energy absorbers (crashworthy fillers in automotive and protective gear [5]).

Despite their potential, widespread deployment is hindered by fabrication limitations (traditional methods like powder foaming) lack precision for complex geometries), knowledge gaps (incomplete data on shear/dynamic behavior and graded porosity effects), design barriers (absence of standardised guidelines for application-specific optimisation) and scepticism towards new materials. However, advanced fabrication technologies, such as additive manufacturing, are overcoming these hurdles. All of the additive manufacturing technologies offer precise control over cell shape, size, and distribution on a certain level of the scale, depending on the printing accuracy. These methods surpass traditional methods like melt/powder foaming and replication techniques in terms of fabrication accuracy and adaptability, while in some cases, the costs and fabrication speed are still in favour of the traditional methods [6]. They also enable the integration of digital twins using three-dimensional (3D) models obtained from computed tomography (CT) for iterative design..

As the use of cellular structures grows, it is essential for engineers, material scientists, and commercial entities to understand their behavior under various loads to optimise performance through customised designs. Combining different base materials with tailored internal structures can achieve unique mechanical and thermal properties [7]. Advanced additive manufacturing enables the creation of complex cellular metamaterials designed for specific applications through computational simulations and topological optimisation [8].

The mechanical properties of cellular (meta)materials depend on factors like relative density (porosity), base material (metal or non-metal), morphology (pore size and shape), topology (pore distribution) and fillers [1]. The most important factor is relative density, which is calculated as the ratio of the bulk density of the foam to the solid density of the material, while the porosity is then determined by subtracting relative density from 1. In general, the higher the porosity, the lower the mechanical properties, which can also be analytically calculated using the empirical equations given in [4]. Careful selection of these parameters and proper fabrication can yield desired mechanical, damping, and thermal properties [4,5]. Detailed geometry and mechanical behavior of fabricated structures can be evaluated using CT scanning [9]. High-quality 3D data acquisition is crucial for building precise digital twins, which aid in developing new cellular structures with advanced material engineering techniques.

Standard mechanical tests like compression, tension, and bending are well-documented, but data on shear and dynamic testing are limited. Recent studies have explored cellular structures' dynamic and impact behavior, but a detailed analyzis of functionally graded porosity is still needed [10–12]. Specifically designed internal structures can optimise mechanical responses for applications in safety, defence, and crashworthiness [13].

In general, the cellular metamaterial's unit cell size is in the range of millimetres, while also micro-architected cellular structures and

DOI: 10.5545/sv-jme.2025.1363

nano-lattices with unit cell sizes below 1 µm have been developed, driven by the need to control band gaps in phononic metamaterials [14,15]. These structures offer unique properties like tailorable stiffness and auxetic behavior. However, further research is needed on their mechanical behavior, fabrication optimisation, and biocompatibility for medical applications [16].

This review systematically investigates the design, fabrication, and mechanical behavior of cellular metamaterials under various loading conditions, with a focus on their specific energy absorption (SEA) capabilities and its relationship to the base material, geometry and loading conditions. Understanding these relationships and the distinct deformation mechanisms of cellular metamaterials is crucial, as it enables the tailored design of high-performance cellular materials for diverse engineering applications. This study's significance lies in providing critical insights for optimising metamaterial design, which is essential for advancing fields such as automotive crashworthiness, aerospace impact resistance, and biomedical engineering. In summary, there is a clear need for more research on detailed geometry characterisation and the development of digital twins to create new geometries and optimised fabrication processes. The group at the University of Maribor is working to address these gaps in metamaterials research.

2 METHODS AND MATERIALS

The following section categorises (meta)materials based on their topology and manufacturing processes. Figure 1 illustrates the progression from primitive to advanced geometries over the last two decades in the research group at the University of Maribor.

The geometry and properties of cellular metamaterials presented in Fig. 1 are provided in the next paragraphs. The fabrication methods are given as follows: investment casting (IC), (aluminium), selective electron beam melting (SEBM) (titanium), powder bed fusion (PBF) (stainless steel), photopolymerisation (VAT) (photopolymer), gas injection (GI) (aluminum), powder metallurgy (PM) (aluminium), explosive compaction (EC) (copper).

2.1 Open-cell Foams

Open-cell foams are materials characterised by an interconnected network of pores, which allow air or fluids to pass through (Fig. 1b). These foams are highly versatile and are used in various applications due to their unique properties. In the furniture industry, polymeric open-cell foams are commonly used for sofa cushions, foam mattresses, and car seats because they can be easily compressed and then naturally return to their original shape. Additionally, they are employed in acoustic and soundproofing applications. Metal open-cell foams, produced through methods like investment casting, are valued for their lightweight and high-strength properties, making them suitable for use in automotive, aerospace, and other engineering fields [17]. The mechanical properties of open-cell foams can be further enhanced by introducing fillers, such as polymers, into the cellular structure. Additionally, open-cell foams can be used as fillers for foam-filled tubes [18]. This adaptability and multifunctionality make open-cell foams necessary in modern engineering and design.

The impact of the base material on the mechanical properties of open-cell foams is well-documented, with numerous empirically established relationships linking the base material and cell morphology to the properties of the cellular material. The metals and alloys used for metal foams must also be lightweight to retain the advantage of low relative density over conventional solid materials. Therefore, the most commonly used metals for cellular materials include aluminium, magnesium, titanium, and their alloys.

The influence of cell morphology on the mechanical properties of regular and irregular open-cell materials has been extensively studied using representative unit cells. However, since the geometry of fabricated open-cell foams often deviates from geometric regularity, many researchers have also examined the cell morphology of these fabricated foams [19]. The mechanical behavior of open-cell foam can be further enhanced by introducing polymer fillers into the cellular structures [18].

2.2 Closed-cell Foams

Closed-cell foam's interconnected, sealed cells provide higher stiffness and water resistance, are suitable for shock absorption and thermal insulation (Fig. 1a). Powder metallurgy is a standard method for producing closed-cell aluminium foams [20]. This involves heating a precursor (aluminium, silicon, and titanium hydride) within a mould, allowing it to expand and fill the cavity. After cooling, the foam is extracted and sectioned. The mechanical behavior of these foams has been thoroughly investigated under free and laterally constrained compression, and it was proved that the behavior of the cell material could be adequately described with a single,

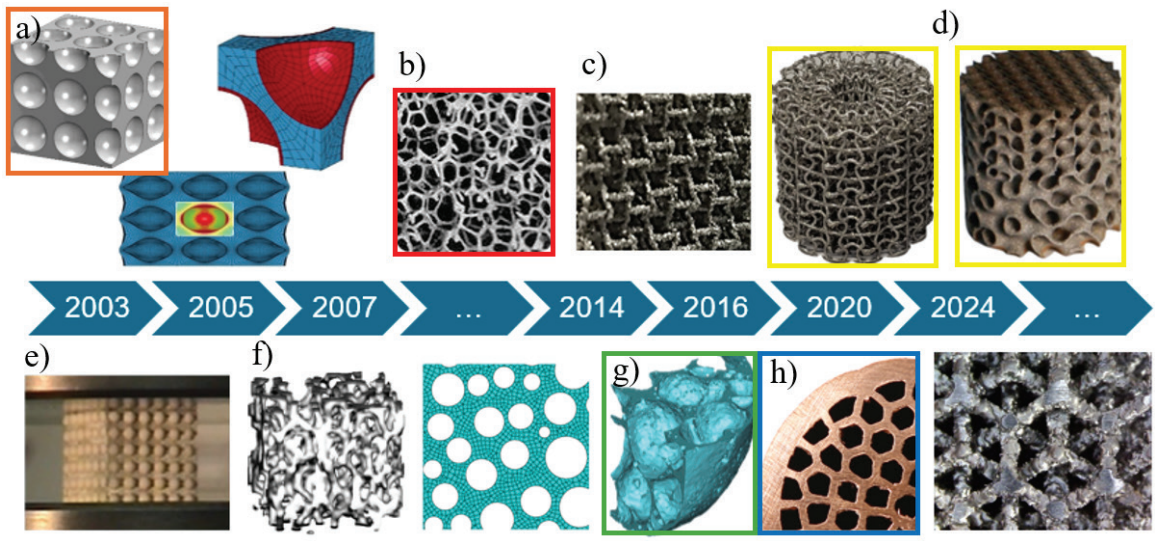

Fig. 1. Research of cellular metamaterials in recent years: from primitive to advanced cellular geometry; a) closed-cell foams, b) IC, C) SEBM, d) PBF, e) VAT, f) GI, g) PM, and h) EC

geometrically uniform cell [21]. Applications include ex-situ and in-situ foam-filled tubes, where the latter, produced directly within the tube, demonstrates enhanced stiffness due to improved bonding [22]. Furthermore, closed-cell foam can be integrated into auxetic aluminium alloy panels to improve their mechanical performance [22].

2.3 UniPore Structure

The UniPore structure, characterised by longitudinal pores, is fabricated by explosively welding thin-walled inner tubes within an outer tube (Fig. 1h) [23]. This process involves densely packing the outer tube with smaller diameter inner tubes along its length, resulting in a uniform porous cross-section. However, variations in collision angles during welding due to the inner tubes' curvature can lead to inconsistent interface formation, a phenomenon supported by computational simulations [24].

To address these limitations, a novel UniPore fabrication method has been recently developed [25]. This approach utilises rolling thin metal foil with acrylic spacer bars, followed by explosive compaction. This technique ensures a stable collision angle, similar to conventional explosive welding, leading to more uniform welding interfaces. The production process, demonstrated with copper, allows for the use of various metallic foils. Notably, this method offers flexibility in tailoring external dimensions, pore size, internal wall thickness, and porosity to meet specific application requirements.

2.4 Advanced Pore Morphology (APM) Foam

Advanced Pore Morphology (APM) foam, a hybrid cellular material featuring interconnected, sphere-like closed-cell pores within a solid outer skin, was pioneered at Fraunhofer IFAM in Bremen, Germany (Fig. 1g) [26]. This unique structure offers a balance of high surface area and structural integrity, making it attractive for applications requiring energy absorption and thermal management. The fabrication begins with the compaction and rolling of an AlSi7 alloy combined with a TiH2 foaming agent, yielding an expandable precursor. This precursor is subsequently granulated and subjected to thermal decomposition of the TiH2 in a continuous belt furnace, resulting in spherical foam elements. The internal structure of APM foam has been extensively characterised [9,27], revealing its tailored pore distribution and connectivity. Notably, APM elements have demonstrated efficacy as filler material in foam-filled tubes [28,29], enhancing their mechanical performance under impact loading.

2.5 Predesigned Structures

Advanced fabrication techniques, particularly additive manufacturing, enable the creation of complex, pre-designed cellular structures with tailored mechanical properties (Fig. 1d) [6,30,31]. This includes the development of three-dimensional auxetic cellular materials, such as those built from interconnected inverted tetrapods [32,33] and chiral auxetic designs [34]. Inverted tetrapod structures are constructed by stacking unit cells in layers, resulting in a layered 3D auxetic architecture [35]. These structures, along with chiral auxetic designs based on the 10th eigenmode of a regular cubic unit cell [36], are typically modelled using computer aided design (CAD) software and fabricated using additive manufacturing technologies. The mechanical performance of these auxetic structures can be further enhanced by incorporating polymeric fillers [37], offering a route to multi-functional materials.

Furthermore, triply periodic minimal surfaces (TPMS) represent a class of periodic cellular materials with significant potential in diverse engineering applications. TPMS are intricate 3D topologies that minimise surface area within defined boundaries and exhibit periodicity in three orthogonal directions [38,39]. They partition space into interconnected domains without enclosed voids, leading to unique topological characteristics. This makes them highly suitable for applications ranging from tissue and structural engineering to thermal management and fluid transport [38,40]. Their optimised thermal and electrical conductivity and controlled fluid permeability make them promising candidates for advanced heat exchangers, filters, and catalytic reactors. The ability to precisely control the geometric parameters of TPMS through additive manufacturing opens up new avenues for designing materials with tailored functional properties.

3 DESIGN AND CHARACTERISATION

Cellular metamaterials are engineered materials with cellular structures that exhibit unique mechanical, thermal, acoustic, or electromagnetic properties not found in conventional materials. Their design involves careful selection of the unit cell geometry, size, arrangement, and constituent material to achieve the desired macroscopic behavior. This often entails intricate topologies like lattices, honeycombs, or triply periodic minimal surfaces, which are carefully examined using CT scanning. These can be optimised using computational methods like finite element analyzis and topology optimisation to tailor properties like stiffness, strength-to-weight ratio, energy absorption, and wave propagation characteristics. The ability to precisely control the microarchitecture allows for creating materials with unprecedented functionalities, opening doors for applications in diverse fields ranging from aerospace and automotive to biomedical engineering and soft robotics.

A critical aspect of metamaterial design and research involves developing and validating robust computational models, essential for accurately predicting their behavior. These models, often employing techniques like finite element analyzis, must be rigorously validated against experimental data to ensure reliability. The complexity of these models can vary significantly, with simplifications tailored to the specific geometry of the metamaterial and the intended application of the simulation. For instance, simplified models might be used for preliminary design studies. In contrast, more detailed models are necessary to predict complex phenomena like non-linear deformation or dynamic response accurately. Moreover, these validated numerical models can serve as powerful tools for parametric studies, allowing researchers to explore the influence of geometric variations and material properties on the overall performance of the metamaterial, thereby accelerating the design and optimisation process.

3.1 Experimental Testing

Experimental characterisation of cellular metamaterials has predominantly focused on compression testing, revealing a characteristic mechanical response: an initial elastic region, followed by a plateau phase denoting progressive cell collapse, and finally, a densification regime. To gain deeper insights into deformation mechanisms, micro-computed tomography (μCT) has been employed to visualise and quantify internal structural changes during the compression of closed-cell aluminium foams [41]. This technique has facilitated detailed analyzes of pore collapse and crack propagation, contributing to a fundamental understanding of foam behavior under load [42].

Beyond compression, extensive studies have investigated the mechanical response of various closed-cell foams under diverse loading conditions, including bending [43–47]. Similarly, Advanced pore morphology (APM) foams and APM-filled tubes have been

subjected to both compression [28] and bending tests [29], with in-situ geometric analyzis conducted to track deformation evolution [48].

The influence of loading rate on mechanical behavior has also been of considerable interest. High-strain-rate compression testing, utilising the split Hopkinson pressure bar (SHPB) apparatus, has been used to assess the dynamic response of closed-cell aluminium foams [49]. Studies employing powder guns have further extended the investigation of high-strain-rate behavior to both open-cell [43] and closed-cell foams [50] as well as auxetic structures [33,51], revealing rate-dependent phenomena such as inertial effects and material strengthening.

Furthermore, three-point bending tests have been instrumental in evaluating the flexural performance of foam-filled tubes [29,44,45], providing data on bending stiffness, energy absorption, and failure modes. Recent investigations have also explored the shear response of open-cell foams [52] and auxetic cellular structures [53], contributing to a more comprehensive understanding of their anisotropic mechanical behavior.

The combined use of these experimental techniques, complemented by advanced imaging and analyzis, allows for a thorough characterisation of the mechanical behavior of cellular metamaterials, providing critical data for the design and optimisation of these materials for diverse engineering applications.

3.2 Homogenised Computational Models

For computational modelling of closed-cell foam behavior, a simplified yet practical approach employed within Abaqus finite element (FE) software involves a homogenised material model, specifically the crushable foam model with volumetric hardening. Leveraging the axial symmetry of the experimental specimens, axisymmetric boundary conditions were applied, significantly reducing computational cost while maintaining accuracy. An explicit solver was utilised to capture the dynamic nature of foam deformation [50].

The crushable foam constitutive model parameters were determined through an optimisation algorithm, where the computational response was iteratively matched to the experimental quasi-static (Q-S) compression data (Figs. 2 and 3). This optimisation ensured that the model accurately represented the foam's behavior under low strain rate conditions. Subsequently, the optimised material model was employed for high strain rate (HSR) simulations, demonstrating a remarkable agreement with experimental HSR data (Fig. 2).

The difference between the experimental and computational results across quasi-static and high-strain rate regimes is noteworthy. The only observable discrepancy occurs at the initial stages of the HSR response, where the computational model fails to capture the initial stress peak observed experimentally. This stress peak, a direct consequence of the impact-induced collision in the experimental setup, represents a transient phenomenon characteristic of the initial impact phase. However, as demonstrated by the subsequent correlation between experimental and simulated data, this initial peak does not significantly influence the overall global deformation behavior of the foam [33]. The use of this simplified model allows for efficient simulations while still retaining the overall mechanical response of the closed-cell foam.

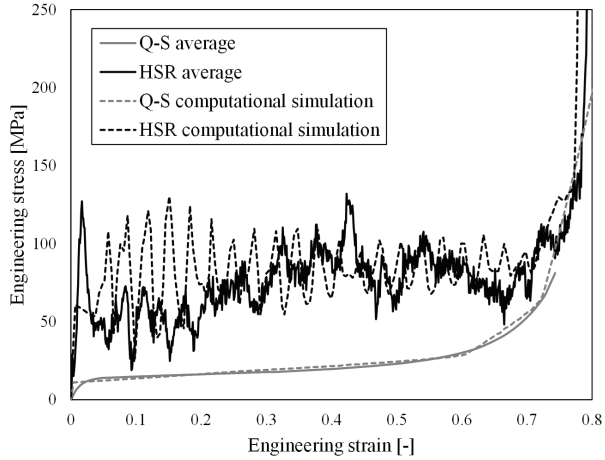

Fig. 2. Comparison between the computational and experimental results under Q-S at loading velocity 0.01 mm/s and HSR at loading velocity 250 m/s

Under quasi-static loading, the specimen exhibits a uniform deformation pattern, indicative of a homogeneous stress distribution throughout the sample (Fig. 3). In contrast, HSR loading induces a distinct shift in the deformation mode, characterised by localised deformation concentrated at the impact interface between the loading plate and the specimen. This localisation signifies the influence of inertial effects and stress wave propagation at high strain rates, leading to a non-uniform deformation profile. The observed difference in deformation patterns highlights the significant impact of loading rate on the material's mechanical response.

This can be further used to develop modern crash absorbers, where the validated FE models enable the development of new foam-filled auxetic panels with a tailored response, where different geometries, sheet thicknesses, densities and distributions of the foams can be virtually tested before fabrication. The deformation behavior of that

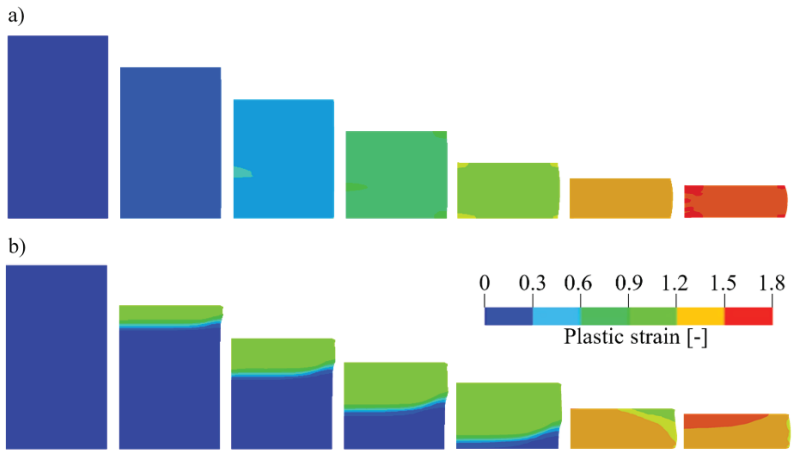

Fig. 3. Comparison between the Q-S and HSR deformation responses of closed-cell foam modelled with homogenised computational model (PEEQ - equivalent plastic strain)

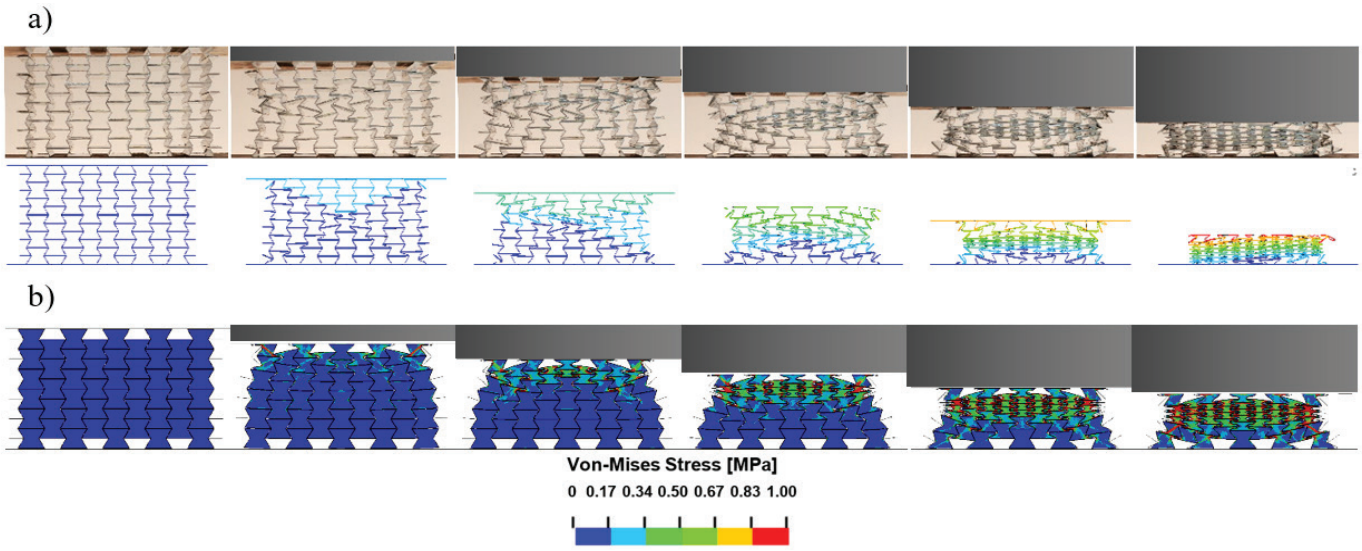

Fig. 4. Comparison of deformation behaviour of: a) empty, and b) foam-filled crash absorber [55]

kind of absorber is shown in Fig. 4b, where the crash absorber is filled with Polyurethane (PU) foam. This will hopefully lead to the application of modern crash absorption systems on newly built roads or blast protection elements in buildings [54].

3.3 Discrete Computational Models

Discrete computational models, while demanding higher computational resources than homogenised models, provide a more accurate representation of metamaterial deformation behavior. Beam finite elements are predominantly employed for strut-based cellular structures, such as open-cell foams and auxetic designs [11,56,57]. This approach allows for a detailed analyzis of individual strut deformation and interaction.

The generation of TPMS lattice computational models is facilitated by shell finite elements, utilising the MSLattice code [58] to define the fundamental lattice geometry. Subsequently, meshing is performed using PrePoMax software, and boundary conditions are defined within the LS-PrePost environment. Inverse parametric computational simulations are conducted to refine material parameters to account for manufacturing imperfections, particularly plate thickness variations. This indirect incorporation of imperfections enhances the model's fidelity.

The validation of these discrete TPMS lattice models involves comparing their mechanical response, specifically stress-strain relationships and deformation patterns, to quasi-static experimental data from reference [59] for each analyzed geometry and relative density. Furthermore, the computational deformation behavior is validated through comparisons with experimental observations recorded by high-definition video cameras. Figure 5 illustrates the comparative deformation behavior of diamond TPMS lattices with varying relative densities, demonstrating a high correlation between experimental and computational results.

Volume finite elements could also be employed for the discretisation of open-cell foams. Achieving an accurate geometric representation of fabricated aluminium open-cell foam samples necessitates high-resolution micro-computed tomography (μCT) scans. These high-resolution scans are crucial for capturing the intricate geometric details of the foam's porous structure and enabling precise segmentation of the metallic phase from the void space. This precise segmentation is essential for generating reliable volume finite element meshes and critical for accurate computational modelling of the foam's mechanical behavior.

4 OPTIMISATION AND DEVELOPMENT OF NEW GEOMETRIES

Validated computational models provide a powerful platform for developing and optimising novel metamaterials. For instance, topology optimisation techniques have been employed to generate

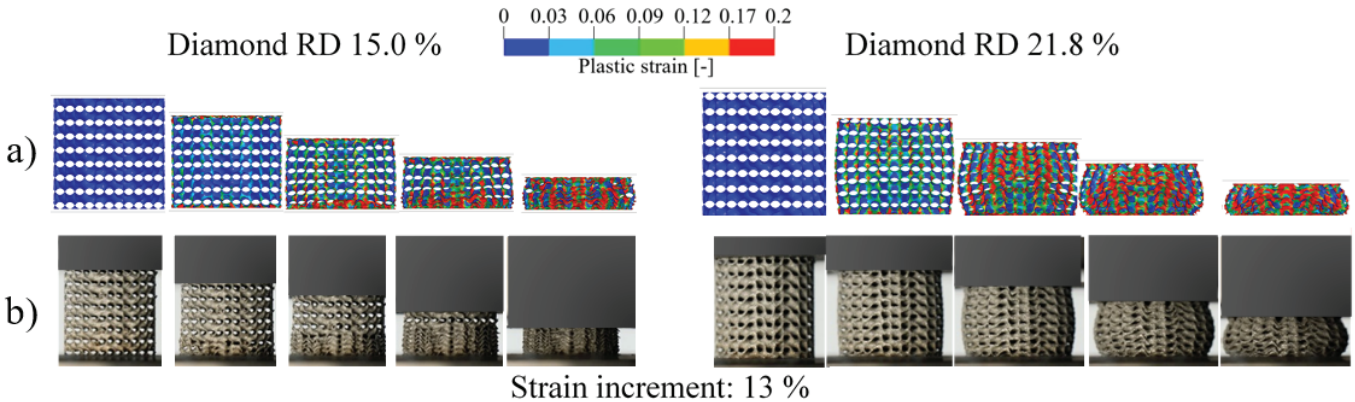

Fig. 5. Comparison between a) computational, and b) experimental results in case of TPMS structures modelled with shell finite elements

new auxetic geometries [60]. These studies used a 2D plane stress state simplification to model the auxetic structure, focusing on a single unit cell of the periodic structure as the optimisation domain. To further reduce the computational cost, only one-quarter of this unit cell was modelled, with the remaining portion represented by appropriate double symmetry boundary conditions. This simplification is justified by the prevalence of double symmetry in many existing auxetic structures, including re-entrant hexagons, symmetric chiral designs, and sinusoidal ligament configurations.

Triply periodic minimal surface (TPMS) lattices, inherently mathematical designs, benefit significantly from advanced fabrication methods. These methods enable the creation of graded or hybrid structures, where diverse TPMS geometries are strategically combined to enhance topological features and achieve desired properties. To accurately predict the mechanical behavior of additively manufactured uniform TPMS lattices made of stainless steel 316L under quasi-static and dynamic loading, a FE computational model was developed in LS-DYNA. This validated model was then used to simulate the performance of a newly designed hybrid TPMS cellular lattice featuring spatially varying gyroid and diamond cells in both longitudinal (the diamond and gyroid cells are on top of each other) and radial (the diamond and gyroid cells are concentric) directions (Fig. 6). Experimental validation of the fabricated hybrid lattices demonstrated a high correlation with the computational predictions [61], confirming the model's accuracy and predictive capabilities.

Building upon existing 3D conventional chiral unit cell designs [57,62], novel 3D axisymmetric chiral structures exhibiting negative and zero Poisson's ratios have been developed. This innovation involves mapping the conventional tetra-chiral unit cell into an axisymmetric space, resulting in a new class of 3D axisymmetric chiral architectures (ACS structures). These structures are fabricated using additive manufacturing techniques (Fig. 7), enabling the precise realisation of complex geometries.

Experimental compression tests were conducted to validate the computational modelling of these axisymmetric chiral structures. The resulting experimental data was used to refine and validate the computational models. Subsequently, these validated models were employed to evaluate the performance of new axisymmetric chiral structures featuring graded cell configurations.

The analyzis revealed that these newly developed axisymmetric structures demonstrate significantly enhanced mechanical properties compared to conventional 3D chiral structures (the SEA is comparable to structures made of titanium and much higher than in structures made of copper). This improvement is attributed to the optimised geometry and graded cell arrangements, offering potential advantages in applications requiring tailored mechanical responses.

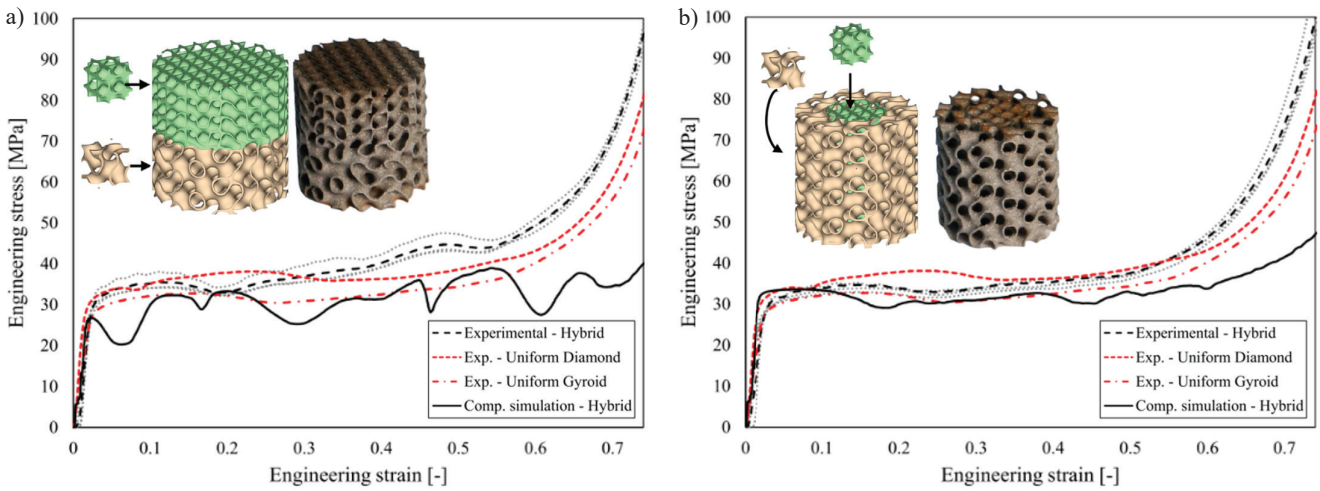

Fig. 6. Comparison between the computational and experimental results for: a) linear, and b) radial hybrid TPMS lattices [61]

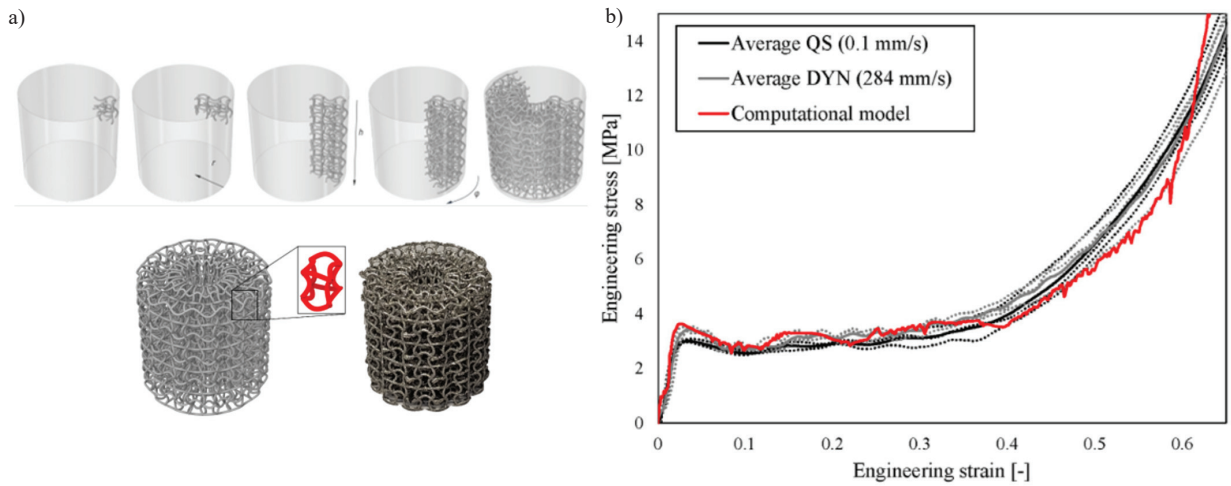

Fig. 7. Design of the: a) axisymmetric auxetic structure, and b) comparison between the computational and experimental results under quasi-static (QS) and dynamic (DYN) loading conditions [57]

5 CONCLUSIONS AND OUTLOOK

This review systematically examined cellular metamaterials' design, fabrication, and mechanical behavior across quasi-static and dynamic loading regimes. Figure 8 illustrates the SEA up to 50 % strain for these structures under compression loading to facilitate a comparative analyzis of energy absorption capabilities.

In Figure 8, darker shading corresponds to specimens with lower porosity within each analyzed group of cellular structures, while lighter shading indicates higher porosity specimens. A clear trend emerges: porosity and base material significantly influence SEA capacity. Lower porosity structures and stiffer base materials (e.g., high Young's modulus alloys) exhibit superior SEA.

Notably, closed-cell foams, TPMS structures, and UniPore structures exhibit consistently high SEA values at 50 % strain, suggesting their suitability for applications requiring efficient energy dissipation within this strain range. However, a key distinction arises with UniPore structures, where densification initiates at 50 % strain (Fig. 8). Consequently, the SEA reported for UniPore structures at this strain level represents their total SEA capacity, limiting their applicability in higher strain scenarios. In contrast, closed-cell foams (Fig. 8) and other analyzed cellular structures exhibit densification at significantly higher strain levels, enabling them to achieve greater total SEA capacity beyond 50 % strain. This demonstrates that while UniPore structures provide good energy absorption at low strain, closed-cell foams and TPMS structures outperform UniPore structures at strains >50 % due to delayed densification.

Furthermore, the observed differences in SEA capacity can be attributed to the distinct deformation mechanisms exhibited by these structures. Closed-cell foams, for example, undergo progressive cell wall buckling and crushing, leading to sustained energy absorption over a wider strain range. TPMS structures, with their complex interconnected geometries, exhibit a combination of bending, stretching, and buckling, contributing to their high SEA and controlled deformation behavior. UniPore structures, with their unidirectional pore channels, primarily deform through axial compression, leading to rapid densification and limited energy absorption at higher strains.

Understanding these deformation mechanisms and their influence on SEA capacity is crucial for the tailored design of cellular structures for specific applications. For instance, materials with high SEA at high strain rates are essential for occupant protection in automotive crashworthiness. In aerospace applications, lightweight structures with high SEA are desirable for impact resistance and vibration damping. By leveraging the insights gained from experimental and computational analyzes, researchers can optimise the design of cellular metamaterials to meet the stringent demands of various engineering applications, driving innovation in transportation, construction, and biomedical engineering.

Future research directions encompass expanded shear and high-strain-rate testing protocols for anisotropic metamaterials and integrating thermal/electrical conductivity into TPMS designs for innovative applications. We also envisage that we will accelerate the discovery of novel architectures using machine learning and AI-driven optimisation.

Computational simulations have emerged as an indispensable tool for the preliminary evaluation of novel cellular designs and for gaining a deeper understanding of the complex deformation behavior exhibited by various cellular structures. This article has showcased a spectrum of computational approaches, ranging from simplified and computationally efficient homogenised models to intricate and time-intensive discrete models employing volume finite elements to represent the entire cellular architecture.

The ongoing advancement of computational power and software capabilities heralds a significant evolution in computational modelling. Specifically, the implementation of mesoscale modelling approaches holds immense promise, enabling the incorporation of fabrication defects and microstructural features into simulations. This enhanced level of detail will lead to more precise virtual prediction capabilities, allowing researchers to accurately anticipate the deformation behavior of cellular metamaterials under diverse loading conditions. Consequently, the optimisation of their mechanical response will become more efficient and reliable, facilitating the development of high-performance cellular materials tailored to specific engineering applications.

Furthermore, the integration of machine learning and artificial intelligence techniques into computational modelling workflows will further accelerate the design and optimisation process. These techniques can be used to perform parametric studies, predict trends, and optimise geometries based on the simulation results. The use of these techniques will lead to faster development times and higher-performing materials.

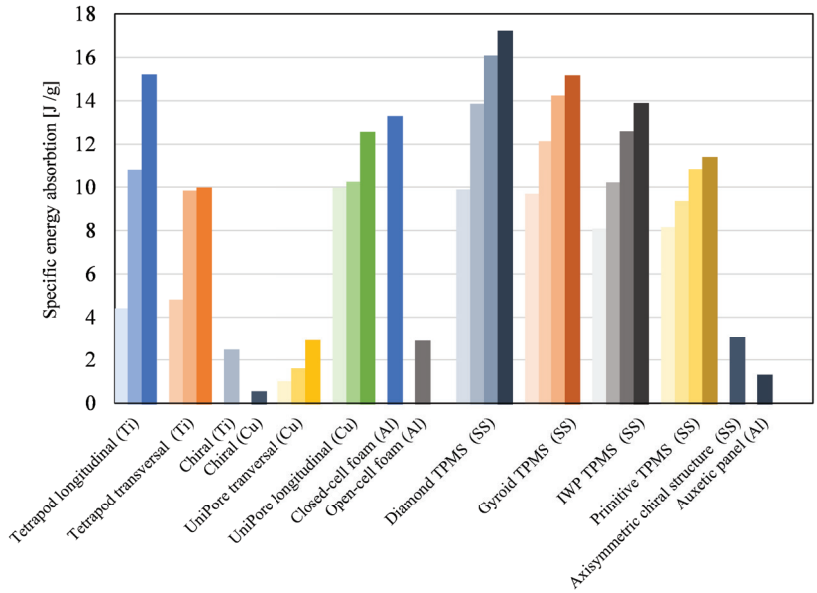

Fig. 8. Comparison of SEA for different cellular metamaterials made from different base materials (Ti-titanium, Cu-copper, Al-aluminium, SS-stainless steel)

This work lays the foundation for the design of multifunctional metamaterials with application-specific performance characteristics. Future research will explore fatigue behavior, adaptive structures, and integration with sensing technologies. The modelling tools and methodologies established here can be used to accelerate innovation in structural materials across a broad spectrum of industries, including aerospace, automotive, defence, and biomedical engineering.

References

[1] Gibson, L.J., Ashby, M.F. *Cellular Solids: Structure and Properties*, Cambridge University Press, Cambridge (1997) **DOI:10.1017/CBO9781139878326**.

[2] Banhart, J. Light-metal foams - History of innovation and technological challenges. *Adv Eng Mater* 15 82-111 (2013) **DOI:10.1002/adem.201200217**.

[3] Vesenjak, M., Fiedler, T., Ren, Z., Öchsner, A. Behaviour of syntactic and partial hollow sphere structures under dynamic loading. *Adv Eng Mater* 10 185-191 (2008) **DOI:10.1002/adem.200700325**.

[4] Ashby, M.F., A. Evans, Fleck, N.A., L.J. Gibson, L.J., Hutchinson, J.W., Wadley, H.N.G. *Metal Foams: A Design Guide*. Elsevier Science, Burlington (2000) **DOI:10.1016/S0261-3069(01)00049-8**.

[5] Lehmhus, D., Vesenjak, M., de Schampheleire, S., Fiedler, T. From stochastic foam to designed structure: Balancing cost and performance of cellular metals, *Materials (Basel)* 10 922 (2017) **DOI:10.3390/ma10080922**.

[6] Körner, C. Additive manufacturing of metallic components by selective electron beam melting - a review. *Int Mater Rev* 61 361-377 (2016) **DOI:10.1080/09506608.2016.1176289**.

[7] Surjadi, J.U., Gao, L., Du, H., Li, X., Xiong, X., Fang, N.X., Lu, Y. Mechanical metamaterials and their engineering applications. *Adv Eng Mater* 21 1800864 (2019) **DOI:10.1002/adem.201800864**.

[8] Gado, M.G., Al-Ketan, O., Aziz, M., Al-Rub, R.A., Ookawara, S. Triply periodic minimal surface structures: Design, fabrication, 3D printing techniques, state-of-the-art studies, and prospective thermal applications for efficient energy utilization, *Energy Technol* 2301287 (2024) **DOI:10.1002/ente.202301287**.

[9] Ulbin, M., Vesenjak, M., Borovinšek, M., Duarte, I., Higa, Y., Shimojima, K., Ren, Z. Detailed analysis of closed-cell aluminum alloy foam internal structure changes during compressive deformation. *Adv Eng Mater* 20 1800164 (2018) **DOI:10.1002/adem.201800164**.

[10] Zheng, Z., Yu, J., Wang, C., Liao, S., Liu, Y. Dynamic crushing of cellular materials: A unified framework of plastic shock wave models. *Int J Impact Eng* 53 29-43 (2013). **DOI:10.1016/j.ijimpeng.2012.06.012**.

[11] Novak, N., Vesenjak, M., Ren, Z. Computational simulation and optimization of functionally graded auxetic structures made from inverted tetrapods. *Phys Status Solidi B* 254 (2017) **DOI:10.1002/pssb.201600753**.

[12] Fíla, T., Koudelka, P., Falta, J., Zlámal, P., Rada, V., Adorna, M., et al. Dynamic impact testing of cellular solids and lattice structures: Application of two-sided direct impact Hopkinson bar. *Int J Impact Eng* 148 (2021) **DOI:10.1016/j.ijimpeng.2020.103767**.

[13] Novak, N., Borovinšek, M., Vesenjak, M., Wormser, M., Körner, C., Tanaka, S., et al. Crushing behavior of graded auxetic structures built from inverted tetrapods under impact. *Phys Status Solidi B* 256 1800040 (2018) **DOI:10.1002/pssb.201800040**.

[14] Mieszala, M., Hasegawa, M., Guillonneau, G., Bauer, J., Raghavan, R., Frantz, C., et al. Micromechanics of amorphous metal/polymer hybrid structures with 3D cellular architectures: Size effects, buckling behavior, and energy absorption capability. *Small* 13 1602514 (2017) **DOI:10.1002/smll.201602514**.

[15] Al-Ketan, O., Rezgui, R., Rowshan, R., Du, H., Fang, N.X., Abu Al-Rub, R.K. Microarchitected stretching-dominated mechanical metamaterials with minimal surface topologies. Adv Eng Mater 20 1800029 (2018) **DOI:10.1002/adem.201800029**.

[16] Kolken, H.M.A., Fontecha Garciam, A., Du Plessis, A., Rans, C., Mirzaali, M.J., Zadpoor, A.A. Fatigue performance of auxetic meta-biomaterials. *Acta Biomater* (2021) **DOI:10.1016/j.actbio.2021.03.015**.

[17] Borovinšek, M., Vesenjak, M., Jože, M., Ren, Z. Computational reconstruction of scanned aluminum foams for virtual testing. *J Serbian Soc Comput Mech* 2 (2008) 16-28.

[18] Duarte, I., Krstulović-Opara, L., Dias-de-oliveira, J., Vesenjak, M. Axial crush performance of polymer-aluminium alloy hybrid foam filled tubes. *Thin-Walled Struct* 138 124-136 (2019) **DOI:10.1016/j.tws.2019.01.040**.

[19] Vesenjak, M., Veyhl, C., Fiedler, T., Analysis of anisotropy and strain rate sensitivity of open-cell metal foam. *Mater Sci Eng A* 541 105-109 (2012) **DOI:10.1016/j.msea.2012.02.010**.

[20] Duarte, I., Vesenjak, M., Vide, M.J. Automated continuous production line of parts, *Metals (Basel)* 9 (2019) 531 **DOI:10.3390/met9050531**.

[21] Duarte, I., Vesenjak, M., Krstulović-Opara, L., Compressive behaviour of unconstrained and constrained integral-skin closed-cell aluminium foam. *Compos Struct* 154 231-238 (2016) **DOI:10.1016/j.compstruct.2016.07.038**.

[22] Duarte, I., Vesenjak, M., Krstulović-Opara, L., Ren, Z. Static and dynamic axial crush performance of in-situ foam-filled tubes. *Compos Struct* 124 128-139 (2015) **DOI:10.1016/j.compstruct.2015.01.014**.

[23] Hokamoto, K., Vesenjak, M., Ren, Z. Fabrication of cylindrical uni-directional porous metal with explosive compaction. Mater Lett 137 323-327 (2014) **DOI:10.1016/j.matlet.2014.09.039**.

[24] Nishi, M., Oshita, M., Ulbin, M., Vesenjak, M., Ren, Z., Hokamoto, K. Computational analysis of the explosive compaction fabrication process of cylindrical uni-directional porous copper. *Met Mater Int* 24 1143-1148 (2018) **DOI:10.1007/s12540-018-0059-x**.

[25] Vesenjak, M., Hokamoto, K., Matsumoto, S., Marumo, Y., Ren, Z. Uni-directional porous metal fabricated by rolling of copper sheet and explosive compaction. Mater Lett 170 39-43 (2016) **DOI:10.1016/j.matlet.2016.01.143**.

[26] Stöbener, K., Lehmhus, D., Avalle, M., Peroni, L., Busse, M. Aluminum foam-polymer hybrid structures (APM aluminum foam) in compression testing. *Int J Solids Struct* 45 5627-5641 (2008) **DOI:10.1016/j.ijsolstr.2008.06.007**.

[27] Ulbin, M., Borovinšek, M., Higa, Y., Shimojima, K., Vesenjak, M., Ren, Z. Internal structure characterization of AlSi7 and AlSi10 advanced pore morphology (APM) foam elements. Mater Lett 136 416-419 (2014) **DOI:10.1016/j.matlet.2014.08.056**.

[28] Duarte, I., Vesenjak, M., Krstulović-Opara, L., Ren, Z. Compressive performance evaluation of APM (Advanced Pore Morphology) foam filled tubes. *Compos Struct* 134 409-420 (2015) **DOI:10.1016/j.compstruct.2015.08.097**.

[29] Vesenjak, M., Duarte, I., Baumeister, J., Göhler, H., Krstulović-Opara, L., Ren, Z. Bending performance evaluation of aluminium alloy tubes filled with different cellular metal cores. *Compos Struct* 234 111748 (2020) **DOI:10.1016/j.compstruct.2019.111748**.

[30] Biasetto, L., Franchin, G., Elsayed, H., Boschetti, G., Huang, K., Colombo, P. Direct ink writing of cylindrical lattice structures: A proof of concept. *Open Ceram* 7 100139 (2021) **DOI:10.1016/j.oceram.2021.100139**.

[31] Bronder, S., Adorna, M., Fíla, T., Koudelka, P,. Falta, J., Jiřroušek, O., Jung, A. Hybrid auxetic structures: Structural optimization and mechanical characterization. *Adv Eng Mater* 23 2001393 (2021) **DOI:10.1002/adem.202001393**.

[32] Novak, N., Vesenjak, M., Ren, Z. Auxetic cellular materials - a Review. *Stroj Vestn-J Mech E* 62 485-493 (2016) **DOI:10.5545/sv-jme.2016.3656**.

[33] Novak, N., Hokamoto, K., Vesenjak, M., Ren, Z. Mechanical behaviour of auxetic cellular structures built from inverted tetrapods at high strain rates. *Int J Impact Eng* 122 83-90 (2018) **DOI:10.1016/j.ijimpeng.2018.08.001**.

[34] Novak, N., Starčevič, L., Vesenjak, M., Ren, Z. Blast response study of the sandwich composite panels with 3D chiral auxetic core. *Compos Struct* 210 167-178 (2019) **DOI:10.1016/j.compstruct.2018.11.050**.

[35] Schwerdtfeger, J., Heinl, P., Singer, R.F., Körner, C. Auxetic cellular structures through selective electron beam melting. *Phys Status Solidi B* 247 269-272 (2010) **DOI:10.1002/pssb.200945513**.

[36] Körner, C., Liebold-Ribeiro, Y. A systematic approach to identify cellular auxetic materials. *Smart Mater Struct* 24 025013 (2014) **DOI:10.1088/0964-1726/24/2/025013**.

[37] Novak, N., Krstulović, L., Ren, Z., Vesenjak, M. Mechanical properties of hybrid metamaterial with auxetic chiral cellular structure and silicon filler. *Compos Struct* 234 111718 (2020) **DOI:10.1016/j.compstruct.2019.111718**.

[38] Kapfer, S.C., Hyde, S.T., Mecke, K., Arns, C.H., Schröder-Turk, G.E., Minimal surface scaffold designs for tissue engineering *Biomaterials* 32 6875-6882 (2011) **DOI:10.1016/j.biomaterials.2011.06.012**.

[39] Diachenko, S.V., Balabanov, S.V., Sychov, M.M., Litosov, G.E., Kiryanov, N.V. The impact of the geometry of cellular structure made of glass-filled polyamide on the energy-absorbing properties of design elements. *Strojn Vest-J Mech E* 70 607-619 (2024) **DOI:10.5545/sv-jme.2024.975**.

[40] Al-Ketan, O., Rowshan, R., Abu Al-Rub, R.K.R. Topology-mechanical property relationship of 3D printed strut, skeletal, and sheet based periodic metallic cellular materials. *Addit Manuf* 19 167-183 (2018) **DOI:10.1016/j.addma.2017.12.006**.

[41] Peroni, L., Avalle, M., Peroni, M. The mechanical behaviour of aluminium foam structures in different loading conditions. *Int J Impact Eng* 35 644-658 (2008) **DOI:10.1016/j.ijimpeng.2007.02.007**.

[42] Tomažinčič, D., Nečemer, B., Vesenjak, M., Klemenc, J. Low-cycle fatigue life of thin-plate auxetic cellular structures made from aluminium alloy 7075-T651. *Fatigue Fract Eng Mater Struct* 42 1022-1036 (2019) **DOI:10.1111/ffe.12966**.

[43] Duarte, I., Krstulović-Opara, L., Vesenjak, M., Characterisation of aluminium alloy tubes filled with aluminium alloy integral-skin foam under axial compressive loads. *Compos Struct* 121 154-162 (2015) **DOI:10.1016/j.compstruct.2014.11.003**.

[44] Duarte, I., Vesenjak, M., Krstulović-Opara, L. Dynamic and quasi-static bending behaviour of thin-walled aluminium tubes filled with aluminium foam. *Compos Struct* 109 48-56 (2014) **DOI:10.1016/j.compstruct.2013.10.040**.

[45] Duarte, I., Vesenjak, M., Krstulović-Opara, L., Anžel, I., Ferreira, J.M.F.F. Manufacturing and bending behaviour of in situ foam-filled aluminium alloy tubes. *Mater Des* 66 532-544 (2015) **DOI:10.1016/j.matdes.2014.04.082**.

[46] Taherishargh, M., Vesenjak, M., Belova, I.V., Krstulović-Opara, L., Murch, G.E., Fiedler, T. In situ manufacturing and mechanical properties of syntactic foam filled tubes. Mater Des 99 356-368 (2016) **DOI:10.1016/j.matdes.2016.03.077**.

[47] Duarte, I., Krstulović-Opara, L., Vesenjak, M. Axial crush behaviour of the aluminium alloy in-situ foam filled tubes with very low wall thickness. *Compos Struct* 192 184-192 (2018) **DOI:10.1016/j.compstruct.2018.02.094**.

[48] Borovinšek, M., Vesenjak, M., Higa, Y., Shimojima, K. Ren, Z. Characterization of geometrical changes of spherical advanced pore morphology (APM) foam elements during compressive deformation, *Materials (Basel)* 12 1088 (2019) **DOI:10.3390/ma12071088**.

[49] Islam, M.A., Brown, A.D., Hazell, P.J., Kader, M.A., Escobedo, J.P., Saadatfar, M. et al. Mechanical response and dynamic deformation mechanisms of closed-cell aluminium alloy foams under dynamic loading. *Int J Impact Eng* 114 111-122 (2018) **DOI:10.1016/j.ijimpeng.2017.12.012**.

[50] Novak, N., Vesenjak, M., Duarte, I., Tanaka, S., Hokamoto, K., Krstulović-Opara, L. et al. Compressive behaviour of closed-cell aluminium foam at different strain rates. *Materials (Basel)* 12 4108 (2019) **DOI:10.3390/ma12244108**.

[51] Novak, N., Vesenjak, M., Tanaka, S., Hokamoto, K. Ren, Z. Compressive behaviour of chiral auxetic cellular structures at different strain rates. *Int J Impact Eng* 141 103566 (2020) **DOI:10.1016/j.ijimpeng.2020.103566**.

[52] Novak, N., Duncan, O., Allen, T., Alderson, A., Vesenjak, M., Ren, Z. Shear modulus of conventional and auxetic open-cell foam. Mech Mater 157 103818 (2021) **DOI:10.1016/j.mechmat.2021.103818**.

[53] Novak, N., Krstulović-Opara, L., Ren, Z., Vesenjak, M. Compression and shear behaviour of graded chiral auxetic structures. *Mech Mater* 148 103524 (2020) **DOI:10.1016/j.mechmat.2020.103524**.

[54] Al-Rifaie, H., Sumelka, W. Auxetic damping systems for blast vulnerable structures. in Voyiadjis, G.Z. (ed.) *Handbook of Damage Mechanics*. Springer, New York. 1-23 (2020) **DOI:10.1007/978-1-4614-8968-9_71-1**.

[55] Novak, N., Al-Rifaie, H., Airoldi, A., Krstulović-Opara, L., Łodygowski, T., Ren, Z., Vesenjak, M. Quasi-static and impact behaviour of foam-filled graded auxetic panel. *Int J Impact Eng* 178 104606 (2023) **DOI:10.1016/j.ijimpeng.2023.104606**.

[56] Novak, N., Vesenjak, M., Krstulović-Opara, L., Ren, Z. Mechanical characterisation of auxetic cellular structures built from inverted tetrapods. *Compos Struct* 196 96-107 (2018) **DOI:10.1016/j.compstruct.2018.05.024**.

[57] Novak, N., Mauko, A., Ulbin, M., Krstulović-Opara, L., Ren, Z., Vesenjak, M., Development and characterisation of novel three-dimensional axisymmetric chiral auxetic structures. *J Mater Res Technol* 17 (2022) 2701-2713 **DOI:10.1016/j.jmrt.2022.02.025**.

[58] Al-Ketan, O., Abu Al-Rub, R.K. MSLattice: A free software for generating uniform and graded lattices based on triply periodic minimal surfaces. *Mater Des Process Commun* 3 205 (2021) **DOI:10.1002/mdp2.205**.

[59] Novak, N., Al-Ketan, O., Krstulović-Opara, L., Rowshan, R., Al-Rub, R.K.A., Vesenjak, M., Ren, Z. Quasi-static and dynamic compressive behaviour of sheet TPMS cellular. *Compos Struct* 266 113801 (2021) **DOI:10.1016/j.compstruct.2021.113801**.

[60] Borovinšek, M., Novak, N., Vesenjak, M., Ren, Z., Ulbin, M. Designing 2D auxetic structures using multi-objective topology optimization. *Mater Sci Eng A* 795 139914 (2020) **DOI:10.1016/j.msea.2020.139914**.

[61] Novak, N., Al-Ketan, O., Borovinšek, M., Krstulović-Opara, L., Rowshan, R., Vesenjak, M., Ren, Z. Development of novel hybrid TPMS cellular lattices and their mechanical characterisation. *J Mater Res Technol* 15 1318-1329 (2021) **DOI:10.1016/j.jmrt.2021.08.092**.

[62] Vesenjak, M., Novak, N., Ren, Z. *Axisymmetric Chiral Auxetic Structure*, EP21197296.3, 2021.

Acknowledgements *The authors acknowledge the Slovenian Research Agency's financial support of national research programme funding No. P2-0063 and basic research project No. J2-60049.*

Received 2025-04-23, revised: 2025-06-09, accepted 2025-08-19 *as Review Scientific Paper 1.02.*

Data Availability *The data that support the findings of this study are available from the corresponding author upon reasonable request.*

Author Contribution *Nejc Novak: Conceptualisation, Formal analysis, Investigation, Methodology, Writing - original draft; Matej Vesenjak: Supervision, Investigation, Methodology, Writing – review & editing; Zoran Ren: Supervision, Funding Acquisition, Writing – review & editing.*

Celostni razvoj, simulacije in eksperimentalna validacija naprednih celičnih metamaterialov

Povzetek *Celični metamateriali nudijo vrhunske lastnosti za inženirstvo, medicino in obrambo, vendar njihov prehod v industrijsko uporabo otežujejo izzivi pri razvoju, izdelavi in karakterizaciji. Ta pregled ponuja povzetek 20 let napredka na področju celičnih struktur, od pen z odprtimi celicami do struktur s trojno periodičnimi minimalnimi površinami (TPMS). Predstavlja nove tehnike izdelave (npr. eksplozijsko varjenje za strukture UniPore) in prikazuje validirane računalniške modele za optimizacijo gradiranih avksetičnih in hibridnih TPMS metamaterialov. Študija kaže, da na absorpcijo energije vplivata predvsem poroznost in osnovni material, pri čemer se zaprto-celične pene in TPMS strukture izkažejo bolje kot druge geometrije. Dodajalne tehnologije omogočajo prostorsko gradiranje s prilagojenimi mehanskimi lastnostmi. To delo pospešuje razvoj metamaterialov naslednje generacije za absorpcijo trkov, zaščito pred eksplozijami in biomedicinske naprave.*

Ključne besede *celične strukture, metamateriali, eksperimentalno testiranje, računalniške simulacije, mehanske lastnosti*

Fusion Behavior of Pure Magnesium During Selective Laser Melting

Snehashis Pal[1,2] ✉ – Matjaž Finšgar[1] – Jernej Vajda[3] – Uroš Maver[3] – Tomaž Brajlih[2] – Nenad Gubeljak[2] – Hanuma Reddy Tiyyagura[4] – Igor Drstvenšek[2]

1 Faculty of Chemistry and Chemical Engineering, University of Maribor, Slovenia
2 Faculty of Mechanical Engineering, University of Maribor, Slovenia
3 Faculty of Medicine, University of Maribor, Slovenia
4 Institute of Optoelectronics, Military University of Technology, Poland
✉ snehashis.pal@um.si.

Abstract *This study examined the melting behavior and flowability of pure magnesium during selective laser melting. The potential to increase product density was also investigated. Various combinations of manufacturing parameters were considered. The laser power was gradually increased in different machine runs, with different scanning speeds for each run to vary the energy density (ED). The laser power ranged from 10 W to 75 W, and the scanning speed ranged from 100 mm/s to 800 mm/s. Lower laser powers resulted in poor melting, while higher laser powers produced better melting, with significant differences even when the ED was the same. High EDs between 3.50 J/mm² and 4.30 J/mm² led to a lack of melting at low laser power and to an unstable melt pool with significant spattering at high laser power. In contrast, moderate EDs in the range of 1.40 J/mm² to 2.90 J/mm² resulted in better density at high laser power. Higher scanning speeds helped to avoid the formation of a dense smog cloud and provided sufficient energy in a short time with the aid of higher laser power. Therefore, increasing both laser power and scanning speed improved melting performance and increased product density. The relative product density ranged from 80 % to 96.5 %. Reducing the layer thickness from 50 µm to 25 µm at a laser power of 40 W resulted in the formation of a well-formed melt pool in some areas and significant melt spattering in others, which led to a deterioration in density.*

Keywords *magnesium, melt pool, laser power, scanning speed, layer thickness, support structure, laser powder bed fusion*

Highlights

- *The fusion and pore formation of Mg during the selective laser melting process were investigated.*
- *Higher energy density (ED) may cause a lack of melting than lower ED due to the high smog formation.*
- *Higher scanning speed with higher laser power can avoid the smog cloud and perform better fusion.*
- *Reducing the layer thickness from 50 µm to 25 µm led to improved melting or massive spattering.*

1 INTRODUCTION

Lightweight materials are essential for a range of applications, particularly in the automotive, aerospace, and electronics industries [1,2]. Reducing component weight can significantly improve overall performance and fuel efficiency [3]. In medical implants, especially for orthopedic applications, lightweight and biodegradable materials are vital [4,5]. Their lightness aids patient mobility, while biodegradability eliminates the need for a second surgery by allowing the implant to dissolve naturally in the body over time [6,7]. Magnesium (Mg) and its alloys are increasingly favored due to their properties, which meet these stringent requirements [8,9]. Mg is not only very light but also offers promising biodegradability and high biocompatibility [10,11]. Mg and Mg-alloys allow regulation of mechanical and corrosive properties, making them suitable for biomedical applications [12]. Furthermore, the mechanical properties of magnesium alloys are similar to those of bone, which is advantageous for orthopedic implants [13].

Despite these benefits, Mg has certain drawbacks, such as a lower melting point and higher reactivity to oxygen and moisture compared to other metals [14,15]. In various applications, proper handling and alloying are required to address these challenges [16,17]. Traditional manufacturing processes have limitations in this regard [18]. However, additive manufacturing (AM) processes offer much greater flexibility than conventional methods [19,20]. AM provides a protective environment for the manufacturing process and enables in-situ alloying, which is crucial when working with reactive materials like magnesium. It can transform complex computer-aided design (CAD) models into single or multiple products, supporting customization and intricate designs [21]. Selective laser melting (SLM), also known as laser powder bed fusion (LPBF), is one of the most popular metal AM technologies for manufacturing metal products [22].

SLM uses an inert gas to reduce the oxygen content in the process chamber, requiring a continuous flow of this gas to maintain the desired oxygen levels [23]. In this process, a laser melts the metal powder track by track and layer by layer [24,25]. The powder particles, typically with diameters of several dozen micrometers, build up the product layer by layer, with each layer usually being 20 to 100 micrometers thick [26,27]. Rapid heating, melting, mixing, and solidification occur during the fusion process in SLM [28,29]. Using Mg in SLM presents significant challenges due to its low melting and boiling points and high flammability [30]. Rapid heating can lead to vaporization and combustion of Mg [2]. The small temperature difference between the melting and boiling points causes the melt pool to become unstable [31]. Additionally, the lightweight nature of Mg poses a problem as it can be easily carried away by inert gas, leading to material loss and the formation of smog that obstructs the laser's operation [16]. These issues significantly affect the SLM

 DOI: 10.5545/sv-jme.2025.1381

process, as material loss from the action zone and smog formation hinder the laser's ability to function effectively [32].

To address these challenges, this study investigated the interactions between the laser and Mg, as well as the thermophysical properties of the melt pools and solidification during the SLM manufacturing process. There are several results in the literature on the density of Mg-alloys fabricated by SLM, but only a few studies focus on improving the density of pure Mg products. To our knowledge, and according to the report by Zeng et al. [33], there is no literature in which a relative density of 98 % was achieved for Mg parts produced by the SLM process. Therefore, in this study, the laser powers and scanning speeds were initially selected based on previous studies by Hu et al. [34] and Yang et al. [5]. Hu et al. [34] obtained the best relative height density of 96.13 % at a high energy density (ED) with a laser power and scanning speed of 90 W and 100 mm/s, respectively. On the other hand, Yang et al. [5] obtained useful results at laser powers and scanning speeds between 20 W to100 W and 100 mm/s to 900 mm/s. Therefore, this study started with a scanning speed of 100 mm/s and a laser power of 10 W to keep the ED within a suitable range. Observations and analyses from this initial phase served as a basis for selecting different combinations of laser power and scanning speed to further investigate these phenomena and achieve better metallurgical properties.

This comprehensive approach aimed to optimize the SLM process for Mg, focusing on understanding and mitigating issues related to rapid heating, material loss, and smog formation. By exploring the effects of different combinations of laser powers and scanning speeds, the study sought to enhance the metallurgical properties of the produced components, paving the way for more effective use of Mg in SLM processes.

2 METHODS AND MATERIALS

2.1 Material

The samples were produced using pure magnesium powder from Nanografi Nano Technology (Germany), and the manufacturing characteristics were analyzed. The spherical powder particles ranged in size from 35 µm to 50 µm, with 5 % of the particles outside this range. After production by centrifugal atomization, the powder was packaged in an inert gas environment. The powder was unsealed to fill the filling chamber after the oxygen concentration was reduced to less than 0.01 % using argon.

2.2 Machining Chamber

The manufacturing behavior was studied using the Arrow Metal Printing – LMP200 SLM machine supplied by Dentas, Slovenia. Argon was used to reduce the oxygen content in the chamber and to keep the O2 level below 10 ppm during sample production. An O2 sensor monitored and automatically adjusted the O2 level by adding argon to the machining chamber when it exceeded 10 ppm. As magnesium is very light, the processing environment contained Mg powder and its fumes. To remove these, the chamber gases were circulated and passed through a filter at a flow rate of 280 L/min. Before production runs began, the laser system was calibrated and a sensor monitored the current laser power. To maintain heat conduction and the material bond between the build plate and the support, the build plate was made of magnesium.

2.2 Support Structure

Several cubic test specimens measuring 6 mm × 6 mm × 6 mm were produced for each test condition. As magnesium has good thermal conductivity and a very high coefficient of thermal expansion (CTE of 26 × 10^{-6} K^{-1}), large thermal stresses and volume changes occur during the SLM process, causing the part to shrink, bend, and eventually self-destruct. Therefore, three types of support structures were used to hold the samples firmly. As shown in Fig. 1, fabrication of the specimens began with 2 mm high supports. In this study, a support structure typically used for the fabrication of stronger materials such as Ti-6Al-4V and AlSi10Mg was employed (see Fig. 1a). This support beam has a smaller diameter neck that facilitates separation of the fabricated part from the support beams. Twenty-five (5 × 5) support beams were placed under the 6 mm × 6 mm base of the cubes.

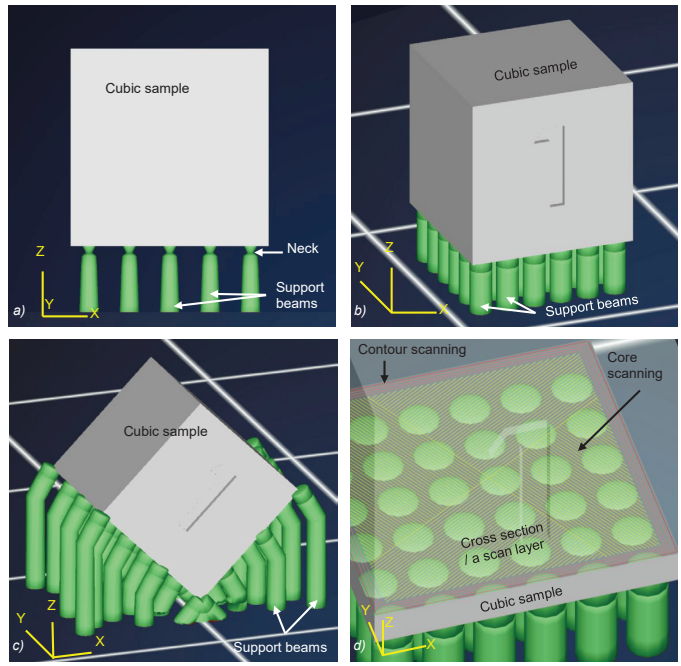

Fig. 1. Supports and scanning patterns; a) support beams with necks, b) cylindrical support beams, c) samples with different orientations, and d) scanning pattern

In this study, the effects of laser parameters at different layer thicknesses and their melting properties with existing supports were investigated. The manufacturing process is costly due to the use of argon and the risk that the failure of a single sample can cause the failure of several samples in the same build. If one sample fails, it can hinder the movement of the recoater, requiring the entire process to be stopped and restarted from the beginning. This research aimed to find a solution to the manufacturing problem when supports are present, as supports are often necessary for the actual production of the part. It is easier to remove samples from the build plate and prepare a smooth build plate again than to produce samples without support. Therefore, in addition to analyzing melting properties, the effect of support, including different support designs, is also examined and reported in this article.

Since the support beam with a neck was not able to prevent the piece from bending, cylindrical beams were used, as shown in Fig. 1b. The beams had diameters of 0.4 mm, with a 6 × 6 array of beams under the 6 mm × 6 mm base of the cubes. Although this support structure was sufficient to prevent most specimens from bending, some specimens still bent or detached from the supports after a few layers were fabricated.

As some specimens bent and moved away from the cylindrical support beams, the orientation of the specimens was changed, as shown in Fig. 1c. However, this orientation increased the bottom surface area, leading to a more uneven surface at the start of

fabrication. Although this support structure held the part firmly in place, the uneven shape and surface formation of the specimens led to the decision in this study to align the cubic specimens so that their base surface remained horizontal. Ultimately, cylindrical support beams are best suited to hold the part when the base of a cubic sample is horizontal.

2.3 Scanning Patterns

The scanning pattern consisted of four successive contours and a checkerboard core scanning pattern, as shown in Fig. 1d. As the area to be scanned for each layer was approximately 6 mm × 6 mm, four sub-squares were scanned in a checkerboard arrangement. Each square was scanned with multiple laser scan tracks, with a 50 % overlap between tracks. The diameter of the laser spot was 70 µm; therefore, the hatch spacing was 35 µm. A larger hatch spacing resulted in a lower product density. Two consecutive scanning tracks were scanned in opposite directions. The scanning tracks were rotated by 60° for successive layers during manufacture. The Yb:glass fiber laser was always focused perpendicular to the powder bed using a telecentric F-theta lens. The telecentric F-theta lens combines the flat-field focusing of a conventional F-theta lens with the vertical positioning of a telecentric lens for object space, ensuring the emerging laser beam is always perpendicular to the target surface across the entire scan field.

Since the diameter of the laser spot is 70 µm and the laser moves at high speed during scanning, which is typical for the SLM process, the space between successive hatches must be considered when measuring the ED. Therefore, the *ED* [J/mm²] can be defined as defined in Eq. (1), where *P*, *v*, and *h* denote the laser power [W], scanning speed [mm/s], and hatch distance [mm], respectively.

$$ED = \frac{P}{v \cdot h}. \quad (1)$$

2.4 Manufacturing Parameters

Laser power, scanning speed, and layer thickness were varied to investigate their effects on the fusion of pure Mg and the potential for sample fabrication. As Mg has low melting and boiling points, the experiments began with low laser power combined with four different scanning speeds. Thus, the ED varied with scanning speed, while laser power remained constant. Subsequently, the laser power was gradually increased from 10 W to 40 W, as shown in Table 1, and combined with four different scanning speeds. Consequently, the ED also changed, ranging from 0.95 J/mm² to 4.29 J/mm². The ED played a significant role in the melting process of Mg and was therefore considered an important fabrication parameter. The hatch distance and layer thickness were kept constant in the initial stage of the study at 35 µm and 50 µm, respectively. Three samples were fabricated for each testing condition.

The most important factor in determining the useful range of parameters is the density of the samples. The proportion of smog formation is also considered. With some parameters, a higher density product can be achieved, but smog formation can cause deterioration in melting at higher scan ranges. A high level of smog in the processing chamber causes the laser rays to be reflected more strongly by the airborne powder particles. Increased vapor also absorbs more of the laser energy, which ultimately prevents the laser beams from reaching the powder bed.

After observing and analyzing the fusion behavior and density results in the first step of the study, the laser power was increased in the second step while maintaining the scanning speeds listed in Table 2. Since higher laser power led to better fusion results and product densities, higher laser powers were selected to analyze their effects. However, scanning speed can also have a significant influence. Therefore, in the second step of the study, the most effective scanning speeds were combined with the increased laser powers. Although scanning speeds of 400 mm/s, 600 mm/s, and 800 mm/s at 40 W resulted in good densities, 400 mm/s, 500 mm/s, and 600 mm/s were chosen at laser powers of 55 W, 65 W, and 75 W, respectively, due to the high ED induction.

Table 1. Manufacturing parameters in the first step of the study

Sample number	Laser power [W]	Scanning speed [mm/s]	Hatch spacing [mm]	Layer thickness [mm]	ED [J/mm²]	Product density [g/cm³]	Relative density [%]
I-1	10	100	0.035	0.050	2.86	-	-
I-2	10	200	0.035	0.050	1.43	-	-
I-3	10	300	0.035	0.050	0.95	-	-
I-4	10	400	0.035	0.050	0.71	-	-
I-5	20	150	0.035	0.050	3.81	-	-
I-6	20	200	0.035	0.050	2.86	-	-
I-7	20	300	0.035	0.050	1.90	-	-
I-8	20	400	0.035	0.050	1.43	-	-
I-9	30	200	0.035	0.050	4.29	-	-
I-10	30	300	0.035	0.050	2.86	-	-
I-11	30	400	0.035	0.050	2.14	-	-
I-12	30	500	0.035	0.050	1.71	-	-
I-13	40	300	0.035	0.050	3.81	-	-
I-14	40	400	0.035	0.050	2.86	1.65	94.91
I-15	40	600	0.035	0.050	1.90	1.61	92.68
I-16	40	800	0.035	0.050	1.43	1.39	80.18

Table 2. Manufacturing parameters in the second step of the study

Sample number	Laser power [W]	Scanning speed [mm/s]	Hatch spacing [mm]	Layer thickness [mm]	ED [J/mm²]	Product density [g/cm³]	Relative density [%]
II-1	55	400	0.035	0.050	3.93	-	-
II-2	65	500	0.035	0.050	3.71	-	-
II-3	75	600	0.035	0.050	3.57	-	-

In the second step of the study, a large amount of smoke and smog was observed when using high laser power and relatively low scanning speed. The lower scanning speed resulted in a high ED. Consequently, the samples were not produced satisfactorily. Therefore, higher scanning speeds were used in the third step of the study to reduce the ED, while the laser power remained the same as in the previous step. These parameters are listed in Table 3.

Table 3. Manufacturing parameters in the third step of the study

Sample number	Laser power [W]	Scanning speed [mm/s]	Hatch spacing [mm]	Layer thickness [mm]	ED [J/mm²]	Product density [g/cm³]	Relative density [%]
III-1	55	700	0.035	0.050	2.24	1.65	94.96
III-2	65	700	0.035	0.050	2.65	1.67	95.95
III-3	75	750	0.035	0.050	2.86	1.68	96.51

Higher laser powers and their adjustable scanning speeds did not yield improved results. Therefore, the optimal laser power and scanning speeds identified in previous studies were used in the fourth step of the study, where a lower layer thickness was selected. As 800 mm/s at a laser power of 40 W resulted in low product density, a reduced scanning speed of 700 mm/s was chosen for this step, as shown in Table 4. These parameters were selected to observe

the effects of different layer thicknesses and the laser absorption characteristics of the powder bed and its top surface.

Table 4. Manufacturing parameters in the fourth step of the study

Sample number	Laser power [W]	Scanning speed [mm/s]	Hatch spacing [mm]	Layer thickness [mm]	ED [J/mm^2]	Product density [g/cm^3]	Relative density [%]
IV-1	40	400	0.035	0.025	2.86	1.54	88.66
IV-2	40	500	0.035	0.025	2.29	1.55	89.34
IV-3	40	600	0.035	0.025	1.90	1.55	89.16
IV-4	40	700	0.035	0.025	1.63	1.55	89.04

2.5 Analysis of Product Properties

The densities were measured on samples that were well fused and capable of providing accurate results. When ethanol was used as a liquid, Archimedes' principle was applied to determine the densities. The weight of each sample was measured in air and then while immersed in the liquid, with an error margin of ±0.0001 g, to calculate the density. The measurement was performed six times to improve the accuracy of the results. Three-dimensional images of the solid and pore zones of the materials were obtained using a ZEISS Xradia 620 Versa nano-computed tomography (nano-CT) scanner (Germany). The porosity of the samples was also observed with a scanning electron microscope (SEM) from Carl Zeiss (Germany), after the samples had been ground 1 mm from the vertical surface and then polished.

3 RESULTS AND DISCUSSION

3.1 Effect of Lower Laser Powers

The powder particles were not well fused at the low laser powers of 10 W and 20 W, even though the energy density was sufficient at lower scanning speeds. At a laser power of 30 W, the particles were adequately fused at scanning speeds of 200 mm/s and 300 mm/s; however, some layers were distorted and delaminated, as shown in Fig. 2. With a further increase in scanning speed to 400 mm/s and 500 mm/s at 30 W laser power, fusion did not occur. Therefore, the samples fabricated using 10 W to 30 W laser power were unsuitable for further studies such as density and porosity measurements.

There are several possible reasons for these results with 10 W to 30 W laser powers. The main reasons may be the low absorption of laser rays by the powder bed and the obstruction of the rays by the dense smog cloud. In laser–material interaction, most laser rays are typically reflected from the top surface of the powder layer [35]. Furthermore, magnesium is a shiny grey metal, which increases this reflection. The process is illustrated by the schematic diagram in Fig. 3a. Therefore, although the power was sufficient, only a small fraction of the laser rays was absorbed by the powder bed. After entering the powder bed, the rays are reflected multiple times within it [36]. The reflection and absorption are shown schematically in Fig. 3b. However, the low laser power of 10 W to 20 W was not sufficient to heat and melt the powder particles.

As the laser power increased to 30 W, the laser rays were sufficient to raise the temperature of the powder bed above 650 °C and melt the powder. Scanning speeds of 200 mm/s and 300 mm/s at 30 W laser power allowed enough time to melt the particles. Although melting occurred due to the greater number of laser rays penetrating the powder layer, as shown in Fig. 3b, the melt pool did not form sufficiently to agglomerate the layers and scan tracks. Therefore, it can be assumed that some areas were melted while others were not. As a result, some plate formation and shifting were observed, as shown in Fig. 2. The plates were shifted by the recoater movement. With a further increase in scanning speed, sintering among the powder particles occurred. Consequently, soft cubic samples were formed at scanning speeds of 400 mm/s and 500 mm/s. These were destroyed during powder removal and detachment from the support structures. Eventually, an increase in scanning speed resulted in better melting.

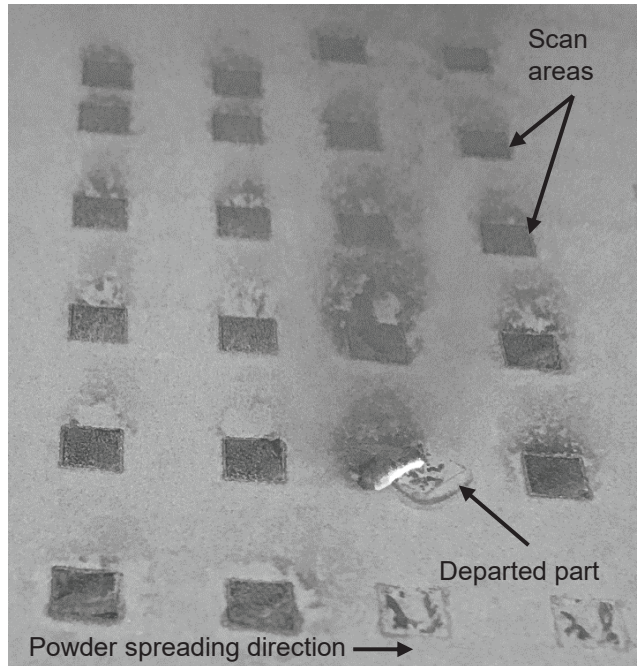

Fig. 2. A photograph during scanning

A large amount of smog was observed in the processing chamber during laser scanning. Although the smog was not detected by any sensor, only the observations made during production are discussed here. Smoke and particle detectors could provide more quantitative results and better control over the melting process. Therefore, it can be assumed that this smog also affects the amount of laser power reaching the powder bed. The smog formed from evaporated and combusted materials and powder particles [37,38]. As Mg has a low melting point and is prone to oxidation, it evaporated and burnt significantly. In addition, due to the cyclone effect above the action zone and the significantly low mass of Mg, the powder particles were easily lifted and mixed into the cyclone, as schematically represented in Fig. 3d. Moreover, powder explosions occurred in the powdered zone due to the expansion of inter-particle inert gas [37]. Consequently, a dense cloud formed above the action zone, with a high probability of impeding the laser from reaching the powder bed. At this point, higher laser power could escape this smog cloud. As a result, higher scanning speeds led to the formation of soft cubes at 30 W laser power.

A further increase in laser power to 40 W enabled the fabrication of some samples, whereas the lowest scanning speed of 300 mm/s did not produce any samples. At higher scanning speeds, however, some good cubes were formed with measurable densities. The laser power of 40 W delivered sufficient energy into the powder layer for good fusion to begin, as shown in Fig. 3c. As discussed, the lower scanning speed did not allow sufficient time to move forward to avoid the smog cloud. When the scanning speed increased to 400 mm/s, better melting occurred. Gradually increasing the scanning speed to 500 mm/s and 600 mm/s resulted in better melting than at 300 mm/s, even though the energy density was higher at the lower scanning speed.

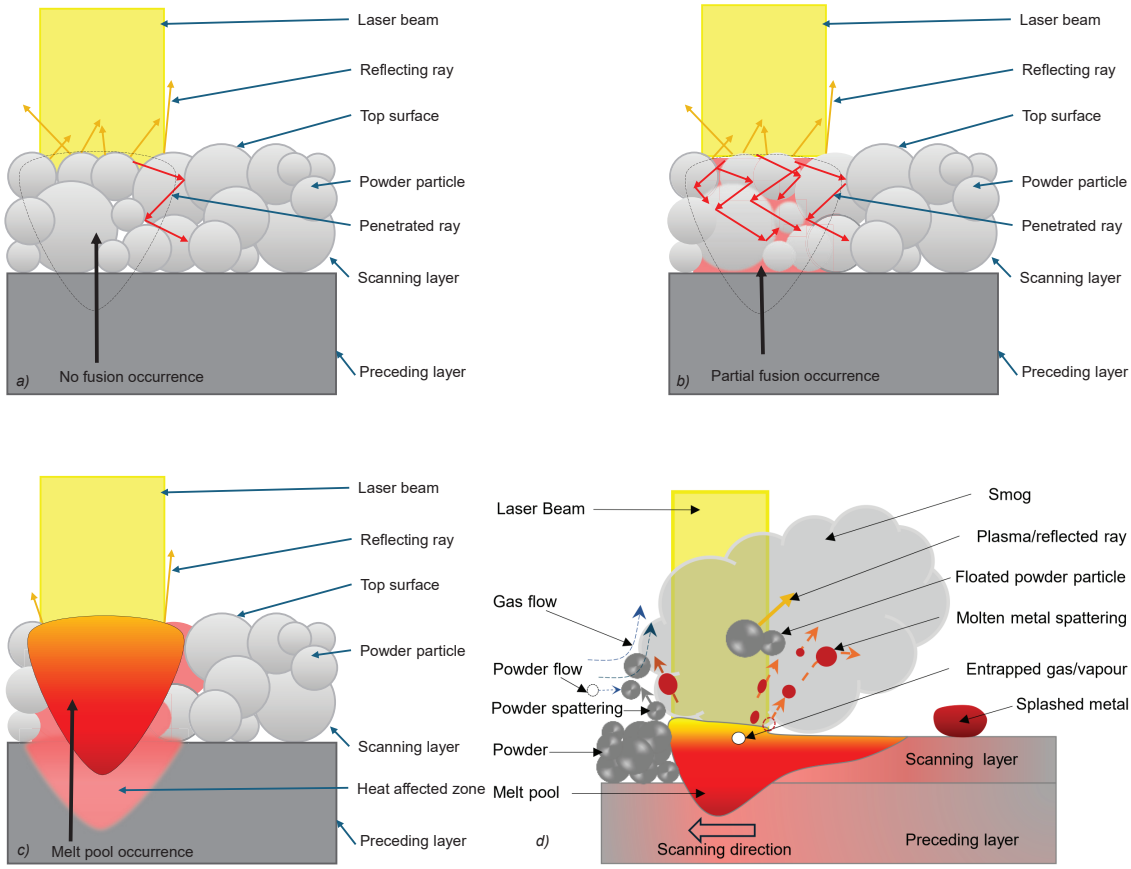

Fig. 3. Fusion characteristics; a) fusion with low laser power, b) fusion with medium laser power, c) melt pool formation with high laser power, and d) smog formation

However, the product density decreased at higher scanning speeds from 400 mm/s to 800 mm/s due to the significantly lower energy density.

There is also a possibility of high ED formation in the melt pool at a low scanning speed of 300 mm/s, which may cause instability in the melt pools and result in melt spattering [39], as shown in Fig. 3d. Additionally, trapped gas bubbles and metal vapor caused explosions in the melt pools [40]. This resulted in significant metal splashes, causing the action zones to lose material. Conversely, the splashed material fell onto the scan area and created some bumpy zones. The loss of material in one area led to an accumulation of powder particles in the subsequent layer at that location, resulting in a higher powder layer height. Consequently, the subsequent layer could not fuse well or form a uniform melt pool, as shown in the SEM images in Fig. 4. This led to insufficient bonding with the previous layer and the formation of a pore. To observe this phenomenon, the sample fabricated with 60 W laser power, 700 mm/s scanning speed, 0.035 mm hatch spacing, and 0.050 mm layer thickness is shown in Fig. 4.

Figure 4 shows that some layers are affected by the phenomena described above. These layers are significantly influenced by highly irregular melt pool and pore formation. Several of these layers are marked by two parallel lines in Fig. 4. These pores also influenced

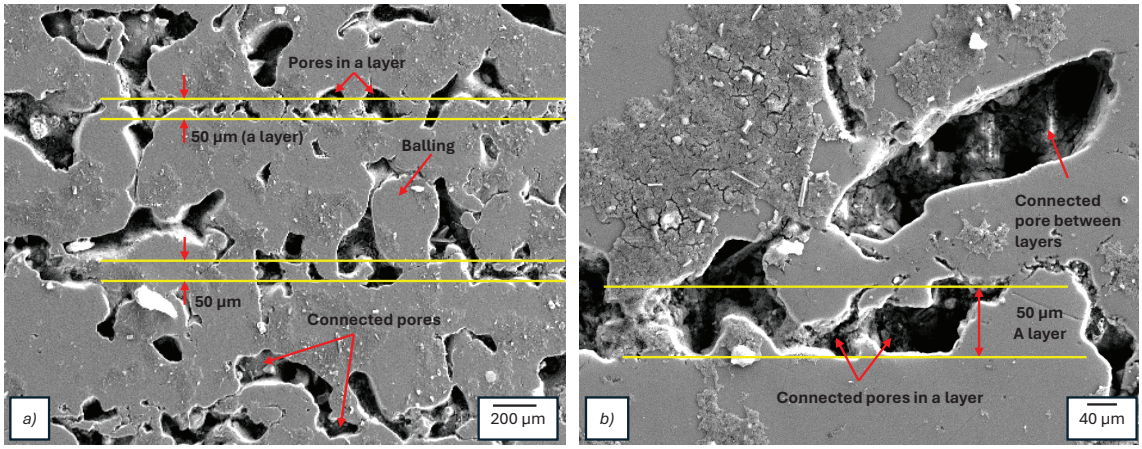

Fig. 4. Common pore characteristics of the samples; a) overall pore formation, with some layers exhibiting high pore content, and b) higher magnification image of the pores in a layer with high pore content

pore formation in subsequent layers. Some pores extended across several layers, forming connected pores between them. Additionally, part of the last scanned layer may exhibit uneven areas due to the deposition of spattered particles and the formation of spheres caused by the balling effect, as shown in Fig. 4a. As a result, this part had to be removed and displaced from the specific manufacturing location by the recoater movement. Ultimately, the combination of 40 W laser power and 300 mm/s scanning speed produced disorganized samples. Therefore, density was not determined for samples produced with these manufacturing parameters.

Comparing the effects of laser power between samples I-5 and I-13, it can be seen that despite the same high ED of 3.81 J/mm², no melting occurs in I-5, while high temperatures and significant spattering of molten metal occur in I-13. The heating rate (scanning speed) played an important role in the fusion mechanisms. Since the ED was very high, there is a high probability that strong vaporization began at the top of the powder bed. After the onset of vaporization, the penetration of the laser beam decreased due to obstruction by the vapor cloud, resulting in insufficient melting of sample I-5. When the scanning speed was increased at the same ED, the laser left the action zone after supplying higher energy in less time. This allowed for a higher probability of melting and a greater energy content in the melt pools. Therefore, a high ED led to high temperatures and a reduction in the viscosity of the melt pools, resulting in spattering of molten metal in sample I-13. To investigate these phenomena in more detail, the part with the lowest density was analyzed using a nano-CT scan and explained with the help of Fig. 5.

Comparing samples I-1, I-6, I-10, and I-14, which have the same ED (2.86 J/mm²) but different laser powers (10 W, 20 W, 30 W, and 40 W), it can be observed that while 10 W to 30 W could not produce a good sample, 40 W resulted in the highest density. Even the significantly low ED of 1.43 J/mm² was sufficient to fabricate a good sample with a laser power of 40 W. In contrast, the same ED of 1.43 J/mm² and higher EDs could not produce a sample when the laser powers were below 40 W. It is therefore clear that lower laser powers perform worse due to insufficient absorption of the laser rays by the powder bed. Here, a good sample refers to one that is well formed with a cubic structure and whose product density can be measured, while other samples are not well formed or fused and do not form a cube.

Since I-16 has the lowest product density among the well-formed samples, this research has taken this sample into account to study the formation and behavior of melt pools. To investigate the effects of the laser parameters and the formation of melt pools, the product with the lowest density was selected. This can provide an indication of the melting mechanism, even if the product was not well manufactured. Therefore, this sample was analyzed with nano-CT scanning and is shown in Fig. 5. The light grey and dark grey areas represent the solid and porous regions, respectively. Successive images are taken at intervals of 5 µm through the vertical direction, which is the build-up direction of the sample. Examining these images, it can be seen that the pores are interconnected. It is also clear that they have irregular shapes, and their sizes vary accordingly.

Based on the pores of sample I-16 and the consolidated patches, certain melting characteristics of this sample can be determined. This indicates that the track was not laid down evenly throughout. There are occasional fluctuations in the melt pools of the track [25]. The pores also varied in size in each direction. Consequently, the density varied both between the layers and between the tracks. For example, the three strips -1, -2, and -3 marked in Fig. 5 can be considered to investigate their melting properties. The width of the stripes is 100 µm, and these stripes can be visualized in all images. However, the region in strip-1 has a higher density than the region in strip-3, indicating that fusion was better in some areas, while in others less material was obtained, and pores were formed. Although this is one possible cause for such melting properties and the formation of porosity, other factors may also contribute. It is an inherent characteristic of SLM that some action zones melt well and form a good melt pool, while others may suffer from lack of melting or spattering of molten metal. This can also be influenced by the different size distribution of the powder particles and the varying powder packing from place to place.

The shape of a melt pool can be understood from any dot (with a small surrounding area) placed on a figure panel in Fig. 5. For example, a red dot is placed on each panel representing the same scan area. Since the following images represent the 5 µm above in the build direction, the same area or location shows the variation of the melt pool in the vertical direction. However, the red dot originated from a pore area that eventually filled with material as it moved in the vertical direction. Similarly, one can visualize and examine the pore and solid zones, which provides insight into the melting properties. As mentioned earlier, these porosities result from evaporation, combustion, material loss, material spattering, and laser shielding by smog [32]. On the other hand, a large number of round patches of solid material in the cross-section of the sample match the section size of the powder particles and could indeed be unmelted powder particles. Better stabilization of the melt pools is required to maximize density. A higher laser power may be preferable to achieve the desired melt pool properties.

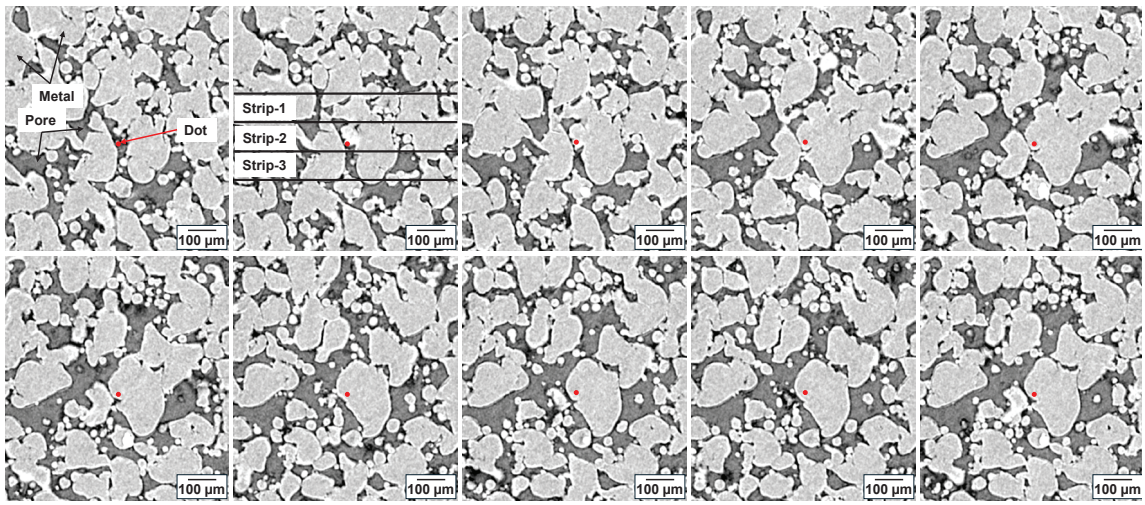

Fig. 5. Nano-CT scanned images showing pores and metallic zones

3.2 Effects of High Laser Powers

As the increase in laser power supported an improved fusion process during manufacturing and resulted in higher product density, the laser power was further increased in the second stage of the study. However, since scanning speed significantly affects the fusion process, the speeds were selected based on findings from the previous study. High ED also led to increased fume and smog generation in the manufacturing chamber. Therefore, to maintain the ED, a scanning speed of 400 mm/s to 600 mm/s was chosen for the second stage. It was observed that higher laser power produced better melt pools; for example, 40 W was more effective than 30 W, although both generated considerable smog. Additionally, although increased vaporization from the top of the powder bed is possible, the resulting vapor also impedes effective laser penetration. Therefore, higher laser power at the outset can lead to excessive energy deposition. The proportion of laser rays reaching the powder bed decreases as vaporization begins. Accordingly, higher laser power can result in improved melt pool formation. With this in mind, a higher laser power was selected for further investigation.

The densities of some samples in the second stage are lower than those prepared with 40 W laser power for samples I-14 to I-16, and some are not well fabricated. Therefore, the densities of these samples cannot be reported. The second stage of the experiment showed strong smog formation in the fabrication chamber. The smog reflected the laser rays even above the intended scanning layer. As a result, insufficient energy was delivered in many areas, which also contributed to a high level of pore formation. However, due to the high laser power, a significant amount of Mg was burnt and vaporized. As previously mentioned, this also created a cyclone above the powder bed, which drew in many Mg powder particles and formed a protective shield. This shield prevented the laser from penetrating the powder layer. Many sparks were observed with the increased number of powder particles in the cyclone, as shown in Fig. 3d. It can be assumed that the laser struck the particles and caused the sparks. As a result, the amount of melting was insufficient to form a good melt pool. Additionally, the formation of smoke, the vaporization of the metal, and the removal of powder particles caused metal loss from the action zone [38]. Consequently, the density decreased, and the samples were damaged during production.

3.3 Effects of High Laser Powers with Higher Scanning Speeds

Since lower scanning speeds combined with higher laser powers resulted in a high ED, the scanning speed was increased in the third step of the study. As a result, the samples were well prepared, as shown in Fig. 6a. Additionally, the densities of the samples increased in this step, as shown in Fig. 6b. When the laser power was lowest at 55 W (in sample III-1) in the third step, the resulting density was low (1.62 g/cm³). However, when the laser power was increased to 65 W and the scanning speed was kept constant at 700 mm/s, the resulting density in sample III-2 increased to 1.63 g/cm³. In sample III-3, which was fabricated with a higher laser power (75 W) and scanning speed (750 mm/s), the density was even higher.

Since a high ED occurred in sample II-1 due to the lower scanning speed compared to sample III-3, a large amount of smog was generated. When the scanning speed was increased at the same laser power, the ED decreased, and fusion and melt pool formation improved. This resulted in successful sample fabrication with high density. The smog and fumes were much lower compared to the

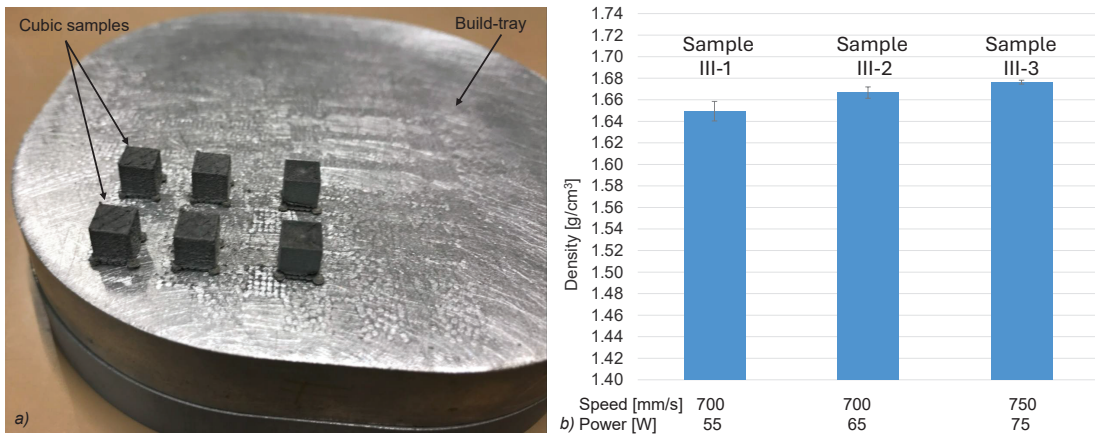

Fig. 6. Samples and density results in the third step of the study; a) photograph of the cubic samples on the build tray; and b) densities

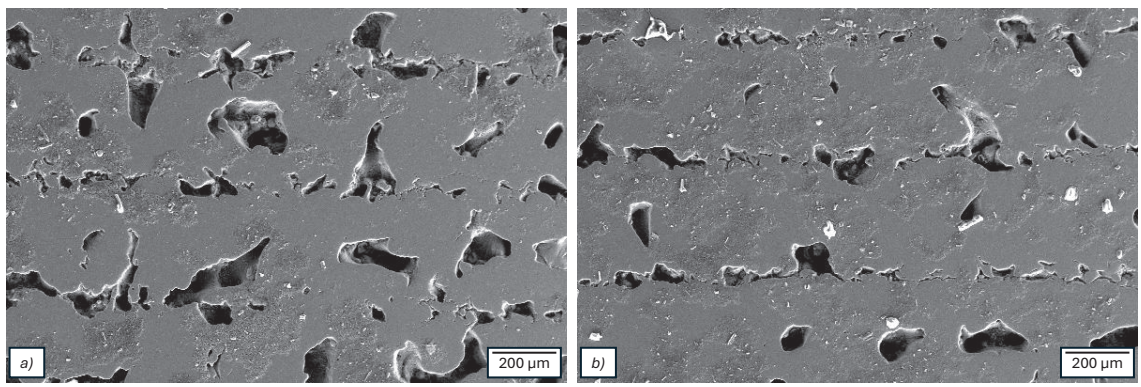

Fig. 7. Difference in porosity; a) sample fabricated with a laser power of 70 W and a scanning speed of 750 mm/s; and b) sample fabricated with a laser power of 80 W and a scanning speed of 800 mm/s

second step of the study. However, increasing the laser power from 55 W to 65 W improved the quality of the melt pools, as indicated by the increase in density. This was confirmed by SEM examinations of other samples produced with a laser power of 70 W and a scanning speed of 750 mm/s, and with a laser power of 80 W and a scanning speed of 800 mm/s, while keeping the other parameters constant. The SEM images of the vertical cross-sections of these samples are shown in Fig. 7.

The SEM images in Fig. 7 clearly show that the quality of the melt pools improved as the laser power increased, reducing gaps between tracks and decreasing pores. Therefore, higher laser power combined with a slightly higher scanning speed helped to melt the powder more effectively and form a better melt pool in sample III-3 compared to sample II-3. As the EDs in the third step of the study were within an appropriate range, less fume and smog were observed.

3.4 Effect in Decreasing the Layer Thickness

By reducing the layer thickness to 25 µm, the density results were slightly lower than those for samples with a higher layer thickness of 50 µm. In the fourth step of the study, the densities were almost the same for all samples, as shown in Fig. 8. Smog formation was almost identical to that of samples fabricated with the same laser power (40 W) in the first step of the study, except at the lowest scanning speed (300 mm/s). As the scanning speed in the fourth step was within the optimal range, smog formation was low. This was due to the uniform effects on the top of the powder layer. As the layer thickness decreased, the total energy input to the powder layer increased, which also increased the thermal energy in the melt pools. This led to a lower viscosity of the melt, resulting in instability of the melt pools and spattering of molten metal [39]. Therefore, the action zone lost more material than the previous samples produced at 50 µm. As a result, the overall density of the samples decreased.

The melting mechanism and the effects of smog can be visualized by examining pore formation in one of the samples, which was produced with a layer thickness of 25 µm. Fig. 8b to d shows the nano-CT images of sample IV-1, which are vertical cross-sectional planes arranged sequentially at intervals of several hundred micrometers. The proportion of pores is visible in these images, indicating that they contain a low, medium, and high proportion of pores, respectively. The density therefore varied significantly within the same scanning layer. In some areas, there was good fusion and stabilized melt pool formation, while in others there was low laser energy or an unstable melt pool with high thermal energy. The smog obstructed the laser, resulting in low energy deposition on the powder bed. As the energy decreased, evaporation also decreased, causing the laser to fall onto the powder bed. When the melt pools accumulate higher energy, the viscosity of the melt may decrease, which can lead to destabilization of the melt pools. This can eventually result in spattering and material loss.

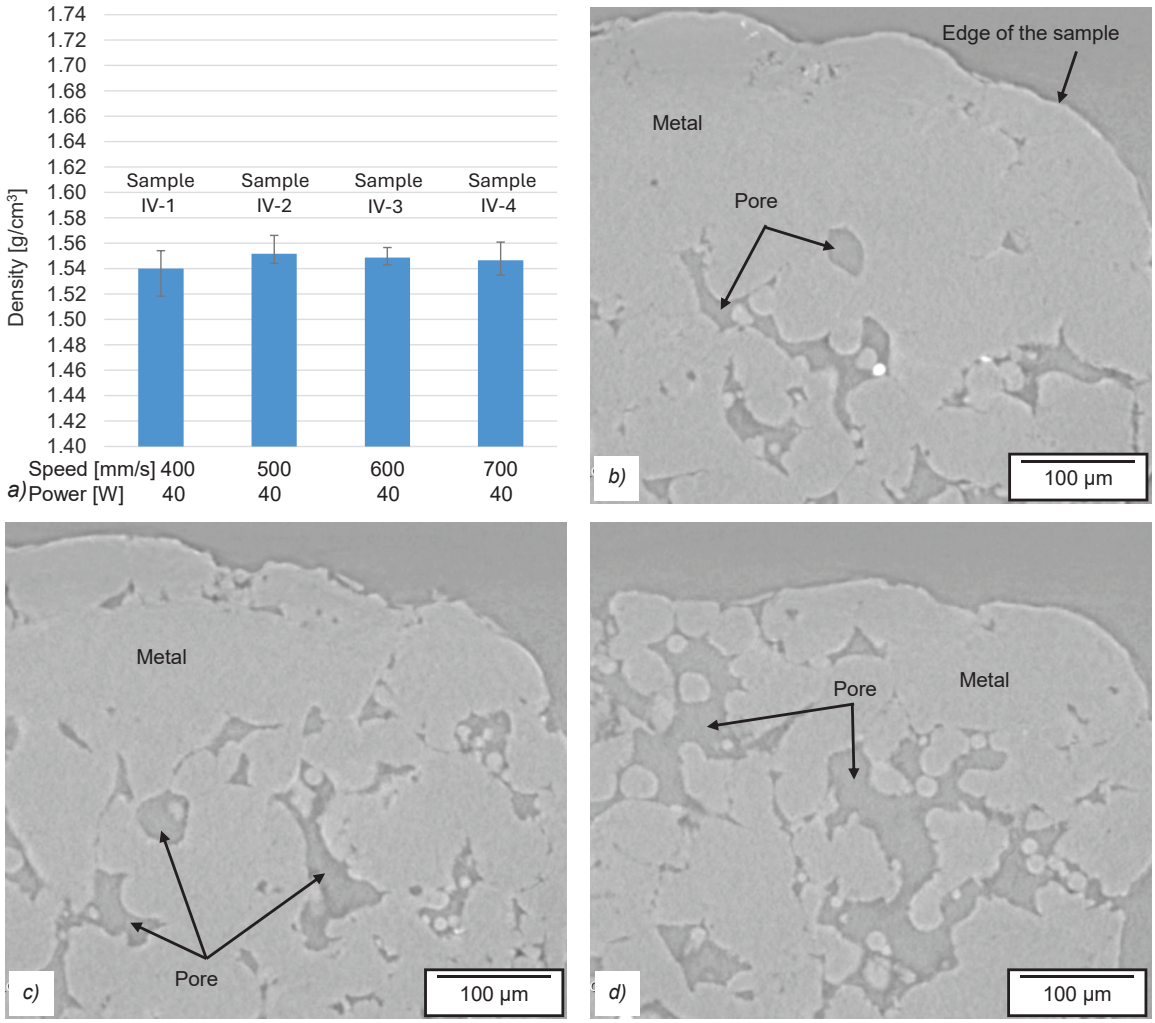

Fig. 8. Densities and porosities of the sample fabricated in the fourth step of the study; a) densities; b) low-porosity site; c) medium-porosity site, and d) high-porosity site

4 CONCLUSIONS

This article investigates and describes the melting properties of magnesium during selective laser melting. The following characteristics are observed and demonstrated using density measurements, as well as images from nano-CT scans and SEM of the samples.

Low laser power is insufficient to melt the powder particles and connect the layers and tracks, even when the ED is the same as with higher laser power. At the same ED, the scanning speed must be increased, which is the main advantage in melting the powder and forming a melt pool. This is due to the ability to avoid the smog clouds formed by the vaporization of materials at the top of the powder bed. The forward movement after the penetration of sufficient energy within a short time results in better fusion. A slower scanning speed with lower power does not provide enough energy before a dense cloud forms and prevents the laser beams from reaching the powder bed.

A high ED causes melt pool instability due to the explosion of melt pools and spattering, resulting in insufficient material and the formation of voids or the inability to form a product. Although reducing the layer thickness enables better melting in some areas, in other areas there is instability in the melt pools, which also worsens the overall density.

References

[1] Zhang, W, Xu, J. Advanced lightweight materials for Automobiles: A review. *Mater Des* 221 110994 (2022) **DOI:10.1016/j.matdes.2022.110994**.

[2] Ng, C.C., Savalani, M., Man, H.C. Fabrication of magnesium using selective laser melting technique. *Rapid Prototyp J* 17 479-490 (2011). **DOI:10.1108/13552541111184206**.

[3] Blanco, D., Rubio, E.M., Lorente, R., Sáenz-Nuño, M.A. Lightweight structural materials in open access: Latest trends. *Materials* 14 6577 (2021) **DOI:10.3390/ma14216577**.

[4] Tiyyagura, H.R., Mohan, T., Pal, S., Mohan, M.K. Surface modification of Magnesium and its alloy as orthopedic biomaterials with biopolymers. Balakrishnan, P., Sreekala, M.S., Sabu T. (eds) *Fundamental Biomaterials: Metals*, Elsevier 197-210 (2018) **DOI:10.1016/B978-0-08-102205-4.00009-X**.

[5] Yang, Y., Wu, P., Lin, X., Liu, Y., Bian, H., Zhou, Y., et al. System development, formability quality and microstructure evolution of selective laser-melted magnesium. *Virtual Phys Prototyp* 11 173-181 (2016) **DOI:10.1080/17452759.2016.1210522**.

[6] Fard, M.G., Sharifianjazi, F., Kazemi, S.S., Rostamani, H., Bathaei, M.S. Laser-based additive manufacturing of magnesium alloys for bone tissue engineering applications: From chemistry to clinic. *J Manuf Mater Process* 6 158 (2022) **DOI:10.3390/jmmp6060158**.

[7] Prakasam, M., Locs, J., Salma-Ancane, K., Loca, D., Largeteau, A., Berzina-Cimdina, L. Biodegradable materials and metallic implants-A review. *J Funct Biomater* 8 44 (2017) **DOI:10.3390/jfb8040044**.

[8] Manakari, V., Parande, G., Gupta, M. Selective laser melting of magnesium and magnesium alloy powders: A review. *Metals* 7 2 (2017) **DOI:10.3390/met7010002**.

[9] Prasad, S.V.S., Prasad, S.B., Verma, K., Mishra, R.K., Kumar, V., Singh, S. The role and significance of Magnesium in modern day research-A review. *J Magnes Alloy* 10 1-61 (2022) **DOI:10.1016/j.jma.2021.05.012**.

[10] Zagórski, I. Surface roughness evaluation of AZ31B magnesium alloy after rough milling using tools with different geometries. *Stroj Vestn-J Mech E* 70 355-368 (2024) **DOI:10.5545/sv-jme.2023.885**.

[11] Staiger, M.P., Pietak, A.M., Huadmai, J., Dias, G. Magnesium and its alloys as orthopedic biomaterials: A review. *Biomaterials* 27 1728-1734 (2006) **DOI:10.1016/j.biomaterials.2005.10.003**.

[12] Kirkland, N.T., Birbilis, N., Staiger, M.P. Assessing the corrosion of biodegradable magnesium implants: A critical review of current methodologies and their limitations. *Acta Biomater* 8 925-936 (2012) **DOI:10.1016/j.actbio.2011.11.014**.

[13] Gu, X.N., Zheng, Y.F. A review on magnesium alloys as biodegradable materials. *Front Mater Sci China* 4 111-115 (2010) **DOI:10.1007/s11706-010-0024-1**.

[14] Munsch, M. Laser additive manufacturing of customized prosthetics and implants for biomedical applications. Brandt, M. (ed.) *Laser Additive Manufacturing* 399-420 (2017) **DOI:10.1016/B978-0-08-100433-3.00015-4**.

[15] Persaud-Sharma, D., Mcgoron, A. Biodegradable magnesium alloys: A review of material development and applications. *J Biomim Biomater Tissue Eng* 12 25-39 (2012) **DOI:10.4028/www.scientific.net/JBBTE.12.25**.

[16] Gray, J.E., Luan, B. Protective coatings on magnesium and its alloys - A critical review. *J Alloys Compd* 336 88-113 (2002) **DOI:10.1016/S0925-8388(01)01899-0**.

[17] Kiani, F., Wen, C., Li, Y. Prospects and strategies for magnesium alloys as biodegradable implants from crystalline to bulk metallic glasses and composites-A review. *Acta Biomater* 103 1-23 (2020) **DOI:10.1016/j.actbio.2019.12.023**.

[18] DebRoy, T., Wei, H.L., Zuback, J.S., Mukherjee, T., Elmer, J.W., Milewski, J.O., et al. Additive manufacturing of metallic components - Process, structure and properties. *Prog Mater Sci* 92 112-224 (2018) **DOI:10.1016/j.pmatsci.2017.10.001**.

[19] Gotlih, J., Karner, T., Belšak, R., Ficko, M., Berus, L., Brajlih, T., et al. Design and manufacturing of conformal cooling channels for injection molding: A review. Karabegovic, I., Kovačević, A., Mandzuka, S. (eds.) *Lect Notes Networks Syst* 687 156-169 (2023) Cham Springer **DOI:10.1007/978-3-031-31066-9_17**.

[20] Drstvenšek, I., Zupanič, F., Bončina, T., Brajlih, T., Pal, S. Influence of local heat flow variations on geometrical deflections, microstructure, and tensile properties of Ti-6Al-4 V products in powder bed fusion systems. *J Manuf Process* 65 382-396 (2021) **DOI:10.1016/j.jmapro.2021.03.054**.

[21] Pal, S., Gubeljak, N., Hudák, R., Lojen, G., Rajťúková, V., Brajlih, T., et al. Evolution of the metallurgical properties of Ti-6Al-4V, produced with different laser processing parameters, at constant energy density in selective laser melting. *Results Phys* 17 103186 (2020) **DOI:10.1016/j.rinp.2020.103186**.

[22] Pal, S., Bončina, T., Lojen, G., Brajlih, T., Švara Fabjan, E., Gubeljak, N., et al. Fine martensite and beta-grain variational effects on mechanical properties of Ti-6Al-4V while laser parameters change in laser powder bed fusion. *Mater Sci Eng A* 892 146052 (2024) **DOI:10.1016/j.msea.2023.146052**.

[23] Kjer, M.B., Pan, Z., Nadimpalli, V.K., Pedersen, D.B. Experimental analysis and spatial component impact of the inert cross flow in open-architecture laser powder bed fusion. *J Manuf Mater Process* 7 143 (2023) **DOI:10.3390/jmmp7040143**.

[24] Wischeropp, T.M., Emmelmann, C., Brandt, M., Pateras, A. Measurement of actual powder layer height and packing density in a single layer in selective laser melting. *Addit Manuf* 28 176-183 (2019) **DOI:10.1016/j.addma.2019.04.019**.

[25] Shrestha, S., Chou, K. Residual heat effect on the melt pool geometry during the laser powder bed fusion process. *J Manuf Mater Process* 6 153 (2022) **DOI:10.3390/jmmp6060153**.

[26] Babič, M., Kovačič, M., Fragassa, C., Šturm, R. Selective laser melting: A novel method for surface roughness analysis. *Stroj Vestn-J Mech E* 70 313-324 (2024) **DOI:10.5545/sv-jme.2024.1009**.

[27] Pal, S., Lojen, G., Hudak, R., Rajtukova, V., Brajlih, T., Kokol, V., et al. As-fabricated surface morphologies of Ti-6Al-4V samples fabricated by different laser processing parameters in selective laser melting. *Addit Manuf* 33 101147 (2020) **DOI:10.1016/j.addma.2020.101147**.

[28] Patil, V.V., Mohanty, C.P., Prashanth, K.G. Parametric optimization of selective laser melted 13Ni400 maraging steel by Taguchi method. *J Manuf Mater Process* 8 52 (2024) **DOI:10.3390/jmmp8020052**.

[29] Pal, S., Lojen, G., Drstvenšek, I. Microstructural phase transformation evolution of Ti-6Al-4V alloy in selective laser melting process. *Metall Mater Eng Congr South-East Eur* 26 (2017).

[30] Ahmadi, M., Tabary, S.A.A.B., Rahmatabadi, D., Ebrahimi, M.S., Abrinia, K., Hashemi, R. Review of selective laser melting of magnesium alloys: advantages, microstructure and mechanical characterizations, defects, challenges, and applications. *J Mater Res Technol* 19 1537-1562 (2022) **DOI:10.1016/j.jmrt.2022.05.102**.

[31] Shen, H., Yan, J., Niu, X. Thermo-fluid-dynamic modeling of the melt pool during selective laser melting for AZ91D magnesium alloy. *Materials* 13 4157 (2020) **DOI:10.3390/ma13184157**.

[32] Ding, R., Yao, J., Du, B., Li, K., Li, T., Zhao, L., et al. Effect of shielding gas volume flow on the consistency of microstructure and tensile properties of 316l manufactured by selective laser melting. *Metals* 11 205 (2021) **DOI:10.3390/met11020205**.

[33] Zeng, Z., Salehi, M., Kopp, A., Xu, S., Esmaily, M., Birbilis, N. Recent progress and perspectives in additive manufacturing of magnesium alloys. *J Magnes Alloy* 10 1511-1541 (2022) **DOI:10.1016/j.jma.2022.03.001**.

[34] Hu, D., Wang, Y., Zhang, D., Hao L., Jiang, J., Li, Z., et al. Experimental Investigation on selective laser melting of bulk net-shape pure Magnesium. *Mater Manuf Process* 30 1298-1304 (2015) **DOI:10.1080/10426914.2015.1025963**.

[35] Zhang, D., Wang, W., Guo, Y., Hu, S., Dong, D., Poprawe, R., et al. Numerical simulation in the absorption behavior of Ti6Al4V powder materials to laser

energy during SLM. *J Mater Process Technol* 268 25-36 (2019) **DOI:10.1016/j.jmatprotec.2019.01.002**.

[36] Tolochko, N.K., Mozzharov, S.E., Yadroitsev, I.A., Laoui, T., Froyen, L., Titov, V.I., et al. Balling processes during selective laser treatment of powders. *Rapid Prototyp J* 10 78-87 (2004) **DOI:10.1108/13552540410526953**.

[37] Yadav, P., Rigo, O., Arvieu, C., Le Guen, E., Lacoste, E. In situ monitoring systems of the SLM process: On the need to develop machine learning models for data processing. *Crystals* 10 524 (2020) **DOI:10.3390/cryst10060524**.

[38] Shan, X., Pan, Z., Gao, M., Han, L., Choi, J.P., Zhang, H. Multi-physics modeling of melting-solidification characteristics in laser powder bed fusion process of 316L stainless steel. Materials 17 946 (2024) **DOI:10.3390/ma17040946**.

[39] Li, Z., Li, H., Yin, J., Li, Y., Nie, Z., Li, X., et al. A Review of spatter in laser powder bed fusion additive manufacturing: in situ detection, generation, effects, and countermeasures. *Micromachines* 13 1366 (2022) **DOI:10.3390/mi13081366**.

[40] Yu, G., Gu, D., Dai, D., Xia, M., Ma, C., Chang, K. Influence of processing parameters on laser penetration depth and melting/re-melting densification during selective laser melting of aluminum alloy. *Appl Phys A Mater Sci Process* 122 891 (2016) **DOI:10.1007/s00339-016-0428-6**.

Acknowledgements *The authors thank the Slovenian Research Agency for funding the research (Grant Nos. GC-0007 P2-0118, P2-0137, P2-0157 J1-2470, J1-2471, J1-4416, J7-4636, J7-50226, J7-50227, J1-60015 and J7-60120). The project is co-financed by the Republic of Slovenia, the Ministry of Education, Science and Sport, and the European Union through the European Regional Development Fund.*

Received 2025-05-09, revised 2025-09-16, 2025-10-13, accepted 2025-10-13 *as Original scientific paper 1.01.*

Data availability *The data that support the findings of this study are available from the corresponding author upon reasonable request.*

Author contribution *Snehashis Pal: Conceptualization, Methodology, Formal analysis, Investigation, Visualization, Writing—original draft; Matjaž Finšgar: Formal analysis, Investigation, Writing—review and editing; Jernej Vajda: Formal analysis, Investigation; Uroš Maver: Formal analysis, Investigation; Tomaž Brajlih: Formal analysis, Investigation; Nenad Gubeljak: Formal analysis, Investigation; Hanuma Reddy Tiyyagura: Conceptualization, Formal analysis, Investigation, Writing—review and editing, Supervision; Igor Drstvenšek: Conceptualization, Formal analysis, Investigation, Writing—review and editing, Supervision.*

Proces spajanja čistega magnezija med selektivnim laserskim taljenjem

Abstract *V raziskavi smo proučevali obnašanje taljenja čistega magnezija in pretočnost njegove taline med selektvinim laserskim taljenjem. Raziskali smo tudi vpliv različnih kombinacij procesnih parametrov na povečanje gostote izdelka. Moč laserja smo postopoma povečevali in pri tem spreminjali hitrosti skeniranja za vsako serijo izdelkov, s čimer smo vplivali na vnos energije v talilni process (ED). Moč laserja se je gibala od 10 W do 75 W, hitrost skeniranja pa od 100 mm/s do 800 mm/s. Z nižjimi močmi laserja nismo dosegli zadovoljivega taljenja materiala, medtem ko so višje moči laserja povzročile boljše taljenje, z znatnimi razlikami tudi pri enakih vnosih energije - ED. Visoka energijska gostota - ED med 3,50 J/mm² in 4,30 J/mm² je povzročila pomanjkljivo taljenje pri nizki moči laserja oziroma nestabilen talilni bazen z znatnim pršenjem materiala pri visoki moči laserja. Nasprotno pa so zmerne ED v območju od 1,40 J/mm² do 2,90 J/mm² povzročile boljšo gostoto pri visoki moči laserja. Višje hitrosti skeniranja so pomagale preprečiti nastanek gostega oblaka smoga in s pomočjo večje laserske moči zagotovile zadostno energijo v kratkem času. Zato je povečanje tako laserske moči kot hitrosti skeniranja izboljšalo učinkovitost taljenja in povečalo gostoto vzorca. Relativna gostota vzorcev se je gibala od 80 % do 96,5 %. Zmanjšanje debeline plasti s 50 µm na 25 µm pri laserski moči 40 W je na nekaterih območjih povzročilo nastanek dobro oblikovanega bazena taline, na drugih pa znatno brizganje taline, kar je povzročilo poslabšanje gostote.*

Ključne besede *magnezij, talilni bazen, moč laserja, hitrost skeniranja, debelina plasti, nosilna struktura, lasersko taljenje praškastega sloja*

Advancing Intelligent Toolpath Generation: A Systematic Review of CAD–CAM Integration in Industry 4.0 and 5.0

Marko Simonič ✉ – Iztok Palčič – Simon Klančnik
University of Maribor, Faculty of Mechanical Engineering, Slovenia
✉ marko.simonic@um.si

Abstract *This systematic literature review investigates advancements in intelligent computer-aided design and computer-aided manufacturing (CAD–CAM) integration and toolpath generation, analyzing their evolution across Industry 4.0 and emerging Industry 5.0 (I5.0) paradigms. Using the theory–context–characteristics–methodology framework, the study synthesizes 51 peer-reviewed studies (from 2000 to 2025) to map theoretical foundations, industrial applications, technical innovations, and methodological trends. Findings reveal that artificial intelligence (AI) and machine learning dominate research, driving breakthroughs in feature recognition, adaptive toolpath optimization, and predictive maintenance. However, human-centric frameworks central to I5.0, such as socio-technical collaboration, remain underexplored. High-precision sectors (aerospace, biomedical) lead adoption, while small and medium enterprises (SMEs) lag due to resource constraints. Technologically, AI-driven automation and STEP-NC standards show promise, yet interoperability gaps persist due to fragmented data models and legacy systems. Methodologically, AI-based modeling prevails (49 % of studies), but experimental validation and socio-technical frameworks are sparse. Key gaps include limited real-time adaptability, insufficient AI training datasets, and slow adoption of sustainable practices. The review highlights the urgent need for standardized data exchange protocols, scalable solutions for SMEs, and human-AI collaboration models to align CAD–CAM integration with I5.0's sustainability and resilience goals. By bridging these gaps, this work provides a roadmap for advancing intelligent, human-centered manufacturing ecosystems.*

Keywords *CAD–CAM integration, Industry 4.0, Industry 5.0, toolpath optimization, AI, theory–context–characteristics–methodology (TCCM)*

Highlights

- *Artificial Intelligence drives CAD–CAM integration but lacks human-centric focus.*
- *High-precision sectors lead; SMEs face adoption barriers.*
- *Interoperability and lack of standardized AI datasets hinder progress.*
- *Review reveals the need for sustainable, scalable solutions.*

1 INTRODUCTION

The manufacturing sector has undergone radical transformation through Industry 4.0 (I4.0), characterized by cyber-physical systems (CPS), internet of things (IoT), and data-driven automation. These technologies have revolutionized production efficiency, enabling real-time monitoring, predictive maintenance, and adaptive workflows [1,2]. By integrating robotics, cloud computing, and artificial intelligence (AI), I4.0 has minimized downtime, optimized resource use and reduced operational costs [3,4].

Building on this foundation, Industry 5.0 (I5.0) emphasizes human-machine collaboration and sustainability, prioritizing ethical resource allocation and workforce upskilling alongside technological advancement [5]. This paradigm shift leverages AI not to replace human expertise, but to augment it, fostering agile, socially responsible manufacturing ecosystems [5]. Computer-aided engineering (CAE) plays a crucial role in this aspect. It enables product design validation [6], process simulation and optimization. This reduces the need for physical prototyping and minimizes costly design errors [7].

Despite the advancements in CAE and integrated design workflows, a significant disconnect often persists between computer-aided design (CAD) and computer-aided manufacturing (CAM) [8]. CAD tools focus on creating detailed, precise models, yet these models do not always seamlessly translate into manufacturable instructions for CAM systems [9,10]. This disparity can lead to communication bottlenecks, inconsistencies in toolpath generation, and rework cycles that undermine efficiency [11,12]. By improving data exchange protocols [13,14], standardizing file formats, and incorporating real-time feedback from manufacturing constraints, organizations can bridge the CAD–CAM gap and accelerate the transition from digital designs to production-ready components [11].

Various approaches have been developed to automate numerical control (NC) code generation directly from CAD models, aiming to streamline the transition from design to manufacturing. Traditional methods typically rely on geometry-based feature recognition [15] and rule-based process planning [16], wherein the system extracts manufacturing features (e.g., holes, pockets, slots) from 3-dimensional (3D) CAD geometry, maps them to corresponding machining operations, and then generates toolpaths and tool selection data. Knowledge-based systems further enhance this pipeline by incorporating predefined machining rules and best practices [17], enabling semi-automated decision-making for process parameters such as spindle speed, feed rate, and cutting depth. Post-processors then translate these planning outputs into machine-specific G-code (or equivalent) formats, ensuring compatibility with diverse computer numerical control (CNC) equipment. While these workflow-oriented techniques have significantly reduced programming time and manual intervention, they often demand expert tuning [18] and may lack flexibility when confronted with complex geometries or evolving production requirements [19]. In recent years, however, AI has begun to complement these conventional strategies, leveraging deep neural

 DOI: 10.5545/sv-jme.2025.1370

networks [20] and reinforcement learning (RL) [21] to automate feature recognition, optimize toolpaths, and continuously refine CAD assumptions in real time [22]. By incorporating AI modules at critical points of the CAD to CAM workflow, manufacturers can achieve adaptive, self-improving systems [23] that further streamline NC code generation and reduce the need for extensive human oversight [24], ultimately closing the design-to-production gap [25].

Recent contributions further illustrate this evolution. CAD-Coder introduces an open-source vision–language model fine-tuned to generate editable CAD code (CadQuery Python) directly from visual input [26]. Similarly, CAD-based automated G-code generation for drilling operations demonstrates an application program interface (API)-driven approach that extracts geometric parameters from CAD models and automatically generates CNC code for drilling tasks without dedicated CAM software [27]. Complementing these, the AutoCAD to G-code converter outlines a workflow for converting AutoCAD designs directly into CNC-compatible G-code [28]. Those strategies range from AI-driven CAD code generation to lightweight API-based tooling.

Despite the growing body of literature on the evolution of manufacturing technologies and the integration of AI in CAD–CAM workflows [29–31], there remains a lack of comprehensive research synthesizing the specific challenges and opportunities in bridging the CAD–CAM disconnect, particularly in the context of I4.0 and I5.0 paradigms. Recent studies have explored individual aspects, such as AI-driven NC code generation or feature recognition [32,33], yet these efforts are often narrow in scope, limited by the time span of analysis, or constrained to specific methodologies. Furthermore, the rapid adoption of human-machine collaboration and sustainable practices in I5.0 underscores the need for an updated, holistic understanding of how these advancements influence design-to-production integration. Consequently, a systematic literature review (SLR) is essential to consolidate and analyze the existing research landscape. This study proposes an SLR of over 50 studies published in the last two decades, employing the theory–context–characteristics–methodology (TCCM) framework [34], to systematically analyze critical gaps, emerging trends and understudied areas that could enhance the CAD and CAM interoperability in modern manufacturing ecosystems shaped by I4.0 and I5.0. Given this focus, the study aims to address the following research questions:

1. Theory: Which theoretical models or frameworks guide the integration of CAD and CAM in I4.0/5.0 settings?
2. Context: In which industrial or organizational contexts is CAD–CAM integration most frequently examined, and what contextual factors shape these efforts?
3. Characteristics: Which key technical or organizational features (e.g., AI-based tools, knowledge-based systems) facilitate or impede CAD–CAM interoperability, and how do they evolve under I4.0 and I5.0 paradigms?
4. Methodology: Which research methods are used to investigate CAD–CAM integration, and how do these methodological choices affect the reliability, scalability, and reproducibility of results?

2 METHODS AND MATERIALS

This section outlines the methodology employed to conduct SLR of studies addressing CAD–CAM integration within the paradigms of I4.0 and I5.0. The approach is designed to systematically identify and synthesize relevant research, ensuring a comprehensive analysis of theoretical frameworks, contextual factors, technical characteristics, and methodological trends. The TCCM framework was selected as the analytical lens due to its ability to structure multidimensional research inquiries and uncover gaps in literature. This section details the data sources, selection criteria, and analytical processes, providing sufficient information for replication and validation by other researchers.

2.1 Research Design and Analytical Framework

The SLR follows a clear, step-by-step process rooted in proven review protocols [35]. It employs the TCCM framework, delivering a well-rounded analysis of the literature while staying true to the study's goals [36]. With a spotlight on CAD–CAM integration, the review digs deepest into the Theoretical and Methodological angles, exploring how challenges are defined, tackled, and resolved. This lens sheds light on practical strategies, tools, and techniques, pinpointing overlooked areas and opening doors to fresh methodological approaches [35].

Compared to alternatives like PRISMA, which prioritize reporting transparency [37], TCCM offers a theory-driven and context-sensitive structure [36]. This is particularly valuable for research of interdisciplinary domains like CAD–CAM integration, where solutions depend on synergies between theoretical foundations, contextual constraints (e.g., industry-specific requirements), system characteristics (e.g., scalability), and methodological rigor. The inclusion of the Methodology dimension allows us to systematically assess how problems are framed, investigated, and resolved in existing research, identifying gaps in methods (e.g., underuse of AI-driven optimization) and opportunities for methodological innovation.

2.2 Data Sources and Study Selection

This review is based on a comprehensive and systematic search of academic and industry-related literature to ensure broad coverage of relevant studies in the domains of CAD/CAM integration, AI in manufacturing, and CNC toolpath optimization. The selected sources include peer-reviewed journal articles, conference papers, and book chapters, along with a curated set of industry reports and white papers to capture practical implementations of emerging technologies.

2.2.1 Data Sources

To maintain academic rigor and reliability, the following key databases were utilized:

- Scopus – for its extensive indexing of engineering and AI-related publications.
- Web of Science – providing a broad range of peer-reviewed studies in advanced manufacturing
- Google scholar & ResearchGate – used selectively to retrieve literature, such as industry reports and white papers, ensuring coverage of real-world implementations and emerging trends.

2.2.2 Search Strategy

A structured search strategy was employed, using Boolean operators to refine results and ensure the retrieval of high-quality studies. The primary search terms used included: CAD–CAM integration, Industry 4.0, Industry 5.0, AI in manufacturing, NC code generation, feature recognition, toolpath optimization, and human-machine collaboration.

To enhance relevance, secondary qualifiers such as sustainability, interoperability, and systematic review were incorporated. The research was limited to studies published between January 2000 and March 2025, ensuring a focus on recent advancements while covering historical developments in AI-driven manufacturing. In addition to direct search results, the reference lists of selected articles were

also reviewed to identify further relevant studies, helping to ensure a comprehensive literature base.

2.2.3 Inclusion and Exclusion Criteria

To maintain focus and relevance, inclusion and exclusion criteria were defined as follows:

- Inclusion Criteria:
  - Studies published between 2000 and 2025, reflecting more than two decades of advancements in CAD–CAM integration.
  - Research addressing CAD–CAM workflows, interoperability, or automation in the context of I4.0 or I5.0.
  - Studies incorporating AI, knowledge-based systems, or other innovative approaches to bridge the CAD–CAM gap.
  - Peer-reviewed articles, conference proceedings, or authoritative reviews offering empirical or theoretical insights.
- Exclusion Criteria:
  - Studies unrelated to manufacturing or CAD–CAM processes (e.g., pure software development without manufacturing applications).
  - Non-English publications or those lacking sufficient methodological detail.
  - Duplicates or redundant publications from the same research group with no significant new contributions.

2.3 Data Extraction and Analysis

Data extraction was conducted manually using a standardized Excel template aligned with the TCCM framework. In addition to capturing the four core dimensions, the template included several other descriptive and analytical fields to support a comprehensive review. Specifically, the following elements were recorded for each study:

- Bibliographic details: Paper title, authors, year of publication, keywords, journal/conference name.
- Research context: Study aim/goals, research goals.
- Analyzed dimensions:
  - Theory: Theoretical models or conceptual frameworks underlying CAD–CAM integration (e.g. systems theory, CPS).
  - Context: Industrial settings (e.g., automotive, aerospace), organizational factors, or sustainability considerations.
  - Characteristics: Technical features (e.g., AI algorithms, file formats) or organizational factors influencing interoperability.
  - Methodology: Research approaches (e.g., case studies, simulations, experiments) and their reported limitations.
  - Analytical fields: identified gaps, suggested future research directions and main findings.

This structured approach enabled both qualitative syntheses, to identify thematic trends, theoretical orientations, and methodological patterns, and basic quantitative summaries, such as publication year distribution and research domain coverage. Data management and visualization were supported using Microsoft Excel and Python, while Zotero was used for literature organization and InstaText assisted in refining the academic writing style. The detailed and traceable extraction process supports transparency and replicability of the review.

3 RESULTS OF THE SYSTEMATIC LITERATURE REVIEW

This section summarizes the results of the reviewed literature on CAD–CAM integration in the context of I4.0 and I5.0. The analysis follows standardized framework, to ensure a structured and comprehensive review. In addition to presenting the evidence, the key patterns, challenges and opportunities are discussed, considering the research objectives.

3.1 Overview of Included Studies

This SLR includes a total of 51 peer-reviewed studies published between 2002 and 2025. Although the search covered the entire period from 2000 to 2025, the earliest relevant study in this period was published in 2002. The overview shows the development of academic interest in CAD–CAM integration in the context of I4.0 and I5.0. Figure 1 shows the number of articles and conference papers published per year as well as a 3-year moving average trend line representing the overall progression of publications.

As can be seen from Fig. 1, the volume of publications remained relatively low and stable between 2002 and 2015, averaging around one to two publications per year. From 2016 onwards, a modest increase can be observed, with more consistent growth after 2018. The number of studies peaked in 2024 with a total of eight publications, indicating increased research attention and relevance of CAD–CAM integration in recent years. The 3-year moving average, marked with a black dashed line in Fig. 1, confirms this upward trend and signals continued momentum in this area.

In terms of dissemination channels, articles dominate the literature and account for most publications, while conference papers have also gained visibility in recent years, particularly from 2019 onwards. This indicates a growing interest in disseminating preliminary or applied research results via academic conferences, possibly reflecting the increasing pace of technological innovation and industry involvement.

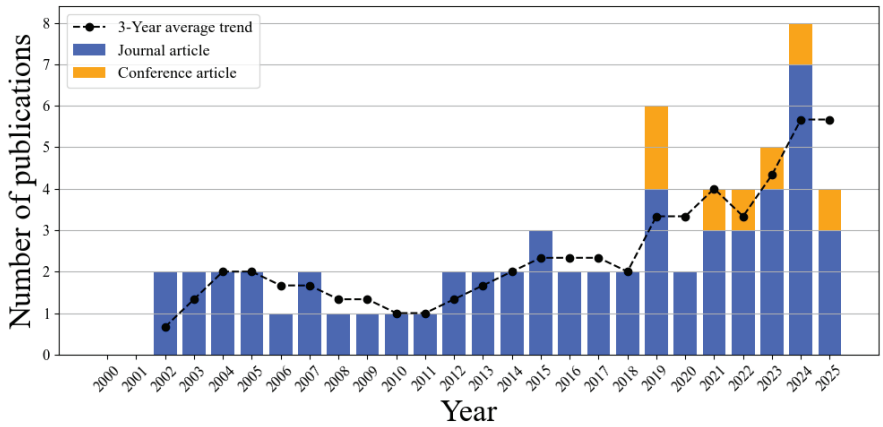

Fig. 1. Annual distribution of articles and conference contributions with a trend line

3.2 Theoretical Foundations

Integrating theoretical foundations into CAD–CAM research is crucial to guide system design, enable model-driven automation and ensure scalability across industrial applications. In the era of I4.0 and more recently I5.0, theory played a central role in aligning smart manufacturing technologies with broader technical, organizational and societal goals. To evaluate the conceptual basis of current research, each study in this review was assessed based on its stated or implied theoretical basis. Based on a thematic analysis, the identified theories were grouped into six overarching categories, which are summarized in Table 1. These categories reflect the main conceptual approaches underlying CAD–CAM integration research over the past 25 years.

Table 1. Theoretical Foundations in CAD–CAM Integration

Category	Description	Examples/Applications
ML & AI	Use of ML algorithms for prediction, classification, or optimization tasks	ANN for process modeling [38] DL for toolpath recognition [39] RL for CNC control [21] GANs for toolpath generation[40]
Optimization algorithms	Swarm-based and evolutionary algorithms applied to improve machining outcomes	NSGA-II for multi-objective optimization [41] PSO for toolpath adaptation [42] GA for machining time reduction [43] GSA for tool selection [44]
Feature/ Knowledge-Based Systems	Utilization of CAD features, KBE, and rule-based decision systems	Feature-based machining [45] Knowledge-based process planning [45] CAD/CAM integration for orthopedic/ dental workflows [46]
CPS/Digital Twins	Digital representations of physical systems for control and maintenance	Digital twins for predictive maintenance [47] Multi-agent systems [48] CPS for smart manufacturing [49]
High-Level Programming / Standards	Abstractions of low-level CNC code through semantic frameworks	STEP-NC for feature-based programming [50] Modular robotic machining [51] AM programming standards [52]
Geometric / Mathematical models	Theories improving geometric modeling and toolpath accuracy	Voxelization for complex surfaces [53] Adaptive isocurves [54] FRep for CAD/CAM correctness [55]

Taken together, these six categories reflect the various theoretical foundations that have shaped research into CAD–CAM integration. In practice, these theoretical categories often merge into hybrid approaches. For instance, ML methods such as artificial neural networks (ANNs) and generative adversarial networks (GANs) are used to enhance CPS and digital twins by predicting toolpaths. Similarly, knowledge-based engineering (KBE) frameworks integrate with high-level standards like STEP-NC (a semantic computer navigated control (CNC programming protocol) to support feature-driven toolpath generation. Optimization approaches like non-dominated sorting genetic algorithms (NSGA-II), particle swarm optimization (PSO), and gravitational search algorithms (GSA) are widely used for machining parameter tuning. Geometric modeling concepts such as function representation (FRep) and voxel-based techniques further reinforce CAD–CAM correctness and accuracy. Such synergies reinforce the impact of each theory and promote innovative CAD–CAM solutions tailored to I4.0 and I5.0 demands. These foundations also overlap with I5.0's focus on human-centeredness, sustainability and resilience. ML and AI support sustainability through predictive maintenance that reduces waste, while CPS improve resilience by enabling adaptive manufacturing systems. However, the limited presence of human-centered theories, such as cognitive ergonomics or socio-technical systems, suggests that CAD–CAM research has not yet fully embraced I5.0's focus on human–machine collaboration, indicating a potential area for theoretical expansion. These categories reflect the main conceptual approaches underlying CAD–CAM integration research over the past 25 years, and their temporal distribution is illustrated in Fig. 2.

3.3 Application Contexts

The studies examined were conducted in a variety of industrial, technical and organizational contexts, reflecting the broad applicability of CAD–CAM integration solutions. Analyzing the contextual focus of the individual studies provides insight into where and how such technologies are used and tested. Based on the content analysis, three main dimensions were identified: industry domains, enterprise types, and technological environments, each depicting unique facets of application environments. These are summarized in Table 2.

While Table 2 summarizes the three primary contextual dimensions (industry domain, enterprise type, and technological environment) it is also important to recognize several recurring challenges in CAD–CAM integration identified across the reviewed studies.

In this context, computer aided process planning (CAPP) systems play a pivotal role in bridging the gap between CAD and CAM. The reviewed studies include manual programming inefficiencies, such as time-consuming G-code authoring and limited reusability of strategies [58]; discontinuities in CAD–CAM-CNC integration, where data loss or misalignment occurs between design, planning, and execution stages [40]; and a lack of feedback and adaptivity,

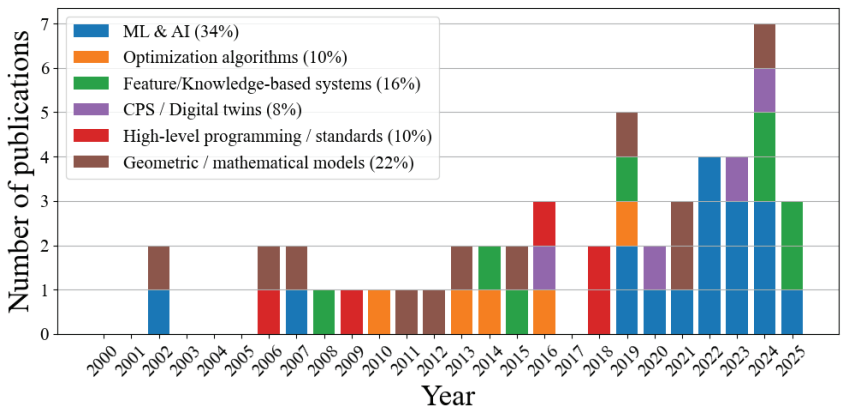

Fig. 2. Annual distribution of studies by theoretical category, with legend showing overall category share

reflected in the absence of closed-loop control or learning capabilities in conventional systems [62].

Toolpath optimization is the most prominent technical theme, appearing in over 40 % of the reviewed studies. It reflects the ongoing challenge of generating efficient and adaptable machining paths, often in connection with precision manufacturing, AI-driven planning, and CNC automation—key elements of I4.0.

Table 2. Application contexts of CAD–CAM integration by dimensions

Dimension	Category / Focus area	Description / Notes
Industry domains	Aerospace, Automotive, Tooling, Die/Mold, Medical, Dental, Orthotics, Micromachining	Common use cases include 5-axis machining, dental restoration, orthotic insole production, etc. [10,46,56]
	Precision manufacturing	Focused on toolpath accuracy, freeform surface machining, CNC optimization [54]
Enterprise type	Large enterprises/labs	Advanced CNC setups, digital twins, robotic systems, smart factories [50]
	Small & medium enterprises (SMEs)	Rapid tooling, low-batch manufacturing, focus on ease of setup and cost-effectiveness [57]
Technological environments	Traditional CAM environments	Focused on automating or enhancing legacy workflows (e.g., manual G-code, static toolpaths) [58]
	Integrated CAD, CAM, CAE, CAPP systems	Studies leveraging interconnected design and manufacturing toolchains [59]
	High-level programming (e.g., STEP-NC)	Transition from G-code to semantic, feature-based CNC programming [60]
	Cloud-based/Adaptive systems	Real-time optimization, digital threads, feedback control, intelligent machining [61]

The rise of cloud-based platforms, digital twins, and adaptive control further supports I4.0 goals of connectivity, flexibility, and real-time responsiveness.

Conversely, applications in dental and orthopedic manufacturing reflect I5.0 priorities, such as personalization and human–machine collaboration. Attention to SMEs also signals a push toward accessible and scalable CAD–CAM solutions. Finally, interest in high-level programming models like STEP-NC marks a shift from rigid G-code to more semantic and interoperable approaches.

3.4 Characteristics of CAD–CAM Integration

The studies examined present a wide range of technical features and architectural implementations designed to improve CAD–CAM integration in the context of I4.0 and I5.0. This section analyzes the functional and technological features reported in the selected literature, focusing on how the integration is realized, what types of automation are implemented and what elements contribute to the adaptability, intelligence and efficiency of the system.

To structure this analysis, the features have been grouped into six overarching themes based on their core function and implementation strategy: AI and ML, toolpath optimization, feature recognition and CAD parsing, real-time systems and feedback, data models & interoperability, and hybrid/integrated architectures. Table 3 provides a summary of the distribution of studies across these thematic categories, along with a selection of representative examples and methodologies that highlight key developments within each group.

The distribution of studies reflects the field's prioritization of AI-driven automation and computational optimization to address CAD–CAM integration challenges. The dominance of AI & ML (31.4 %) and Toolpath optimization (23.5 %) highlights a strong focus on intelligent, adaptive systems capable of self-learning and real-time decision-making. For instance, optimization techniques such as self-supervised DL and evolutionary optimization are increasingly used to automate toolpath generation and process parameter tuning, reducing reliance on manual interventions.

Table 3. Distribution of representative studies across CAD–CAM integration characteristics

Characteristic theme	Description	Share of studies
AI & ML	Self-supervised DL with voxel-based RNNs [58] ANN for adaptive toolpath generation [38] Evolutionary optimization & simulation models [41] Contrastive self-supervision for feature segmentation [63]	31.4 % 16 studies
Toolpath optimization	Voxelization, and B-spline interpolation for smooth toolpaths [64] Deep graph RL for adaptive toolpath optimization [59] Evolutionary algorithms for parameter optimization [44] PSO variants for tool movement constraints [42]	23.5 % 12 studies
Hybrid/ integrated architectures	Semi-automated Matlab for trajectory analysis [56] Strategic frameworks for integrated manufacturing [60]	25.5 % 13 studies
Feature recognition & CAD parsing	STL (stereolitography)-based feature extraction & segmentation [65] DNN on structured descriptors [39]	7.8 % 4 studies
Real-Time systems & feedback	RL model for toolpath control [66] 3D vision for adaptive monitoring [61]	5.9 % 3 studies
Data models & inter-operability	FRep–based CAD/CAM with topology optimization [55] Object oriented model for NC programming [67]	5.9 % 3 studies

Meanwhile, Hybrid/integrated architectures (25.5 %) demonstrate efforts to unify design, simulation, and execution through frameworks like STEP-NC and MATLAB-based tools, reflecting I4.0's emphasis on CPS integration. However, underrepresented themes such as feature recognition & CAD parsing (7.8 %) and data models & interoperability (5.9 %) signal gaps in addressing persistent challenges like dynamic CAD data translation and system interoperability. Similarly, the limited focus on real-time systems & feedback (5.9 %) underscores the need for more empirical validation of adaptive monitoring and control mechanisms in physical machining environments.

3.5 Research Methodologies

The methodological foundations of the reviewed studies highlight the interdisciplinary approaches to CAD–CAM integration, reflecting the field's experimental and computational complexity. Five overarching methodological categories emerged from the analysis (Table 4): (1) AI and ML modeling, (2) simulations and algorithm validation, (3) STEP-NC and CPS system development, (4) experimental machining, and (5) reviews and analytical contributions. Table 4 summarizes these approaches, their key techniques, applications, and representative references.

AI and ML Modeling dominate the field, accounting for 49 % of studies (Figure 3). These works employ various DL architectures, such as ANN, CNN, RL, and generative models. Applications include intelligent toolpath generation, feature recognition, and adaptive machining, underscoring the transformative role of data-driven intelligence in automating and optimizing digital manufacturing processes. Simulations and algorithm validation represent 21.6 %

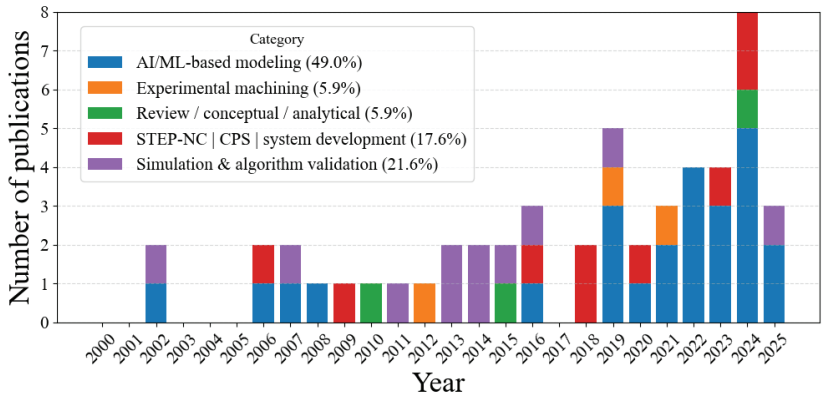

Fig. 3. Yearly distribution of studies by research methodology

of methodologies. Techniques like PSO and numerical simulations are widely used to validate toolpath strategies, cutting parameters, and process control systems in virtual environments. These approaches reduce reliance on physical prototyping by enabling pre-testing of computational models. STEP-NC, CPS, and system development (17.6 % of studies) focus on advancing interoperability in manufacturing systems. Innovations include plug-and-produce automation frameworks, machine-interpretable NC code standards, and architectures validated in industrial robotic environments. These efforts aim to bridge gaps between design and execution phases in CAD–CAM workflows. Experimental machining (5.9% of studies) emphasizes practical validation through CNC machine testing, toolpath design, and process reliability analysis. While underrepresented, these works provide critical insights into the physical realities of CAM execution, such as parameter tuning and material behavior. Reviews and analytical contributions (5.9 %) remain scarce, highlighting a gap in meta-level synthesis and theoretical frameworks. Structured reviews and interdisciplinary conceptual models are needed to unify fragmented advancements and establish robust benchmarks for future research.

Table 4. Overview of methodological approaches in CAD–CAM integration

Research approach	Key techniques/ methods	Example applications	Refs.
AI and ML modeling	DL architectures (ANN,CNN, RL), regression, generative models	Intelligent toolpath generation, feature recognition, adaptive machining	[20–22,30, 67,69,70, 73,74]
Simulations and algorithm validation	PSO, GA, GSA, numerical simulations	Validating toolpath strategies, cutting parameters, process control systems in virtual environments	[42,44,55, 68,69]
STEP-NC, CPS, system development	New system architectures, plug-and-produce frameworks, machine-interpretable NC code standards	Industrial/robotic machining environments	[47–52,70]
Experimental machining	Practical testing of CNC machines, toolpath design, process reliability	Physical realities of CAM execution, parameter tuning	[53,64,71]
Reviews, conceptual, and analytical contributions	Structured reviews, benchmarking frameworks, interdisciplinary conceptual models	Meta-level synthesis, theoretical framework development	[57]

4 DISCUSSION

This SLR synthesizes more than two decades of research on CAD–CAM integration and intelligent toolpath generation through the TCCM framework. The results reveal an evolution from the automation-focused strategies of I4.0 toward I5.0's emphasis on human-centric and sustainable manufacturing. This transition mirrors wider industrial and societal demands for inclusivity, adaptability, and environmental accountability in production systems.

AI and ML dominate the theoretical foundations, underpinning advances in feature recognition, adaptive toolpath planning, and predictive maintenance. However, theoretical models incorporating human factors, socio-technical interaction, and sustainability are scarce, limiting alignment with I5.0 principles. While CPS and digital twins offer strong potential for feedback-driven manufacturing, their industrial deployment remains limited, signaling a gap between conceptual readiness and real-world integration.

From an application standpoint, adoption is concentrated in high-precision industries, where geometric complexity and customization needs justify investment in intelligent CAD–CAM workflows. Although SMEs show growing interest, financial constraints, workforce training needs, and integration barriers hinder uptake. This calls for solutions that are scalable, cost-effective, and compatible with diverse industrial infrastructures. Cloud-based adaptive systems and STEP-NC offer viable alternatives to conventional workflows, but persistent interoperability issues slow adoption.

Technologically, AI-driven automation and optimization dominate CAD–CAM integration, with precision and efficiency as central objectives. Yet, unresolved interoperability challenges (rooted in fragmented data standards, proprietary formats, and insufficient CAD–CAM–CNC integration) limit seamless workflows. Sustainability-focused innovations, such as material efficiency and energy optimization, are increasing but remain secondary to automation goals, indicating the need to embed environmental metrics into core CAD–CAM strategies.

Methodologically, the literature is led by AI/ML-based modeling, followed by simulation-based validation and fewer experimental studies. While virtual and data-driven approaches accelerate design cycles, the lack of experimental verification, standardized datasets, and consistent reporting weakens reproducibility and comparability. Combining physical and virtual validation, and establishing shared benchmarks, would improve industrial credibility and scalability.

Key gaps persist across all TCCM dimensions: the shortage of large, validated datasets; difficulties in freeform surface recognition; limited cross-domain model generalizability; and the lack of robust solutions for real-time toolpath adaptation and force control. The slow adoption of STEP-NC, coupled with cybersecurity and

interoperability constraints, particularly affects SMEs and restricts the scalability of advanced CAD–CAM solutions.

Addressing these gaps will require coordinated research and development efforts across four strategic areas:

1. Comprehensive, annotated, multimodal datasets. Datasets that integrate geometry, process parameters, sensor streams, and toolpath data are essential for developing robust AI models and achieving semantic interoperability through asset administration shells. However, most current studies depend on limited or proprietary datasets, which hampers reproducibility and scalability. Progress is constrained by the absence of standardized formats, low data variability, and intellectual property concerns. Advancing the field will require open-access repositories, harmonized CAD/CAM–sensor datasets, and the use of synthetic data generation to broaden coverage while safeguarding sensitive information.
2. Interpretable, transferable, and robust AI algorithms. Developing AI algorithms that combine interpretability, cross-domain transferability, and operational robustness is crucial for advancing CAD–CAM integration. Hybrid approaches that merge geometric reasoning methods (e.g., voxelization) with simulation-informed training and adaptive control can help bridge the gap between virtual optimization and real-world execution. However, many existing models remain opaque and narrowly specialized, which limits trust, adaptability, and scalability. Progress will depend on the adoption of explainable AI techniques, domain-adaptive learning strategies, and open-source, modular plug-and-play toolkits to facilitate seamless integration into diverse manufacturing environments.
3. Practical implementation of standards. Effective CAD–CAM integration depends on adopting and operationalizing existing yet underutilized standards such as STEP-NC and OPC UA [72]. These can be supported through middleware and integration layers that ensure compatibility across heterogeneous systems, enabling consistent data flow between design, manufacturing, and monitoring environments. Harmonizing communication protocols for Human–Machine Interfaces (HMIs) is equally critical. Advancing this area will require collaborative standard adoption, vendor-neutral integration solutions, and industry-wide alignment on interface and protocol specifications.
4. Human-centered interfaces. Human-centered interfaces should be designed to enhance operator capabilities, aligning CAD–CAM integration with I5.0's collaborative, ethical, and inclusive principles. In this context, inclusive technologies refer to solutions that are accessible across different operator skill levels, adaptable to diverse manufacturing environments (including SMEs), and interoperable with heterogeneous hardware and software systems. Human-centered interfaces will be used as guidelines, which should include:
   - Operator-focused interaction tools – Use visual dashboards, voice-enabled assistants, and intelligent HMIs to improve situational awareness, support explainable AI decisions, and allow timely manual intervention.
   - Integration of advanced LLMs – Incorporate well-known large language models such as GPT-5, LLaMA 3, Claude, and Grok-4 to enable multilingual natural language interaction, real-time troubleshooting, and automated code or G-code optimization.
   - Design engineer practices – Provide structured 3D models with standardized representations (e.g., B-rep, STEP-NC) and embedded machining metadata to ensure smooth downstream use in CAM and HMI systems.
   - Usability, transparency, and adaptability – Maintain operator engagement as active decision-makers, fostering trust and effective human – machine collaboration while ensuring scalability from small workshops to large enterprises.

5 CONCLUSIONS

Over the past two decades, CAD–CAM integration has advanced significantly within the I4.0 and I5.0 paradigms, evolving from automation-focused solutions toward more adaptive, sustainable, and collaborative manufacturing systems. The systematic mapping provided by this review clarifies the field's theoretical foundations, application contexts, technical innovations, and methodological practices, highlighting where progress has been made and where critical work remains. Key strategic directions emerging from this synthesis include:

- Bridging research–practice divides by embedding socio-technical and sustainability considerations directly into CAD–CAM solutions, ensuring they are deployable in diverse industrial contexts.
- Expanding accessibility through scalable, cost-effective integration strategies that address SME-specific constraints without sacrificing interoperability or performance.
- Embedding sustainability as a core metric alongside productivity and precision, ensuring material efficiency, energy optimization, and lifecycle awareness in CAD–CAM workflows.
- Leveraging advanced AI and standards (interpretable models, STEP-NC, and OPC UA) to enable adaptive, interoperable, and future-proof manufacturing ecosystems.

While this review focuses on peer-reviewed literature, future studies should combine industrial case evidence with academic research to capture region-specific practices, operational constraints, and emerging innovations. Addressing these priorities will accelerate the transition toward manufacturing systems that are not only technologically advanced, but also inclusive, resilient, and environmentally responsible—fully embodying the collaborative ethos of I5.0.

References

[1] Horvat, D., Kroll, H., Jäger, A. Researching the effects of automation and digitalization on manufacturing companies' productivity in the early stage of Industry 4.0. *Procedia Manuf* 39 886-893 (2019) **DOI:10.1016/j.promfg.2020.01.401**.

[2] Ojstersek, R., Buchmeister, B., Vujica Herzog, N. Use of data-driven simulation modeling and visual computing methods for workplace evaluation. *Appl Sci* 10 7037 (2020) **DOI:10.3390/app10207037**.

[3] Kovič, K., Ojsteršek, R., Palčič, I. Simultaneous use of digital technologies and industrial robots in manufacturing firms. *Appl Sci* 13 5890 (2023) **DOI:10.3390/app13105890**.

[4] Pozzi, R., Rossi, T., Secchi, R. Industry 4.0 technologies: critical success factors for implementation and improvements in manufacturing companies. *Prod Plan Control* 34 139-158 (2023) **DOI:10.1080/09537287.2021.1891481**.

[5] Aheleroff, S., Huang, H., Xu, X., Zhong, R.Y. Toward sustainability and resilience with Industry 4.0 and Industry 5.0. *Front Manuf Technol* 2 951643 (2022) **DOI:10.3389/fmtec.2022.951643**.

[6] Regassa Hunde, B., Debebe Woldeyohannes, A. Future prospects of computer-aided design (CAD) - a review from the perspective of artificial intelligence (AI), extended reality, and 3D printing. *Results Eng* 14 100478 (2022) **DOI:10.1016/j.rineng.2022.100478**.

[7] Feldhausen, T., Heinrich, L., Saleeby, K., Burl, A., Post, B., MacDonald, E., Saldana, C., Love, L. Review of computer-aided manufacturing (CAM) strategies for hybrid directed energy deposition. *Addit Manuf* 56 102900 (2022) **DOI:10.1016/j.addma.2022.102900**.

[8] Xu, X., Wang, L., Newman, S.T. Computer-aided process planning - a critical review of recent developments and future trends. *Int J Comput Integr Manuf* 24 1-31 (2011) **DOI:10.1080/0951192X.2010.518632**.

[9] Toquica, J.S., Zivanovic, S., Bonnard, R., Rodriguez, E., Alvares, A.J., Ferreira, J.C.E. STEP-NC-based machining architecture applied to industrial robots. *J Braz Soc Mech Sci Eng* 41 314 (2019) **DOI:10.1007/s40430-019-1811-y**.

[10] Lasemi, A., Xue, D., Gu, P. Recent development in CNC machining of freeform surfaces: a state-of-the-art review. *Comput Aided Des* 42 641-654 (2010) **DOI:10.1016/j.cad.2010.04.002**.

[11] Fu, Y., Zhu, G., Zhu, M., Xuan, F. Digital twin for integration of design-manufacturing-maintenance: an overview. *Chin J Mech Eng* 35 80 (2022) **DOI:10.1186/s10033-022-00760-x**.

[12] Han, J., Kang, M., Choi, H. STEP-based feature recognition for manufacturing cost optimization. *Comput Aided Des* 33 671-686 (2001) **DOI:10.1016/S0010-4485(01)00071-9**.

[13] Wu, D., Rosen, D.W., Schaefer, D. Cloud-based design and manufacturing: status and promise. Schaefer, D. (ed.) *Cloud-Based Design and Manufacturing (CBDM)* 1-24 (2014) **DOI:10.1007/978-3-319-07398-9_1**.

[14] Pratt, M.J. Introduction to ISO 10303-the STEP standard for product data exchange. *J Comput Inf Sci Eng* 1 102-103 (2001) **DOI:10.1115/1.1354995**.

[15] Han, J., Pratt, M., Regli, W.C. Manufacturing feature recognition from solid models: a status report. *IEEE Trans Robot Autom* 16 782-796 (2000) **DOI:10.1109/70.897789**.

[16] Xu, X., Hinduja, S. Recognition of rough machining features in 212D components. *Comput Aided Des* 30 503-516 (1998) **DOI:10.1016/S0010-4485(97)00090-0**.

[17] Wu, Z., Liang, C. A review and prospects of manufacturing process knowledge acquisition, representation, and application. *Machines* 12 416 (2024) **DOI:10.3390/machines12060416**.

[18] Al-wswasi, M., Ivanov, A., Makatsoris, H. A survey on smart automated computer-aided process planning (ACAPP) techniques. *Int J Adv Manuf Technol* 97 809-832 (2018) **DOI:10.1007/s00170-018-1966-1**.

[19] Leo Kumar, S.P. State of the art-intense review on artificial intelligence systems application in process planning and manufacturing. *Eng Appl Artif Intell* 65 294-329 (2017) **DOI:10.1016/j.engappai.2017.08.005**.

[20] Zhang, Z., Jaiswal, P., Rai, R. FeatureNet: machining feature recognition based on 3D convolution neural network. *Comput Aided Des* 101 12-22 (2018) **DOI:10.1016/j.cad.2018.03.006**.

[21] Juraev, M., Abrorov, A., Akhmedova, K., Abdullayev, S. Optimization of CNC machining tool paths using reinforcement learning techniques. *Appl Mech Mater* 923 39-48 (2024) **DOI:10.4028/p-4pj98Q**.

[22] Li, C., Zheng, P., Yin, Y., Wang, B., Wang, L. Deep reinforcement learning in smart manufacturing: a review and prospects. *CIRP J Manuf Sci Technol* 40 75-101 (2023) **DOI:10.1016/j.cirpj.2022.11.003**.

[23] Wang, J., Ma, Y., Zhang, L., Gao, R.X., Wu, D. Deep learning for smart manufacturing: methods and applications. *J Manuf Syst* 48 144-156 (2018) **DOI:10.1016/j.jmsy.2018.01.003**.

[24] Bécue, A., Praça, I., Gama, J. Artificial intelligence, cyber-threats and Industry 4.0: challenges and opportunities. *Artif Intell Rev* 54 3849-3886 (2021) **DOI:10.1007/s10462-020-09942-2**.

[25] Kusiak, A. Smart manufacturing. *Int J Prod Res* 56 508-517 (2018) **DOI:10.1080/00207543.2017.1351644**.

[26] Doris, A.C., Alam, M.F., Nobari, A.H., Ahmed, F. CAD-Coder: an open-source vision-language model for computer-aided design code generation. *arXiv* (2025) **DOI:10.48550/arXiv.2505.14646**.

[27] Tzotzis, A., Manavis, A., Efkolidis, N., Kyratsis, P. CAD-based automated G-code generation for drilling operations. *Int J Mechatron Manuf Syst* 13 177-184 (2021) **DOI:10.54684/ijmmt.2021.13.3.177**.

[28] Yarava, V.S. AutoCAD to G-code converter. *IEEE Pune Section International Conference* 1-5 (2021) **DOI:10.1109/PuneCon52575.2021.9686541**.

[29] Nahavandi, S. Industry 5.0-a human-centric solution. *Sustainability* 11 4371 (2019) **DOI:10.3390/su11164371**.

[30] Jamwal, A., Agrawal, R., Sharma, M., Giallanza, A. Industry 4.0 technologies for manufacturing sustainability: a systematic review and future research directions. *Appl Sci* 11 5725 (2021) **DOI:10.3390/app11125725**.

[31] Culot, G., Nassimbeni, G., Orzes, G., Sartor, M. Behind the definition of Industry 4.0: analysis and open questions. *Int J Prod Econ* 226 107617 (2020) **DOI:10.1016/j.ijpe.2020.107617**.

[32] Ding, S., Feng, Q., Sun, Z., Ma, F. MBD-based 3D CAD model automatic feature recognition and similarity evaluation. *IEEE Access* 9 150403-150425 (2021) **DOI:10.1109/ACCESS.2021.3126333**.

[33] Lu, F., Zhou, G., Zhang, C., Liu, Y., Chang, F., Lu, Q., Xiao, Z. Energy-efficient tool path generation and expansion optimisation for five-axis flank milling with meta-reinforcement learning. *J Intell Manuf* (2024) **DOI:10.1007/s10845-024-02412-4**.

[34] Paul, J., Khatri, P., Kaur Duggal, H. Frameworks for developing impactful systematic literature reviews and theory building: what, why and how? *J Decis Syst* 33 537-550 (2024) **DOI:10.1080/12460125.2023.2197700**.

[35] Paul, J., Criado, A.R. The art of writing literature review: what do we know and what do we need to know? *Int Bus Rev* 29 101717 (2020) **DOI:10.1016/j.ibusrev.2020.101717**.

[36] Paul, J., Lim, W.M., O'Cass, A., Hao, A.W., Bresciani, S. Scientific procedures and rationales for systematic literature reviews (SPAR-4-SLR). *Int J Consum Stud* 45 (2021) **DOI:10.1111/ijcs.12695**.

[37] Pati, D., Lorusso, L.N. How to write a systematic review of the literature. *Health Environ Res Des J* 11 15-30 (2018) **DOI:10.1177/1937586717747384**.

[38] Balic, J., Korosec, M. Intelligent tool path generation for milling of free surfaces using neural networks. *Int J Mach Tools Manuf* 42 1171-1179 (2002) **DOI:10.1016/S0890-6955(02)00045-7**.

[39] Yeo, C., Kim, B.C., Cheon, S., Lee, J., Mun, D. Machining feature recognition based on deep neural networks to support tight integration with 3D CAD systems. *Sci Rep* 11 22147 (2021) **DOI:10.1038/s41598-021-01313-3**.

[40] Kaiser, B., Csiszar, A., Verl, A. Generative models for direct generation of CNC toolpaths. *25th International Conference on Mechatronics and Machine Vision in Practice* 1-6 (2018) **DOI:10.1109/M2VIP.2018.8600856**.

[41] Klancnik, S., Brezocnik, M., Balic, J. Intelligent CAD/CAM system for programming of CNC machine tools. *Int J Simul Model* 15 109-120 (2016) **DOI:10.2507/IJSIMM15(1)9.330**.

[42] Hsieh, H.-T., Chu, C.-H. Improving optimization of tool path planning in 5-axis flank milling using advanced PSO algorithms. *Robot Comput Integr Manuf* 29 3-11 (2013) **DOI:10.1016/j.rcim.2012.04.007**.

[43] Dodok, T., Čuboňová, N. Optimization and efficiency of toolpath generation in CAD/CAM system. *MATEC Web Conf* 299 03001 (2019) **DOI:10.1051/matecconf/201929903001**.

[44] Hrelja, M., Klancnik, S., Balic, J., Brezocnik, M. Modelling of a turning process using the gravitational search algorithm. *Int J Simul Model* 13 30-41 (2014) **DOI:10.2507/IJSIMM13(1)3.248**.

[45] Leo Kumar, S.P., Jerald, J., Kumanan, S. Feature-based modelling and process parameters selection in a CAPP system for prismatic micro parts. *Int J Comput Integr Manuf* 1-17 (2014) **DOI:10.1080/0951192X.2014.953586**.

[46] Obrovac, K., Staroveški, T., Vuković-Obrovac, J., Klaić, M. System for automated production of custom made shoe insoles. *Stroj Cas J Mech Eng* 74 81-88 (2024) **DOI:10.2478/scjme-2024-0035**.

[47] Kubota, T., Hamzeh, R., Xu, X. STEP-NC enabled machine tool digital twin. *Procedia CIRP* 93 1460-1465 (2020) **DOI:10.1016/j.procir.2020.06.004**.

[48] Nilsson, A., Danielsson, F., Svensson, B. From CAD to plug & produce: a generic structure for the integration of standard industrial robots into agents. *Int J Adv Manuf Technol* 128 5249-5260 (2023) **DOI:10.1007/s00170-023-12280-6**.

[49] Monostori, L., Kádár, B., Bauernhansl, T., Kondoh, S., Kumara, S., Reinhart, G., Sauer, O., Schuh, G., Sihn, W., Ueda, K. Cyber-physical systems in manufacturing. *CIRP Ann* 65 621-641 (2016) **DOI:10.1016/j.cirp.2016.06.005**.

[50] Suh, S.-H., Chung, D.-H., Lee, B.-E., Shin, S., Choi, I., Kim, K.-M. STEP-compliant CNC system for turning: data model, architecture, and implementation. *Comput Aided Des* 38 677-688 (2006) **DOI:10.1016/j.cad.2006.02.006**.

[51] Toquica, J.S., Živanović, S., Alvares, A.J., Bonnard, R. A STEP-NC compliant robotic machining platform for advanced manufacturing. *Int J Adv Manuf Technol* 95 3839-3854 (2018) **DOI:10.1007/s00170-017-1466-8**.

[52] Bonnard, R., Hascoët, J.-Y., Mognol, P., Stroud, I. STEP-NC digital thread for additive manufacturing: data model, implementation and validation. *Int J Comput Integr Manuf* 31 1141-1160 (2018) **DOI:10.1080/0951192X.2018.1509130**.

[53] Kukreja, A., Dhanda, M., Pande, S. Efficient toolpath planning for voxel-based CNC rough machining. *Comput Aided Des Appl* 18 285-296 (2020) **DOI:10.14733/cadaps.2021.285-296**.

[54] Ding, S., Mannan, M.A., Poo, A.N., Yang, D.C.H., Han, Z. Adaptive iso-planar tool path generation for machining of free-form surfaces. *Comput Aided Des* 35 141-153 (2003) **DOI:10.1016/S0010-4485(02)00048-9**.

[55] Popov, D., Kuzminova, Y., Maltsev, E., Evlashin, S., Safonov, A., Akhatov, I., Pasko, A. CAD/CAM system for additive manufacturing with a robust and efficient topology optimization algorithm based on the function representation. *Appl Sci* 11 7409 (2021) **DOI:10.3390/app11167409**.

[56] Maltauro, M., Vargiu, E., Tozzi, F., Ciocca, L., Meneghello, R. A semi-automated tool for digital and mechanical articulators comparative analysis of condylar path elements. *Comput Biol Med* 186 109724 (2025) **DOI:10.1016/j.compbiomed.2025.109724**.

[57] Matta, A.K., Raju, D.R., Suman, K.N.S. The integration of CAD/CAM and rapid prototyping in product development: a review. *Mater Today Proc* 2 3438-3445 (2015) **DOI:10.1016/j.matpr.2015.07.319**.
[58] Yavartanoo, M., Hong, S., Neshatavar, R., Lee, K.M. CNC-Net: self-supervised learning for CNC machining operations. *arXiv* (2023) **DOI:10.48550/arXiv.2312.09925**.
[59] Ye, L. Design and manufacturing of mechanical parts based on CAD and CAM technology. *Eng Res Express* 6 045411 (2024) **DOI:10.1088/2631-8695/ad8056**.
[60] Cha, J.-M., Suh, S.-H., Hascoet, J.-Y., Stroud, I. A roadmap for implementing new manufacturing technology based on STEP-NC. *J Intell Manuf* 27 959-973 (2016) **DOI:10.1007/s10845-014-0927-2**.
[61] Pivkin, P., Nazarenko, E., Grechishnikov, V., Kuznetsov, V., Uvarova, L., Ershov, A., Yazev, A., Nadykto, A. Digital cyber-physical system for designing and manufacturing of conical end mill. *E3S Web Conf* 592 05024 (2024) **DOI:10.1051/e3sconf/202459205024**.
[62] Zavalnyi, O., Zhao, G., Liu, Y., Xiao, W. Optimization of the STEP-NC compliant online toolpath generation for T-spline surfaces using convolutional neural network and random forest classifier. *IOP Conf Ser Mater Sci Eng* 658 012015 (2019) **DOI:10.1088/1757-899X/658/1/012015**.
[63] Wang, J., Zhu, H., Guo, H., Mamun, A.A., Xiang, C., Lee, T.H. Few-shot point cloud semantic segmentation via contrastive self-supervision and multi-resolution attention. *2023 IEEE International Conference on Robotics and Automation (ICRA)* 2811-2817 (2023) **DOI:10.1109/ICRA48891.2023.10160429**.
[64] Obrovac, K., Raos, P., Staroveški, T., Brezak, D. A method for generating toolpaths in the manufacturing of orthosis molds with a five-axis computer numerical control machine. *Machines* 12 740 (2024) **DOI:10.3390/machines12100740**.
[65] Balič, J., Klančnik, S., Brezovnik, S. Feature extraction from CAD model for milling strategy prediction. *Stroj Vestn-J Mech E* 301-307 (2008).
[66] Zhang, Y., Li, Y., Xu, K. Reinforcement learning-based tool orientation optimization for five-axis machining. *Int J Adv Manuf Technol* 119 7311-7326 (2022) **DOI:10.1007/s00170-022-08668-5**.
[67] Rauch, M., Laguionie, R., Hascoet, J.-Y., Xu, X. Enhancing CNC manufacturing interoperability with STEP-NC. *J Mach Eng* 9 26-37 (2009).
[68] Mladenovic, G., Tanovic, L., Ehmann, K. Tool path generation for milling of free form surfaces with feed rate scheduling. *FME Trans* 43 9-15 (2015) **DOI:10.5937/fmet1501009m**.
[69] Dhanda, M., Pande, S. Adaptive tool path planning strategy for freeform surface machining using point cloud. *Comput Aided Des Appl* 16 289-307 (2018) **DOI:10.14733/cadaps.2019.289-307**.
[70] Liao, J., Huang, Z. Data model-based toolpath generation techniques for CNC milling machines. *Front Mech Eng* 10 1358061 (2024) **DOI:10.3389/fmech.2024.1358061**.
[71] Giannakis, A., Vosniakos, G.C. Parametric multi-axis tool path planning for CNC machining: the case of spur gears. *Int J Manuf Res* 7 354 (2012) **DOI:10.1504/IJMR.2012.050101**.
[72] Ji, T., Xu, X. Exploring the integration of cloud manufacturing and cyber-physical systems in the era of Industry 4.0 - an OPC UA approach. *Robot Comput Integr Manuf* 93 102927 (2025) **DOI:10.1016/j.rcim.2024.102927**.

Acknowledgement *The authors acknowledge the financial support from the Slovenian Research Agency (Research Core Funding No. P2-0157).*

Received: 2025-04-24, revised: 2025-08-08, accepted 2025-09-22
as Review Scientific Paper 1.02.

Data Availability *The data that support the findings of this study are not available due to project confidentiality.*

Author contributions *Marko Simonič: Conceptualization, Methodology, Formal analysis, Writing – original draft, and Writing – review & editing; Iztok Palčič: Conceptualization, Methodology, Formal analysis, Writing – original draft, and Writing – review & editing; Simon Klančnik: Conceptualization, Methodology, Formal analysis, Writing – original draft, and Writing – review & editing. All authors have read and agreed to the published version of the manuscript.*

Inteligentno generiranje poti orodja: sistematični pregled integracije CAD–CAM v Industriji 4.0 in 5.0

Povzetek *Pregled literature raziskuje napredek na področju integracije računalniško podprtega konstruiranja in računalniško podprte proizvodnje (CAD–CAM) ter generiranja poti orodja, pri čemer analizira razvoj v okviru Industrije 4.0 in Industrije 5.0 (I5.0). S pomočjo pristopa po teoriji–kontekstu–značilnostih–metodologiji (TCCM) študija sintetizira 51 recenziranih raziskav (v obdobju 2000–2025) ter analizira teoretične osnove, industrijske aplikacije, tehnične inovacije in metodološke trende. Ugotovitve razkrivajo, da raziskave močno zaznamujejo umetna inteligenca (UI) in strojno učenje, ki poganjata preboje na področju prepoznavanja značilnosti, adaptivne optimizacije poti orodja in napovednega vzdrževanja. Vendar pa človeško-usmerjene rešitve, ki so osrednjega pomena za I5.0, kot je sociotehnično sodelovanje, ostajajo premalo raziskana. Panoge z visoko natančnostjo (letalska in vesoljska, biomedicinska) vodijo pri uvajanju, medtem ko mala in srednja podjetja (MSP) zaostajajo zaradi omejenih virov. S tehnološkega vidika obetajo avtomatizacija, ki temelji na UI in standardi STEP-NC, a vrzeli v interoperabilnosti ostajajo zaradi razdrobljenih podatkovnih modelov in zastarelih sistemov. Metodološko prevladuje modeliranje na osnovi UI (49 % raziskav), eksperimentalna validacija in sociotehnična ogrodja pa ostajata redka. Ključne vrzeli, ki so bile zaznane v študiji, vključujejo omejeno sprotno prilagodljivost, pomanjkanje zadostnih učnih podatkovnih zbirk za učenje modelov UI, ter počasno uvajanje trajnostnih praks. Pregled poudarja nujnost standardiziranih protokolov za izmenjavo podatkov, razširljivih rešitev za malo serijsko proizvodnjo ter razvoj modelov sodelovanja med človekom in UI, ki bi CAD–CAM integracijo uskladili s trajnostnimi in odpornimi cilji I5.0. Z odpravljanjem teh vrzeli prispeva pregled k oblikovanju načrta za napredno, inteligentno in človeku usmerjeno proizvodno okolje.*

Ključne besede *CAD–CAM integracija, Industrija 4.0, Industrija 5.0, optimizacija poti orodja, umetna inteligenca (UI), teorija–kontekst–značilnosti–metodologija (TCCM)*

Comparison of 1D Euler Equation Based and 3D Navier-Stokes Simulation Methods for Water Hammer Phenomena

Nejc Vovk – Jure Ravnik ✉
Faculty of Mechanical Engineering, University of Maribor, Slovenia
✉ jure.ravnik@um.si

Abstract *Water hammer phenomena in pipelines can induce significant transient pressure surges, leading to structural failures and operational inefficiencies. This study presents a comparative analyzis of two numerical approaches for simulating water hammer: a one-dimensional (1D) inviscid model with added friction based on the Euler equations and the method of characteristics, and a three-dimensional (3D) viscous model utilizing the Navier-Stokes equations in OpenFOAM. Benchmarking problems are solved first, then both methods are used to study a 3.4 km long DN400 pipeline subject to sudden pump failure by analyzing pressure surges, cavitation, and water column separation. The 1D model effectively predicts transient pressure waves and cavitation conditions with minimal computational cost, while the 3D model provides a detailed representation of multiphase flow dynamics, including cavitation bubble growth and collapse via the volume of fluid method. To mitigate adverse effects, a dynamic combination air valve is introduced, and its effectiveness in reducing pressure surges and cavitation is demonstrated. The results highlight the trade-offs between computational efficiency and accuracy in modelling water hammer events and underscore the importance of protective measures in pipeline systems.*

Keywords *water hammer, cavitation, water column separation, CFD, Euler equation, Navier-Stokes equations, OpenFOAM, method of characteristics*

Highlights

- *A 1D inviscid and 3D viscous simulation models were developed for water hammer simulations.*
- *The developed models were compared and used on an example of a 3.4 km long pipeline undergoing sudden pump failure.*
- *Advantages and disadvantages of inviscid versus viscous modelling are discussed.*
- *Results of simulation of cavitation bubble growth on a pipeline with and without a dynamic combination air valve are presented and compared.*

1 INTRODUCTION

The phenomenon of water hammer in pipelines, particularly during sudden flow blockages, has received significant attention in the field of hydraulic engineering. Water hammer is characterized by transient pressure surges that occur when the flow of fluid is abruptly stopped or altered, often leading to severe mechanical stress on pipeline systems.

Traditionally, water hammer analyzis has relied on one-dimensional (1D) inviscid models based on the Euler equations with additional consideration of steady or unsteady friction and the method of characteristics [1]. These models provide a simplified representation of fluid dynamics, allowing for efficient simulations of pressure transients in pipelines and can include cavitation phenomena [2]. More recently, three-dimensional (3D) viscous models based on the Navier-Stokes equations have been employed to provide a more detailed representation of fluid behavior, including the effects of viscosity and turbulence. These models can simulate complex interactions between fluid phases, such as cavitation bubble dynamics and water column separation. The choice between 1D and 3D models often depends on the specific requirements of the analyzis, including computational resources, desired accuracy, and the complexity of the system being studied. While 1D models are computationally efficient and suitable for preliminary assessments, 3D models offer a more comprehensive understanding of fluid dynamics in complex systems.

Numerical simulations of water hammer have been widely studied using computational fluid dynamics (CFD). Cao et al. [3] analyzed transient flow in pipelines, emphasizing its importance in urban water systems and hydropower. Khan et al. [4] investigated hydropower penstocks, showcasing CFD's role in modelling water hammer, cavitation, and column separation. They performed transient CFD simulations for different load rejection conditions using Ansys CFX by modifying the URANS equations.

The impact of pipe material properties on water hammer dynamics has been studied extensively. Morvarid et al. [5] analyzed viscoelastic pipe wall effects on pressure fluctuations using the method of characteristics and turbulence modelling. Protective systems like hydropneumatic tanks were investigated by El-Hazek and Halawa [6], showing their effectiveness in damping pressure surges.

Air entrainment has been explored as a mitigation strategy. Zhang et al. [7] demonstrated that air pockets can absorb pressure surges in gravitational pipe flows. Additionally, Meng et al. [8] highlighted the influence of flow velocity and pipe wall roughness, finding that higher velocities and roughness exacerbate pressure surges, underscoring their importance in pipeline design.

Nikpour et al. [9] emphasized the role of CFD in understanding cavitation and its link to water hammer, crucial for preventing failures in hydraulic systems. They used Ansys Fluent and have shown CFD can be successfully employed in modelling of water hammer phenomena. Ansys Fluent was also used by Han et al. [10] to show that rapid valve closures amplify water hammer pressures, highlighting the need for controlled valve operations. Zhang et al. [11] proposed a dynamic mesh simulation method to analyze transient behavior in pipelines with moving isolation devices, aiding in the design of resilient systems. Aguinaga et al. [12] proposed a mechatronic approach to control water hammer, integrating mechanical, electrical,

DOI: 10.5545/sv-jme.2025.1340

and hydraulic systems for better transient pressure management. Wu et al. [13] reviewed transient flow percussion theory, emphasizing its role in preventing water hammer in long-distance pipelines. Yang et al. [14] validated 3D CFD simulations as effective tools for analyzing valve-induced water hammer and its impact on pipeline integrity.

The interaction between water hammer waves and centrifugal pumps has also been a subject of investigation. Zhang et al. [15] explored the dynamic interactions between valve-closure water hammer waves and pump components, revealing that these interactions can lead to substantial pressure variations and fluid-induced forces on the pump.

Malesinska et al. [16] analyzed the effects of sudden cross-section changes on water hammer, showing that abrupt geometry variations significantly influence transient pressure waves. Lupa et al. [17] reviewed water hammer impacts on hydraulic systems, highlighting the importance of empirical validation for simulation reliability.

In the present work we focus on the comparison of two methods for assessing flow conditions in a pipeline after a sudden discharge decrease: the 1D inviscid simulation with added friction model and the 3D viscous simulation. In the following subsections we present both methods and then apply them to the analyzis of a 3.4 km long pipeline, which experiences a sudden drop of discharge due to the failure of the electrical grid to deliver power to the pumping station. The 1D solver is based on the method of characteristics and is capable of simulating water hammer in pipelines with various boundary conditions. The 3D model is implemented into OpenFOAM, [18], 3D Navier-Stokes solver, and supports cavitation and multiphase flow. By comparing the results we are able to identify the strengths and weaknesses of both methods.

2 METHODS

2.1 1D Solver

When neglecting viscosity the Euler equation describes the momentum balance in the fluid system and at the same time the mass balance is described by the continuity equation. When taking the pipe deformation into account the mass conservation equation reads:

$$\frac{\partial p}{\partial t}+\rho c^2\frac{\partial v}{\partial x}=0. \tag{1}$$

Here the pressure wave speed is:

$$c=\sqrt{\frac{1}{\rho}\left(\chi+\frac{D}{Ee}\right)^{-1}}, \tag{2}$$

with E the Young's modulus, e the wall thickness, D the pipe diameter and χ the compressibility.

The law of conservation of momentum is established using the force balance and reads as:

$$\frac{\partial v}{\partial t}=-\frac{1}{\rho}\frac{\partial p}{\partial x}-\frac{2fv^2}{D}\operatorname{sgn}(v)-g\sin\alpha, \tag{3}$$

where sgn(v) is the sign of the velocity. The effect of viscosity is modelled with the Fanning friction coefficient f and the wall stress τ_w. The wall stress is calculated using the quadratic law of resistance as $\tau_w=\frac{1}{2}\rho f v^2$.

2.1.1 Method of Characteristics

We solve the coupled Eqs. (1) and (3) using the method of characteristics, [19]. The method of characteristics is a numerical method for solving hyperbolic partial differential equations. It is based on the observation that the solution of a first-order partial differential equation can be represented as a family of curves (characteristics) in the domain of the independent variables. The method of characteristics is well suited for solving these equations as it can capture the shock waves and other discontinuities that arise in the flow. When we combine the two equations with the Lagrange multiplier $\lambda=\pm\rho_c$ we obtain a system of two equations named C^+ and C^-:

$$C^+:\frac{v_{i,j+1}-v_{i-1,j}}{\Delta t}+\frac{g}{c}\frac{H_{i,j+1}-H_{i-1,j}}{\Delta t}+\frac{2fv_{i-1,j}^2}{D}\operatorname{sgn}(v_{i-1,j})=0, \tag{4}$$

$$C^-:\frac{v_{i,j+1}-v_{i+1,j}}{\Delta t}-\frac{g}{c}\frac{H_{i,j+1}-H_{i+1,j}}{\Delta t}+\frac{2fv_{i+1,j}^2}{D}\operatorname{sgn}(v_{i+1,j})=0. \tag{5}$$

The equations are discretized in space (Δx) and time (Δt), and the solution is obtained by iterating through the grid points, where the time and position step are connected via $\Delta x=c\Delta t$. The unknowns in these equations are the flow velocity and piezometric head at location i at time j+1: $v_{i,j+1}$ and $H_{i,j+1}$. Piezometric head is calculated as $H=p/\rho g+z$. Fig. 1 shows the characteristics C^+ and C^- and the intersections where we can calculate the values of the unknown fields. Index i denotes location along the pipe, index j denotes time.

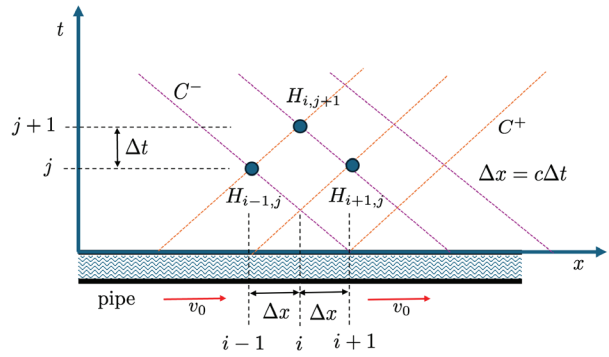

Fig. 1. The characteristics C^+ and C^-

Boundary conditions can be either known values of head or discharge. For example, if the discharge is known on the left side (i=0), the boundary condition for head can be calculated from the Eq. (5) and reads:

$$v_{0,j+1}=v_0,$$

$$H_{0,j+1}=H_{1,j}+\frac{c}{g}\left(v_{0,j+1}-v_{1,j}+\frac{2f\Delta t}{D}v_{1,j}^2\operatorname{sgn}(v_{1,j})\right).$$

At the other side of the pipe (i=N) the head is known. If there is an open reservoir a there, then the head is equation to the elevation, and the discharge is calculated from the Eq. (4):

$$H_{N+1,j+1}=z_{N+1},$$

$$v_{N+1,j+1}=v_{N,j}-\frac{g}{c}(H_{N+1,j}-H_{N,j})-\frac{2f\Delta t}{D}v_{N,j}^2\operatorname{sgn}(v_{N,j}).$$

The friction factor is calculated from the steady state discharge. Assuming known pipe length, the elevation difference between inlet and outlet and the discharge of the friction factor can be calculated from Eq. (4).

We developed the 1D model primarily to discover if conditions, which would enable cavitation are present in the pipeline. Thus, when pressure drops below the vapor pressure, we assume that cavitation occurs. If the simulation continues beyond this time instant, the cavitation is not modelled, but rather only the pressure is limited to

the vapor pressure. A detailed model of cavitation is implemented in the 3D model.

2.1.2 1D Model Validation

To validate the 1D solver, we compared the results to the experimental data from the literature. The researchers [20,21] performed an experiment by creating a pressure wave with a rapid valve closure. A 37.23 m long copper pipe (d=22.1 mm) connected to two reservoirs was used. The pipe was installed so that it rises by 2.03 m in the flow direction.

The fluid flowed through the pipe at a speed of 0.3 m/s. The static pressure in the upstream reservoir was h=32 m. A ball valve was installed at the end of the pipe, which closed in 0.009 s with the help of a torsion spring. The propagation speed of the pressure waves is given as 1319 m/s. We used a time step of $\Delta t=10^{-5}$ s and a spatial step of Δx = 1.319 cm using 2823 nodes. The friction factor was set to f = 0.009. In Figure 2 we compare the results of the simulations with our method and the experimentally measured values [21] and numerical simulation with steady friction factor [20]. We find a good agreement, especially when the pressure wave arrives first at the measurement point, as the error in pressure surge is less than 2 %. This is the most important part for further calculations, as the highest overpressure and the longest lasting under-pressure are measured at the first pressure wave in the pipeline. We notice that later in the simulation, the simulated wavefronts are sharper in our result compared to the experimental data. This is due to the use of steady state friction factor, which does not account for the transient nature of flow. Our results compare well with the numerical results of Wan et al. [20], who also used a steady state friction factor. The use of an unsteady friction factor would improve the results, but this is not the focus of our study.

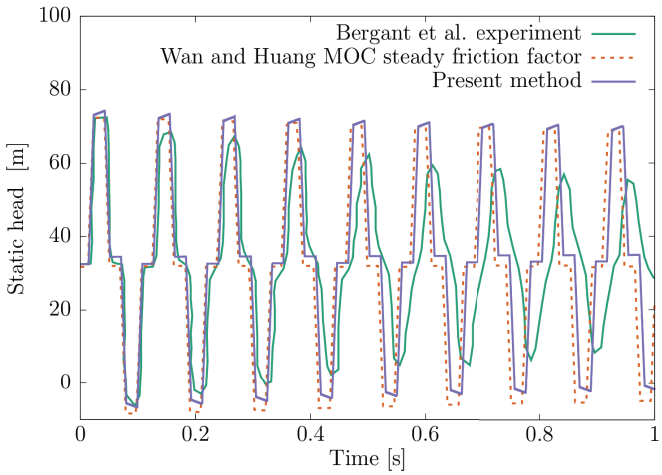

Fig. 2. Comparison of the temporal development of the static head in the center of the pipeline where time zero corresponds to the moment when the valve starts to close

2.2 3D Navier-Stokes Solver

For the 3D pressure surge calculations, we used the open-source software package OpenFOAM v11 [18], which allows simulations of multiphase fluid flows and includes models for cavitation. An analyzis of the numerical results was carried out with the open-source software package ParaView 5.12 [22].

To simulate multiphase flow, we employed the volume of fluid (VOF) method [23-28], which is a numerical technique for capturing the interface between two immiscible fluids. The VOF method models the interface by solving a single set of Navier-Stokes equations for the mixture and introduces a volume fraction field to track the distribution of each fluid within the computational domain. The volume fraction field is a scalar field that represents the fraction of each phase in a given cell. The continuity equation is:

$$\frac{\partial \rho_m}{\partial t} + \nabla \cdot (\rho_m \mathbf{u}) = 0, \tag{6}$$

where $\mathbf{u}$ is the flow velocity field and ρ_m the mixture density, calculated via the mixing rule from the liquid phase (index l) and gas phase (index v) partial mass densities:

$$\rho_m = \alpha \rho_v + (1-\alpha)\rho_l, \tag{7}$$

Here α is the gas phase volume fraction. Momentum conservation is described by the Navier-Stokes equations:

$$\frac{\partial (\rho_m \mathbf{u})}{\partial t} + \nabla \cdot (\rho_m \mathbf{u} \otimes \mathbf{u}) = -\nabla p + \nabla \cdot \mathbf{T} + f_\sigma, \tag{8}$$

where p is the pressure and $f_\sigma = \sigma_\kappa \nabla \alpha$ the source of momentum due to surface tension between the gas and liquid phase, where σ=0.07 N/m is the surface tension coefficient for water and water vapor and κ is the interface curvature [18]. Tensor $\mathbf{T}$ is the deviatoric part of Cauchy stress tensor, which includes viscosity calculated using the mixing rule, as well as the Reynolds stresses, arising from turbulence, and need to be modelled. To close the system of equations, we use the Menter's kOmegaSST turbulence model [29]. In the past, it has been discussed, that standard two-equation turbulence models tend to overpredict the eddy viscosity in vapor-liquid mixture zones, suppressing the natural unsteadiness of cavitation [30,31]. This has been solved by Reboud et al. [32], who introduced a correction term for eddy viscosity, improving the modelling of phenomena such as periodic vapor cloud shedding in turbulent cavitation flows [33]. Since our study focuses on pressure-wave propagation and column separation, rather than the detailed structure or dynamics of cavitation, we have not applied the Reboud correction. Moreover, the occurrence of periodic cavitation phenomena, such as cavity shedding, is not expected under the conditions considered in our simulations.

The VoF method requires solving an additional equation for the volume fraction field α:

$$\frac{\partial \alpha}{\partial t} + \nabla \cdot (\alpha \mathbf{u}) = S^+ - S^-, \tag{9}$$

where S^+ and S^- are source due to evaporation and condensation. To model turbulence, we chose the Menter kOmegaSST [29] turbulence model.

Finally, we solve the energy equation, which includes the effects of phase change in the S_T term:

$$\frac{\partial T \rho_m}{\partial t} + \frac{\partial E_k \rho_m}{\partial t}\frac{1}{c_{v,m}} + \nabla \cdot (\rho_m \mathbf{u} E_k)\frac{1}{c_{v,m}} + \nabla \cdot (\rho_m \mathbf{u} T) =$$
$$= \nabla \cdot \left(\frac{k_m}{\rho_m c_{p,m}} \nabla T \right) + \nabla \cdot (\rho_m \mathbf{u} p)\frac{1}{c_{v,m}} + \rho_m (\mathbf{u} \nabla \mathbf{g})\frac{1}{c_{v,m}} + S_T, \tag{10}$$

where E_k is the kinetic energy calculated as $E_k = 1/2|\mathbf{u}|^2$ and $c_{p,m}$, $c_{v,m}$ the specific heats. The first term on the right-hand side includes the thermal conductivity of the mixture, k_m, that incorporates the molecular thermal conductivity as well as the turbulent thermal conductivity.

We model cavitation using the Schnerr-Sauer et. al. [34] model, by modifying the source terms S^+ and S^- in (9) as:

$$S^+ = C_v \frac{3\alpha(1-\alpha)}{R_b}\sqrt{\frac{2}{3}\frac{\max[p_v - p, 0]}{\rho_l}}, \tag{11}$$

$$S^{-} = C_c \frac{3\alpha(1-\alpha)}{R_b}\sqrt{\frac{2}{3}\frac{\max[p-p_v,0]}{\rho_l}}. \quad (12)$$

Here R_b is the cavitation cloud diameter and p_v is the vapor pressure.

At last, the relation between pressure and density was computed using linear compressibility χ as

$$\chi_m = \alpha\chi_v + (1-\alpha)\chi_l, \quad (13)$$

and

$$d\rho_m = \chi_m dp \quad (14)$$

serves as the equation of state.

In short, the comparison of the considered phenomena between 1D and 3D simulations goes as follows:

- In 1D, no velocity profile develops, since velocity has one component that points downstream of the pipe. In 3D, we account for the viscosity, which, along with the no-slip boundary condition on the wall, develops a velocity profile.
- In 1D, we solve for the wave propagation and do not account for cavitation that might occur as a result of sudden depressurization. In 3D, we model cavitation through extra terms in the energy equation.
- In the 3D simulations we do not account for the deformation of the pipe walls.

2.2.1 3D Model Validation

Wang et. al. [35] performed an experiment to investigate the water hammer phenomenon in a pipeline with a sudden valve closure. The pipeline is 5.692 m long, DN 40 and made of plexiglass. The Darcy-Weisbach friction factor of the system ranged between 0.034 and 0.055 (Fanning factor 0.0085 to 0.0138). In their study, multiple scenarios were investigated by varying the static pressures in Tank 1 and Tank 2. This approach allowed them to achieve different initial flow velocities corresponding to different static heads in the pipeline. For the purposes of comparison, we selected the case with an initial velocity of 1.148 m/s and a static head of 1.55 m in Tank 2. After closure, they measured the pressure head versus time. For the remaining details of the experimental apparatus, the reader is directed to the reference [35].

We recreated the experiment numerically using a 2D axisymmetric approach and compared different mesh densities (Fig. 3) and time steps (Fig. 4). We observe good convergence with both mesh density and time step, and the results are in agreement with the experimental data. The error in the prediction of the maximum pressure between simulation and experiment amounts to around 2 % for the coarse and medium meshes, and 1.5 % for the fine mesh. The time step analyzis shows that the solution does not change significantly when decreasing the time step value tenfold. When the time step is decreased by a factor of 100, numerical instability is observed. We attribute this to the fact that for very small time steps approaching machine double-precision limits, the transport phenomena become dominated by the accumulation term. This term can reach disproportionately large values due to the combination of very small time increments and the accumulation of machine precision errors, which are of a similar magnitude to the time step itself.

The experimental pressure history, however, exhibits a substantially broader pulse following cavity collapse than predicted in our rigid-wall simulations. The duration of the experimental pulse is governed by the round-trip wave travel time $2L/c_{eff}$, where the effective wave speed c_{eff} depends not only on fluid compressibility but also on the compliance of the pipeline and reservoir walls. These elastic effects are absent from our rigid-wall model and therefore shorten the simulated pulse relative to the experiment. In addition, the experimental traces display damped oscillatory tails after the main impulse. The fact that Wang et al. observed the same repeatable waveform across all BV2 valve closure cases strongly supports the interpretation that these features are systematic instrumentation effects rather than random measurement noise. Further broadening of the measured signal could also arise from the influence of elbows and fittings, which extend the effective propagation path and introduce partial reflections and scattering. Taken together, these structural and instrumental effects smear and lengthen the measured time history compared with the rigid-wall model used here.

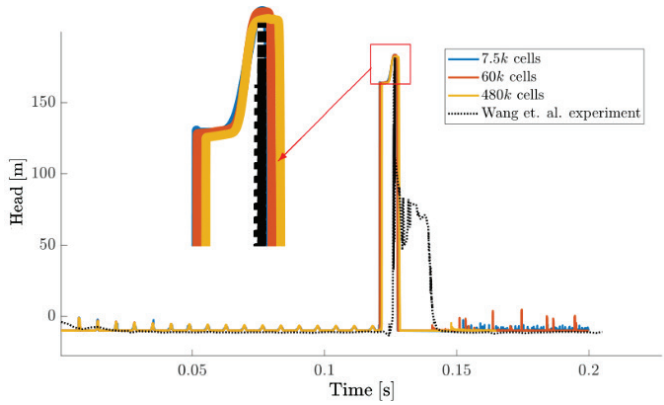

Fig. 3. Pressure head versus time for different mesh densities

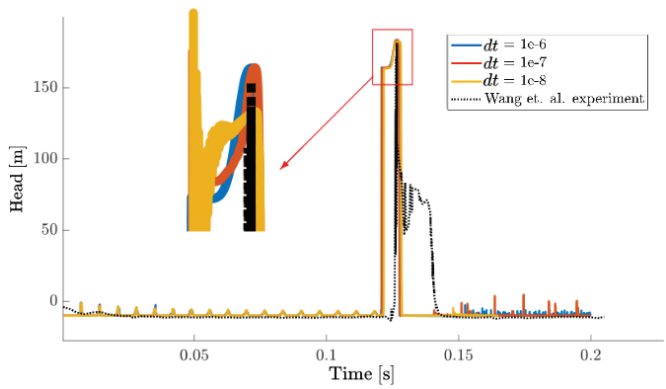

Fig. 4. Pressure head versus time for different time steps, for mesh with 7500 cells

2.3 Pipeline Length

The length of the pipeline is an important parameter in the water hammer analyzis. The longer the pipeline, the longer the time it takes for the pressure wave to travel from the valve to the end of the pipeline. This can result in higher pressure surges and longer duration of underpressure. While for 1D simulations the pipeline length is easily adjusted, for 3D simulations the computational cost increases with the length of the pipeline. Time step analyzis in the previous section showed that good results are achieved when the pressure wave does not travel more than one element within one time step, i.e. time step is limited by the Courant-Friedrichs-Lewy (CFL) condition. This sets the limit for the pipeline length in 3D simulations due to the computational effort required.

3 RESULTS

3.1 The Pipeline

To test and compare the 1D and 3D approaches we simulate a pipeline with a length of $L = 3408.45$ m and a diameter of DN400,

which connects a pumping station and a reservoir and assumes an electrical power failure, which stops the pump. The pipeline is made of 17 steel segments; its profile is shown in Fig. 5. The inner diameter of the pipe is 400.1 mm, the outer 406.4 mm, the wall thickness is 6.3 mm. Height difference between the pumping station and the outlet is z_0=8.16 m. The Young's modulus of E=207·109 Pa is used. In normal operation we consider water (ρ=999.84 kg/m^3, χ=4.54·10^{-10} Pa^{-1}, ν=1.005·10^{-6} m^2/s) flowing at a rate of Q_0 = 750 m^3/h with an average velocity of v_0=1.66 m/s. The pressure wave speed in these conditions, Eq. (2), is c=1310 m/s, which gives a characteristic wave travel time of $\tau=L/c$=2.6 s. The friction factor is calculated for each pipe segment separately; the average is f_{ave}=0.0067±2.79·10^{-5}.

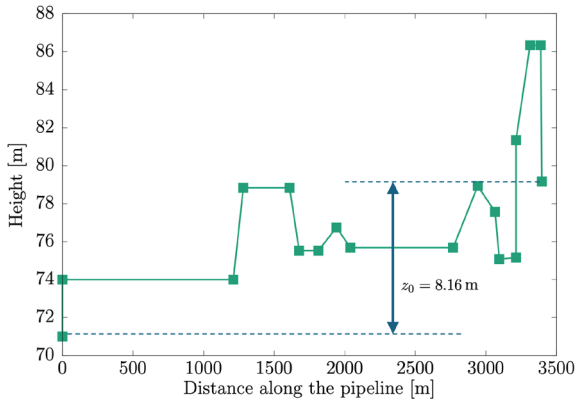

Fig. 5. A 17-segment pipeline profile with length of 3408.45 m

We assume that electrical power supply fails, which stops the pump. The discharge decreases from Q_0 to $Q_{\min}=\beta Q_0$ in t_{stop}. The pressure wave travels from the pumping station to the reservoir, where it reflects and travels back. At β=0 the discharge is $Q_{\min}$=0 meaning that the power loss completely blocks the flow. This represents the worst-case scenario, as it results in the highest-pressure surges in the pipeline. For 0<β<1 the discharge is not completely blocked. We assume that between t_0 and $t=t_{stop}$ linear upstream end discharge variation:

$$Q(t)=\begin{cases}\beta Q_0+(1-\beta)Q_0\left(1-\dfrac{t}{t_{stop}}\right) & t\le t_{stop}\\ \beta Q_0 & t>t_{stop}\end{cases}. \quad (15)$$

The pump manufacturers estimated the time in which the discharge stops after electrical power failure at t_{stop} is 15 s to 20 s. To estimate the worst-case scenario, we make the following estimate. The pump is rotating at ω_0=1488 rpm, has a moment of inertia of I=3.614 kg/m^2, its pump efficiency is η=0.72 and has the electrical power of P_{el}=132 kW and provides 40.2 m of pressure head. We first estimate the useful work $P=\rho g\Delta h Q_0/\eta$=14 kW. This gives a normal operation torque of $M_0=P/\omega_0$=732 Nm. The pump stops when the kinetic energy of the rotating parts is converted to the potential energy of the water column. We assume that the average torque is half of the normal operation torque and write a differential equation for the angular acceleration:

$$\frac{d\omega}{dt}=-\frac{P}{2\omega_0 I}. \quad (16)$$

After integration up to time t_{stop} we are able to estimate the time when the pump stops:

$$t_{stop}=\frac{2\omega_0^2 I}{P}=1.5\text{ s}. \quad (17)$$

This value serves as the worst-case scenario in the analyzis below.

3.2 1D Simulation Results

In this section we present the results obtained using the developed 1D inviscid solver. We focus specifically on the time frame before cavitation occurs as the objective of this work is to identify the pump failure conditions that lead to cavitation. Detailed simulation including cavitation were done with the 3D viscous solver and are presented in the next section. If cavitation does occur in the 1D simulation, we limit the pressure to vapor pressure and let the simulation continue.

3.2.1 Grid Sensitivity Analyzis

In Table 1 we show three sets of numerical parameters used in simulations. We compare the results of the simulations with the parameters $\mathcal{A}$, $\mathcal{B}$ and $\mathcal{C}$ at time t=3.4τ (Fig. 6). By calculating the relative difference between the head and velocity profiles we obtain the values shown in Table 1. The relative difference norm is calculated as: $\sum_i\left(f_i^a-f_i^b\right)^2/\sum_i\left(f_i^a\right)^2)^{1/2}$, where f is either head or velocity, i is the index of the node and $a,b=\mathcal{A}$, $\mathcal{B}$ or $a,b=\mathcal{B}$, $\mathcal{C}$. We observe that the difference in results between numerical parameter sets $\mathcal{B}$ and $\mathcal{C}$ is very small, which shows that the numerical parameters do not affect the results. We use parameters $\mathcal{B}$ in all further simulations.

Table 1. Time step, distance between nodes and the number of nodes used for sensitivity analyzis

Numerical parameters	Time step Δt [s]	$\Delta x=c\Delta t$ [cm]	Number of nodes	Norm head	Norm velocity
$\mathcal{A}$	10^{-3}	131	2627		
$\mathcal{B}$	10^{-4}	13.1	26047	0.0413	0.0663
$\mathcal{C}$	5·10^{-5}	6.55	52067	0.0018	0.0029

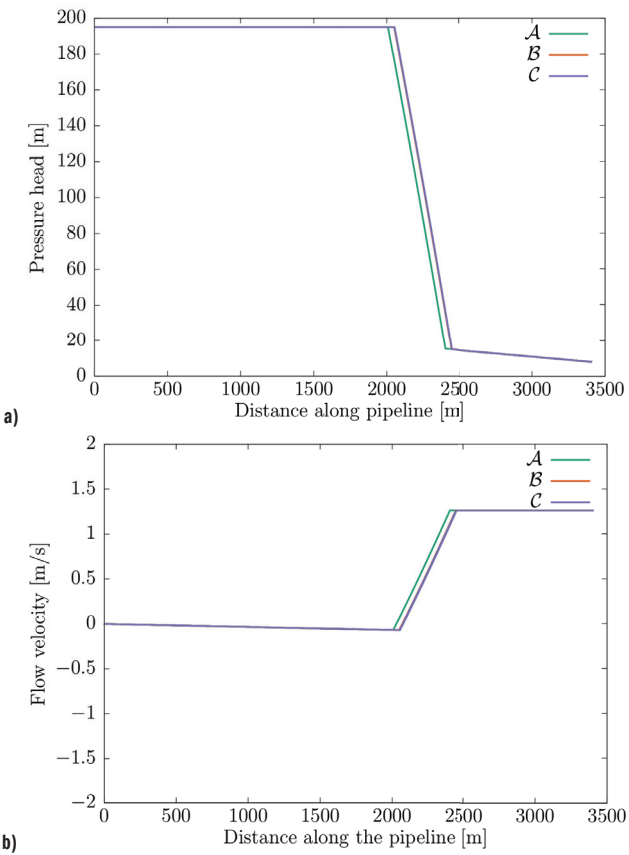

Fig. 6. a) Head, and b) velocity profile at t = 3.4 τ

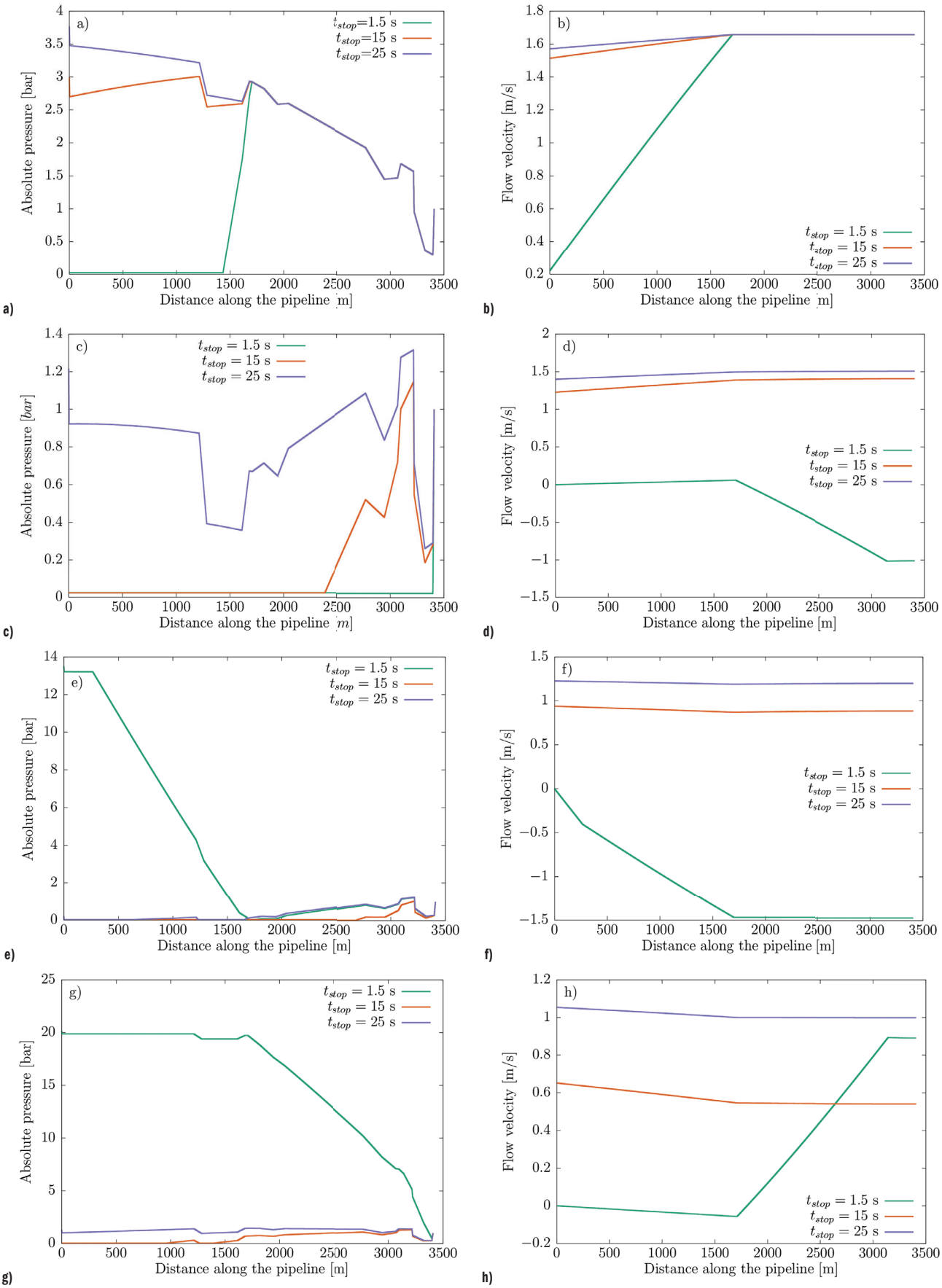

Fig. 7. a), c), e), g) Absolute pressure, and b), d), f), h) flow velocity profiles for three stopping times and four-time instants: a), b) $t=0.5\tau=1.3$ s, c), d) $t=1.5\tau=3.9$ s, e), f) $t=2.5\tau=6.5$ s and g), h) $t=3.5\tau=9.1$ s

3.2.2 Discharge stops completely, $\beta=0$

We simulate the worst-case scenario, when the discharge stops completely, $\beta=0$ and consider three stopping times: $t_{stop}=1.5$ s, which represent the worst case scenario, $t_{stop}=15$ s, which is the pump manufactures estimate and $t_{stop}=25$ s. Figure 7 shows absolute pressure and flow velocity profiles for four-time instances. At half of the characteristic time, the pressure wave has travelled through half of the pipeline. In the case of a fast interruption of the flow, we see that the flow has stopped in the first half of the pipeline and the pressure there has dropped to the vapor pressure. In the case of slow interruption, the flow velocity in the first half of the pipeline only decreases, and the pressure drops, but not yet to the vapor pressure. At $t=1.5\tau$, the pressure wave has already been reflected from the end of the pipeline and travels back to the pump. In the case of a rapid interruption of the flow, we see that the water in the second half of the pipeline flows towards the pump and the pressure wave consequently also moves towards the pump. When it reaches it at $t=2\tau$, it will cause a sharp increase in pressure there. If we look at the pressure curve for $t_{stop}=15$ s, we can see that the pressure has now also fallen to the vapor pressure in this case. In the case of $t_{stop}=25$ s, the pressure is still falling but has not yet reached the vapor pressure. Nevertheless, the vapor pressure also occurs in this case, as can be seen from the pressure curve at $t=2.5\tau$. At the same time, we see at $t=2.5\tau$ that in the case of $t_{stop}=1.5$ s the pressure in the part of the pipeline near the pump has increased significantly, which is a result of the sudden stop of the water flowing towards the pump. This phenomenon is greatly

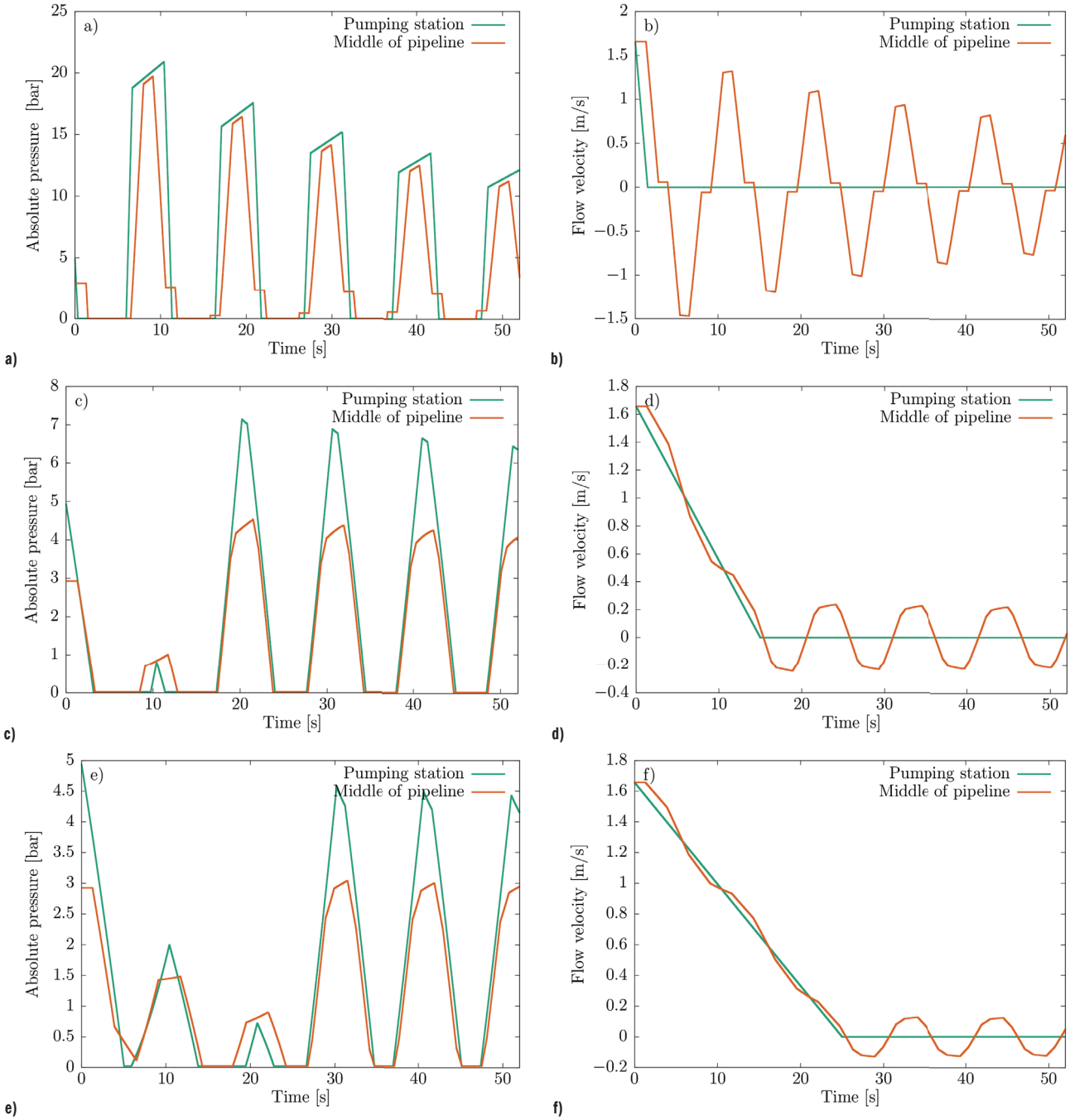

Fig. 8. Time traces of absolute pressure (left) and flow velocity (right) for three flow stopping times: a), b) $t_{stop}=1.5$ s, c), d) $t_{stop}=15$ s, e), f) $t_{stop}=25$ s

attenuated in cases where the time for the flow to stop is longer, as it occurs later when the water velocity decreases and then hits the pump at a much lower speed.

Figure 8 shows the time histories of absolute pressure and flow velocity at the center of the pipeline and at the beginning of the pipeline near the pump. Green line denotes the values at the pumping station, orange the values at the middle of the pipeline. The results are shown up to 52 s, which is twenty characteristic times. The simulation results are shown for three flow stopping times, for t_{stop}=1.5 s, t_{stop}=15 s and t_{stop}=25 s. We notice considerable differences in the progression. At a very fast stop, t_{stop}=1.5 s, the pressure wave travels back and forth along the pipeline and at the selected location we observe a clear and distinct velocity fluctuation between positive values (flow from the pump to the end of the pipeline) and negative values (flow back from the end of the pipeline to the pump). The pressure behaves similarly, with the difference that in the part where the pressure drops, it quickly reaches the vapor pressure and the growth of the water vapor column begins. The 1D simulation does not take cavitation into account, so the results in this part show a constant vapor pressure of 2337 Pa. When the flow stop is slower, there is interference between the pressure waves travelling back and forth along the pipeline and between the consequences of the slow decrease in velocity. In both cases, t_{stop}=15 s and t_{stop}=25 s the stopping time is longer than the characteristic time τ=2.6 s. Due to this interaction, we see that up to t_{stop} there is no enormous increase in pressure, but this increase is smaller. Even later, when a more significant increase in pressure occurs, we see that the maximum pressure in the system is much lower than in the case of a rapid flow interruption.

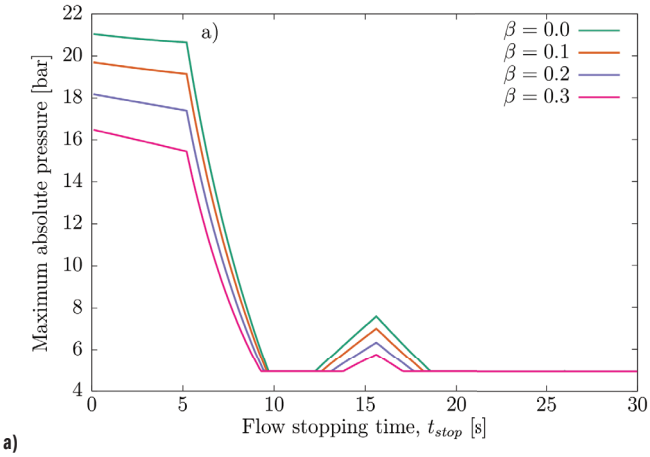

a)

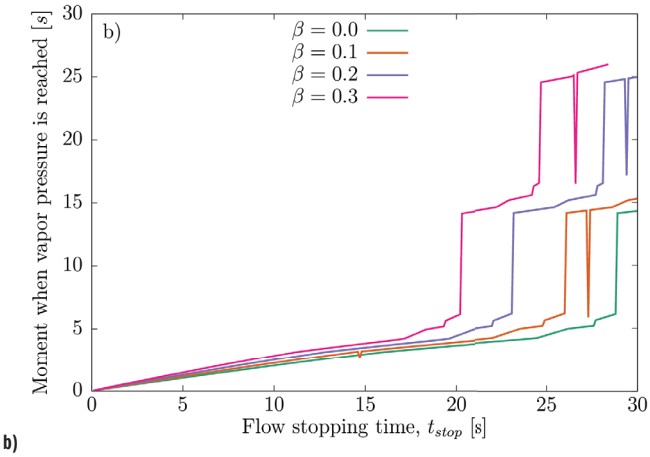

b)

Fig. 9. a) Maximal absolute pressure in the pipeline, and b) the moment when vapor pressure is reached versus flow stopping time t_{stop} for different β

In Figure 9 we show the maximum absolute pressure that occurs in the pipeline as a function of the flow stop time tstop. We see that in the case of a very fast flow interruption, when the flow is interrupted before the pressure wave has travelled through the pipeline and back, i.e. when $t_{stop}<2\tau$=5.2 s, a very large pressure increase occurs in the system. The increase corresponds to the Joukowsky pressure $\Delta p=\rho c v_0$=21.7 bar. If the flow is closed slower than 2τ=5.2 s, the Joukowsky pressure is not reached. At about $t_{stop}=4\tau$=10.4 s the maximum pressure drops and reaches the value of normal operation. Interestingly, if the stopping time corresponds to three or four propagation times of the pressure wave through the system $4\tau<t_{stop}=8\tau$, we see a further, smaller increase in the maximum pressure. This is due to the interference between the propagating wave and the point at which the flow is interrupted. When interpreting this diagram, it must be emphasized that the maximum pressure in the system occurs after the moment when vapor pressure has been reached in the system. Since the numerical model presented in this section limits the pressure to vapor pressure and does not take cavitation into account, the values are too high. A more accurate 3D model, which is presented in the next section, shows that the maximum pressure is lower.

At the same time, in Fig. 9, we show the moment when the pressure drops to vapor pressure depending on the time in which the flow is interrupted. We note that regardless of whether the flow is interrupted very quickly (1.5 s) or slowly (45 s), the vapor pressure is always reached. If the discharge reduction is very slow and lasts longer than approximately 45 s, we see that pressure does not decrease to vapor pressure and at the same time it does not increase anywhere in the pipeline. Given that the estimate of the flow interruption time obtained from the pump manufacturer indicates a time of about 20 s, it means that measures are needed in the proposed pipeline to mitigate the consequences of the formation of pressure waves due to the failure of the pump power supply. We see that the case when the flow is completely interrupted (β=0) is the most demanding case from an engineering point of view, since vapor pressure occurs first in this case and the highest pressure achieved in the system is the highest. Therefore, the results at β=0 can be considered as the worst possible scenario and if in a real system the pump allows some flow, this alleviates the situation.

3.3 3D Viscous Simulation Results

3.3.1 Reduced Length Pipeline

The computational requirements for a 1D simulation of the full length (3.4 km) pipeline for 50 s using a million time steps are about 10 minutes on a single core. The computational requirements for a 3D simulation of the full-length pipeline are much higher, as the number of nodes in the 3D mesh would be at a minimum about 10^6 and the time step is limited by the CFL condition. The computational requirements for a 3D simulation of the full-length pipeline are about 1000 times higher than for a 1D simulation. This means that the computational requirements for a 3D simulation of the full-length pipeline are about 104 hours, which is prohibitive.

To reduce the computational cost, we simulate a shorter pipeline (L_r=120 m) with the same diameter (DN400) and the same discharge (Q_0=750 m^3/h) while at the same time at linearly reduced pressure drop. We calculated equivalent flow stopping times for the reduced pipeline so that their ratio to the characteristic time is the same as for the full-length pipeline, i.e. $t_{stop,120\ m}/(L_r/c)=t_{stop,3400\ m}/\tau$. To capture the rapid transient dynamics of column separation and the subsequent water hammer, a time discretization of at least one microsecond was required, resulting in several million time steps for a full-length

pipeline simulation. By reducing the numerical pipeline length while preserving equivalent stopping times, the total number of required time steps was decreased, reducing computational time from several weeks to a few days per simulation.

The results show that a large cavitation bubble forms behind the pump and due to energy lost for this process the pressure wave reaches smaller absolute pressure values as compared to the inviscid simulation results. Figure 10 shows the pressure curve just downstream of the pump, for different pump stopping times. We find that the magnitude of the pressure surge is largest for stopping time 1.5 s and amounts to 7.4 bar. We tested shorter stopping times as well and found similar maximal pressure surges for them. At a stopping time of 15 s we find that the magnitude of the pressure surge is lower and amounts to 6.3 bar. As the pump stopping time is further extended, the magnitude of the pressure surge decreases. We begin to observe the phenomenon when the pressure wave reflected from the outlet returns to the pump before cavitation occurs. The lower values of the pressure surge can be explained by analyzing the average velocity in the pipeline in Fig. 11. At the moment when the cavitation bubble collapses the flow velocity is lower in the case of longer pump stopping time. A long pump stopping time causes deceleration of the average water velocity in the pipeline, which can be seen in the enlarged image in Fig. 11. The pump stopping time can thus be interpreted as a relaxation rate, which determines the point in time when the cavitation bubble will start to grow. This is evident in Fig. 12, where the cavitation bubble length is shown. The cavitation bubble stops growing when the water velocity in the pipeline is zero.

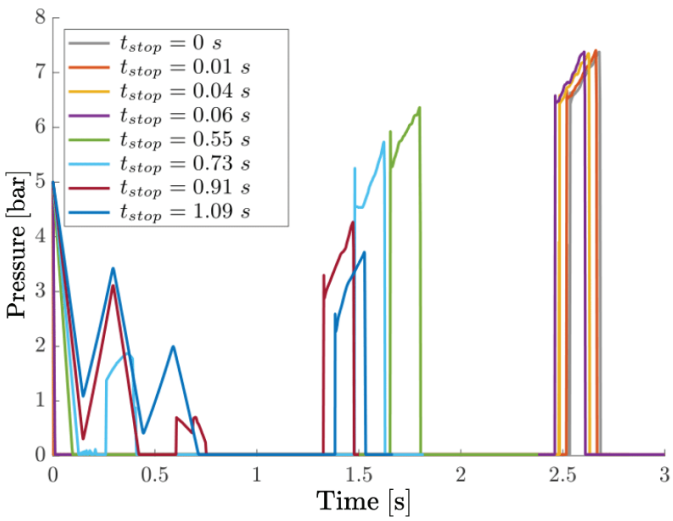

Fig. 10. Pressure time traces for different flow stopping times

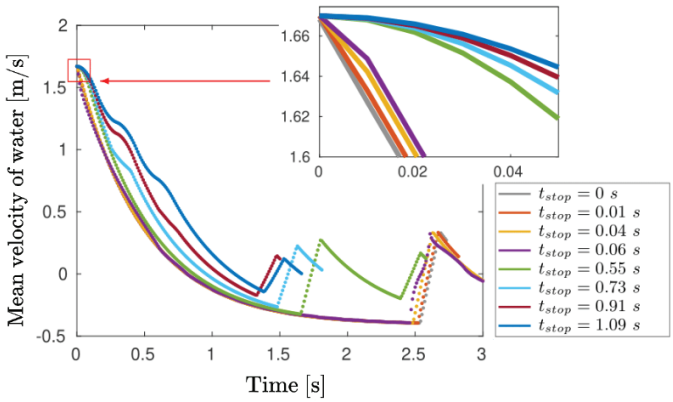

Fig. 11. Average flow speed for different flow stopping times

Figure 13 shows the maximal length of the cavitation bubble and the maximal absolute pressure for different pump stopping times. We see that the maximal length of the cavitation bubble is largest for the shortest pump stopping time and amounts to ≈ 0.55 m. The maximal length of the cavitation bubble decreases with increasing pump stopping time. The maximal absolute pressure is largest for the shortest pump stopping time and amounts to 7.4 bar. The maximal absolute pressure also decreases with increasing pump stopping time. The maximal absolute pressure is lower than in the inviscid simulation, which is due to the energy lost for the cavitation process.

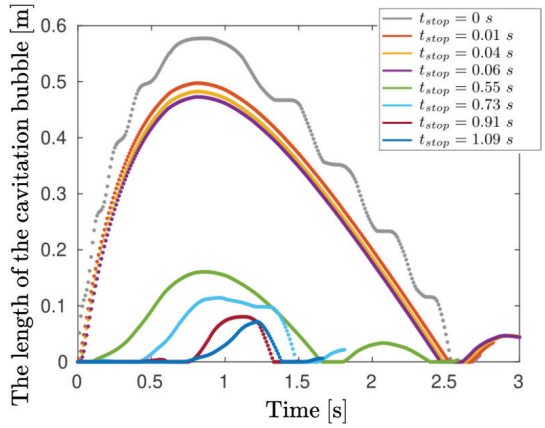

Fig. 12. Length of cavitation bubble for different pump stop times

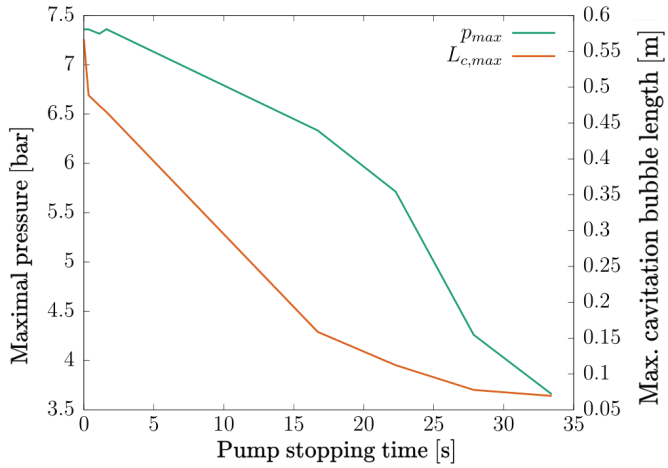

Fig. 13. Maximal length of cavitation bubble and maximal absolute pressure for different pump stopping times

3.3.2 Dynamic Combination Air Valve Simulation

Both 1D and 3D simulations showed that in the case of sudden loss of electrical power supplying the pump a pressure surge occurs, vapor pressure is reached in the pipeline and cavitation occurs. One possible measure that could be taken to mitigate the consequences of the pressure surge and cavitation, is to install a dynamic combination air valve behind the pump outlet.

The dynamic combination air valve opens when the pressure exceeds or is below a certain value and allows the water to flow out or air to be sucked into the pipeline. We simulate the pipeline with the dynamic combination air valve installed and compare the results with the case when the dynamic combination air valve is not installed. We study the use of ARI D-070 dynamic combination air valve [36] for which discharge versus pressure drop curves are available from the manufacturer. The simulation domain is only the first 24 m of the

pipeline with the dynamic combination air valve installed, details are shown in Fig. 14.

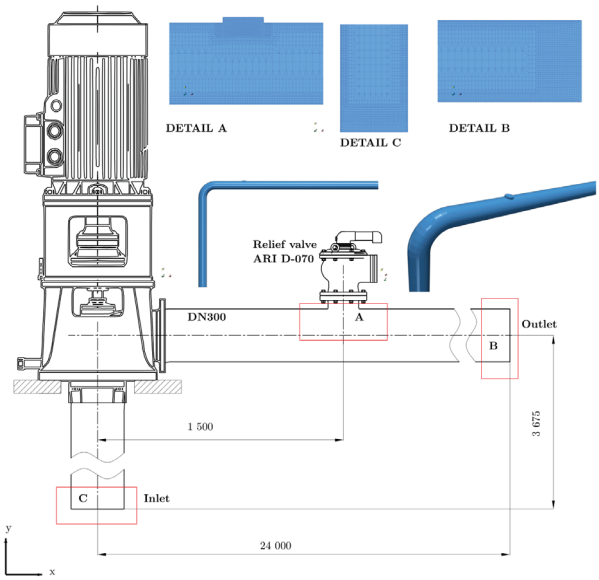

Fig. 14. Geometry of the 3D simulation domain with the dynamic combination air valve installed

The boundary conditions used were defined as follows. The discharge at the inlet linearly had the turbulent flow profile shape and the discharge decreased to zero in the chosen flow stopping time tstop. No change in the pressure and the water vapor volume fraction was assumed to occur across the inlet surface.

No slip boundary condition was used on the pipe wall. Wall functions were used for turbulent quantities.

The flow velocity at the dynamic combination air valve is modelled based on the difference between the pressure in the pipeline and the atmospheric pressure:

$$u_y|_{vent} = \begin{cases} -K\sqrt{\dfrac{p_{atm}-p}{\rho_a}}, & p < p_{atm}, \\ 0\,\bar{m}/s, & p > p_{atm} \end{cases} \tag{18}$$

where $K=0.7$ was calibrated based on the manufacturer's pressure drop curve and $\rho_a=1.225$ kg/m^3 is the air density. The fluid volume fraction depends on the flow direction. When the pressure inside the pipeline exceeds the external pressure, the medium is water; when the external pressure is higher, air enters instead. The negative sign in front of K arises from the chosen coordinate system (see Fig. 14), where the inflow of air is defined in the negative y-direction. At this boundary, a zero pressure gradient is imposed. At the outlet, the pressure is fixed at $p=497{,}000$ Pa, and outflow boundary conditions are applied to the velocity. In Figure 15 we show a comparison of pipelines with and without a dynamic combination air valve. The left panel shows a comparison of the growth of the cavitation bubble. The right panel shows the entry of air through the dynamic combination air valve due to the pressure drop in the pipeline. The results are shown for an equivalent pump stop time $t_{stop}=1.5$ s. When the pump stops, we observe the growth of the cavitation bubble in both cases. The ingress of air into the pipeline leads to an increase in the average pressure, so that the cavitation bubble collapses earlier in the case of using a dynamic combination air valve.

The results of the pressure surge for the cases with and without a dynamic combination air valve are shown in Fig. 16. The use of a dynamic combination air valve reduces the size of the pressure surge by a third. The reason for the faster collapse of the cavitation bubble and thus the smaller size of the pressure surge can be found in the analyzis of the pressure conditions downstream of the pump before the pressure surge is triggered, in Fig. 17. Here we can see the increase in pressure in the system, which is due to the ingress of air from the environment. The pressure rises above the saturation pressure, which prevents further growth of the cavitation bubble and causes its premature collapse.

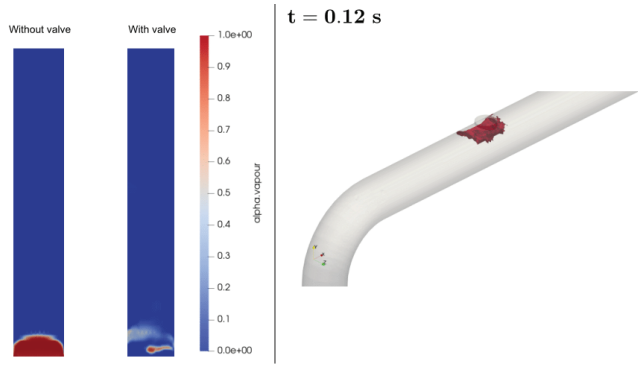

Fig. 15. Comparison of water vapor content in the pipeline with and without the dynamic combination air valve

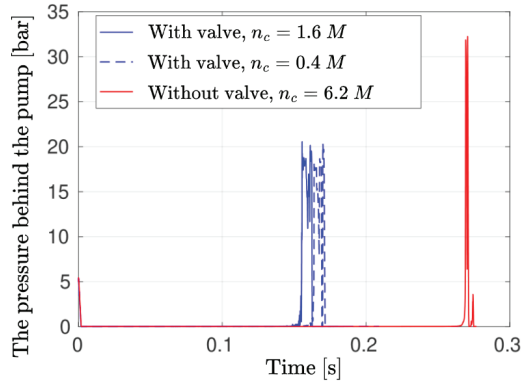

Fig. 16. Pressure surge in the pipeline with and without the dynamic combination air valve

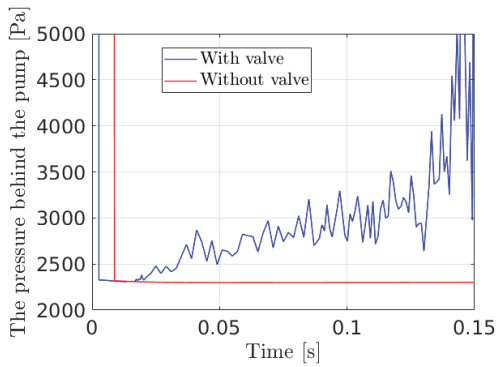

Fig. 17. Pressure at the start of the pipeline, directly after the pump

4 CONCLUSIONS

We have developed and compared a 1D inviscid and a 3D viscous numerical simulation tool to model the pressure surge and pressure drop in a pipeline subjected to a sudden suspension of flow. The main advantage of the inviscid simulation is that it can be performed with minimal computational resources for pipeline systems at an engineering level. It can correctly predict the pressure surge and the presence of the conditions that would lead to pressure dropping to vapor pressure. However, it does not model cavitation dynamics. On the other hand, viscous 3D simulation is severely limited by

computational resources, making it impossible to simulate a pipeline over its entire length. We have shown that with the necessary steps it is possible to obtain good results for an equivalent short pipeline. The main advantage of viscous simulations is the fact that it is possible to model water phase change and the influence of these changes on the flow dynamics in a detailed 3D model.

This advantage becomes particularly clear when the case of simulation of the pipeline with a dynamic combination air valve. Such a simulation is not possible with an inviscid simulation but gives an important insight into the efficiency of such a valve as protection against pressure surges or cavitation. Our simulations have shown that such a measure significantly alters the flow dynamics in the pipeline. The valve releases air into the system when the pressure drops, which prevents the formation of a vacuum and consequently prevents the pipe from flattening. At the same time, the valve allows air and water to be released from the pipeline at the moment when the pressure wave returns and the pressure rises. This reduces the maximum pressure reached in the system and protects the pipeline from rupture.

References

[1] Kjerrumgaard Jensen, R., Kær Larsen, J., Lindgren Lassen, K., Mandø, M., and Andreasen, A. Implementation and validation of a free open source 1D water hammer code. *Fluids* 3 64 (2018) **DOI:10.3390/fluids3030064**.

[2] Sadafi, M., Riasi, A., Nourbakhsh, S. A. Cavitating flow during water hammer using a generalized interface vaporous cavitation model. *J Fluids Struct* 34 190-201 (2012) **DOI:10.1016/j.jfluidstructs.2012.05.014**.

[3] Cao, Y., Zhou, L., Ou, C., Fang, H., Liu, D. 3D CFD simulation and analyzis of transient flow in a water pipeline. *J Water Supply Res Technol-Aqua* 71 751-767 (2022) **DOI:10.2166/aqua.2022.023**.

[4] Khan, F., Kumar, A., Abbas, A., Gupta, D.P., Binjolkar, P. Computational fluid dynamics based transient investigation of the penstock in a hydropower plant. *IOP Conf Ser-Earth Environ Sci* 1411 012059 (2024) **DOI:10.1088/1755-1315/1411/1/012059**.

[5] Morvarid, M., Rezghi, A., Riasi, A., Haghighi Yazdi, M. 3D numerical simulation of laminar water hammer considering pipe wall viscoelasticity and the arbitrary Lagrangian-Eulerian method. *World J Eng* 15 298-305 (2018) **DOI:10.1108/WJE-08-2017-0236**.

[6] El-Hazek, A., Halawa, M. Optimum hydro pneumatic tank sizing to protect transmission pipelines supply system against water hammer. *Eng Res J (Shoubra)* 53 212-221 (2024) **DOI:10.21608/erjsh.2023.241739.1228**.

[7] Zhang, B., Wan, W., Shi, M. Experimental and numerical simulation of water hammer in gravitational pipe flow with continuous air entrainment. *Water* 10 928 (2018) **DOI:10.3390/w10070928**.

[8] Meng, Q.Z., Yang, C., Liu, L.S., Wang, Z. Effect of wall roughness and flow velocity on water hammer. *Adv Mater Res* 1014 185-191 (2014) **DOI:10.4028/www.scientific.net/AMR.1014.185**.

[9] Nikpour, M.R., Nazemi, A.H., Dalir, A.H., Shoja, F., Varjavand, P. Experimental and numerical simulation of water hammer. *Arab J Sci Eng* 39 2669-2375 (2014) **DOI:10.1007/s13369-013-0942-1**.

[10] Han, Y., Shi, W., Xu, H., Wang, J., Zhou, L. Effects of closing times and laws on water hammer in a ball valve pipeline. *Water* 14 1497 (2022) **DOI:10.3390/w14091497**.

[11] Zhang, K., Zeng, W., Simpson, A.R., Zhang, S., Wang, C. Water hammer simulation method in pressurized pipeline with a moving isolation device. *Water* 13 1794 (2021) **DOI:10.3390/w13131794**.

[12] Aguinaga, A., Cando, E., Orquera, E. The Mechatronic approach in the mathematical modelling and simulation to control the water hammer in hydraulic facilities. *Proc 9th World Congr Mech Chem Mater Eng* 101 (2023) **DOI:10.11159/icmie23.101**.

[13] Wu, L., You, R., Wang, W., Zhang, F. Status of research on water hammer effect in long distance pressure pipelines. *J Eng Res Rep* 23 204-211 (2022) **DOI:10.9734/jerr/2022/v23i12778**.

[14] Yang, S., Wu, D., Lai, Z., Du, T. Three-dimensional computational fluid dynamics simulation of valve-induced water hammer. *Proc Inst Mech Eng C-J Mech Eng Sci* 231 2263-2274 (2017) **DOI:10.1177/0954406216631780**.

[15] Zhang, W., Yang, S., Wu, D., Xu, Z. Dynamic interaction between valve-closure water hammer wave and centrifugal pump. *Proc Inst Mech Eng C-J Mech Eng Sci* 235 6767-6781 (2021) **DOI:10.1177/09544062211000768**.

[16] Malesinska, A., Kubrak, M., Rogulski, M., Puntorieri, P., Fiamma, V., Barbaro G. Water hammer simulation in a steel pipeline system with a sudden cross section change. *J Fluids Eng* 143 091204 (2021) **DOI:10.1115/1.4050728**.

[17] Lupa, S.-I., Gagnon, M., Muntean, S., Abdul-Nour, G. The impact of water hammer on hydraulic power units. *Energies* 15 1526 (2022) **DOI:10.3390/en15041526**.

[18] Weller, H.G., Tabor, G., Jasak, H., Fureby, C. A tensorial approach to computational continuum mechanics using object-oriented techniques. *Comp Phys* 12 620-631 (1998) **DOI:10.1063/1.168744**.

[19] Douglas, J.Jr., Russell, T.F. Numerical methods for convection-dominated diffusion problems based on combining the method of characteristics with finite element or finite difference procedures. *SIAM J Numer Anal* 19 871-885 (1982) **DOI:10.1137/0719063**.

[20] Wan, W. Huang, W. Water hammer simulation of a series pipe system using the MacCormack time marching scheme. *Acta Mech* 229 3143-3160 (2018) **DOI:10.1007/s00707-018-2179-2**.

[21] Bergant, A., Simpson, R.A., Vitkovsky, J. Developments in unsteady pipe flow friction modelling. *J Hydraul Res* 39 (2001) 249-257 **DOI:10.1080/00221680109499828**.

[22] Ayachit, U., Geveci, B., Avila, L. *The ParaView guide: Updated for ParaView version 4.3*, Technical report (2015).

[23] Cazzoli, G., Falfari, S., Bianchi, G.M., Forte, C., Catellani, C. Assessment of the cavitation models implemented in OpenFOAM® under DI-like conditions. *Energy Proc* 101 638-645 (2016) **DOI:10.1016/j.egypro.2016.11.081**.

[24] Koch, M. Lechner, C., Reuter, F., Köhler, K., Mettin, R., Lauterborn, W. Numerical modeling of laser generated cavitation bubbles with the finite volume and volume of fluid method, using OpenFOAM. *Comput Fluids* 126 71-90 (2016) **DOI:10.1016/j.compfluid.2015.11.008**.

[25] Ngoc, T.V., Luan, M.N., Hieu, N.K. Numerical modelling of freestream cavitating flow through ship propeller using OpenFOAM. *IOP Conf Ser Mater Sci Eng* 1109 (2021) 012048 **DOI:10.1088/1757-899X/1109/1/012048**.

[26] Pendar, M.-R., Roohi, E. Investigation of cavitation around 3D hemispherical head-form body and conical cavitators using different turbulence and cavitation models. *Ocean Eng* 112 287-306 (2016) **DOI:10.1016/j.oceaneng.2015.12.010**.

[27] Zhang, H., Zhang, L. Numerical simulation of cavitating turbulent flow in a high head Francis turbine at part load operation with OpenFOAM. *Procedia Eng* 31 156-165 (2012) **DOI:10.1016/j.proeng.2012.01.1006**.

[28] Savio, A., Cianferra, M., Armenio, V. Analysis of performance of cavitation models with analytically calculated coefficients. *Energies* 14 6425 (2021) **DOI:10.3390/en14196425**.

[29] Menter, F.R. Elements of industrial heat transfer predictions. *16th Braz Congr Mech Eng (COBEM)* Uberlandia (2001).

[30] Sorgüven, E., Schnerr, G.H. Modified k - ω model for simulation of cavitating flows. *Proc Appl Math Mech* 2 386-387 (2003) **DOI:10.1002/pamm.200310177**.

[31] Kevorkijan, L., Pezdevsek, M., Bilus, I., Hren, G. Cavitation erosion modelling - comparison of different driving pressure approaches. *Int J Simul Model* 22 233-244 (2023) **DOI:10.2507/IJSIMM22-2-639 233**.

[32] Reboud, J.-L., Stutz, B., Coutier, O. Two phase flow structure of cavitation: Experiment and modeling of unsteady effects. *3rd Int Symp Cavit*, Grenoble 28 1-8 (1998).

[33] Peters, A., El Moctar, O. Numerical assessment of cavitation-induced erosion using a multi-scale Euler-Lagrange method. *J Fluid Mech* 894 A19 (2020) **DOI:10.1017/jfm.2020.273**.

[34] Schnerr, G.H., Sauer, J., Physical and numerical modeling of unsteady cavitation dynamics. *Proc 4th Int Conf Multiphase Flow*, New Orleans (2001).

[35] Wang, H., Zhou, L., Liu, D. Experimental investigation of column separation using rapid closure of an upstream valve. *Appl Sci* 13 12874 (2023) **DOI:10.3390/app132312874**.

[36] Aquestia.com. *https://www.arivalves.com/products/water-supply/item/d-070-dynamic-combination-air-valve*, accessed 2024-09-01.

Acknowledgements *The authors would like to acknowledge the support of their respective institutions and the company Rudis, l.l.c. Trbovlje.*

Received: 2025-04-08, revised: 2025-07-04, 2025-09-13, accepted: 2025-09-19 *as Original Scientific Paper 1.01.*

Conflict of interest *The authors declare that there is no conflict of interest.*

Data availability *The data that support the findings of this study are available from the corresponding author upon reasonable request.*

Author contribution *Nejc Vovk: Investigation, Writing - review & editing; Jure Ravnik: Methodology, Software, Supervision, Writing - original draft, Writing - review & editing.*

Primerjava simulacij vodnega udara na podlagi 1D Eulerjeve enačbe in 3D Navier-Stokesove enačbe

Povzetek *Pojav vodnega udara v cevovodih lahko povzroči porast tlaka, kar vodi do strukturnih okvar cevovodov. Ta študija predstavlja primerjalno analizo dveh numeričnih pristopov za simulacijo vodnega udara: enodimenzionalni (1D) neviskozni model z dodanim trenjem, ki temelji na Eulerjevih enačbah in metodi karakteristik, ter tridimenzionalni (3D) viskozni model, ki uporablja Navier-Stokesove enačbe v OpenFOAM simulacijskem okolju. Najprej je prikazana validacija pristopov, nato obe metodi uporabimo za simulacijo 3,4 km dolgega cevovoda DN400, ki je izpostavljen nenadni okvari črpalke, kjer analiziramo tlačni udar s pretrganjem vodnega stoplca. 1D model učinkovito napoveduje prehodne tlačne valove in kavitacijske pogoje z minimalnimi računskimi stroški, medtem ko 3D model zagotavlja podrobno študijo dinamike večfaznega toka, vključno z rastjo in kolapsom kavitacijskih mehurjev po metodi končnih volumnov. Za ublažitev neželenih efektov je predlagan kombinirani zračni ventil, za katerega smo dokazali učinkovitost pri zmanjševanju tlačnega udara in kavitacije. Rezultati poudarjajo kompromise med računsko učinkovitostjo in natančnostjo pri modeliranju pojavov vodnega udara in poudarjajo pomen zaščitnih ukrepov v cevovodnih sistemih.*

Ključne besede *vodni udar, kavitacija, pretrganje vodnega stolpca, CFD, Eulerjeva enačba, Navier-Stokesove enačbe, OpenFOAM, metoda karakteristik.*

Analysis of Gas Flow Distribution in a Fluidized Bed Using Two-Fluid Model with Kinetic Theory of Granular Flow and Coupled CFD-DEM: A Numerical Study

Matija Založnik - Matej Zadravec ✉
Faculty of Mechanical Engineering, University of Maribor, Slovenia
✉ matej.zadravec@um.si

Abstract *Fluidized bed systems are widely used in chemical and process engineering due to their excellent heat and mass transfer properties. Numerical modeling plays a crucial role in understanding and optimizing these systems, with the two-fluid model enhanced by the kinetic theory of granular flow (TFM-KTGF) and the coupled computational fluid dynamics-discrete element method (CFD-DEM) emerging as leading techniques. This study employs both models to simulate gas-solid interactions and evaluates their performance using a benchmark single-spout fluidized bed case validated against experimental data. Subsequently, the influence of particle presence on gas flow distribution through a non-uniform distribution plate is analyzed. The results show that the common assumption of proportional flow distribution based on the opening area fraction is inaccurate, particularly in the presence of particles. Both numerical models capture this behavior, with TFM-KTGF showing trends comparable to the coupled CFD-DEM approach but at significantly reduced computational cost. The findings highlight the importance of accounting for particle dynamics in distribution plate design and promote the TFM-KTGF approach as a promising alternative for large-scale simulations.*

Keywords *fluidized bed, distribution plate, two-fluid model with kinetic theory of granular flow, coupled CFD-DEM, flow distribution*

Highlights

- *Two models (TFM-KTGF and CFD-DEM) simulate gas-solid flow in fluidized beds.*
- *Models validated against experiments, showing good particle behavior prediction.*
- *Gas flow depends on particles, not just plate geometry.*
- *CFD-DEM captures local effects; TFM-KTGF is faster and predicts overall trends.*

1 INTRODUCTION

Fluidized bed systems are widely used in various industrial applications due to their excellent heat and mass transfer characteristics. Their applications range from chemical reactors and drying processes to coating technologies and catalytic cracking. Despite these advantages, fluidized beds remain inherently complex systems, where interactions between the gas and solid phases must be thoroughly understood to ensure efficient and stable operation [1,2].

With recent advances in computational modeling, the two-fluid model with added kinetic theory of granular flow (TFM-KTGF) and the coupled computational fluid dynamics-discrete element method (CFD-DEM) have emerged as powerful tools for simulating the complex behavior of fluidized bed systems. The TFM-KTGF approach treats both the gas and solid phases as interpenetrating continua within the Eulerian-Eulerian framework, with kinetic theory of granular flow (KTGF) playing a key role in characterizing particle behavior and inter-particle interactions. In contrast, the coupled CFD-DEM approach models the motion and interactions of individual particles in a Lagrangian framework, while the gas phase is treated using computational fluid dynamics (CFD) in the Eulerian framework. Although the coupled CFD-DEM approach provides a detailed resolution of particle dynamics, its complexity and high computational cost make it less practical for large-scale simulations compared to TFM-KTGF [3].

Esgandari et al. [4] conducted a direct comparison between these two modeling approaches in fluidized single- and multi-spout bed systems. Their study demonstrated that the TFM-KTGF approach could successfully replicate key hydrodynamic features observed in the more computationally intensive coupled CFD-DEM approach. Similarly, Ostermeier et al. [5] compared both numerical models for gas-solid fluidized beds and reported consistent global trends between them. These findings highlight why the TFM-KTGF approach is increasingly favored in both research and industry, offering reduced computational times while maintaining comparable predictive accuracy. Additional studies have examined the capabilities and limitations of both models through practical multiphase case studies of fluidized bed systems [6-9].

Flow distribution plays a crucial role in the proper functioning of fluidized bed systems, directly influencing particle mixing and the effectiveness of heat and mass transfer. One of the most essential components for ensuring optimal flow is the gas distribution plate (also referred to as the distributor), which governs the efficiency of gas introduction into the particle bed. Numerous designs for distribution plates have been proposed in the literature for various applications [10,11]. A numerical analysis of gas flow distribution across a distribution plate in a Wurster coater setup was performed by Kevorkijan et al. [12], using the coupled CFD-DEM approach. Their study revealed that both particle loading and inlet airflow rate significantly impact the uniformity of gas distribution across the distribution plate.

Recent studies have further examined distributor performance, pressure drop, and mixing efficiency in both industrial and laboratory systems, emphasizing that distributor geometry and particle properties critically influence hydrodynamic behavior inside the system. Gonzalez-Arango and Herrera [13] used CFD to study how

DOI: 10.5545/sv-jme.2025.1365

the geometries of different gas-phase distributors inside the fluidized bed affect the pressure drop and particle mixing. Their findings highlight that both the physical design and material selection of distribution plates can substantially impact system performance. The optimization of a uniform distributor inside a fluidized reactor was carried out by Singh et al. [14] using CFD, providing an example of the effective use of modeling tools for equipment optimization.

Although distribution plates are often designed based on open area fractions, this geometric assumption neglects particle effects that can significantly modify local gas flow through resistance, clustering, and particle-fluid interactions. While TFM-KTGF and coupled CFD-DEM have been widely used to analyze fluidized bed hydrodynamics, few studies have investigated how particles influence gas distribution through non-uniform distribution plates. To address this gap, the present study employs both TFM-KTGF and coupled CFD-DEM modeling to evaluate deviations from theoretical, area-based flow distributions and to provide insights for more accurate distribution plate design. This approach improves our understanding of why simplified assumptions sometimes fail in real-world applications, especially when complex physical phenomena are involved. The analysis was conducted on a laboratory-scale fluidized bed equipped with a distribution plate featuring non-uniform opening sizes, as shown in Fig. 1.

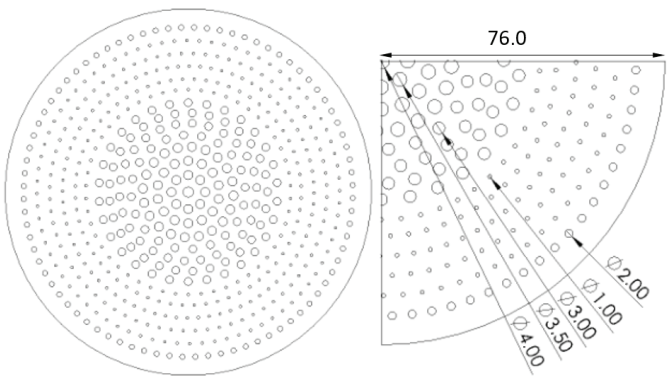

Fig. 1. A distribution plate with non-uniform opening sizes in a laboratory-scale fluidized bed system was used for the numerical analysis

2 METHODS

2.1 Two-Fluid Model with Kinetic Theory of Granular Flow

In the TFM approach, both the gas and solid phases are treated as independent continua, each governed by its own set of conservation equations. For a non-reactive, transient, isothermal system composed of spherical particles, the governing equations for mass and momentum conservation are expressed as follows:

$$\frac{\partial}{\partial t}\left(\alpha_g \rho_g\right)+\nabla\left(\alpha_g \rho_g \mathbf{v_g}\right)=0, \tag{1}$$

$$\frac{\partial}{\partial t}\left(\alpha_s \rho_s\right)+\nabla\left(\alpha_s \rho_s \mathbf{v_s}\right)=0, \tag{2}$$

$$\frac{\partial}{\partial t}\left(\alpha_g \rho_g \mathbf{v_g}\right)+\nabla\left(\alpha_g \rho_g \mathbf{v_g}\mathbf{v_g}\right)= =-\alpha_g \nabla p+\nabla\boldsymbol{\tau}_\mathbf{g}+\alpha_g \rho_g \mathbf{g}+\beta\left(\mathbf{v_s}-\mathbf{v_g}\right), \tag{3}$$

$$\frac{\partial}{\partial t}\left(\alpha_s \rho_s \mathbf{v_s}\right)+\nabla\left(\alpha_s \rho_s \mathbf{v_s}\mathbf{v_s}\right)= =-\alpha_s \nabla p-\nabla p_s++\nabla\boldsymbol{\tau}_\mathbf{s}+\alpha_s \rho_s \mathbf{g}+\beta\left(\mathbf{v_g}-\mathbf{v_s}\right), \tag{4}$$

where the subscripts g and s denote the gas and solid phases, respectively. Here, α_i represents the volume fraction, ρ_i the density, v_i the velocity, p_s the solid pressure, $\boldsymbol{\tau}_\mathbf{i}$ the stress tensor, g the gravitational acceleration, and β the momentum exchange coefficient, which is computed using a drag model. The solid pressure and the stress tensor of the solid phase are calculated as follows:

$$p_s=\alpha_s \rho_s \Theta_s+2\rho_s\left(1+e_{ss}\right)\alpha_s^2 g_{0,ss}\Theta_s, \tag{5}$$

$$\boldsymbol{\tau}_\mathbf{i}=\mu_s\left[\nabla\mathbf{v_s}+\left(\nabla\mathbf{v_s}\right)^T\right]+\lambda_s\left(\nabla\mathbf{v_s}\right), \tag{6}$$

where Θ_s is the granular temperature, e_{ss} is the restitution coefficient, $g_{0,ss}$ is the radial distribution function, μ_s is the granular viscosity, and λ_s is the bulk viscosity. The radial distribution function is a correction factor that accounts for the increased probability of particle collisions as the solid phase becomes dense. It is calculated using the following equation:

$$g_{0,ss}=\left[1-\sqrt[3]{\frac{\alpha_s}{\alpha_{s,max}}}\right]^{-1}, \tag{7}$$

where $\alpha_{s,max}$ represents the packing limit. The granular viscosity, which is related to the particle motion and interactions, is calculated using the following expressions [15,16]:

$$\mu_s=\mu_{s,kin}+\mu_{s,col}, \tag{8}$$

$$\mu_{s,kin}=\frac{\alpha_s d_s \rho_s \sqrt{\Theta_s \pi}}{6\left(3-e_{ss}\right)}\left[1+\frac{2}{5}\left(1+e_{ss}\right)\left(3e_{ss}-1\right)\alpha_s g_{0,ss}\right], \tag{9}$$

$$\mu_{s,col}=\frac{4}{5}\alpha_s \rho_s d_s g_{0,ss}\left(1+e_{ss}\right)\sqrt{\frac{\Theta_s}{\pi}}. \tag{10}$$

where d_s is the particle diameter. The bulk viscosity characterizes the material's response to changes in pressure and stress and is calculated by the equation proposed by Lun et al. [17]:

$$\lambda_s=\frac{4}{3}\alpha_s \rho_s d_s g_{0,ss}\left(1+e_{ss}\right)\sqrt{\frac{\Theta_s}{\pi}}. \tag{11}$$

The granular temperature Θ_s is a parameter introduced into the two-fluid model (TFM) through the KTGF. It quantifies the random fluctuations in particle velocity arising from collisions. The transport equation for the granular temperature is given as follows:

$$\frac{3}{2}\left[\frac{\partial}{\partial t}\left(\alpha_s \rho_s \Theta_s\right)+\nabla\left(\alpha_s \rho_s \mathbf{v_s}\Theta_s\right)\right]= =\left(-p_s\mathbf{I}+\boldsymbol{\tau}_\mathbf{s}\right):\nabla\mathbf{v_s}+\nabla\left(\kappa_{\Theta_s}\nabla\Theta_s\right)-\gamma_{\Theta_s}+\phi_{gs}, \tag{12}$$

where $\mathbf{I}$ is the identity tensor, κ_{Θ_s} is the diffusion coefficient, γ_{Θ_s} represents the collisional dissipation of energy, and ϕ_{gs} denotes the interphase energy transfer due to particle-gas interactions. The first term on the right-hand side of the granular temperature equation corresponds to energy production; the second term represents the diffusion of granular temperature; the third accounts for energy dissipation due to particle collisions; and the final term describes the energy exchange between the gas and solid phases. The diffusion coefficient is calculated using the following expression [15]:

$$\kappa_{\Theta_s}=\frac{15 d_s \rho_s \alpha_s \sqrt{\Theta_s \pi}}{4\left(41-33\eta\right)}\left[1+\frac{12}{5}\eta^2\left(4\eta-3\right)\cdot\right. \left.\cdot\alpha_s g_{0,ss}+\frac{16}{15\pi}\left(41-33\eta\right)\eta\alpha_s g_{0,ss}\right], \tag{13}$$

where η is a dimensionless parameter calculated as:

$$\eta=\frac{1}{2}\left(1+e_{ss}\right). \tag{14}$$

The collisional dissipation of energy represents the rate at which energy is dissipated within the solid phase due to collisions between particles. It is calculated using the following equation [17]:

$$\gamma_{\Theta_s} = \frac{12\left(1-e_{ss}^2\right)g_{0,ss}}{d_s\sqrt{\pi}}\rho_s\alpha_s^2\Theta_s^{\frac{3}{2}}. \tag{15}$$

Lastly, the interphase energy transfer is described by the following equation [18]:

$$\varphi_{gs} = -3\beta\Theta_s. \tag{16}$$

In this work, the Syamlal-O'Brien drag model, which is based on the terminal velocity of particles, is employed [19]. The momentum exchange coefficient β is calculated using the following equation:

$$\beta = \frac{3\alpha_s\alpha_g\rho_g}{4v_{r,s}^2 d_s}C_D\left(\frac{Re_s}{v_{r,s}}\right)\left|\mathbf{v_s}-\mathbf{v_g}\right|, \tag{17}$$

where $v_{r,s}$ is the terminal particle velocity, d_s is the particle diameter, C_D is the drag coefficient, and Re_s is the Reynolds number for the solid phase. The drag coefficient, originally derived by Dalla Valle [20], is calculated as follows:

$$C_D = \left(0.63+\frac{4.8}{\sqrt{\frac{Re_s}{v_{r,s}}}}\right)^2. \tag{18}$$

The terminal particle velocity for the solid phase is calculated using the following expression [21]:

$$v_{r,s} = 0.5A - 0.03Re_s + 0.5\sqrt{\left(0.06Re_s\right)^2 + 0.12Re_s\left(2B-A\right)+A^2}, \tag{19}$$

with

$$A = \alpha_g^{4.14}, \tag{20}$$

and

$$B = \begin{cases} 0.8\alpha_g^{1.28} & \text{for} \quad \alpha_g \le 0.85 \\ \alpha_g^{2.65} & \text{for} \quad \alpha_g \ge 0.85 \end{cases}. \tag{21}$$

2.2 Coupled CFD-DEM

In the coupled CFD-DEM approach, the hydrodynamic behavior of the gas within a gas-solid fluidized bed is modeled using CFD to solve the conservation equations. The particles in the system are modeled using the discrete element method (DEM), which governs their motion and interactions based on Newton's second law of motion [22]. In the CFD-DEM coupling, the solid volume fraction field is computed using a volumetric diffusion Lagrangian-Eulerian mapping, which smoothly distributes each particle's volume to the surrounding cells while conserving the total solid phase volume. For particle i with mass m_i, the following set of equations is solved:

$$m_i\frac{d\mathbf{v_i}}{dt} = \sum_{j=1}^{n}\mathbf{F_{ij}^c} + \mathbf{F_i^f} + \mathbf{F_i^g}, \tag{22}$$

$$I_i\frac{d\boldsymbol{\omega}_\mathbf{i}}{dt} = \sum_{j=1}^{n_i}\mathbf{M_{ij}}, \tag{23}$$

where $\mathbf{v_i}$ is the translational velocity of the particle, ω_i is the angular velocity, $\mathbf{F_{ij}^c}$ and $\mathbf{M_{ij}}$ are the contact force and torque resulting from particle interactions with other particles and walls, $\mathbf{F_i^f}$ is the force due to particle-fluid interactions, $\mathbf{F_i^g}$ is the gravitational force, and I_i is the moment of inertia. Particle-particle and particle-wall interactions are described using a soft-sphere model, where normal and tangential forces relative to the contact are modeled separately [23]. The normal contact force component is modeled using the Hysteretic linear spring model [24], as shown below:

$$\mathbf{F_{ij}^{n,t}} = \begin{cases} \min\left(K_l s^t, \mathbf{F_{ij}^{n,(t-\Delta t)}} + K_u\Delta s\right) & \text{if} \quad \Delta s \ge 0 \\ \max\left(\mathbf{F_{ij}^{n,(t-\Delta t)}} + K_u\Delta s, 0.001K_l s^t\right) & \text{if} \quad \Delta s \le 0 \end{cases}, \tag{24}$$

$$\Delta s = s^t - s^{t-\Delta t}, \tag{25}$$

where $\mathbf{F_{ij}^{n,t}}$ and $\mathbf{F_{ij}^{n,(t-\Delta t)}}$ are the normal forces acting on particle i at the current and previous time steps, Δt is the time step size, s is the contact overlap, and K_l and K_u are the loading and unloading contact stiffnesses, determined by the particle properties as:

$$\frac{1}{K_l} = \begin{cases} \frac{1}{K_{L,p_1}} + \frac{1}{K_{L,p_2}} & \text{for particle-particle contact} \\ \frac{1}{K_{L,p}} + \frac{1}{K_{L,w}} & \text{for particle-wall contacts} \end{cases}, \tag{26}$$

$$K_u = \frac{K_l}{e_{ss}^2}, \tag{27}$$

where subscripts 1 and 2 represent two contacting particles. The individual stiffnesses associated with a particle and a wall are calculated as:

$$K_{l,p} = E_p L, \tag{28}$$

$$K_{l,w} = E_w L, \tag{29}$$

where E is the Young's modulus and L is the particle size. The tangential contact force is modeled using the linear spring Coulomb limit model. If the tangential force is assumed to be purely elastic, it can be calculated using the following equation:

$$\mathbf{F_{ij,e}^{\tau,t}} = \mathbf{F_{ij}^{\tau,(t-\Delta t)}} - K_\tau\Delta s_\tau, \tag{30}$$

where $\mathbf{F_{ij}^{\tau,(t-\Delta t)}}$ is the tangential contact force at the previous time step, K_τ is the tangential stiffness, and Δs_τ is the tangential overlap difference between two time steps. Since this model does not allow the tangential force to exceed Coulomb's limit, the complete expression is given as follows:

$$\mathbf{F_{ij}^{\tau,t}} = \min\left(\left|\mathbf{F_{ij,e}^{\tau,t}}\right|, \mu\mathbf{F_{ij,e}^{n,t}}\right)\frac{\mathbf{F_{ij,e}^{\tau,t}}}{\left|\mathbf{F_{ij,e}^{\tau,t}}\right|}, \tag{31}$$

where μ is the friction coefficient. For a more detailed description of the model, the reader is encouraged to consult the literature by Walton and Braun [24] and Cundall and Strack [22].

The effect of fluid flow across the particle bed is modeled using a two-way coupled CFD-DEM approach. The force $\mathbf{F_i^f}$ consists of drag and pressure contributions, as shown below:

$$\mathbf{F_p} = -V_p\Delta p, \tag{32}$$

$$\mathbf{F_D} = \frac{1}{2}\beta\rho_g A_p\left|\mathbf{v_g}-\mathbf{v_{s,i}}\right|\left(\mathbf{v_g}-\mathbf{v_{s,i}}\right), \tag{33}$$

where V_p is the particle volume, Δp is the local pressure gradient, A_p is the projected particle area in the direction of the flow, and $\mathbf{v_g}-\mathbf{v_{s,i}}$ is the relative velocity between particle i and the fluid. The Syamlal-O'Brien drag model was again used to calculate the momentum exchange coefficient, as described in the equations shown above. In both numerical models, the $k-\omega$ *SST* turbulence model was employed [25].

2.3 Model Validation

The validation of both the TFM-KTGF and coupled CFD-DEM models was performed using a benchmark single-spout fluidized bed case. The simulation results were compared with experimental data reported by Van Buijtenen et al. [26]. In that study, particle velocities

were measured using particle image velocimetry (PIV) and positron emission particle tracking (PEPT) systems at two different heights: 0.05 m and 0.10 m from the bottom, as indicated by the red dashed lines in Fig. 2.

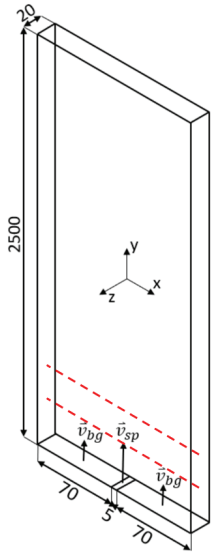

Fig. 2. Schematic of the single-spout fluidized bed used for model validation, where the red dashed lines indicate the locations where particle velocities were measured

Simulations were performed using two software packages: ANSYS Fluent [27] for hydrodynamics and ANSYS Rocky [28] for DEM. A uniform numerical mesh consisting of 58,000 hexahedral elements was used for both models. The system under study contained 12,000 spherical glass particles, each with a uniform diameter of 3 mm and a density of 2505 kg/m^3. The restitution coefficients for all interactions were set to 0.97, while the friction coefficients for particle-particle and particle-wall interactions were set to 0.1 and 0.3, respectively, consistent with previous studies [26,29,30].

Table 1. Simulation parameters used for the validation study

Parameter	Value
Material	Glass
Number of particles, N	12000
Particle diameter, d_s	3 mm
Particle density, ρ_s	2505 kg/m^3
Restitution coefficient, e_{ss}	0.97
Particle-particle friction coefficient, μ_{p-P}	0.1
Particle-wall friction coefficient, μ_{p-w}	0.3
Spout velocity, $\mathbf{v_{sp}}$	43.5 m/s
Background velocity, $\mathbf{v_{bg}}$	2.4 s
Total simulation time, t	20 s
CFD time step, Δt_{CFD}	10^{-5} s

The spout and background velocities at the inlet were set to 43.5 m/s and 2.4 m/s, respectively, with the pressure outlet set to ambient pressure. All walls were assigned with no-slip boundary conditions. The total simulation time for both models was set to 20.0 s, with a CFD time step of 10^{-5} s, while the DEM time step was calculated automatically within ANSYS Rocky based on the hysteretic linear spring model [31]. A summary of all simulation parameters used in this study is presented in Table 1.

Figure 3 compares the particle velocity profiles in y direction at different simulation times. Figures 3a, b and c show results from the TFM-KTGF approach, while Figs. 3d, e and f present results from the coupled CFD-DEM approach at t = 6 s (Figs. 3a and d), t = 18 s (Figs. 3b and e), and as a time-averaged profile (Figs. 3c and f).

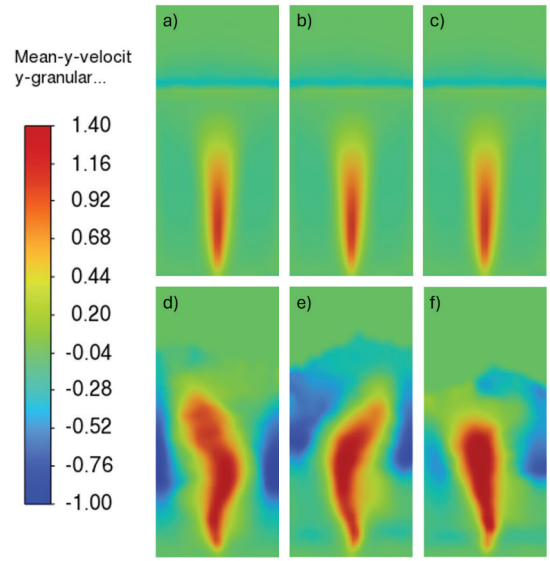

Fig. 3. a), b) and c) Average particle velocity in the y direction obtained using the TFM-KTGF approach, and d) e) and f) coupled CFD-DEM approach at: a) and d) t = 6 s, b) and e) t = 18 s, and c) and f) as a time-averaged result

It is evident that the particle velocities obtained using the TFM-KTGF approach exhibit a very uniform profile throughout the simulation. This behavior arises from the nature of the TFM-KTGF model, in which particles are treated as a continuum phase. In this framework, there is no discrete mechanism driving the fluid to interact with particles in a way that would cause substantial variations in the velocity profile over time. In contrast, the velocity profiles obtained from the coupled CFD-DEM approach show a noticeable change as time progresses. This is because the direct interactions between particles and the airflow influence particle velocities, causing the profile to evolve dynamically over time.

The time-averaged particle velocity profiles in y direction, along the length of the fluidized bed at heights of 0.05 m and 0.10 m from the bottom, were compared with experimental data. The results are shown in Fig. 4. Good agreement between the numerical model predictions and the experimental data is observed, particularly at the height of 0.05 m from the bottom. Both numerical models produced similar velocity trends, demonstrating the validity of both approaches for simulating fluidized bed behavior.

Figure 5 shows the time-averaged particle velocity vectors obtained from PIV and PEPT measurements by Van Buijtenen et al. [26], along with the corresponding results from this study. Good agreement was observed between both the TFM-KTGF and coupled CFD-DEM approaches and the experimental data. In the coupled CFD-DEM approach, intensive circulation patterns are clearly visible, closely matching the experimental observations from PIV and PEPT. In contrast, the TFM-KTGF results show less pronounced circulation. The slight differences observed between the PIV and PEPT vector fields are attributed to challenges inherent in the experimental setup, as described by Van Buijtenen et al. [26].

In summary, both the TFM-KTGF and coupled CFD-DEM approaches for simulating single-spout fluidized beds provide satisfactory predictions of flow dynamics when compared with experimental results obtained using PIV and PEPT, despite slight deviations. Both models showed good agreement with the experimental particle velocity data, as shown in Fig. 3, confirming

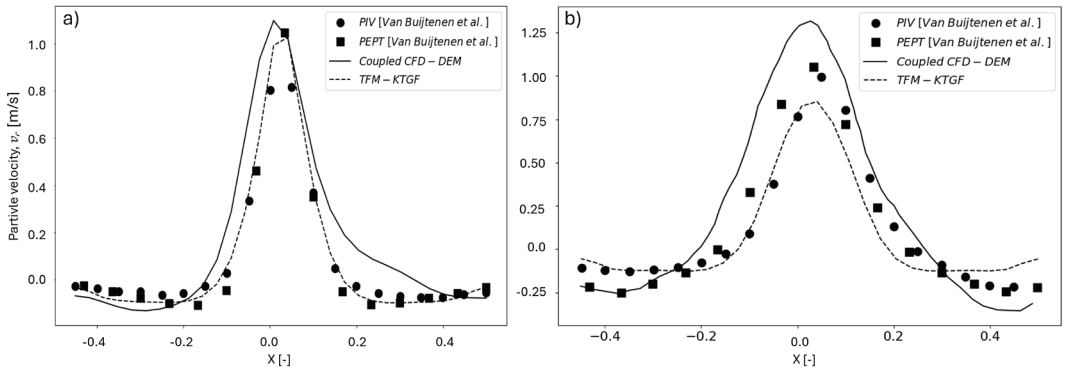

Fig. 4. Time-averaged particle velocity profiles in y direction along the length of the single-spout fluidized bed system at heights of a) 0.05 m, and b) 0.10 m from the bottom

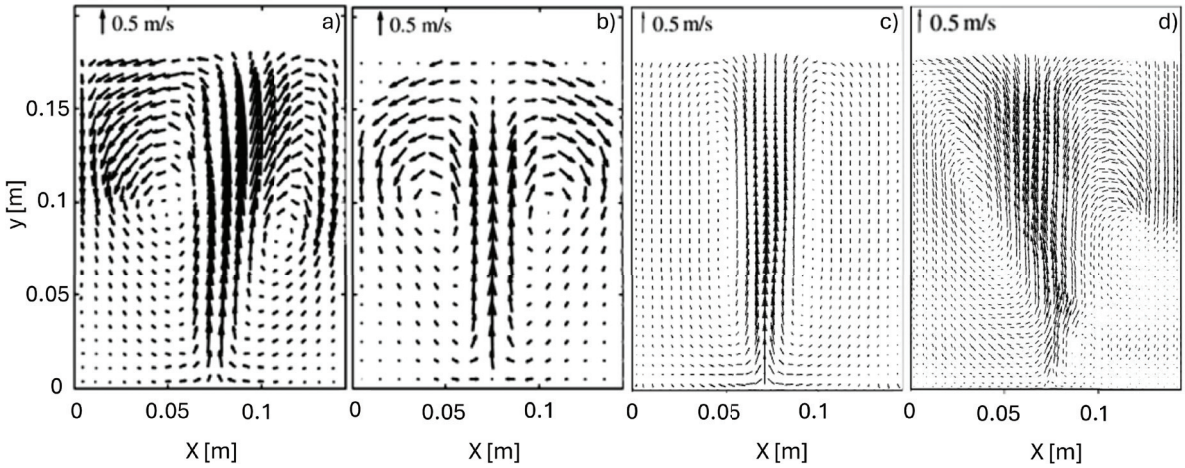

Fig. 5. Time-averaged particle velocity vector fields in the single-spout fluidized bed system; a) velocity PIV [26], b) velocity PEPT [26], velocity TFM-KTGF, and d) velocity coupled CFD-DEM

their reliability of these models for further analyses of flow distribution through a non-uniform distribution plate.

2.4 Flow Distribution Analysis

The flow distribution analysis was conducted on the geometry of a laboratory-scale fluidized bed system with a non-uniform distribution plate, as shown in Fig. 6. The colored sections on the distribution plate (Fig. 6c) represent different groups of openings: cyan indicates 4 mm, magenta 3.5 mm, red 3 mm, blue 1 mm, and green 2 mm. To reduce computational cost and simulation time, the geometry was symmetrically reduced to a quarter section, while preserving the essential flow characteristics.

As in the validation study, ANSYS Fluent [27] and ANSYS Rocky [28] were used to simulate multiphase flow using the TFM-KTGF and coupled CFD-DEM numerical models, respectively. Both approaches used the same numerical mesh, consisting of 1.5 million polyhedral elements. The simulations were performed with a total of 300 g of zeolite particles, with diameters ranging from 0.5 mm to 5 mm. The detailed particle size distribution is provided in Table 2, and the bulk particle density was set to 770 kg/m^3. These values were selected based on the work of Zadravec et al. [32] to reflect realistic conditions in a laboratory-scale fluidized bed system. In the TFM-KTGF approach, where particles are represented as a continuous phase, the particle size distribution was first determined using the population balance model (PBM). The discrete method was applied, in which the overall particle size distribution is discretized into a finite number of size classes. From this distribution, the Sauter mean diameter was evaluated and used in the TFM-KTGF model. This ensures that the influence of the particle size distribution is captured in an averaged manner while maintaining the computational framework of the two-fluid model. The interaction parameters, including restitution and friction coefficients for particle-particle and particle-wall contacts, were based on literature values [32] and are summarized in Table 3.

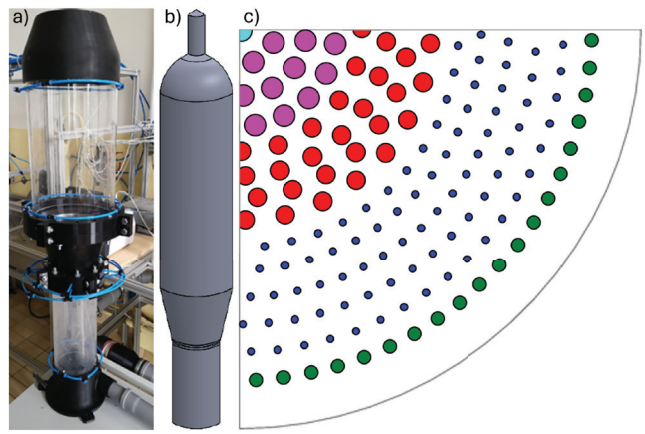

Fig. 6. a) Laboratory-scale fluidized bed system, b) the simplified geometry, and c) distribution plate geometry used in the analysis

Air was introduced into the system through the bottom inlet at volume flow rates ranging from 50 m^3/h to 70 m^3/h, increasing in increments of 5 m^3/h to examine the effect of inlet velocity on flow distribution. Ambient pressure was applied at the outlet, and symmetry boundary conditions were imposed on the cut planes to represent the quarter geometry. All other walls were assigned no-slip boundary conditions to accurately capture near-wall interactions.

The total simulation time for each case was set to 5 s, with a CFD time step size of 10^{-4} s, while the DEM time step was calculated automatically, as in the validation case [31]. This ensured sufficient temporal resolution to capture flow evolution and particle behavior throughout the system.

Table 2. Zeolite particle size distribution

Particle size [mm]	0.5	1.0	2.0	3.15	5.0
Mass fraction [%]	0.5	0.8	3.5	77.3	17.9

Table 3. Restitution and friction coefficients used in this analysis

	Particle-Particle	Particle-Wall
Restitution coefficient	0.1	0.5
Friction coefficient	0.6	0.5

The complete set of parameters used in flow distribution simulations is summarized in Table 4.

Table 4. Simulation parameters used for the flow distribution study

Parameter	Value
Material	Zeolite
Total mass of particles, m_s	300 g
Particle diameter, d_s	Table 2
Particle density, ρ_s	770 kg/m^3
Restitution coefficient	Table 3
Friction coefficient, μ	Table 3
Inlet volume flow rate, V	[50, 55, 60, 65, 70] m^3/h
Total simulation time, t	5.0 s
CFD time step, Δt_{CFD}	10^{-4} s

3 RESULTS AND DISCUSSION

To thoroughly examine the effect of particsles on airflow distribution through the fluidized bed distribution plate, multiple simulation cases were performed. These included simulations of the system without particles, to establish the baseline flow distribution in an empty geometry, and simulations with particles using the TFM-KTGF and coupled CFD-DEM models to assess the influence of particles on flow distribution.

The objective was to compare the simulation results with the theoretical flow distribution, which assumes that air distributes proportionally according to sthe opening fraction of each hole size group on the distribution plate. In other words, the flow rate through each group of openings was assumed to correspond to its relative area fraction on the plate.

Figure 7 compares the theoretical flow distribution, based on the open-area fraction, with the simulation results under different operating conditions. The solid lines represent the theoretical flow fractions for each group of openings, while the symbols and dashed lines correspond to the simulation data at various inlet flow rates. Results are presented for both an empty system (without particles) and a fluidized system (with particles), evaluated using two multiphase modeling approaches: TFM-KTGF and coupled CFD-DEM. The figure illustrates that the actual flow distribution deviates from the theoretical prediction even in the absence of particles, with these deviations becoming more pronounced when particles are introduced. In particular, the system containing particles shows clear shifts in the flow fractions through each opening group (e.g. 3 mm, 3.5 mm and 4 mm opening groups experience increased flow relative to the geometric assumption, while the 1 mm and 2 mm groups exhibit reduced flow). Furthermore, increasing the inlet air flow rate slightly

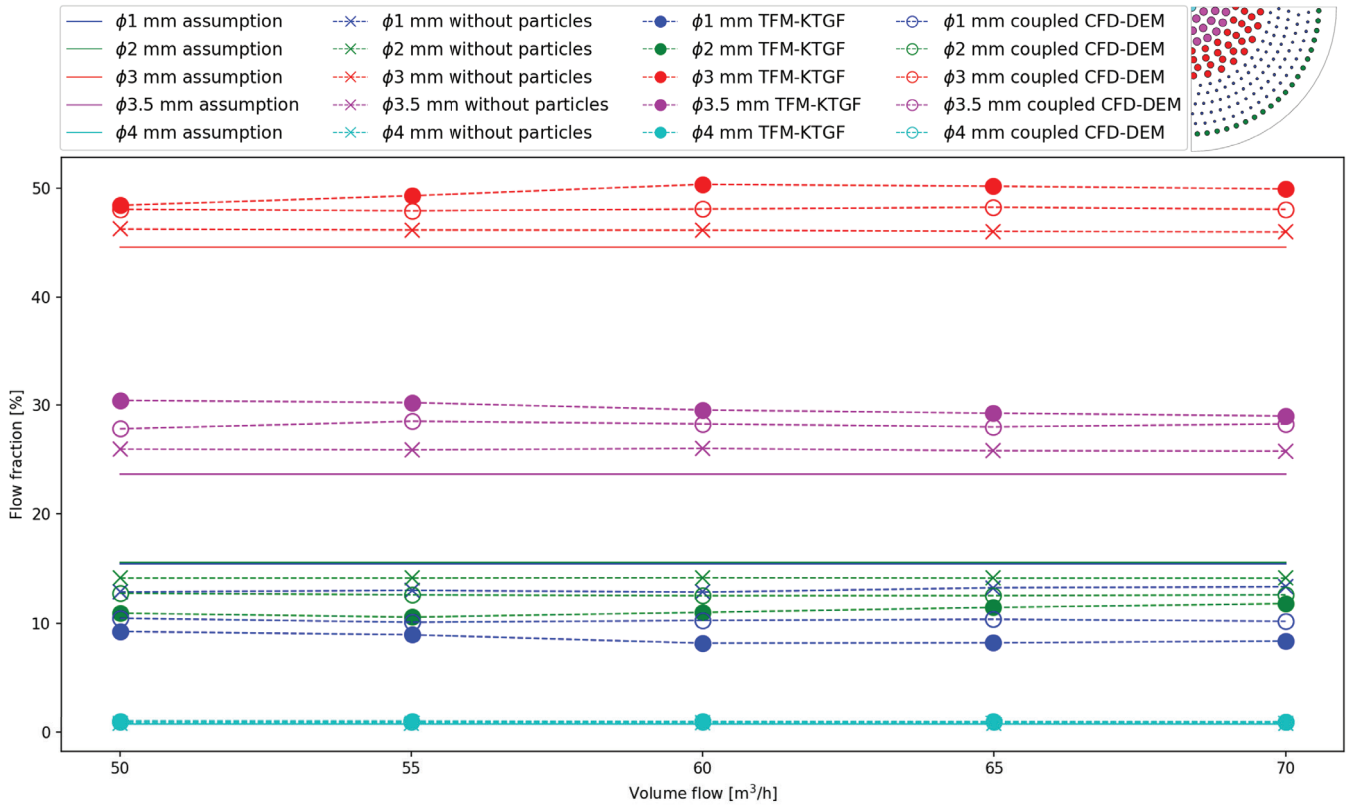

Fig. 7. Flow distribution through distribution plate openings of different sizes at various inlet air volume flow rates

alters the distribution, indicating that operating conditions influence how gas is channeled through the distributor.

These findings highlight that particle interactions introduce additional resistance and non-uniformity in local flow paths that cannot be captured by geometric assumptions alone, emphasizing the importance of modeling approaches that explicitly account for the particle phase.

A broader overview of the flow distribution is presented in Fig. 8, where the flow fractions for each opening size group are averaged across all inlet air flow rates. The results again confirm a significant mismatch between the theoretical distribution and the actual simulated distribution, particularly in the presence of particles.

Differences between the results obtained using the TFM-KTGF approach and those from the coupled CFD-DEM approach are also evident. These differences stem from the fundamental modeling approaches: TFM-KTGF treats the particle phase as a continuum, whereas the coupled CFD-DEM explicitly tracks individual particles. This distinction influences not only the flow predictions but also the computational performance of each model.

From a computational perspective, the TFM-KTGF approach proved to be significantly more efficient. Because it does not resolve individual particle trajectories, it requires far fewer computational resources than the coupled CFD-DEM model, which solves the equations of motion for each particle. In our simulations, the TFM-KTGF model completed each run approximately five times faster than the coupled CFD-DEM model on the same hardware. This substantial difference in computational time underscores the appeal of TFM-KTGF for large-scale simulations involving high particle counts.

4 CONCLUSIONS

In this study, we investigated gas flow distribution through a non-uniform distribution plate in a laboratory-scale fluidized bed system using two numerical approaches: TFM-KTGF and coupled CFD-DEM. Both approaches were employed to examine their behavior and predictive capability in a laboratory-scale fluidized bed. CFD-DEM provides detailed particle behavior, capturing particle-fluid interactions and heterogeneities, while TFM-KTGF efficiently predicts global flow trends. Using both methods allows us to evaluate how particle effects influence gas distribution and to assess the validity of the continuum assumptions in the TFM framework. Both models were validated against experimental data from a single-spout fluidized bed and demonstrated satisfactory agreement in predicting particle velocity profiles and overall flow behavior. These results confirm that both approaches can capture the essential features of fluidized bed dynamics.

This study demonstrates that particle effects can substantially alter the flow distribution in non-uniform distribution plates, despite the conventional assumption that gas flows proportionally to open area. By explicitly comparing the TFM-KTGF and coupled CFD-DEM approaches, we evaluated these deviations and provided evidence that particle-fluid interactions must be considered in distributor design. Incorporating the non-uniform plate geometry alongside realistic particle behavior bridges the gap between theoretical assumptions and actual flow patterns, offering a framework to guide improved design strategies for laboratory-scale fluidized beds.

Both numerical approaches captured the dynamic behavior of the particles, albeit with some differences.

The coupled CFD-DEM approach provided more detailed results by tracking individual particles, their interactions, and their influence on the flow, highlighting particle-fluid interactions that are not captured by simple geometric assumptions. In contrast, the TFM-KTGF approach treats the particle phase as a continuum, which smooths out these details but still accurately represents the overall behavior on a global scale. A key advantage of the TFM-KTGF approach is its computational efficiency: in this study, it completed the simulations approximately five times faster than the coupled CFD-DEM approach on the same hardware, making it a practical choice for larger systems.

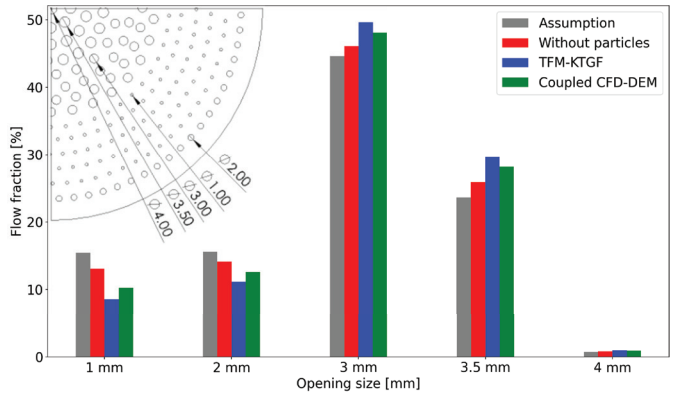

Fig. 8. Flow distribution through distribution plate openings of different sizes, averaged across all inlet air volume flow rate cases

While the coupled CFD-DEM approach captures particle-scale effects with high fidelity, its computational cost makes applications to large or industrial-scale fluidized beds impractical with current resources. Conversely, the TFM-KTGF model, though efficient, relies on a continuum treatment of the granular phase, which may smooth out local heterogeneities such as clustering or jet instabilities. These differences highlight that each model has inherent limitations, and their predictions should be interpreted within the context of laboratory-scale systems.

It should be emphasized that the present simulations were performed for laboratory-scale geometries, and direct extrapolation of the findings to full industrial-scale fluidized beds requires caution. Although the observed trends provide valuable guidance for distributor plate design, additional validation at pilot or industrial scale would be necessary to fully confirm the transferability of these results. Future work should therefore focus on bridging the gap between laboratory validation and industrial application.

References

[1] Daizo, K., Levenspiel, O. *Fluidization Engineering, 2nd ed*. Butterworth Publishers, Stoneham (1991).

[2] Fan, L.S., Zhu, C. *Principles of Gas-Solid Flows*. Cambridge University Press, Port Chester (1999) **DOI:10.1017/CBO9780511530142**.

[3] Michaelides, E.E., Sommerfeld, M., van Wachem, B. Multiphase Flows with Droplets and Particles, 3rd ed. CRC Press, Boca Raton (2022) **DOI:10.1201/9781003089278**.

[4] Esgandari, B., Rauchenzauner, S., Goniva, C., Kieckhefen, P., Schneiderbauer, S. A comprehensive comparison of two-fluid model, discrete element method and experiments for the simulation of single- and multiple-spout fluidized beds. *Chem Eng Sci* 267 118357 (2023) **DOI:10.1016/j.ces.2022.118357**.

[5] Ostermeier, P., Vandersickel, A., Gleis, S., Spliethoff, H. Numerical approaches for modeling gas-solid fluidized bed reactors: Comparison of models and application to different technical problems. *J Energy Resour Technol* 141 070707 (2019) **DOI:10.1115/1.4043327**.

[6] Liu, D., van Wachem, B. Comprehensive assessment of the accuracy of CFD-DEM simulations of bubbling fluidized beds. *Powder Technol* 343 145-158 (2019) **DOI:10.1016/j.powtec.2018.11.025**.

[7] Agrawal, V., Shinde, Y., Shah, M.T., Utikar, R.P., Pareek, V.K., Joshi, J.B. Effect of drag models on CFD-DEM predictions of bubbling fluidized beds with Geldart D particles. *Adv Powder Technol* 29 2658-2669 (2018) **DOI:10.1016/j.apt.2018.07.014**.

[8] Zhang, Q., Cai, W., Lu, C., Gidaspow, D., Lu, H. Modified MFIX code to simulate hydrodynamics of gas-solids bubbling fluidized beds: A model of coupled kinetic theory of granular flow and discrete element method. *Powder Technol* 357 417-427 (2019) **DOI:10.1016/j.powtec.2019.08.056**.

[9] Alobaid, F., Epple, B. Improvement, validation and application of CFD/DEM model to dense gas-solid flow in a fluidized bed. *Particuology* 11 514-526 (2013) **DOI:10.1016/j.partic.2012.05.008**.

[10] Geldart, D., Baeyens, J. The design of distributors for gas-fluidized beds. *Powder Technol* 42 (1985) 67-78, **DOI:10.1016/0032-5910(85)80039-5**.

[11] Karri, S.B.R., Knowlton, T.M. *4 - Gas distributor and plenum design in fluidized beds*. Yang, W.-C. (ed.) *Fluidization, Solids Handling, and Processing*, William Andrew Publishing, Westwood 209-235 (1999) **DOI:10.1016/B978-081551427-5.50006-5**.

[12] Kevorkijan, L., Zadravec, M. Numerične simulacije toka tekočine in delcev v granulatorju z lebdečim slojem. *Anali PAZU* 12 17-30 (2022) **DOI:10.18690/analipazu.12.1.17-30.2022**.

[13] Gonzalez-Arango, D.I., Herrera, B. Evaluation of the flow distribution system influence on mixing efficiency in a fluidized bed for low-size Geldart B particles: A case study using CFD. *S Afr J Chem Eng* 52 325-335 (2025) **DOI:10.1016/j.sajce.2025.03.007**.

[14] Singh, R., Marchant, P., Golczynski, S. Modeling and optimizing gas solid distribution in fluidized beds. *Powder Technol* 446 120145 (2024) **DOI:10.1016/j.powtec.2024.120145**.

[15] Syamlal, M., Rogers, W., O'Brien, T. *MFIX Documentation: Theory Guide* US Department of Energy, Morgantown (1993) **DOI:10.2172/10145548**.

[16] Gidaspow, D., Bezburuah, R., Ding, J. Hydrodynamics of circulating fluidized beds, kinetic theory approach. *7th Fluidization Conference* 75-82 (1992).

[17] Lun, C., Savage, S., Jeffrey, D., Chepurniy, N. Kinetic theories for granular flow: Inelastic particles in Couette flow and slightly inelastic particles in a general flowfield. *J Fluid Mech* 140 223-256 (1984) **DOI:10.1017/S0022112084000586**.

[18] Ding, J., Gidaspow, D. A bubbling fluidization model using kinetic theory of granular flow, *AIChE J* 36 523-538 (1990) **DOI:10.1002/aic.690360404**.

[19] Syamlal, M., O'Brien, T. *A Generalized Drag Correlation for Multiparticle Systems*, Unpublished report (1987).

[20] Dalla Valle, J.M. *Micrometrics, the Technology of Fine Particles*, Pitman (1948).

[21] Garside, J., Al-Dibouni, M.R. Velocity-voidage relationships for fluidization and sedimentation in solid-liquid systems. *Ind Eng Chem Process Des Dev* 16 206-214 (1977) **DOI:10.1021/i260062a008**.

[22] Cundall, P.A., Strack, O.D.L. A discrete numerical model for granular assemblies. *Géotechnique* 29 (1979) 47-95 **DOI:10.1680/geot.1979.29.1.47**.

[23] Wassgren, C., Curtis, J.S. The application of computational modeling to pharmaceutical materials science. *MRS Bull* 31 900-904 (2006) **DOI:10.1557/mrs2006.210**.

[24] Walton, O.R., Braun, R.L. Viscosity, granular-temperature, and stress calculations for shearing assemblies of inelastic, frictional disks. *Journal Rheol* 30 949-980 (1986) **DOI:10.1122/1.549893**.

[25] Menter, F.R. Two-equation eddy-viscosity turbulence models for engineering applications. *AIAA Journal* 32 1598 (1994) **DOI:10.2514/3.12149**.

[26] van Buijtenen, M.S., van Dijk, W.-J., Deen, N.G., Kuipers, J.A.M., Leadbeater, T., Parker, D.J. Numerical and experimental study on multiple-spout fluidized beds. *Chem Eng Sci* 66 (2011) 2368-2376 **DOI:10.1016/j.ces.2011.02.055**.

[27] ANSIS Inc. *Ansys® Academic Research, Release 23.1, Help System, Solver Theory, Multiphase Flow Theory*, ANSIS (2023).

[28] ANSIS Inc. *Ansys® Academic Research, Release 23.1, Help System, DEM-CFD Coupling Technical Manual*, ANSIS (2023).

[29] Jajcevic, D., Siegmann, E., Radeke, C., Khinast, J.G. Large-scale CFD-DEM simulations of fluidized granular systems. *Chem Eng Sci* 98 298-310 (2013) **DOI:10.1016/j.ces.2013.05.014**.

[30] Goniva, C., Kloss, C., Deen, N.G., Kuipers, J.A., Pirker, S. Influence of rolling friction on single spout fluidized bed simulation. *Particuology* 10 582-591 (2012) **DOI:10.1016/j.partic.2012.05.002**.

[31] ANSIS Inc. *Ansys® Academic Research, Release 25.1, Rocky Technical Manual: 5.2. Timestep Calculation*, ANSIS (2023).

[32] Zadravec, M., Orešnik, B., Hriberšek, M., Marn, J. Two-step validation process of particle mixing in a centrifugal mixer with vertical axis. *Proc Inst Mech Eng-E* 232 29-37 (2018) **DOI:10.1177/0954408916678267**.

Acknowledgements *The authors would like to express their sincere gratitude to the professors, assistants, and colleagues at the Faculty of Mechanical Engineering, University of Maribor for their valuable support and constructive discussions throughout this work. We also gratefully acknowledge the financial support provided by the Slovenian Research Agency (ARRS) under the framework of Research Program P2-0196: Power, Process, and Environmental Engineering.*

Received: 2025-04-23, Revised: 2025-09-09, Accepted: 2025-09-24
as Original Scientific Paper 1.01.

Data availability *The data that support the findings of this study are available from the corresponding author upon reasonable request.*

Authors contribution *Matija Založnik: Formal analysis, Investigation, Writting - original draft, Writing – review & editing, Software, Visualization; Matej Zadravec: Methodology, Project Administration, Supervision.*

Analiza distribucije toka plina v lebdečem sloju z uporabo modela dveh tekočin s kinetično teorijo granularnega toka in sklopljenega CFD-DEM: numerična študija

Povzetek *Sistemi z lebdečim slojem se pogosto uporabljajo v kemičnem in procesnem inženirstvu zaradi svojih odličnih sposobnosti prenosa toplote in snovi. Numerično modeliranje ima ključno vlogo pri razumevanju in optimizaciji teh sistemov, pri čemer se med vodilne uveljavljata model dveh tekočin, dopolnjen s kinetično teorijo granularnega toka (TFM-KTGF) in sklopljena računalniške dinamike tekočin z metodo diskretnih elementov (CFD-DEM). V tej študiji sta uporabljena oba modela za simulacijo interakcij med plinom in trdnimi delci ter ovrednotena njuna učinkovitost na primeru eksperimentalnega primera iz literature. Analiziran je bil tudi vpliv delcev na porazdelitev toka plina skozi ne-uniformno distribucijsko ploščo. Rezultati kažejo, da je pogosta predpostavka o sorazmerni porazdelitvi toka glede na delež odprtin nepravilna, zlasti v prisotnosti delcev. Oba numerična modela zajameta to vedenje, pri čemer TFM-KTGF kaže trende primerljive s sklopljenim CFD-DEM pristopom a pri bistveno nižjih računskih časih. Ugotovitve poudarjajo pomen upoštevanja dinamike delcev pri oblikovanju distribucijskih plošč ter promovirajo uporabo TFM-KTGF kot obetavno alternativo za simulacije na velikih sistemih.*

Ključne besede *lebdeči sloj, distribucijska plošča, model dveh tekočin s kinetično teorijo granularnega toka, sklopljen CFD-DEM, distribucija toka*

Fatigue of Triply Periodic Minimal Surface (TPMS) Metamaterials – a Review

Žiga Žnidarič ✉, Branko Nečemer, Nejc Novak, Matej Vesenjak, Srečko Glodež
University of Maribor, Faculty of Mechanical Engineering, Slovenia
✉ ziga.znidaric@um.si

Abstract *A review of the fatigue behavior of triply periodic minimal surface (TPMS) metamaterials with consideration for their fabrication is presented in this paper. The review analyses the most common TPMS geometries used due to their mechanical characteristics. Production methods and the base materials used are presented with the key advantages and drawbacks. Furthermore, the mechanical characteristics of cellular structures with emphasis on TPMS geometries are described. Lastly, the state-of-the-art findings of their fatigue behavior are analyzed and explained. Based on the findings in this article, cellular geometries based on TPMS are superior to conventional cellular structures when comparing their fatigue life. Because of the smooth transitions between struts or surfaces, the stress distribution is much more uniform without stress concentration zones.*

Keywords *cellular structures, TPMS metamaterials, production technologies, mechanical characterization, fatigue behavior*

Highlights

- *The general characteristics of cellular structures, with focus on TPMS geometries, are explained.*
- *Fabrication techniques used to produce TPMS metamaterials are briefly introduced.*
- *Fatigue behavior of TPMS metamaterials is presented and compared.*

1 INTRODUCTION

Cellular structures are materials composed of solid edges or faces that are arranged in patterns to fit a certain space. They are inspired by porous materials found in nature, such as bone, wood, coral and honeycombs [1]. Their main benefits are high strength and excellent energy absorption at a relatively low weight. Due to these qualities, cellular materials are being analyzed and applied in industries like aerospace, sports, automotive and medicine [2,3]. Cellular materials can be broadly categorized into three types. The first are open-cell structures (Fig. 1b). The voids and pores inside the structures are interconnected, meaning a fluid could flow freely through the material. In contrast, closed-cell structures (Fig. 1c) feature isolated voids. The third category are honeycomb cellular structures, comprised of repeating cells in two dimensions that resemble the hexagonal pattern found in natural honeycombs (Fig. 1a) [4].

However, due to the increasing number of newly engineered materials, designed to exhibit unusual or tunable mechanical, acoustic or electromagnetic properties that are known as metamaterials [5], they can be further categorized in more detail as shown in Fig. 2. Porosity or relative density are typically used to describe metamaterials. Porosity refers to the fraction of the material's volume that is made up of voids or pores, while relative density compares the density of the cellular material to that of the solid material [2,6]. Additionally, plateau stress, densification strain and energy absorption (SEA) are critical in characterizing the mechanical response of these materials [7]. They can achieve an auxetic response with the right combination of cell topology and morphology. This means that they have a negative Poisson's ratio, so when a compressive force is applied, the material contracts laterally, unlike typical materials that expand. This behavior leads to benefits such as increased stiffness, high energy absorption and enhanced shear stiffness [8]. Geometries that exhibit this type of response are typically strut-based lattices and chiral structures. They are designed to be lightweight yet highly efficient in distributing forces. A negative aspect of these types of structures is their sharp transitions in areas where their struts meet. This can negatively affect their mechanical properties, especially whenever dynamic loads are applied [9–12].

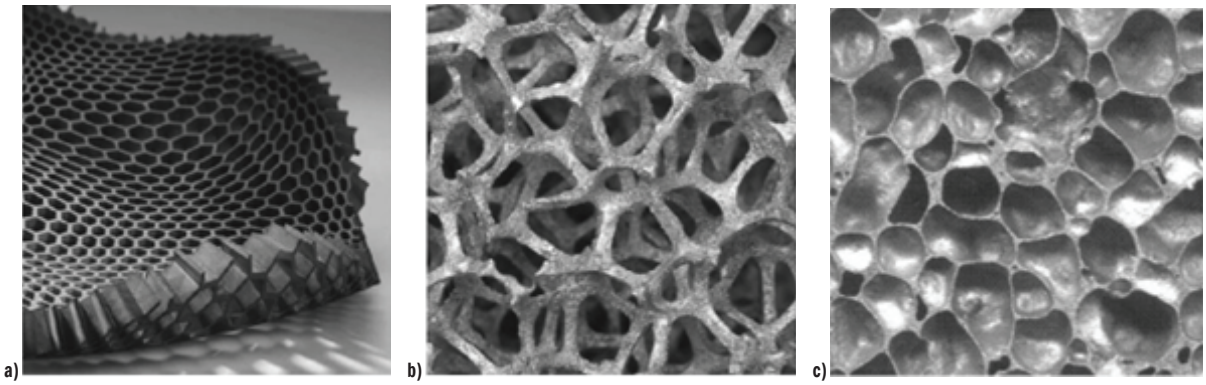

Fig. 1. a) Honeycomb, b) open-cell and c) closed-cell cellular structures, reproduced from [4]

Another type of architected cellular structures that do not have this drawback are TPMS geometries, which are usually geometrically more complex but offer highly efficient structural performance such as compressive strength, elastic modulus and energy absorption due to their smooth surface transitions [13,14].

Because of their unique properties, they have gained attention in various applications, e.g. energy absorption, thermal management, fluid mixing and biomedical engineering [15–18]. With the proper production method, unit cell selection and grading, TPMS structures were shown to closely mimic human bone's mechanical properties, such as strength, stiffness and porosity [19]. This makes them viable for manufacturing personalized bone implants [20,21]. Additionally, these mechanical properties make them suitable for applications as energy absorbers, such as components designed to assure controlled deformation during a crash in the transport industry [22]. TPMS metamaterials are not only used in mechanical applications. Certain geometries are being investigated for use in the static mixing of fluids. Their geometries enhance turbulence and mixing efficiency, making them suitable for pH control and inline coagulation applications in water treatment systems [23]. Some TPMS configurations are increasingly being integrated into heat exchangers. They improve heat transfer efficiency due to their high surface area to volume ratio, which leads to better heat transfer and thermal efficiency [17,24–27].

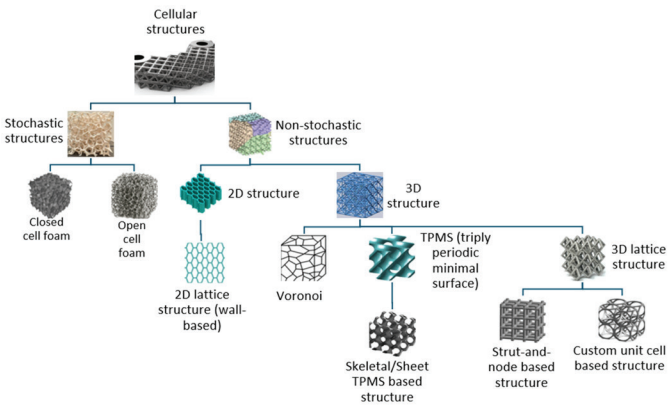

Fig. 2. Categorisation of cellular materials, reproduced from [28]

In addition to the mechanical and thermal properties of TPMS metamaterials, like other cellular materials, understanding their long-term mechanical performance under cyclic loading conditions remains essential [29]. Many of their main applications include bone implants and crash absorbers. These components are often subjected to repeated mechanical loads. Under such conditions, fatigue behavior becomes a critical design consideration, since failure may occur even before the loads reach the static mechanical limits of the structure [30]. Fatigue analyzis of TPMS metamaterials is therefore vital in ensuring their long-term performance. Research on the fatigue behavior of cellular materials has slowly increased over the past years. However, TPMS metamaterials only have a handful of scientific publications that have analyzed their response under cyclic loading. This paper aims to review different types of TPMS geometries, production methods, and mechanical and fatigue properties to better understand their advantages and limitations. Lastly, outlines for future research are given.

2 TPMS GEOMETRIES

2.1 Most Common TPMS Geometries

The design and geometries of TPMS structures can be tailored for specific properties. They can be adjusted to achieve desired porosity and stiffness, making them ideal for lightweight structures or scaffolds in tissue engineering [27]. Additionally, their shapes and continuity influence local stress distributions and fatigue resistance. For example, smooth and continuous surfaces reduce stress concentrations, while sharp transitions act as fatigue crack initiation sites. Euler and Lagrange first studied the theory behind minimal surfaces in a three-dimensional space. The name refers to surfaces with a mean curvature of zero at every point [31]. Meusnier discovered the most primitive examples of this with the help of an analytical approach to calculate the mean curvature of a catenoid and helicoid [32]. These surfaces can be described using a general implicit equation of the form:

$$f(x,y,z)=C. \tag{1}$$

Equation (1) defines a surface in a three-dimensional space. For it to exhibit the mean-zero curvature and periodicity characteristic of TPMS, the function must be expressed using specific trigonometric formulations. Some of the most common examples are presented in Table 1. These trigonometric functions divide space into two domains as the equation approaches zero. The resulting domains can be identical in shape or differ from one another. By adjusting the constants within the function, the topology of the surface can be modified, resulting in different TPMS configurations. Because these types of structures are fully defined with an equation, they allow for great freedom when modelling [32-34]. The first triply periodic minimal surfaces were described by Schwarz in 1865 [31] and Neovius in 1883 [35]. They are defined as continuous, non-self-intersecting structures that extend infinitely in three principal directions. They exhibit periodicity and crystallographic space group symmetry [36]. Using this definition, Alen Schoen built upon Schwarz's foundational discoveries. The most common TPMS geometries with their implicit equations are presented in Table 1. The first surface model that fits these requirements is called Schwarz Primitive. It has two intertwined congruent labyrinths, each with the shape of an inflated tubular version of the simple cubic lattice [37]. If we replace the shape of the lattice with a diamond bond structure, we get the so-called Diamond surface [37]. The Gyroid was discovered by Alan Schoen in 1970 and is an infinitely connected triply periodic minimal surface. It is an intermediate between the aforementioned Diamond and Schwarz Primitive surfaces. This geometry is found in butterfly wings and is widely used in fluid transport and mixing [27].

Table 1. Common TPMS geometries and their corresponding equations

Name	Equation	Model
Schwarz Primitive	$\cos(x)+\cos(y)+\cos(z)=0$	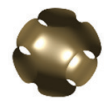
Diamond	$\cos(x)\cdot\cos(y)\cdot\cos(z)-$ $-\sin(x)\cdot\sin(y)\cdot\sin(z)=0$	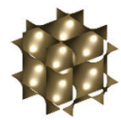
Gyroid	$\sin(x)\cdot\cos(y)+\sin(y)\cdot\cos(z)+$ $+\sin(z)\cdot\cos(x)=0$	
I-Wrapped Package (I-WP)	$\cos(x)\cdot\cos(y)+\cos(y)\cdot\cos(z)+$ $+\cos(z)\cdot\cos(x)=0$	

Lastly, the I-Wrapped Package (I-WP) was described by Alan Schoen in 1970. It is characterized by its two to four self-intersecting

Schoenflies surfaces [37]. In engineering applications, TPMS metamaterials are typically designed with relative density ranging from 0.1 to 0.5, and unit cell sizes commonly falling within the range of 1 mm to 6 mm, depending on the chosen manufacturing process [38-41].

2.2 TPMS Structure Generation

The above presented geometries are based on surfaces. To be able to test them and make physical specimens, they must be assigned a volume. There are two ways of generating a volumetric model from the sheet-based geometries. In the first instance, a thickness is assigned to the surface model. With altering the wall thickness, the relative density of the structure changes. These geometries are called sheet-based TPMS structures. The second method uses the implicit surfaces and divides the domain around them into two solids [42]. Depending on the chosen TPMS design, the resulting domains can be identical or different from one another. By adjusting the constant C in Eq. (1), it is possible to control the domains shape. Figure 3 shows how the resulting geometries differ, depending on which method was used to generate them. Further modifications made by changing the values in the implicit functions, while still retaining smooth transitions between cells can be made easily. The first modification that can be made is changing the relative density. As previously mentioned, it can be altered by changing the C constant. Suppose C is not constant, and we assign a function that changes its value depending on the location in the coordinate system. In that case, we can achieve graded structures with different relative densities and mechanical properties throughout their geometries [20].

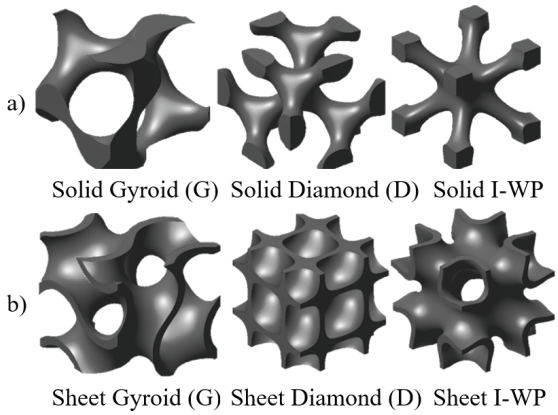

Fig. 3. Difference between: a) skeletal-TPMS metamaterials, and b) sheet-TPMS metamaterials, adapted from [43]

Another type of grading can be achieved by changing the size of individual cells. This changes the surface area and pore sizes while retaining a constant relative density. Liu et al. [40] described how this is achieved mathematically and is showcased in Fig. 4. It was observed that cell-size adjustments do not cause as substantial of a change in the mechanical properties of TPMS metamaterials as density gradients do. This is because larger cells negatively affect the mechanical properties, which is also where the geometries failed in testing. The last method is cell type grading or multimorphology. It is obtained by transitioning between different types of TPMS geometries while retaining smooth surface transitions. This is done by dividing the volume into different subdomains. If the equations that describe the unit cells have the same value at the intersections of these domains, we can achieve a continuous surface connecting them [44,45].

Graded designs not only influence mechanical stiffness but also play a role in fatigue behavior, since density, cell-size or cell-type variations can either mitigate or amplify local strain accumulation during cyclic loads.

In addition to their mechanical response, these geometrical choices also determine how TPMS structures can be produced. For example, sheet-based designs have thin walls needing higher resolutions to achieve smooth transitions when compared to skeletal-based structures. Graded or multimorphology designs add further challenges, as variations in cell size and topology can prove too challenging for certain manufacturing processes. Because of this, the next section presents the main technologies used to produce TPMS structures.

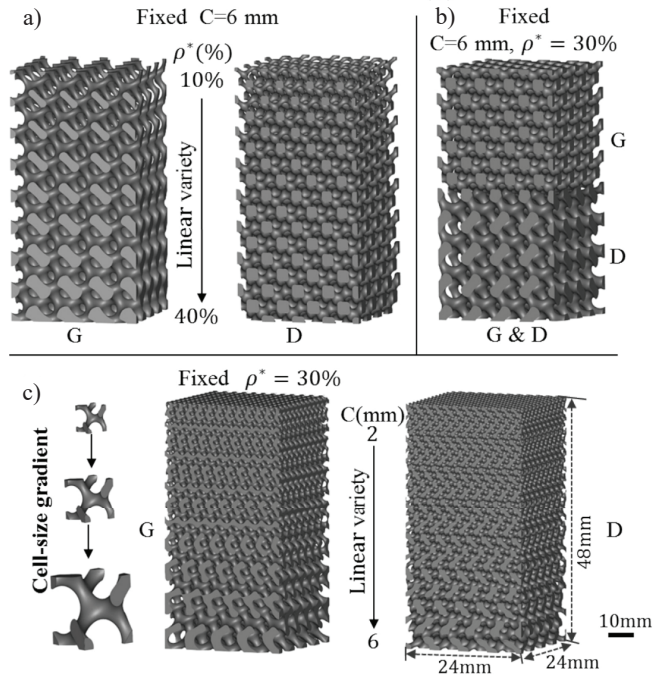

Fig. 4. Designed models of gradient samples; a) in relative density, b) in heterostructure and c) in cell size. Reproduced from [40]

3 PRODUCTION TECHNOLOGIES OF TPMS STRUCTURES

Because of their complexity, TPMS structures can only be produced with limited technologies. The most common and widespread is additive manufacturing (AM). It enables the creation of complex geometries that are difficult or impossible to achieve with traditional methods. Even with the advancements in AM technologies, the porous features and complex geometries still represent a challenge for layer-by-layer manufacturing [27].

3.1 Powder Bed Fusion – Laser Beam/Metals (PBF-LB/M)

PBF-LB/M, sometimes referred to as selective laser melting (SLM), is a type of laser powder bed fusion (LPBF), which falls under the broader category of powder bed fusion (PBF) technologies. In PBF-LB/M fabrication, a high-power laser is used to fully melt metallic powders to create structures. Not all of the powder gets melted. The remaining media supports the next layers [27]. With PBF-LB/M, both the size of the laser spot and material grain size influence the quality of the final product. The most commonly used materials in PBF-LB/M manufacturing are Ti6Al4V and 316L stainless steel [46–49]. Metals are used instead of polymers for applications that require greater strength. Another advantage of these two materials is their corrosion resistance and biocompatibility, making them

excellent for use in medical fields as porous bone scaffolds [47,49]. The aerospace industry is another sector that has been utilizing AM metamaterials made with PBF-LB/M for less demanding, lightweight components, with TPMS geometries slowly being integrated [50]. The manufacturing accuracy of TPMS structures with PBF-LB/M is influenced by the designed thickness and overhang angle, mainly because of unmelted material particles sticking to the surface [51]. These regions accelerate fatigue crack initiation and should be removed or minimized with post-treatments to improve fatigue life [18,46].

3.2 Powder Bed Fusion – Laser Beam/Polymers (PBF-LB/P)

As the name suggests, PBF-LB/P works on the same principle as PBF-LB/M technologies, but this process only sinters or bonds the material together without fully melting it. Commonly used materials include semi-crystalline and amorphous polymers, ceramics, metals such as Ti6Al4V and CoCr, and various polymer composites. The resulting parts are somewhat porous, making them suitable for vibration absorption [27]. They are also of a good enough quality to be compared to the ideal geometries used in numerical tests. Their mechanical characteristics are greatly influenced by the relative density and porosity of the sintered material [52]. The main advantage of this method is the possibility of mixing different types of powder material, enhancing their mechanical properties, and achieving controlled degradation [53].

3.3 Vat Photopolymerization – Photoinitiated (VPP-PI)

A different approach to additive manufacturing is VPP-PI. It uses a photosensitive liquid material that cures layer by layer using ultraviolet or another special light source [27]. The designs can be produced with high accuracy depending on the size of the light spot, and mechanical properties depend on the specimen's geometry and post-curing time [54]. The main drawback of this technique is the limited number of materials that can be utilized, but this number is slowly growing with materials such as Biomed Amber making their appearance [55]. Instead of using a light spot to trace each layer, a screen can also be used to project an entire layer at once. This approach reduces build times while maintaining high precision. This process's main limitation is the projection's resolution, as the pixel size determines the print accuracy. Additionally, the build volume is generally smaller than when using a laser due to the projection system [27]. Despite these limitations, it is being used to produce and analyze complex TPMS geometries intended for use as electromagnetic absorbers in the field of high-temperature electromagnetic wave absorption [56]. Although this method produces smoother surfaces, the limited material options restrict usability and research, even though surface quality suggests potential improvements in fatigue life over powder-based approaches.

3.4 Material Extrusion – Thermal Rheological Behavior/Polymers (MEX-TRB/P)

Probably the most well-known additive manufacturing method is fused deposition modelling, or MES-TRB/P. This is most used in commercially available AM technologies. Material is melted and extruded layer by layer to build the desired part. This type of manufacturing is of lower precision than VPP-PI or PBF-LB/M, and many support structures are needed, resulting in wasted material and rough surface finishes [27]. Despite its limitations, MEX-TRB/P offers an effective way of producing geometries quickly and for a relatively low price from polylactic acid (PLA), acrylonitrile butadiene styrene (ABS) or similar polymer materials and comparing results of different types of geometries [57]. An advantage of this production method is the possibility of reasonably quickly constructing specimens from two or more other materials, creating so-called interpenetrating phase composites (IPC) [58].

3.5 AM-assisted/Hybrid Casting

A newer way of manufacturing cellular structures is so-called hybrid casting. The first step in the process is creating an AM model of metamaterial samples using castable wax resin. The samples are connected to each other with channels (Fig. 5a). A mold is then created with Ransom & Randolph "Platinum Investment & Binder" around the wax structure, followed by a burnout cycle (Fig. 5b and c). The resulting mold can be used to cast complex geometries such as TPMS structures. The process is described in more detail in the work of Singh et al. [59]. When TPMS structures made with this new hybrid technology were compared with ones created with PBF, the cast specimens exhibited a longer fatigue life. This improvement is primarily attributed to smoother surfaces, reduced porosity and more rounded geometrical transitions achieved by the casting process. These microstructural and geometric advantages, in turn, result in less fatigue ratcheting and strain accumulation during cyclic loading. The same authors have used this new process to embed the specimens within another material, creating IPCs [60]. Interestingly, they observed that the mechanical response of Al-ceramic and steel-Al interpenetrating phase composites considerably differs from the performance of the base materials. This production method could significantly increase the availability of cellular structures and their use in real-world applications, since casting enables the production of many products at a lower cost.

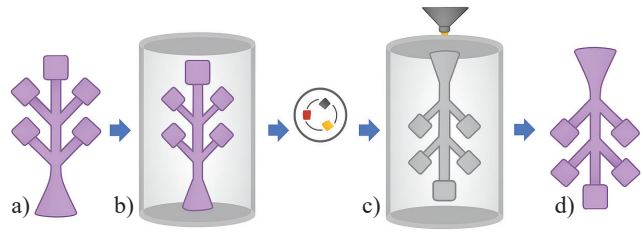

Fig. 5. Schematic of the hybrid casting production process; a) additively manufactured wax resin samples, b) creation of mold used for casting, c) casting of specimens, and d) cast specimens

4 MECHANICAL CHARACTERIZATION OF TPMS STRUCTURES

Mechanical characterization of TPMS structures is commonly performed under quasi-static loading; however, many of the observed mechanisms, such as buckling, densification and deformation mode (stretching- or bending-dominated), directly affect fatigue resistance.

It is essential to analyze the structures across multiple orders of magnitude to characterize cellular materials and understand their deformation behavior. At the macroscopic level, entire components or representative test samples typically comprise at least 5 to 7 cells (3 cells for 2D geometries [61]) in each direction are used in an analyzis. This scale allows for the statistical evaluation of mechanical properties, such as elastic modulus, Poisson's ratio and plateau stress. When analyzing at the mesoscopic scale, the focus shifts to individual cells within the material. They are influenced by the geometry, choice of base material, and, in some cases, gases caught in the cells. The last microscopic scale describes the base material from which the cellular structures are made. This includes chemical elements, pores and possible inclusions. When analyzing cellular materials, it is

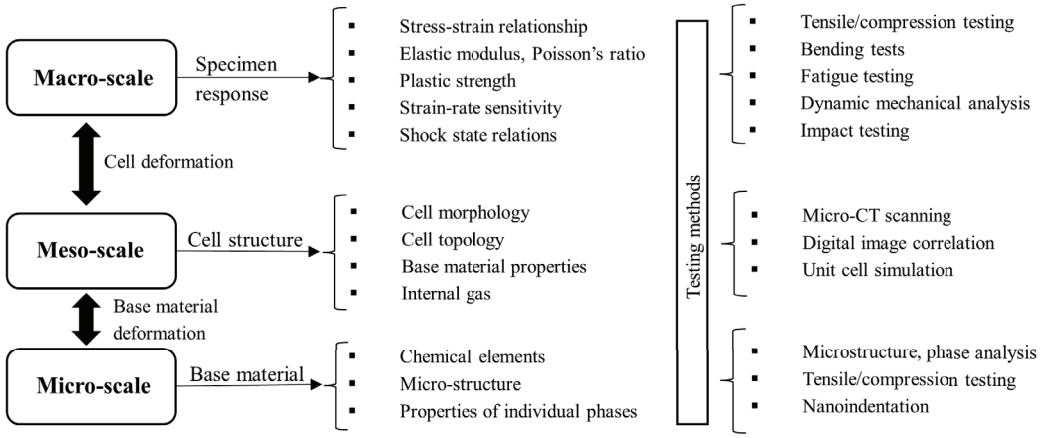

Fig. 6. Properties and characteristics at different scales for cellular materials

essential to understand the connections between the different orders of magnitude to be able to examine the mechanical response. The mechanisms at the micro and meso scales determine macroscopic properties. For instance, global macroscopic deformation reflects the nominal strain observed in the material. In contrast, local macroscopic deformation corresponds to the global response at the mesoscopic level or the deformation behavior of individual cells. The exact correlation between mesoscopic local strain and microscopic global strain can be made, representing the base material strain [62]. Properties, characteristics and testing methods at different scales for cellular materials are graphically presented in Fig. 6.

A typical compressive stress-strain response of cellular structures can be divided into three distinct deformation stages, as illustrated in Fig. 7. The initial elastic stage is known as the pre-collapse stage and is characterized by a nearly linear response of the material. This is caused by the elastic deformation of cell walls in the material. When the strain in the material reaches a point where it starts to deform plastically, and the cells begin to buckle, bend or collapse, it enters the so-called plateau stage. It is characterized by a significant increase in strain with minimal increase in stress, resulting in a nearly horizontal stress-strain response. This phase is responsible for the material's energy absorption capabilities. As the deformation increases, the cellular structure becomes increasingly compressed and compact, leading to the densification stage. In this final phase, the collapsed cell walls come in contact with each other, and the material acts more like a solid specimen. This results in a steep rise in the stress-strain curve, so-called densification [63–66].

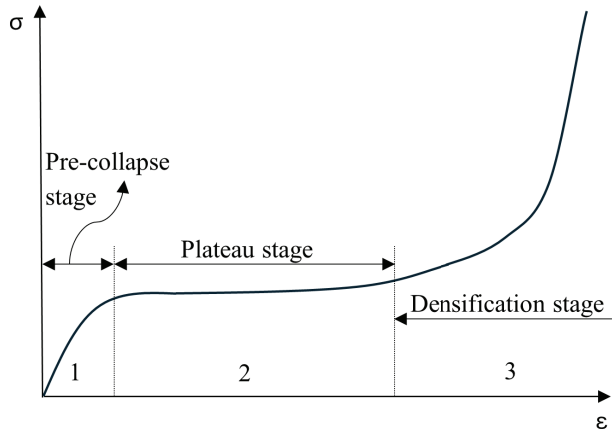

Fig. 7. Characteristic quasi-static compressive stress-strain curve for cellular materials

Deformation velocity is another critical factor that influences the mechanical response of cellular materials. Under quasi-static loading conditions, where the deformation occurs at a very low strain rate, materials typically have a homogeneous response throughout their entire volume. In this regime, the structures deform uniformly until local instabilities or imperfections cause the collapse of individual layers or regions. On the other hand, when the specimens are subjected to high-speed loading, such as impact or impulse, the material exhibits a different behavior [62]. It usually becomes stiffer, and the deformation localizes at the point of loading. Instead of a uniform collapse, a localized deformation forms at the loading point, known as a so-called shock front [67]. This behavior is essential in applications involving fast, dynamic loads where a lot of energy must be absorbed quickly, such as in a crash [62,68]. When subjected to a macroscopic load, static or dynamic, cellular structures can deform by a combination of bending, twisting or stretching [69]. If the struts support mainly axial loads and collapse by stretching, the geometry is referred to as stretching-dominated. In contrast, if the deformation occurs primarily through bending of the struts or cell walls, the structure is considered bending-dominated. Most cellular solids, such as metal foams, are bending-dominated. Consequently, they exhibit lower strength and stiffness compared to stretching-dominated geometries [70]. Another way of determining what mechanism is more prevalent in a geometry is by plotting their mechanical properties obtained from uniaxial tests using the Gibson–Ashby scaling power law [2]:

$$M = C\bar{\rho}^{n}. \tag{2}$$

In this relation, M is the normalized mechanical property, and $\bar{\rho}$ is the relative density. The parameters C and n are obtained by fitting experimental data, with the exponent n in particular serving as an indicator of the dominant deformation mechanism [71]. If the value of n is below 2, then the geometry is stretching-dominated, while anything above is considered bending-dominated. Following this criterion, sheet-based TPMS metamaterials are stretching-dominated, while skeletal-based geometries are bending-dominated, with the exception being the skeletal gyroid [70].

Knowing these deformation mechanisms allows us to evaluate advanced cellular geometries such as TPMS, which offer unique mechanical advantages to conventional materials. As already mentioned, their properties are influenced by the manufacturing process, material selection and unit cell geometry. Unlike conventional strut-based geometries, their uninterrupted surfaces enhance their mechanical efficiency under various loading conditions. Several studies have been conducted proving this fact [63–66]. They

all concluded that TPMS structures outperform other designs when subjected to compressive and tensile loads, with the Diamond and Gyroid sheet geometries outperforming other structures.

Table 2 shows the mechanical properties of several cellular materials made from Ti6Al4V under quasi-static compressive loading. The base material was selected due to its excellent corrosion resistance, favorable strength-to-weight ratio and AM capabilities, making it common in the field of cellular structures. Structures made from materials with comparable properties can be expected to exhibit similar performance under equivalent conditions. Elastic modulus and strength of TPMS metamaterials are greatly influenced by the type of unit cell and base material selection. How the shape of the unit cell affects the elastic modulus is graphically presented in Fig. 8, which was prepared by the authors based on the data reported in the literature and summarized in Table 2. The results demonstrate that for a given relative density, TPMS structures such as Gyroid and I-WP achieve a significantly higher elastic modulus compared to strut-based lattices. Strut-based geometries generally show lower stiffness but can still offer comparable compressive strength depending on density. Open-cell foams exhibit the lowest strength values, confirming the superior load-bearing capacity of TPMS structures. Using PBF-LB/M with Ti6Al4V alloy, Gain et al. [20] were able to closely mimic the elastic modulus, compressive strength and tensile strength of human cortical bone with graded TPMS metamaterials. A similar study was conducted by Wang et al. [21], where cubic, octet and TPMS gyroid lattice structures were fabricated to mimic natural bone. The gyroid structure was found to have the highest elastic modulus and yield strength.

Porosity is another parameter influencing the mechanical characteristics of TPMS structures, and it was investigated by Cai et al. [72]. Results comparing the different iterations showed that both yield strength and modulus of elasticity decreased when porosity was increased. Another observation was that the failure mechanism changed. While low-porosity geometries broke down via buckling, high-porosity specimens endured micro-fractures under load. The introduction of functionally graded porosity with a varying density across different regions of the structure was demonstrated to enhance mechanical strength and energy absorption capacity by Liu et al. [40], Zhang et al. [73] and Shi et al. [44]. This results from mitigating stress concentrations and providing a more uniform load distribution. Since porosity influences crack initiation and propagation, these results link structural design and fatigue strength. Higher porosity often reduces fatigue life due to stress concentration and easier crack initiation.

Several studies have emerged in recent years exploring possible alternative designs and their advantages. Isotropy would be an excellent characteristic for load-bearing and energy-absorption implications, meaning the material has the same response under loads in all orientations. Fu et al. [74] designed and tested such structures by performing Boolean operations. The new isotropic hollow cellular structures had a higher Young's modulus and better energy absorption properties than the original designs. In works [44,45], hybrid designs have been shown to improve energy absorption efficiency and yield strength under both static and dynamic loading conditions.

Table 2. Compressive mechanical characteristics of common cellular and TPMS shapes made from Ti6Al4V

The shape of base cell	Relative density [-]	Compressive strength	Elastic modulus E [GPa]	Ref.
Gyroid (TPMS)	0.1-0.4	16.44-275.17	1.21-10.60	[75-77]
I-WP (TPMS)	0.1-0.4	9.81-306.62	0.94-3.2	[77]
Diamond (strut-based)	0.13-0.4	21.00-118.80	0.4-6.5	[78,79]
Cubic (strut-based)	0.3-0.6	7.28-163.02	0.57-14.59	[80]
Foam (open-cell)	0.08-0.1	3.80-4.50	0.19-0.49	[81]
Rhombic dodecahedron (strut-based)	0.14-0.38	12.4-112.8	0.54-6.34	[81]

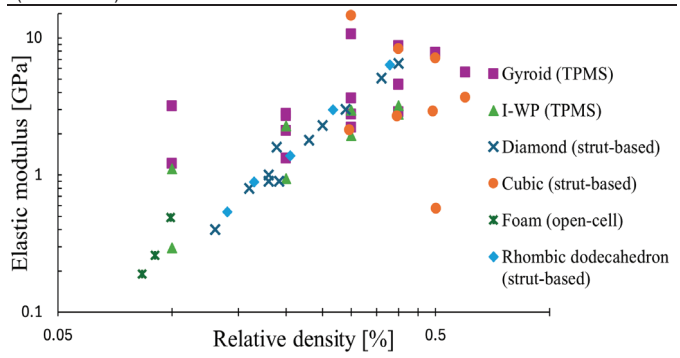

Fig. 8. Graphical comparison of elastic modulus of different cellular structures made from Ti6Al4V

5 FATIGUE BEHAVIOR OF TPMS STRUCTURES

When designing cellular structures, their fatigue behavior has become a critical consideration, particularly for those that are intended to be used in load-bearing applications. As highlighted by Benedetti et al. [82] in their literature review, the majority of fatigue design methods rely on experiments, which are time-consuming, expensive and able to handle only selected architectures and materials. While there are theoretical approaches, they can result in inappropriate estimates of the material parameters [83]. They did highlight, however, that with the amount of numerical methods, machine learning algorithms and data-driven approaches being developed in recent years, they could predict complex nonlinear relationships. Despite this promise, predictive modelling of TPMS fatigue life remains challenging. Classical finite element analyzis can capture stress distributions, but it struggles to account for manufacturing defects, surface roughness and microstructural variability. This makes purely numerical predictions unreliable without experimental calibration. By training on experimental datasets, data-driven methods, including machine learning, could capture complex mechanisms and fatigue response. However, such models require large datasets and careful validation. The integration of physics-based simulations with machine learning is therefore emerging as a promising direction. Reflecting these challenges, Nečemer et al. [29] also noted that the fatigue performance of cellular materials under cyclic loading remains underexplored and requires further investigation. While TPMS metamaterials exhibit substantial potential as lightweight structural materials, their fatigue behavior is still limited and warrants further investigation. They are especially of interest because of their smooth transitions between struts, avoiding stress concentrations which could promote better fatigue life. Most studies until now have focused on the impact of manufacturing and topology on their mechanical response [63–66]. Even though these types of structures are being investigated for use in applications where damage is a result of repetitive, low-intensity loads, only a handful of studies have been conducted [30]. In this section, relevant scientific articles on the fatigue behavior of TPMS metamaterials are presented.

The defining characteristic of TPMS metamaterials is their topology, which dictates how they deform under loading. Different types of TPMS unit cells have been evaluated for their fatigue performance, stress distribution and failure mechanisms. This is presented in Table 3, where common TPMS and regular cellular structures are presented with their fatigue properties. Fatigue strength is the maximum stress a material can withstand for a specified number of loading cycles without failure, while the fatigue ratio, or sometimes called fatigue endurance ratio, is the fatigue strength

Table 3. Fatigue properties of different metamaterials

The shape of base cell	Material	Relative density [-]	Ultimate cycles	Fatigue strength [MPa]	Fatigue ratio [-]	Ref.
Gyroid (TPMS)	316L	0.15	2·106	9.1	0.35	[30]
Gyroid (TPMS)	316L	0.15	2·106	11.7	0.45	[30]
Gyroid (TPMS)	Ti6Al4V	0.31	106	14.3	0.18	[84]
Diamond (TPMS)	Ti6Al4V	0.31	106	18.4	0.17	[84]
Schwarz Primitive (TPMS)	Ti6Al4V	0.31	106	13.6	0.21	[84]
I-WP (TPMS)	NiTi	/	106	2.08	0.33	[85]
BCC (strut-based)	NiTi	/	106	1.88	0.34	[85]
Cubic (strut-based)	Ti6Al4V	0.37	107	75	0.48	[86]
Rhombic dodecahedron (strut-based)	Ti6Al4V	0.8	107	13.9	0.2	[86]

divided by yield strength. It can be observed that there is a large variation in fatigue ratios between Ti6Al4V and 316L Gyroid structures. This can be attributed to a number of factors, with the most influential being the high ultimate strength of Ti6Al4V compared to 316L stainless steel. Others may include surface quality of specimens, porosity, relative density and testing parameters. Yang et al. [30] investigated a Gyroid structure fabricated with PBF-LB/M and subjected to compression-compression cyclic fatigue. Their study concluded that TPMS geometries have a higher fatigue resistance than strut-based lattice structures, primarily due to their stretch-dominated deformation mechanism. The failure analyzis showed that fatigue cracks formed at nodal intersections, leading to 45° diagonal fracture bands. A similar result was achieved by Soro et al. [84] under tension-tension loading conditions for three different TPMS geometries. They also outperformed regular strut-based lattices, with fatigue cracks initiating at the surface, highlighting the importance of post-treatment. Jiang et al. [87] performed experimental testing and finite element analyzis (FEA) on four TPMS metamaterials (Gyroid, Diamond, I-WP, Schwarz Primitive) to evaluate their torsional and fatigue resistance. They found that the Schwartz Primitive shape exhibits superior torsional and fatigue resistance. I-WP structures showed lower torsional fatigue resistance because of their bending-dominated deformation. This failure was initiated at the curved junctions, with stress concentrations occurring in all four structures during the compression process. These aligned closely with the regions exhibiting larger strain. The same four TPMS geometries were analyzed by Bobbert et al. [88] under compression-compression loading. The change in loading conditions resulted in the Schwarz Primitive geometry having the shortest fatigue life, while all the other specimens varied between $1 \cdot 10^5$ cycles and $7 \cdot 10^5$ cycles. The samples failed under a 45° angle, aligning with the observations made by Yang et al. [30] under the same loading conditions. Importantly, they highlighted a greater fatigue resistance compared to other AM porous materials. Even when loaded with stress levels as high as 60 % of their yield stress, some variants managed to exceed the usual threshold of $1 \cdot 10^6$ cycles used for these types of AM materials. Another study comparing different geometries was conducted by Singh et al. [59]. They compared Gyroid and I-WP metamaterials made from AlSi10Mg using powder bed fusion (PBF). They were subjected to load-controlled cyclic loading. They found that Gyroid designs outperformed I-WP specimens. Overall, they had comparable or lower fatigue ratcheting and higher stiffness. In particular, the Gyroid structures with 30 % relative density consistently demonstrated longer fatigue lives with lower comparable damage metrics. Overall, these studies indicate that the fatigue performance of TPMS metamaterials is largely determined by the topology and deformation mode, with stretching-dominated geometries such as Gyroid being better suited for compression and tension loading, while the Primitive geometry exhibits better fatigue life when subjected to bending loads. Bending-dominated geometries, such as I-WP, on the other hand, tend to concentrate stresses at curved junctions, making them less efficient under loads and more prone to earlier fatigue failure.

Mechanical performance, surface quality, and fatigue behavior are all impacted by the manufacturing process used to produce specimens. Because of this, several publications were conducted to determine how the different technologies affect fatigue life. Tilton et al. [89] investigated TPMS scaffolds fabricated with Ti6Al4V via PBF. The process left behind unwanted surface characteristics like partially melted powder and their agglomerations. These unwanted surface characteristics were initiation sites for fatigue failure. A

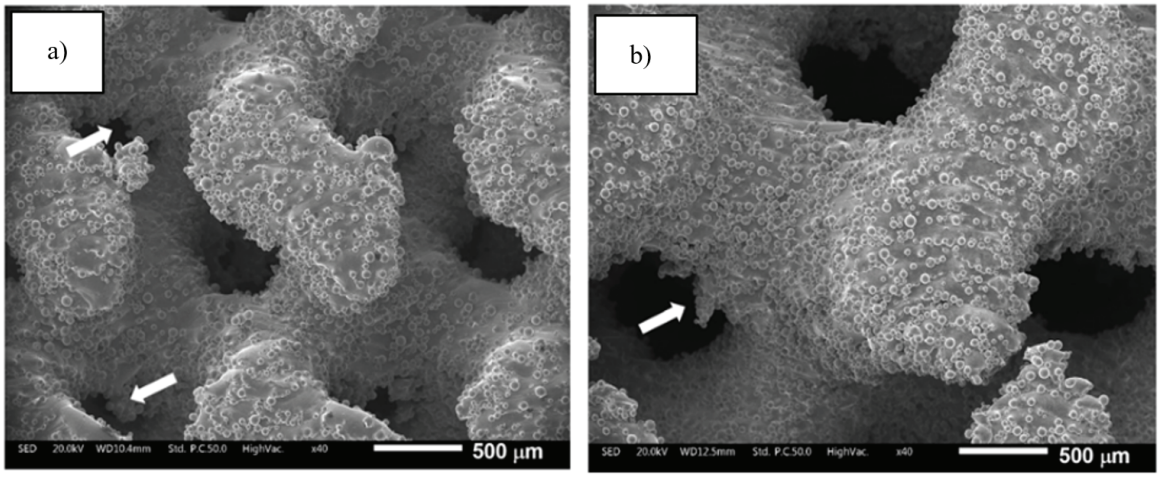

Fig. 9. SEM micrograph of TPMS metamaterials with; a) 1.5 mm, and b) 2.5 mm unit cell size, adapted from [90]

similar study was done by Ren et al. [85], but with nickel-titanium as the base material. Similar results were achieved with unmelted or partially melted particles on the surface of the structures. Cracks appear at the root of powder particles attached to the surface. The I-WP lattice structure seemed to slightly benefit in avoiding powder adhesion. Even though AM has come a long way, it still has some limitations. In a study by Emanuelli et al. [90], TPMS samples made with PBF from β-Ti21S alloy were investigated. They concluded that this material exhibits promising mechanical and biological properties for femoral implants. However, its main drawback was poor printability, which impacted pore size and fatigue resistance. They also highlighted surface irregularities and agglomerations, pointed out in Fig. 9, caused by unmelted material particles.

Studies on possible post-treatment methods that would improve surface quality, reduce stress concentrations, and eliminate manufacturing defects have been conducted to try to mitigate some of the inherent drawbacks of AM technologies. Liu et al. [91] studied the impact of high isostatic pressing (HIP) and electropolishing (ELP) on the fatigue life of diamond and gyroid TPMS structures. HIP is a process in which high pressures are applied at elevated temperatures to enhance the material's ductility and improve mechanical performance. This process resulted in a decline in surface roughness, reduced micro porosities, and released residual stresses in the Ti6Al4V specimens. Because of this, the fatigue ratio of bending-dominated TPMS structures improved from 0.11 to 0.26 and from 0.59 to 0.69 for the stretching-dominated structures. As in previous studies, the absence of surface particles enhanced the fatigue resistance by reducing crack initiation zones. Similar results were achieved by Singh et al. [59]. They examined heat-treated AlSi10Mg TPMS structures fabricated with PBF. The process significantly improved the fatigue resistance compared to as-built structures. This was due to a slower fatigue damage accumulation in the heat-treated samples. The most significant effect was seen in Gyroid 30 % density geometries. These findings confirm that different heat treatments effectively enhance the fatigue life of TPMS structures made with AM methods. Other methods to improve the surface quality of specimens are chemical etching, shot peening, and sandblasting. Araya-Calvo et al. [76] compared as-built and chemically etched Ti6Al4V structures and concluded that the post-treated samples had an approximately 20 % improved fatigue resistance. They also demonstrated better biocompatibility and surface morphology. The effect of chemical etching is shown in Fig. 10. The as-built specimens show a significantly rough surface due to the adhesion of partially melted powder particles. The post-treatment resulted in a smoother surface, which resulted in improved fatigue resistance.

An advantage of mechanical post-treatments such as shot peening and sandblasting is the compressive residual stresses they leave behind on the surface, which was investigated by Jiang et al. [92] and Was et al. [93]. These delay crack initiation and extend fatigue life. This was studied by Yang et al. [30] on sandblasted Gyroid structures. The fatigue resistance increased from 0.35 for the as-built samples to 0.45 for the sandblasted specimens. In addition to the residual

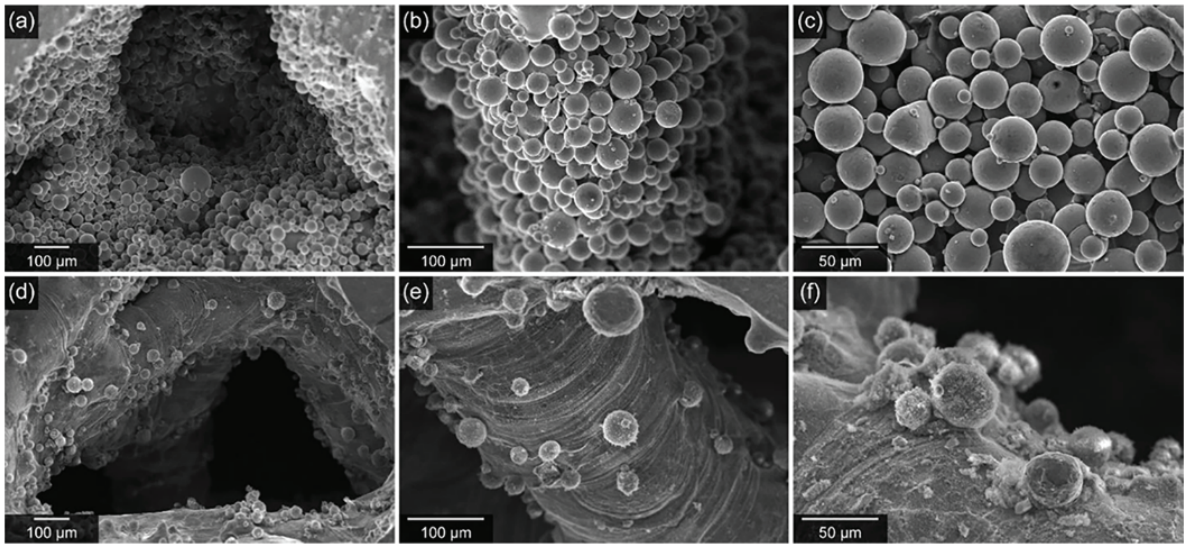

Fig. 10. Comparison of a) b) c) as-built with d) e) f) chemically etched specimens, reproduced from [76]

Table 4. Summary table of post-processes with their mechanisms and effect on fatigue life

Post-processing method	Mechanism	Effect on fatigue life	Reference
Hot isostatic pressing (HIP) (applied in combination with ELP)	Removes microporosity, relieves residual stress, improves ductility	Improved fatigue ratio from 0.11 to 0.26 (Gyroid) and from 0.59 to 0.69 (Diamond)	Liu et al. [91]
Electropolishing (ELP) (applied in combination with HIP)	Reduces surface roughness, removes powder particles	Improved fatigue ratio from 0.11 to 0.26 (Gyroid) and from 0.59 to 0.69 (Diamond)	Liu et al. [91]
Heat treatment	Slows fatigue damage accumulation, improves microstructure	Improved fatigue life due to lower fatigue ratcheting	Singh et al. [59]
Chemical etching	Smooths surface, removes powder particles	Improved fatigue resistance, especially at lower stress levels	Araya-Calvo et al. [76]
Sandblasting	Removes powder particles, introduces compressive residual stress	Fatigue resistance increased from 0.35 to 0.45	Yang et al. [30]
Shot peening	Removes powder particles, introduces compressive residual stress	Extended fatigue life because of delayed crack initiation	Jian et al. [92], Was et al. [93]

stresses, the process removed partially melted powder particles, reducing stress concentrations and crack initiation zones. Their results show that surface treatments are a highly effective way of mitigating fatigue failure, especially when working with AM-fabricated TPMS structures. Table 4 summarizes the main post-processing methods investigated for TPMS structures. In it, the mechanisms by which each technique improves fatigue life are highlighted, and results are presented to provide a clearer overview.

Among the potential applications of TPMS cellular structures, the biomedical field has the most studies, particularly for use as bone scaffolds [94–96]. Slowly, they are also being considered for dental implants, as numerically investigated by Kök et al. [97]. Compared to standard dental implants, they showed 15 % less stress-shielding and still complied with the number of cycles required by DIN EN ISO 14801, resulting in a 45 % reduction in weight.

6 CONCLUSIONS

This review of recent studies confirms that TPMS structures are a versatile class of cellular structures with a broad potential. Their continuous geometry based on mathematical equations offers advantages in terms of mechanical properties, unit cell design, and tunability. Compared to traditional strut-based cellular structures, they demonstrate superior mechanical performance under static and dynamic loads because of their smoother stress distribution, especially in the Gyroid and Diamond unit cell shapes. They also mitigate failure caused by stress concentrations, which are common in strut-based designs.

A general observation across the analyzed studies is that the mechanical properties of TPMS structures depend not only on the relative density and cell type but can also be significantly enhanced by improving surface quality and reducing unit cell size. Because they are almost entirely fabricated with AM technologies, the resulting specimens have unwanted leftover material particles, and their agglomerations stuck to the surfaces. This implies that post-processing treatments such as sandblasting, electropolishing, and chemical treatments are essential for achieving consistent results. It can be expected that newer approaches like plasma electropolishing will also become increasingly relevant for producing smoother surfaces and improving fatigue performance in TPMS structures. Research in applications such as medicine, energy, sound absorption, dental implants, vibration absorption, static mixing, and heat transfer highlights the benefits of the tunable geometry of TPMS metamaterials. These diverse areas of study suggest a broad potential in future technologies.

The paper gives an overview of the fatigue behavior of TPMS cellular structures with consideration for their fabrication and characterization. Based on the reviewed literature, we can draw the following conclusions:

- TPMS geometries consistently outperform conventional strut-based lattice structures in both static and dynamic loading scenarios. The best-performing unit cell geometries are Gyroid and Diamond structures.
- The properties of TPMS metamaterials are closely tied to the manufacturing process. Most are fabricated with AM methods that introduce surface imperfections that must be reduced with post-treatments to improve fatigue life.
- Advanced TPMS design strategies, such as different types of grading and multimorphology designs, enable mechanical tuning. These allow the development of application-specific materials.

Although considerable progress has been made in optimising the mechanical properties of TPMS metamaterials through unit cell design, there is considerable potential for further improvements, especially with grading strategies, hybrid geometries, and multi-material integration. In conclusion, TPMS metamaterials represent structurally efficient, customizable and application-specific cellular materials that show promising results for use in fields such as biomedical engineering, energy absorption applications, and thermal management.

7 SUGGESTIONS FOR FUTURE RESEARCH WORK

Despite significant research in the design and mechanical characterization of TPMS metamaterials, not much emphasis has been placed on their fatigue behavior which is evident in the limited number of publications. Future work should firstly focus on achieving good reproductivity. This could be done by using specimens of similar size, relative density and production methods if possible. The results would give us a more general understanding of their properties and be a good foundation for analyzing more complex factors. After this a logical next step would be to analyze how different mean stresses and strains affect their fatigue life. Most tests up to this point have been uniaxial which is sufficient if the loads are mostly in one direction. With more complex spaces being filled with TPMS metamaterials, multiaxial tests should be considered for future work. Outside factors such as impacts could cause deformations and failure in directions not accounted for in uniaxial tests. Lastly, because these types of structures can be utilized as fluid mixers and heat exchangers, studying the effects that temperature has on its fatigue life could prove beneficial to prevent premature failure caused by temperature fluctuations.

References

[1] Neff, C., Hopkinson, N., Crane, N.B. Experimental and analytical investigation of mechanical behavior of laser-sintered diamond-lattice structures. *Addit Manuf* 22 807-816 (2018) **DOI:10.1016/j.addma.2018.07.005**.

[2] Gibson, L.J., Ashby, M.F. *Cellular Solids* (1997) Cambridge University Press, Cambridge **DOI:10.1017/CBO9781139878326**.

[3] Costanza, G., Solaiyappan, D., Tata, M.E. Properties, Applications and Recent Developments of Cellular Solid Materials: A Review. *Materials* 16 7076 (2023) **DOI:10.3390/ma16227076**.

[4] Nečemer, B. *Low Cycle Fatigue of Auxetic Cellular Structures*. PhD thesis (2021) Univerza v Mariboru, Maribor. (in Slovene)

[5] Azevedo Vasconcelos, A.C., Schott, D., Jovanova, J. Hybrid mechanical metamaterials: Advances of multi-functional mechanical metamaterials with simultaneous static and dynamic properties. *Heliyon* 11 e41985 (2025) **DOI:10.1016/j.heliyon.2025.e41985**.

[6] Ashby, M.F. *Metal Foams* (2000) Elsevier, Oxford.

[7] Wu, J., Zhang, X., Liu, K., Cheng, Q., He, Y., Yin, J. Auxetic hierarchical metamaterials with programmable dual-plateau energy absorption and broadband vibration attenuation. *Eng Struct* 330 119912 (2025) **DOI:10.1016/j.engstruct.2025.119912**.

[8] Novak, N., Vesenjak, M., Ren, Z. Auxetic cellular materials - A review. *Stroj Vestn-J Mech E* 62 485-493 (2016) **DOI:10.5545/sv-jme.2016.3656**.

[9] Žnidarič, Ž., Nečemer, B., Novak, N., Glodež, S. Fatigue Analysis of Axisymmetric Chiral Cellular Structures Made out of 316L Stainless Steel. *Materials* 17 24 (2024) **DOI:10.3390/ma17246152**.

[10] Bai, L., Gong, C., Chen, X., Zheng, J., Xin, L., Xiong, Y., et al. Quasi-Static compressive responses and fatigue behaviour of Ti-6Al-4V graded lattice structures fabricated by laser powder bed fusion. *Mater Des* 210 (2021) **DOI:10.1016/j.matdes.2021.110110**.

[11] Boniotti, L., Beretta, S., Foletti, S., Patriarca, L. Strain concentrations in BCC micro lattices obtained by AM. *Proc Struct Integr* 7 166-173 (2017) **DOI:10.1016/j.prostr.2017.11.074**.

[12] Boniotti, L., Beretta, S., Patriarca, L., Rigoni, L., Foletti, S. Experimental and numerical investigation on compressive fatigue strength of lattice structures of AlSi7Mg manufactured by SLM. *Int J Fatigue* 128 105181 (2019) **DOI:10.1016/j.ijfatigue.2019.06.041**.

[13] Mishra, A., Jatti, V.S., Sefene, E.M., Makki, E. Homogenization of Inconel 625 based periodic auxetic lattice structures with varying strut thickness. *APL Mater* 12 021128 (2024) **DOI:10.1063/5.0195388**.

[14] Zhang, Y., Zhang, J., Zhao, X., Li, Y., Che, S., Yang, W., et al. Mechanical behaviors regulation of triply periodic minimal surface structures with crystal twinning. *Addit Manuf* 58 103036 (2022) **DOI:10.1016/j.addma.2022.103036**.

[15] Luo, D., Su, J., Zou, Y., Hua, S., Cheng, L., Qi, D., et al. 3D-printed triply periodic minimal surface bioceramic scaffold for bone defect treatment with tunable structure and mechanical properties. *Ceram Int* 50 39020-39031 (2024) **DOI:10.1016/j.ceramint.2024.07.268**.

[16] Xu, D., Lin, M. Design controllable TPMS structures for solar thermal applications: A pore-scale vs. volume-averaged modeling approach. *Int J Heat Mass Tran* 201 123625 (2023) **DOI:10.1016/j.ijheatmasstransfer.2022.123625**.

[17] Ouda, M., Al-Ketan, O., Sreedhar, N., Hasan Ali, M.I., Abu Al-Rub, R.K., Hong, S., et al. Novel static mixers based on triply periodic minimal surface (TPMS) architectures. *J Environ Chem Eng* 8 104289 (2020) **DOI:10.1016/j.jece.2020.104289**.

[18] Zhang, L., Feih, S., Daynes, S., Chang, S., Wang, M.Y., Wei, J., et al. Energy absorption characteristics of metallic triply periodic minimal surface sheet structures under compressive loading. *Addit Manuf* 23 505-515 (2018) **DOI:10.1016/j.addma.2018.08.007**.

[19] Naghavi, S.A., Tamaddon, M., Marghoub, A., Wang, K., Babamiri, B.B., Hazeli, K., et al. Mechanical characterisation and numerical modelling of TPMS-Based Gyroid and Diamond Ti6Al4V Scaffolds for Bone Implants: An Integrated Approach for Translational Consideration. *Bioengineering* 9 504 (2022) **DOI:10.3390/bioengineering9100504**.

[20] Gain, A.K., Cui, Y., Zhang, L. Pore-gradient Ti6Al4V alloy mimicking the properties of human cortical bones: The design of TPMS structures by selective laser melting. *Mater Sci Eng A* 915 147220 (2024) **DOI:10.1016/j.msea.2024.147220**.

[21] Wang, N., Meenashisundaram, G.K., Chang, S., Fuh, J.Y.H., Dheen, S.T., Senthil Kumar, A. A comparative investigation on the mechanical properties and cytotoxicity of Cubic, Octet, and TPMS gyroid structures fabricated by selective laser melting of stainless steel 316L. *J Mech Behav Biomed* 129 105151 (2022) **DOI:10.1016/j.jmbbm.2022.105151**.

[22] Cresswell, N.D., Ameri, A.A.H., Wang, J., Wang, H., Hazell, P., Escobedo-Diaz, J.P. Characterization and modelling of triply periodic minimum surface (TPMS) lattice structures for energy absorption in automotive applications. *Characterization of Minerals, Metals, and Materials* 2024 295-305 (2024) **DOI:10.1007/978-3-031-50304-7_28**.

[23] Ouda, M., Thesis, M. *The application of Triply Periodic Minimal Surfaces in Static Mixing* (2019) Khalifa University, Abu Dhabi.

[24] Gado, M.G., Al-Ketan, O., Aziz, M., Al-Rub, R.A., Ookawara, S. Triply periodic minimal surface structures: Design, fabrication, 3D printing techniques, state-of-the-art studies, and prospective thermal applications for efficient energy utilization. *Energy Technol* 12 2301287 (2024) **DOI:10.1002/ente.202301287**.

[25] Liu, J., Cheng, D., Oo, K., McCrimmon, T.L., Bai, S. Design and additive manufacturing of TPMS heat exchangers. *Appl Sci* 14 3970 (2024) **DOI:10.3390/app14103970**.

[26] Beer, M., Rybár, R. Optimisation of heat exchanger performance using modified gyroid-based TPMS structures. *Processes* 12 2943 (2024) **DOI:10.3390/pr12122943**.

[27] Feng, J., Fu, J., Yao, X., He, Y. Triply periodic minimal surface (TPMS) porous structures: From multi-scale design, precise additive manufacturing to multidisciplinary applications. *Int J Extrem Manuf* 4 022001 (2022) **DOI:10.1088/2631-7990/ac5be6**.

[28] Koroľ, M., Török, J., Monka, P.P., Baron, P., Mrugalska, B., Monkova, K. Researching on the effect of input parameters on the quality and manufacturability of 3D-printed cellular samples from nylon 12 CF in synergy with testing their behavior in bending. *Polymers* 16 1429 (2024) **DOI:10.3390/polym16101429**.

[29] Nečemer, B., Vesenjak, M., Glodež, S. Fatigue of cellular structures - A review. *Stroj Vestn-J Mech E* 65 525-536 (2019) **DOI:10.5545/sv-jme.2019.6070**.

[30] Yang, L., Yan, C., Cao, W., Liu, Z., Song, B., Wen, S., et al. Compression-compression fatigue behaviour of gyroid-type triply periodic minimal surface porous structures fabricated by selective laser melting. *Acta Materialia* 181 49-66 (2019) **DOI:10.1016/j.actamat.2019.09.042**.

[31] Schwarz, H.A. *Gesammelte Mathematische Abhandlungen* (1890) Springer Berlin **DOI:10.1007/978-3-642-50665-9**.

[32] Meeks, W.H., Pérez, J. The classical theory of minimal surfaces. *Bull Am Math Soc* 48 325-407 (2011) **DOI:10.1090/S0273-0979-2011-01334-9**.

[33] Neuberger, J.W. *Sobolev Gradients and Differential Equations* (2010) Springer, Berlin Heidelberg **DOI:10.1007/978-3-642-04041-2**.

[34] Meeks, W.H., Tinaglia, G. Triply periodic constant mean curvature surfaces. *Adv Math* 335 809-837 (2018) **DOI:10.1016/j.aim.2018.07.018**.

[35] Neovius, E.R. *Bestimmung Zweier Spezieller Periodischer Minimalflächen* (1883) Frenckell, Helsingfors.

[36] Hyde, S., Blum, Z., Landh, T., Lidin, S., Ninham, B.W., Andersson, S., Larsson, K. *The Language of Shape: The Role of Curvature in Condensed Matter: Physics, Chemistry and Biology* (1996) Elsevier Science, Amsterdam.

[37] Schoen, A.H. Triply-periodic minimal surfaces (TPMS). *https://schoengeometry.com/e-tpms.html*, accessed on 2025-10-17.

[38] Araya, M., Jaskari, M., Rautio, T., Guillén, T., Järvenpää, A. Assessing the compressive and tensile properties of TPMS-Gyroid and stochastic Ti64 lattice structures: A study on laser powder bed fusion manufacturing for biomedical implants. *J Sci-Adv Mater Devices* 9 100663 (2024) **DOI:10.1016/j.jsamd.2023.100663**.

[39] Mishra, A.K., Chavan, H., Kumar, A. Effect of cell size and wall thickness on the compression performance of triply periodic minimal surface based AlSi10Mg lattice structures. *Thin-Walled Struct* 193 111214 (2023) **DOI:10.1016/j.tws.2023.111214**.

[40] Liu, F., Mao, Z., Zhang, P., Zhang, D.Z., Jiang, J., Ma, Z. Functionally graded porous scaffolds in multiple patterns: New design method, physical and mechanical properties. *Mater Des* 160 849-860 (2018) **DOI:10.1016/j.matdes.2018.09.053**.

[41] Barba, D., Alabort, E., Reed, R.C. Synthetic bone: Design by additive manufacturing. *Acta Biomater* 97 637-656 (2019) **DOI:10.1016/j.actbio.2019.07.049**.

[42] Yeranee, K., Rao, Y. A review of recent investigations on flow and heat transfer enhancement in cooling channels embedded with triply periodic minimal surfaces (TPMS). *Energies* 15 8994 (2022) **DOI:10.3390/en15238994**.

[43] Yeranee, K., Rao, Y. Triply periodic minimal surfaces thermal hydraulic effects. *https://encyclopedia.pub/entry/39188* accessed on 2025-10-17.

[44] Shi, X., Jiang, W., Song, K., Zhang, C., Liu, T., Liao, W. Energy absorption capability of graded hybrid triply periodic minimal surface structures based on fracture zone controlling. *Adv Eng Mater* 26 10 (2024) **DOI:10.1002/adem.202301847**.

[45] Novak, N., Al-Ketan, O., Borovinšek, M., Krstulović-Opara, L., Rowshan, R., Vesenjak, M., et al. Development of novel hybrid TPMS cellular lattices and their mechanical characterisation. *J Mater Res Technol* 15 1318-1329 (2021) **DOI:10.1016/j.jmrt.2021.08.092**.

[46] Yan, C., Hao, L., Hussein, A., Young, P. Ti-6Al-4V triply periodic minimal surface structures for bone implants fabricated via selective laser melting. *J Mech Behav Biomed Mater* 51 61-73 (2015) **DOI:10.1016/j.jmbbm.2015.06.024**.

[47] Yang, L., Yan, C., Han, C., Chen, P., Yang, S., Shi, Y., 2018. Mechanical response of a triply periodic minimal surface cellular structures manufactured by selective laser melting. *Int J Mech Sci* 148 149-157 (2018) **DOI:10.1016/j.ijmecsci.2018.08.039**.

[48] Yang, L., Yan, C., Han, C., Chen, P., Yang, S., Shi, Y. Mechanical response of a triply periodic minimal surface cellular structures manufactured by selective laser melting. *Int J Mech Sci* 148 149-157 (2018) **DOI:10.1016/j.ijmecsci.2018.08.039**.

[49] Ma, S., Tang, Q., Han, X., Feng, Q., Song, J., Setchi, R., et al. Manufacturability, mechanical properties, mass-transport properties and biocompatibility of triply periodic minimal surface (TPMS) porous scaffolds fabricated by selective laser melting. *Mater Des* 195 109034 (2020) **DOI:10.1016/j.matdes.2020.109034**.

[50] Khan, N., Riccio, A. A systematic review of design for additive manufacturing of aerospace lattice structures: Current trends and future directions. *Prog Aerosp Sci* 149 101021 (2024) **DOI:10.1016/j.paerosci.2024.101021**.

[51] Fan, X., Tang, Q., Feng, Q., Ma, S., Song, J., Jin, M., et al. Design, mechanical properties and energy absorption capability of graded-thickness triply periodic minimal surface structures fabricated by selective laser melting. *Int J Mech Sci* 204 106586 (2021) **DOI:10.1016/j.ijmecsci.2021.106586**.

[52] Jia, H., Lei, H., Wang, P., Meng, J., Li, C., Zhou, H., et al. An experimental and numerical investigation of compressive response of designed Schwarz Primitive triply periodic minimal surface with non-uniform shell thickness. *Extreme Mech Lett* 37 100671 (2020) **DOI:10.1016/j.eml.2020.100671**.

[53] Xu, Y., Ding, W., Chen, M.G., Guo, X., Li, P., Li, M.Q. Porous iron-reinforced polylactic acid TPMS bio-scaffolds: Interlocking reinforcement and synergistic degradation. *Mater Des* 231 112026 (2023) **DOI:10.1016/j.matdes.2023.112026**.

[54] Pehlivan, F. Enhancing tensile properties of polymer-based triply periodic minimal surface metamaterial structures: Investigating the impact of post-curing time and layer thickness via response surface methodology. *Polym Eng Sci* 64 5915-5928 (2024) **DOI:10.1002/pen.26958**.

[55] Araya, M., Murillo, J., Vindas, R., Guillén, T. Compressive behavior of SLA open-cell lattices: A comparison between triply periodic minimal surface gyroid and stochastic structures for artificial bone. *Materialia* 38 102233 (2024) **DOI:10.1016/j.mtla.2024.102233**.

[56] Lu, J., Sheng, M., Gong, H., Jing, J., Zhou, X., Bi, J., et al. Lightweight, ultra-broadband SiOC-based triply periodic minimal surface meta-structures for electromagnetic absorption. *Chem Eng J* 488 151056 (2024) **DOI:10.1016/j.cej.2024.151056**.

[57] Mishra, A.K., Kumar, A. Compression Behavior of Triply Periodic Minimal Surface Polymer Lattice Structures. *Exp Mech* 63 609-620 (2023) **DOI:10.1007/s11340-023-00940-3**.

[58] Wang, K., Wang, H., Zhang, J., Fan, X. Mechanical behavior of interpenetrating phase composite structures based on triply periodic minimal surface lattices. *Compos Struct* 337 (2024) **DOI:10.1016/j.compstruct.2024.118044**.

[59] Singh, A., Jaber, A., Karathanasopoulos, N. Fatigue performance of TPMS-based AlSi10Mg architected cellular materials fabricated via hybrid and powder bed fusion methods. *Int J Fatigue* 193 118044 (2025) **DOI:10.1016/j.ijfatigue.2024.108758**.

[60] Singh, A., Al-Ketan, O., Karathanasopoulos, N. Hybrid manufacturing and mechanical properties of architected interpenetrating phase metal-ceramic and metal-metal composites. *Mater Sci Eng A* 897 146322 (2024) **DOI:10.1016/j.msea.2024.146322**.

[61] Nečemer, B., Lampret, P., Glodež, S. Fatigue behaviour of different chiral auxetic structures using a numerical approach. *Structures* 76 109007 (2025) **DOI:10.1016/j.istruc.2025.109007**.

[62] Sun, Y., Li, Q.M. Dynamic compressive behaviour of cellular materials: A review of phenomenon, mechanism and modelling. *Int J Impact Eng* 112 74-115 (2018) **DOI:10.1016/j.ijimpeng.2017.10.006**.

[63] Sokollu, B., Gulcan, O., Konukseven, E.I. Mechanical properties comparison of strut-based and triply periodic minimal surface lattice structures produced by electron beam melting. *Addit Manuf* 60 103199 (2022) **DOI:10.1016/j.addma.2022.103199**.

[64] Yadav, P., Kushwaha, A., Shukla, M. Analysis of compression behavior of TPMS and strut type lattice structures using finite element method. *NanoWorld J* 9 687-692 (2023) **DOI:10.17756/nwj.2023-s1-131**.

[65] Al-Ketan, O., Rowshan, R., Abu Al-Rub, R.K. Topology-mechanical property relationship of 3D printed strut, skeletal, and sheet based periodic metallic cellular materials. *Addit Manuf* 19 167-183 (2018) **DOI:10.1016/j.addma.2017.12.006**.

[66] Abou-Ali, A.M., Lee, D.W., Abu Al-Rub, R.K. On the effect of lattice topology on mechanical properties of sls additively manufactured sheet-, ligament-, and strut-based polymeric metamaterials. *Polymers* 14 4583 (2022) **DOI:10.3390/polym14214583**.

[67] Zou, Z., Reid, S.R., Tan, P.J., Li, S., Harrigan, J.J. Dynamic crushing of honeycombs and features of shock fronts. *Int J Impact Eng* 36 165-176 (2009) DOI:10.1016/j.ijimpeng.2007.11.008.

[68] Tan, P.J., Reid, S.R., Harrigan, J.J., Zou, Z., Li, S. Dynamic compressive strength properties of aluminium foams. Part I-experimental data and observations. *J Mech Phys Solids* 53 2174-2205 (2005) **DOI:10.1016/j.jmps.2005.05.007**.

[69] Khaderi, S.N., Deshpande, V.S., Fleck, N.A. The stiffness and strength of the gyroid lattice. *Int J Solids Struct* 51 3866-3877 (2014) **DOI:10.1016/j.ijsolstr.2014.06.024**.

[70] Al-Ketan, O., Rowshan, R., Abu Al-Rub, R.K. Topology-mechanical property relationship of 3D printed strut, skeletal, and sheet based periodic metallic cellular materials. *Addit Manuf* 19 167-183 (2018) **DOI:10.1016/j.addma.2017.12.006**.

[71] Deshpande, V.S., Ashby, M.F., Fleck, N.A. Foam topology: bending versus stretching dominated architectures. *Acta Mater* 49 1035-1040 (2001) **DOI:10.1016/S1359-6454(00)00379-7**.

[72] Cai, Z., Liu, Z., Hu, X., Kuang, H., Zhai, J., 2019. The effect of porosity on the mechanical properties of 3D-printed triply periodic minimal surface (TPMS) bioscaffold. *Bio-Des Manuf* 2 242-255 (2019) **DOI:10.1007/s42242-019-00054-7**.

[73] Zhang, C., Jiang, Z., Zhao, L., Guo, W., Jiang, Z., Li, X., et al. Mechanical characteristics and deformation mechanism of functionally graded triply periodic minimal surface structures fabricated using stereolithography. *Int J Mech Sci* 208 106679 (2021) **DOI:10.1016/j.ijmecsci.2021.106679**.

[74] Fu, J., Sun, P., Du, Y., Li, H., Zhou, X., Tian, Q. Isotropic design and mechanical characterization of TPMS-based hollow cellular structures. *Compos Struct* 279 114818 (2022) **DOI:10.1016/j.compstruct.2021.114818**.

[75] Zaharin, H.A., Abdul Rani, A.M., Azam, F.I., Ginta, T.L., Sallih, N., Ahmad, A., et al. Effect of unit cell type and pore size on porosity and mechanical behavior of additively manufactured Ti6Al4V scaffolds. *Materials* 11 2402 (2018) **DOI:10.3390/ma11122402**.

[76] Araya-Calvo, M., Järvenpää, A., Rautio, T., Morales-Sanchez, J.E., Guillen-Girón, T. Comparative fatigue performance of as-built vs etched Ti64 in TPMS-gyroid and stochastic structures fabricated via PBF-LB for biomedical applications. *Rapid Prototyp J* 30 217-230 (2024) **DOI:10.1108/RPJ-04-2024-0152**.

[77] Li, Y., Liu, B., Li, Z., Kuai, Z., Du, W., Zhang, Q., et al. Design and compression behavior exploration of skeletal and sheet triply periodic minimal surface structures. *Adv Eng Mater* 26 2301589 (2024) **DOI:10.1002/adem.202301589**.

[78] Heinl, P., Müller, L., Körner, C., Singer, R.F., Müller, F.A. Cellular Ti-6Al-4V structures with interconnected macro porosity for bone implants fabricated by selective electron beam melting. *Acta Biomater* 4 15361544 (2008) **DOI:10.1016/j.actbio.2008.03.013**.

[79] Heinl, P., Körner, C., Singer, R.F. Selective Electron Beam Melting of Cellular Titanium: Mechanical Properties. *Adv Eng Mater* 10 882-888 (2008) **DOI:10.1002/adem.200800137**.

[80] Parthasarathy, J., Starly, B., Raman, S., Christensen, A. Mechanical evaluation of porous titanium (Ti6Al4V) structures with electron beam melting (EBM). *J Mech Behav Biomed Mater* 3 249-259 (2010) **DOI:10.1016/j.jmbbm.2009.10.006**.

[81] Cheng, X.Y., Li, S.J., Murr, L.E., Zhang, Z.B., Hao, Y.L., Yang, R., et al. Compression deformation behavior of Ti-6Al-4V alloy with cellular structures fabricated by electron beam melting. *J Mech Behav Biomed Mater* 16 153-162 (2012) **DOI:10.1016/j.jmbbm.2012.10.005**.

[82] Benedetti, M., du Plessis, A., Ritchie, R.O., Dallago, M., Razavi, N., Berto, F. Architected cellular materials: A review on their mechanical properties towards fatigue-tolerant design and fabrication. *Mater Sci Eng R-Rep* 144 100606 (2021) **DOI:10.1016/j.mser.2021.100606**.

[83] Klemenc, J. Influence of fatigue-life data modelling on the estimated reliability of a structure subjected to a constant-amplitude loading. *Reliab Eng Syst Saf* 142 238-247 (2015) **DOI:10.1016/j.ress.2015.05.026**.

[84] Soro, N., Saintier, N., Merzeau, J., Veidt, M., Dargusch, M.S. Quasi-static and fatigue properties of graded Ti-6Al-4V lattices produced by laser powder bed fusion (LPBF). *Addit Manuf* 37 101653 (2021) **DOI:10.1016/j.addma.2020.101653**.

[85] Ren, Y., Li, Y., Yang, L., Chen, Y., Yan, C., Liu, B., et al. Compressive properties and fatigue performance of NiTi lattice structures optimized by TPMS. *Mater Sci Addit Manuf* 3 3380 (2024) **DOI:10.36922/msam.3380**.

[86] Zhao, S., Li, S.J., Hou, W.T., Hao, Y.L., Yang, R., Misra, R.D.K. The influence of cell morphology on the compressive fatigue behavior of Ti-6Al-4V meshes fabricated by electron beam melting. *J Mech Behav Biomed Mater* 59 251-264 (2016) **DOI:10.1016/j.jmbbm.2016.01.034**.

[87] Jiang, J., Cao, Z., Wu, J., Lu, H., Zhang, J. Investigation of torsional and fatigue resistance properties based on triply periodic minimal surfaces (TPMS). *J Phys Conf Ser* 2879 012043 (2024) **DOI:10.1088/1742-6596/2879/1/012043**.

[88] Bobbert, F.S.L., Lietaert, K., Eftekhari, A.A., Pouran, B., Ahmadi, S.M., Weinans, H., et al. Additively manufactured metallic porous biomaterials based on minimal surfaces: A unique combination of topological, mechanical, and mass transport properties. *Acta Biomater* 53 572-584 (2017) **DOI:10.1016/j.actbio.2017.02.024**.

[89] Tilton, M., Borjali, A., Griffis, J.C., Varadarajan, K.M., Manogharan, G.P. Fatigue properties of Ti-6Al-4V TPMS scaffolds fabricated via laser powder bed fusion. *Manuf Lett* 37 32-38 (2023) **DOI:10.1016/j.mfglet.2023.06.005**.

[90] Emanuelli, L., Babaei, M., De Biasi, R., du Plessis, A., Trivisonno, A., Agostinacchio, F., et al. Optimising β-Ti21S alloy lattice structures for enhanced femoral implants: A study on mechanical and biological performance. *Materials* 18 170 (2025) **DOI:10.3390/ma18010170**.

[91] Liu, Z., Gong, H., Gao, J. Enhancement in the fatigue resistances of triply periodic surfaces-based scaffolds. *Int J Mech Sci* 245 108119 (2023) **DOI:10.1016/j.ijmecsci.2023.108119**.

[92] Jiang, X.P., Wang, X.Y., Li, J.X., Li, D.Y., Man, C.S., Shepard, M.J., et al. Enhancement of fatigue and corrosion properties of pure Ti by sandblasting. *Mater Sci Eng A* 429 30-35 (2006) **DOI:10.1016/j.msea.2006.04.024**.

[93] Was, G.S., Pelloux, R.M. The Effect of shot peening on the fatigue behavior of alloy 7075-T6. *Metall Trans A* 10 656-658 (1979) **DOI:10.1007/BF02658332**.

[94] Ni, X., Sun, Q., Wang, J., Zhang, D., Jin, X., Yang, Q., et al. Development and characterization of minimal surface tantalum scaffold with high strength and superior fatigue resistance. *J Mater Res Technol* 36 1226-1239 (2025) **DOI:10.1016/j.jmrt.2025.03.108**.

[95] Polley, C., Radlof, W., Hauschulz, F., Benz, C., Sander, M., Seitz, H. Morphological and mechanical characterisation of three-dimensional gyroid structures fabricated by electron beam melting for the use as a porous biomaterial. *J Mech Behav Biomed Mater* 125 104882 (2022) **DOI:10.1016/j.jmbbm.2021.104882**.

[96] Mahmoud, D., Al-Rubaie, K.S., Elbestawi, M.A. The influence of selective laser melting defects on the fatigue properties of Ti6Al4V porosity graded gyroids for bone implants. *Int J Mech Sci* 193 106180 (2021) **DOI:10.1016/j.ijmecsci.2020.106180**.

[97] Kök, H.I., Kick, M., Akbas, O., Stammkötter, S., Greuling, A., Stiesch, M., et al. Reduction of stress-shielding and fatigue-resistant dental implant design through topology optimization and TPMS lattices. *J Mech Behav Biomed Mater* 165 106923 (2025) **DOI:10.1016/j.jmbbm.2025.106923**.

Acknowledgement *The authors acknowledge the financial support of the Research Core Funding (No. P2-0063), Basic Postdoc Research Project (No. Z2-50082) and Basic Research Project (No. J2-60049) from the Slovenian Research and Innovation Agency.*

Received: 2025-04-25, Revised: 2025-09-05, Accepted: 2025-09-24
as a Review Scientific Paper (1.02).

Data Availability *All data supporting the study's findings are included in the paper.*

Author Contribution *Žiga Žnidarič: Writing – original draft, Investigation; Branko Nečemer: Supervision and Resources; Nejc Novak: Supervision and Resources; Srečko Glodež: Conceptualization Writing – review & editing; Matej Vesenjak: Writing – review & editing.*

AI Assisted Writing *AI tool ChatGPT was used for grammar and language editing, as well as picture editing. All content and conclusions remain the responsibility of the authors.*

Utrujanje metamaterialov na osnovi trojno-periodičnih minimalnih površin (TPMS) - Pregled

Povzetek *Članek predstavlja celovit pregled obnašanja metamaterialov, zasnovanih na trojno-periodičnih minimalnih površinah (TPMS), pri obremenitvah zaradi utrujanja, s posebnim poudarkom na vplivu tehnologije njihove izdelave. V prispevku so podrobno analizirane različne geometrije TPMS, ki so v zadnjih letih pridobile veliko pozornosti zaradi izjemnega razmerja med trdnostjo in maso ter sposobnosti nadzora mehanskih lastnosti s prilagajanjem geometrijskih parametrov. Predstavljene so sodobne metode izdelave TPMS struktur s poudarkom na dodajalnih tehnologijah, kjer je za osnovni material privzeta titanova in jeklena zlitina. Za vsak material so navedene ključne prednosti, omejitve in vpliv proizvodnega procesa na končne mehanske lastnosti struktur. Poleg tega članek obravnava mehanske značilnosti celičnih gradiv, pri čemer je poseben poudarek namenjen TPMS strukturam, ki zaradi svoje topologije omogočajo enakomerno porazdelitev napetosti in visoko absorpcijo mehanske energije. V nadaljevanju so predstavljene najnovejše raziskave in ugotovitve glede vedenja TPMS metamaterialov pri utrujanju. Analiza kaže, da TPMS celične strukture izkazujejo bistveno boljšo odpornost proti utrujanju v primerjavi s konvencionalnimi celičnimi metamateriali. Ključni razlog za to je njihova gladka, zvezna geometrija brez ostrih robov ali stičnih točk, kar zmanjšuje koncentracijo napetosti in omogoča bolj homogeno porazdelitev napetosti skozi celotno strukturo. Na podlagi predstavljenih rezultatov lahko zaključimo, da TPMS metamateriali predstavljajo perspektivno smer razvoja naprednih lahkih konstrukcijskih materialov, ki združujejo visoko trdnost, odpornost proti utrujanju in prilagodljivost geometrije glede na specifične zahteve uporabe.*

Ključne besede *celične strukture, TPMS metamateriali, proizvodne tehnologije, mehanska karakterizacija, obnašanje pri utrujanju*

Contents

9 770039 248001
ISSN 0039-2480

https://www.sv-jme.eu/